AFAL-TR-76-33

INFRARED DETECTOR RESEARCH

Department of Physics
Syracuse University
Syracuse, New York

AUGUST 1976

Final Report April 1972 - September 1976

Approved for public release; distribution unlimited

Air Force Avionics Laboratory
Air Force Systems Command
Wright Patterson Air Force Base, Ohio

DISCLAIMER NOTICE

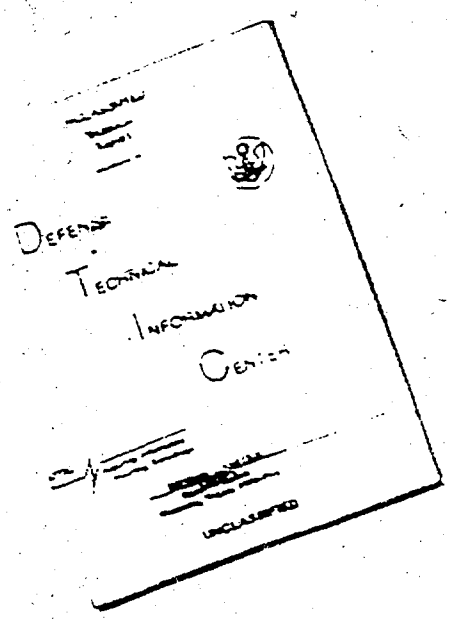

THIS DOCUMENT IS BEST QUALITY AVAILABLE. THE COPY FURNISHED TO DTIC CONTAINED A SIGNIFICANT NUMBER OF PAGES WHICH DO NOT REPRODUCE LEGIBLY.

NOTICE

When Government drawings, specifications, or other data are used for any purpose other than in connection with a definitely related Government procurement operation, the United States Government thereby incurs no responsibility nor any obligation whatsoever; and the fact that the government may have formulated, furnished, or in any way supplied the said drawings, specifications, or other data, is not to be regarded by implication or otherwise as in any manner licensing the holder or any other person or corporation, or conveying any rights or permission to manufacture, use, or sell any patented invention that may in any way be related thereto.

This report has been reviewed by the Information Office (OI) and is releasable to the National Technical Information Service (NTIS). At NTIS, it will be available to the general public, including foreign nations.

This technical report has been reviewed and is approved for publication.

THAD PICKENPAUGH, Project Engineer
Electro-Optic Detectors Group
Electro-Optics Technology Branch

DONALD J. PEACOCK, Actg. Chief
Electro-Optic Detectors Group
Electro-Optics Technology Branch

FOR THE COMMANDER

WILLIAM C. SCHOONOVER, Chief
Electro-Optics Technology Branch
Electronic Technology Division

Copies of this report should not be returned unless return is required by security considerations, contractual obligations, or notice on a specific document.

SECURITY CLASSIFICATION OF THIS PAGE (When Data Entered)

REPORT DOCUMENTATION PAGE

READ INSTRUCTIONS BEFORE COMPLETING FORM

1. REPORT NUMBER: AFAL-TR-76-83	2. GOVT ACCESSION NO.
3. RECIPIENT'S CATALOG NUMBER	
4. TITLE (and Subtitle): INFRARED DETECTOR RESEARCH	5. TYPE OF REPORT & PERIOD COVERED: FINAL REPORT April 1972-September 1975
6. PERFORMING ORG. REPORT NUMBER	
7. AUTHOR(s): Henry Levinstein, Timothy Braggins, Kevin Riley, Moshe Lanir	8. CONTRACT OR GRANT NUMBER(s): F33615-73-C1066
9. PERFORMING ORGANIZATION NAME AND ADDRESS: Department of Physics, Syracuse University, Syracuse, N. Y. 13210	10. PROGRAM ELEMENT, PROJECT, TASK AREA & WORK UNIT NUMBERS
11. CONTROLLING OFFICE NAME AND ADDRESS: Air Force Avionic Laboratory, Wright-Patterson Air Force Base, OH 45433	12. REPORT DATE: August 1976
	13. NUMBER OF PAGES: 31
14. MONITORING AGENCY NAME & ADDRESS(if different from Controlling Office)	15. SECURITY CLASS. (of this report): UNCLASSIFIED
	15a. DECLASSIFICATION/DOWNGRADING SCHEDULE

16. DISTRIBUTION STATEMENT (of this Report)

UNLIMITED

DISTRIBUTION STATEMENT A
Approved for public release;
Distribution Unlimited

17. DISTRIBUTION STATEMENT (of the abstract entered in Block 20, if different from Report)

UNLIMITED

18. SUPPLEMENTARY NOTES

19. KEY WORDS (Continue on reverse side if necessary and identify by block number)

Infrared detectors
Boron-doped Silicon
Mobility
PbSnTe
HgCdTe
Crystal growth
Photovoltaic response
Photoconductivity

20. ABSTRACT (Continue on reverse side if necessary and identify by block number)

PART I. The carrier concentration and mobility, as measured by the Hall effect, have been analyzed by computer for a series of boron-doped silicon samples with impurity densities between 10^{13} cm^{-3} and 10^{18} cm^{-3}. The determination of the density of compensating donors from both types of analysis is in good agreement. The effect of the non-parabolicity of the silicon valence band on the temperature dependence of the mobility has been investigated. Good agreement as to the temperature dependence of the mobility has been found when the valence band non-parabolicity is taken into account in the analysis of the mobility.

DD FORM 1 JAN 73 1473 EDITION OF 1 NOV 65 IS OBSOLETE

UNCLASSIFIED

20 ABSTRACT (cont.)

(PART I.) Scattering by ionized and neutral impurities and acoustic and optical phonons has been included in the mobility analysis.

PART II. Three types of metal impurities were diffused into lead-tin telluride and their effect on the electrical and optical properties of the host material was investigated. It was observed that antimony, cadmium and a mixture of cadmium and indium all can turn p-type lead-tin telluried into n-type, but the physical characteristics of the tin telluride into n-type, but the physical characteristics of the doped materials differ considerably. When Cd was diffused into 10^{19} cm^{-3} p-type (PbSn)Te, we obtained material with free electron density of 10^{17} cm^{-3}. Comparison of the temperature dependence of the Hall, coefficient, mobility and the optical energy gap revealed close similarity to results obtained from measurements on pure annealed n-type (Pb,Sn)Te. Antimony diffused lead-tin telluried, on the other hand, has free electron concentration of 10^{19} cm^{-3} which is the same order of magnitude as the hole density of the as-grown crystal. In both cases, the as-grown and the Sb diffused materials, strong degeneracy is observed. Using Cd and Sb diffusion techniques, sensitive photodiodes have been fabricated and detailed photoresponse measurements were performed. From these data the fundamental absorption edge behavior was investigated. The results have been compared with data obtained from transmission measurements and with theoretical calculations. In the case of the degenerate material a shift in the fundamental absorption edge was observed. This behavior is in agreement with our calculations based on a model suggested by Burstein. Photoconductivity measurements on the above materials could not be done since the free carrier concentration was too high. However, when we diffused lead-tin telluride with a source of cadmium-indium alloy, a resistivity of 10^{3} ohm-cm and carrier density of 10^{14} were measured at 77K. Photoconductivity measurements were carried out on this material. From spectral response analysis and x-ray examination it was concluded that both the optical energy gap and the crystal lattice parameter increased as a result of the diffusion.

PART III. Crystal growth of $Hg_{1-x}Cd_xTe$ by means of solid state recrystallization and slush recrystallization has been examined in this study. For solid state recrystallization the parameters were found to be the quench rate, the anneal temperature and the partial pressure of mercury at the anneal temperature. For material with $x \approx .20$ optimal values for these parameters are 50 ℓ/min. 690°C, and 20 atm. respectively. For slush recrystallization the critical parameter is the temperature gradient in which crystal growth occurs. A gradient of 10°C/cm has been used in this study. Crystal quality was determined by Berg-Barrett X-ray topography.

FORWARD

Work on infrared detectors was started at Syracuse University in February 1948 under Air Force contract W33-038 AC 15160. It was continued under successive Air Force contracts until 1975. The research has represented a continuing effort in the development and analysis of new infrared detector materials, the construction of detectors from these materials as well as measurement and analysis of the parameters of these detectors. The two most important accomplishments of the work at Syracuse University have been the development of the first liquid nitrogen cooled detector in the 3-6 μm range to be used in the U. S. aircraft (PbTe), and the first detector in the 8-14 μm range which did not require liquid helium but could be operated with mechanical coolers (Ge:Hg). In addition, a great deal of progress has been made in developing test techniques, in preparing and understanding the behavior of impurities in InSb and in Ge. Most recently, p and n type impurities in silicon have been studied. Currently both HgCdTe and PbSnTe are being prepared in our laboratory and an effort is being made to prepare better and more reproducible material and to understand the behavior of both materials.

During the tenure of the Air Force Contracts there have been more than 50 publications in scientific journals. Most have been results of our research, some have been review papers. In addition, there have been many invited talks at scientific meetings such as the American Optical Society, the Symposium on Molecular Spectroscopy, the National Aerospace Conference and at classified meetings such as IRIS. Below are some representative publications.

High-Frequency Resistance of Photoconducting Films

R. Broudy and H. Levinstein, Phys. Rev. 94, 290-292 (1954).

Effect of Oxygen on the Electrical Properties of Lead Telluride Films

D. E. Bode and H. Levinstein, Phys. Rev. 96, 259-265 (1954).

Infrared Properties of Gold in Gold in Germanium

L. F. Johnson and H. Levinstein, Phys Rev. 117, 1191-1203 (1960).

Surface-Dependent 1/f Noise in Germanium

A. U. MacRae and H. Levinstein, Phys. Rev. 119, 62-69 (1960).

A Status Report on Infrared Detectors (Review Article)

P. Bratt, W. Engeler, A. U. MacRae, J. Pehek, H. Levinstein

Infrared Phys. 1 (1961).

Photoconductivity in P-Type Indium Antimonide with Deep Acceptor Impurities

W. Engeler, C. R. Stannard, H. Levinstein, Journ. Phys. Chem. Sol.

22, 249-254 (1961).

Oscillatory Photoconductivity in InSb

W. Engeler, C. R. Stannard, H. Levinstein, Phys. Rev. Letters 7, (1961).

Preparation and Properties of Mercury Doped Germanium

S. Borrello and H. Levinstein, J. Appl. Phys. 33, 2947-2950 (1962).

Extrinsic Detectors (Invited Review Article)

H. Levinstein, Appl. Optics, 4, 639 (1965).

Recombination Radiation from InSb

J. Pehek, H. Levinstein, Phys. Rev. 140, A576-A586 (1965).

Oscillatory Photoconductivity in InSb

H. J. Stocker, C. R. Stannard, H. Levinstein, Phys. Rev. 150, 163 (1966).

Measurement of Lifetime in Photoconductors by Means of Optical Beating

C. Penchina and H. Levinstein, Infrared Physics 6, 173 (1966).

Photoconductivity in InSb - GaSb and InAs - GaAs alloys

J. Wrobel and H. Levinstein, Infrared Physics 7, 201 (1967).

Infrared Detectors (Review Article)

H. Levinstein, Analytical Chemistry 41, 81A (1969).

Extended Wavelength Tuning of PbSnTe Lasers

P. Norton, P. Chia, T. Braggins and H. Levinstein, Appl. Lett. 158 (

Thermalization Time of Hot Photoexcited Holes in p-Type Germanium

P. Norton, and H. Levinstein, Phys. Rev. B6, 478 (1972).

Determination of Compensation Density by Hall and Mobility Analysis in Copper Doped Germanium, P. Norton and H. Levinstein, Phys Rev. B6, 470 (1972).

Recombination Cross Section for Holes at Singly Ionized Copper Impuriti[illegible] in Germanium, P. Norton and H. Levinstein, Phys. Rev. 6, 489 (197[illegible]

Recombination of Electrons at Ionized Donors in Silicon at Low Temperatu[illegible]

P. Norton, T. Braggins, H. Levinstein, Phys. Rev. Letters 30 (197[illegible].

Impurity and Lattice Scattering Parameters as Determined from Hall and Mobility Analysis in n-Type Silicon, P. Norton, T. Braggins, H. Levinstein, Phys. Rev. B8, 5632 (1973).

Infrared Detectors in Remote Sensing (Invited Review Paper)

H. Levinstein and J. Mudar, Prov. IEEE 63, 6 (1975).

A by-product of this work on detectors has been the training of a large number of scientists on a Ph. D., M. S. and B. S. level who now staff many of the infrared and semiconductor laboratories in government and industry and universities. A representative list is given below

Santa Barbara Research Center

Donald Bode, Peter Bratt, Howard Davis, Frank Renda, Paul Chia, Arthur Lockwood.

Bell Telephone Labs

Leo F. Johnson, Alfred U. MacRae, Paul Norton.

Texas Instruments

Werner Beyen, Seb Borello, Joseph Wrobel.

Lockheed

Wayne Rudolf, Sherman Golub.

Honeywell

Robert Broudy.

General Electric

Channing Dichter, William Engeler.

Westinghouse

Timothy Braggins.

U. S. Government

Marvin Lasser (Chief Scientist U. S. Army), Dean Mitchell (NSF). John Stannard (NRL), Paul LoVecchio (NVL-U. S. Army).

University

Carl Stannard (SUNY, Binghamton), Claude Penchina (Univ. of Mass.)

Because of the diversity of work performed on this contract, this final report is being issued in four parts, each with its own table of contents and references. Part I is "Analysis of Carrier Concentration and Mobility in Boron-doped Silicon". Part II is "Absorption Edge Shift in Heavily Doped Lead-Tin Telluride". Part III is "Crystal Growth and Analysis of HgCdTe". Part IV, the Appendix, is a reprint of a paper "Impurity and Lattice Scattering Parameters as Determined from Hall and Mobility Analysis in "n" Type Silicon". This work was performed while this contract was in force. The work in Part I of this report was performed by Timothy Braggins, in Part II by Moshe Lanir, and Part III by Kevin Riley. Mr. Chin Shih Huang is currently working on junction characteristics of PbSnTe. This work is of preliminary nature and is not reported here.

As Project Director of this and preceeding contracts beginning in 1948, I would like to thank my students both past and present for their efforts. Without them, this work would not have been possible. I would also like to express my appreciation to the administrators at Wright Patterson AFB who, over the years, have approved contracts and permitted them to continue uninterrupted until 1975. Above all I would like to thank Mr. Thad Pickenpaugh who, as project engineer, has helped me when he could, has encouraged me when I needed encouragement and has seen to it that our work has gone on smoothly and successfully.

Henry Levinstein

Project Director

TABLE OF CONTENTS

PART I

ANALYSIS OF CARRIER CONCENTRATION AND MOBILITY IN BORON-DOPED SILICON

TABLE OF CONTENTS (cont.)

TABLE OF CONTENTS (cont.)

PART III

PREPARATION AND ANALYSIS OF HgCdTe

TABLE OF CONTENTS (cont.)

PART I

ANALYSIS OF CARRIER CONCENTRATION AND MOBILITY IN BORON-DOPED SILICON

CHAPTER I

INTRODUCTION

The goal of this study has been to measure and compare with theory the temperature dependence of the hole mobility in p-type silicon. Under the influence of an electric field the free charge carriers in a semiconductor will acquire a drift velocity. This drift velocity is the net result of the momentum gained by the carrier from the electric field and the momentum lost due to collisions which tend to randomize the carrier's momentum. The mobility is defined as the magnitude of the drift velocity per unit electric field. The different types of collisions which the carriers undergo will determine the drift velocity and thus the mobility. For temperatures above absolute zero the inherent thermal motion of the crystal lattice will provide an upper limit to the mobility. Also, impurities, which disrupt the periodicity of the lattice, can cause scattering of the carriers. At low temperatures scattering by ionized and neutral impurities will predominate, while at higher temperatures scattering by lattice vibrations(acoustic and optical phonons) will predominate. Thus, in calculating the mobility over substantial temperature intervals one must account for all of the above scattering mechanisms.

The Hall effect has been used to measure the carrier concentration and mobility as a function of temperature for a series of boron-doped silicon samples. Boron-doped silicon was chosen since boron is the shallowest acceptor in silicon and this material is widely available. Boron is a Group III substitutional acceptor in silicon. The four valence electrons of the Group IV silicon atom form covalent bonds with its four

nearest neighbors of the diamond-type crystal lattice. When a boron atom replaces one of the silicon atoms, there will be only three electrons available for the covalent bonds and consequently one bond will be incomplete. Boron is therefore termed an acceptor because it can "accept" an additional electron to complete the covalent bond. In realistic material there also will be Group V impurities which can "donate" their extra electron not required for bonding with the silicon atoms. When there are more acceptors than donors the material will be p-type. The extra electrons from the donors can complete the bond missing due to the boron atoms. This process is call compensation. The missing electron from an uncompensated boron acceptor can be considered as a positively charged hole. At low temperatures the hole will be bound to the boron impurity atom by the coulomb potential. However, at high temperatures the hole will have enough thermal energy to be excited from the bound state and move freely throughout the crystal. Thus, as the temperature changes, the density of thermally excited carriers can change by many orders of magnitude. From an analysis of the data for carrier concentration as a function of temperature, the density of acceptors and compensating donors may be obtained.

The mobility at low temperatures is sensitive to the density of compensating donors due to ionized impurity scattering. A comparison of the calculated mobility with the measured mobility will also allow us to determine the density of compensating donors. Agreement in determining the donor density by the two methods is one means of evaluating the validity of the mobility theory. The mobility theory is also evaluated by a detailed comparison between the temperature dependence of the

calculated and measured mobility.

The different scattering mechanisms which contribute to the mobility have different temperature and energy dependences, and the computational tasks involved in these calculations can become quite formidable. For this reason we have used digital computers utilizing numerical methods and curve fitting techniques in analyzing our data.

Transport properties such as mobility are related to the crystal's band structure through the particular energy versus wave vector relationship. For the silicon valence band the constant energy surfaces are warped rather than spherical and at higher energies away from the band edge the valence band becomes non-parabolic. This non-parabolicity has a marked effect on the temperature dependence of the mobility and plays a key role in the explanation of our experimental results. The valence band structure is considered in detail in Chapter II. The approximations we have used in describing the valence band and the effect of the valence band structure on the effective mass of the carriers is discussed. The energy level of the boron acceptor state and its excited state spectrum are also given.

In Chapter III we present the theory by which we have calculated the mobility. The relaxation times for the different types of scattering as modified by a non-parabolic band structure are given. The adjustable parameters used to compare the theory with the experimental results are explained. Also presented are the details of the analysis of carrier concentration as a function of temperature.

The experimental techniques and apparatus we have used in measuring the Hall effect are described in Chapter IV. The constraints of theory

and their effect on our measurements are discussed.

Our experimental results, namely carrier concentration and mobility as a function of temperature, are given in Chapter V. The mobility theory formulated in Chapter III is compared with our experimental results and the determination of the parameters used in the mobility analysis is discussed. Good agreement is found for the density of compensating donors when the mobility analysis is compared with the analysis of the carrier concentration data.

Our results are examined in the light of the published work of other authors in Chapter VI.

We present a summary of our results and the conclusions drawn from them in Chapter VII.

CHAPTER II

THE SILICON VALENCE BAND

A. Valence Band Structure

The valence band structure of silicon has been calculated from theory by Kane.[1] It consists of three bands which are termed the light hole band, the heavy hole band and the split-off band. The light and heavy hole bands are degenerate at the Brillouin zone center ($\vec{k} = 0$) while the third band is displaced downward in energy (split off) at $\vec{k} = 0$ by the spin-orbit coupling. The constant energy surfaces of the light and heavy hole bands are warped rather than spherical. They can be described for small $\vec{k}$ by the familiar energy versus wave vector relationship

$$E = Ak^2 \pm [B^2k^4 + C^2(k_x^2 k_y^2 + k_y^2 k_z^2 + k_z^2 k_x^2)]^{1/2} , \qquad (1)$$

where $k = |\vec{k}|$, $\pm$ corresponds to the heavy and light hole bands respectively, and A, B, and C are the inverse mass band parameters. Although warped, the bands are parabolic ($E \propto k^2$) as described by equation (1). However, for larger values of $\vec{k}$ away from the band edge the bands become non-parabolic. Indeed for certain directions in $\vec{k}$-space, the light hole band becomes almost as heavy as the heavy hole band.[1]

Kane has determined the valence energy band structure of silicon from the general secular equation which can be written in a convenient form[2] where $\vec{k}$ can easily be represented in polar coordinates k, θ, ϕ. In the following we have slightly modified the notation of Asche and Borzeszkowski.[3]

The secular equation is

$$ak^6 + bk^4 + ck^2 + d = 0 \,, \tag{2}$$

with

$$a = (A + 2B)(A - B)^2 - 3C^2\mu(A - B) + (N - 3B^2)(2N + 3B)\,q \,,$$

$$b = 3(A^2 - B^2 - \mu C^2)(E - \tfrac{\Delta}{3}) \,,$$

$$c = 3AE(E - \tfrac{2}{3}\Delta) \,,$$

$$d = E^2 (E - \Delta) \,,$$

$$\mu = \sin^2\theta(\sin^2\theta\cos^2\phi\sin^2\phi + \cos^2\theta) \,,$$

$$q = \sin^4\theta\cos^2\theta\cos^2\phi\sin^2\phi \,,$$

where E is the hole energy counted positively from the band edge (as will be done so throughout this work), Δ is the spin-orbit splitting energy, A, B, and C are the inverse mass band parameters, and N is a cyclotron resonance constant related to B and C by $N^2 = 3C^2 + 9B^2$. The solutions of equation (2) are complicated functions of energy and direction and only approximate analytical solutions have been obtained.[4] If the interaction between the light and heavy hole bands and the split-off band is ignored, the resulting general secular equation will factor into a part quadratic in k^2 and a part linear in k^2. The E versus k^2 relationship given by equation (1) is an exact solution of the quadratic factor while the linear factor describes the split-off band.[5] In this limit ($E << \Delta$), all three bands become parabolic. We shall consider this limit

in choosing the form of our solution of equation (2).

For the mobility calculation we have simplified the band structure by isotropically averaging over the different directions of $\vec{k}$. The spherically averaged values of the angular dependent quantities μ and q together with the other constants required in equation (2) are listed in Table I. Taking the energy, E, as a parameter, we have solved for the roots of equation (2) using the Newton-Raphson method. The spherically symmetric solutions, $k^2 = F(E)$, for the three bands are shown in Figure 1. For a parabolic band a graph of E versus k^2 would yield a straight line. The departure from linearity, thus demonstrating the non-parabolicity of the bands, is evident from Figure 1. For a non-parabolic band the effective mass is no longer a constant but depends on energy. The appropriate energy dependent effective mass for a spherical non-parabolic energy band is given by[6,7]

$$1/m^*(E) = (1/\hbar^2 k)\partial E/\partial k. \qquad (3)$$

As mentioned above the bands become parabolic as the energy approaches zero. With this limit in mind we define the solutions of the secular equation to be of the form

$$k_i^2 = (2m_i^*/\hbar^2)\gamma_i(E) \ , \qquad (4)$$

where i is an index for the band considered, m_i^* is the effective mass in a region close to the band edge, and $\gamma_i(E)$ is a function of the energy such that $\lim_{E\to 0} \gamma_i(E) = E$. With the dispersion relation in a form as given in equation (4) , we obtain for the energy dependent effective mass

$$m_i^*(E) = m_i^* \gamma_i'(E) \quad , \tag{5}$$

where $\gamma_i'(E) = \partial\gamma_i(E)/\partial E$. In the limit of low energies the dispersion relation (4) reduces to that of a spherical parabolic band with an effective mass m_i^*. The band non-parabolicity can be characterized by the change in slope of the E versus k^2 curve of Figure 1 as the energy increases. This change in slope, $(\partial k_i^2/\partial E)/(2m_i^*/\hbar^2) = \gamma_i'(E)$, is plotted as a function of energy in Figure 2. The parabolic limit reached at low energies is clearly evident.

For the band structure as given in Figure 1, we have obtained for the band-edge average effective mass of the light holes, $m_1^* = .153\ m_e$, and of the heavy holes, $m_2^* = .503\ m_e$, where m_e is the free electron mass. With these effective masses and the k^2 versus E values from Figure 1, we have fit k^2 to a polynomial in powers of E. These polynomial expansions for the $\gamma_i(E)$ are given in Appendix I. As the split-off band is separated in energy at $\vec{k} = 0$ from the light and heavy hole bands, it is of considerably less importance in transport calculations. For this reason we have assumed a parabolic dispersion relation

$$k_3^2 = (2m_3^*/\hbar^2)(E - \Delta) \tag{6}$$

with an effective mass $m_3^* = .234\ m_e$. Thus, in the notation used for the dispersion relation in equation (4), we have $\gamma_3(E) = E - \Delta$.

B. Impurity states

Impurity states in silicon and germanium have been of considerable theoretical and experimental interest. The ground state and excited state binding energies and the degeneracies of these states have been

calculated for neutral hydrogenic acceptors in silicon by Schechter[8] and Mendelson and Shultz.[9] Both authors have used a variational approach to find the energy eigenvalues of the impurity state in the effective mass approximation. Some recent work has emphasized the difference between terms in the effective mass Hamiltonian with cubic symmetry and those with cubic as well as spherical symmetry.[10, 11] Other work has involved the use of pseudopotential theory to describe the potential of the impurity atom.[12]

The spacing between the ground state and some of the excited states and the degeneracies of the states has been determined experimentally by an analysis of infrared absorption spectra.[13,14,15] These spacings are shown in Figure 3 for the boron impurity in silicon. The energy differences between the ground state and several of the excited states have been used in our analysis of the carrier concentration as a function of temperature. The formulation of the carrier concentration and mobility analysis are given in the following chapter.

CHAPTER III

FORMULATION OF MOBILITY AND CARRIER CONCENTRATION ANALYSIS

A calculation of the hole mobility in silicon is quite complex. The peculiarities of a degenerate, warped and non-parabolic valence band require a theory which has not yet been formulated in complete generality. Scattering by acoustic and optical phonons, and ionized and neutral impurities must all be accounted for to describe the mobility over wide temperature ranges. In addition, interband as well as intraband scattering must be considered. As each scattering mechanism has its own dependence on carrier energy, a simple closed form expression for the total mobility as a function of temperature cannot be obtained. We shall first discuss each of the four scattering mechanisms and then take up the task of combining them to compute the mobility. Lastly, we shall consider a method for the analysis of the carrier concentration as a function of temperature.

Using the spherically averaged valence band structure given in Chapter II, we have been able to remove the warped nature of the valence band from the mobility calculation. Using a spherical rather than a warped band has been considered by Costato et al.[16] to be a reasonable approximation since the ohmic mobility is, by symmetry for cubic crystals, a scalar quantity. Also, Lawaetz[17] has shown that the warped nature of the valence band will not alter the temperature dependence of the acoustic mobility but only its magnitude. As the magnitude of the acoustic phonon contribution to the mobility is a parameter which will be determined by fitting the mobility theory to the experimental data, such effects will be contained in this constant.

The non-parabolicity of the valence band also introduces an additional complexity. Acoustic phonon scattering in non-parabolic bands has been considered by Radcliffe.[18] Optical phonon and ionized impurity scattering have been considered by Barrie.[6] The procedure used by these authors to include the band non-parabolicity consisted of modifying the relaxation time for a given scattering process by replacing the energy independent effective mass of the parabolic band by the energy dependent effective mass of the non-parabolic band. Of course, the appropriate dispersion relation for the non-parabolic band, equation (4), also must be used in calculating the relaxation time in order to obtain the proper energy dependence. Zawadski and Szymanska[19] have pointed out that this is not the only correction which should be made. The relaxation time for elastic scattering can be written as $1/\tau(E) \propto \rho(E)W(E)$, where $\rho(E)$ is the density of states per unit energy and $W(E)$ is the scattering probability. Radcliffe and Barrie have correctly modified the density of states. However, the scattering probability must also be modified by using proper carrier wavefunctions for a non-parabolic band. Zawadski and Szymanska have calculated the relaxation times for several scattering processes for electrons in InSb taking these considerations into account. However, this has not been done for holes in non-parabolic, degenerate valence bands. In our calculation of the mobility we have used relaxation times appropriate to degenerate, parabolic valence bands and modified them according to the prescription of Barrie[6] and of Radcliffe.[18]

The relaxation time for a given scattering process is denoted by τ_{ij}^{a} where a is the scattering process under consideration and the

subcripts i and j indicate the initial and final band respectively of the scattered carrier. Thus, $i \neq j$ for interband scattering and $i = j$ for intraband scattering where $i,j = 1,2,3$ for the three bands considered. Interband scattering has been considered only between the light and heavy hole bands and only for the acoustic phonon scattering process. We shall now discuss each of the four scattering mechanisms and define their relaxation times.

We have based our treatment of the acoustic phonon scattering mechanism on the theory of Bir, Normantus and Pikus.[20] This theory differs from simpler treatments of mobility in degenerate valence bands in that different relaxation times are found for the light and heavy holes. Also, interband as well as intraband scattering is included. Using the procedure outlined by Bir et al., we have evaluated the relaxation times for scattering by acoustic phonons.[21] The relaxation times can be expressed in terms of a single constant, τ_o, which controls the overall magnitude of acoustic phonon scattering. We have included nonparabolicity in a manner similar to Radcliffe.[18] We thus obtain:

$$\frac{1}{\tau_{11}^{ac}} = \frac{1.61}{\tau_o} \gamma_1^{1/2}(x)\, \gamma_1'(x)\, T^{3/2} \tag{7a}$$

$$\frac{1}{\tau_{22}^{ac}} = \frac{.959}{\tau_o} \gamma_2^{1/2}(x)\, \gamma_2'(x)\, T^{3/2} \tag{7b}$$

$$\frac{1}{\tau_{12}^{ac}} = \frac{-.224}{\tau_o} \gamma_1^{1/2}(x)\, \gamma_1'(x)\, T^{3/2} \tag{7c}$$

$$\frac{1}{\tau_{21}^{ac}} = \frac{.224}{\tau_o}\left\{\frac{m_2^*(E)}{m_1^*(E)}\right\}^{5/2} \gamma_2^{1/2}(x)\, \gamma_2'(x)\, T^{3/2} \quad , \tag{7d}$$

$$\frac{1}{\tau_{33}^{ac}} = \frac{1}{\tau_o}\left(x - \frac{\Delta}{kT}\right)^{1/2} T^{3/2} \quad , \tag{7e}$$

where $x = E/kT$, $\gamma_i(x)$ is given by $\gamma_i(E) = kT\gamma_i(x)$, and $\gamma_i'(x) = \partial\gamma_i(x)/\partial x$.

The relaxation time for scattering by non-polar optical phonons has been given by Conwell.[22] Barrie[6] has discussed the modifications required for a non-parabolic band structure. The intraband relaxation time so obtained is:

$$\frac{1}{\tau_{ii}^{op}} = \frac{1}{\tau_o} T^{1/2} W\theta\left[n\, \gamma_i^{1/2}\left(x + \frac{\theta}{T}\right) \gamma_i'\left(x + \frac{\theta}{T}\right) + (n+1)\, \gamma_i^{1/2}\left(x - \frac{\theta}{T}\right) \gamma_i'\left(x - \frac{\theta}{T}\right)\right]$$

$$i = 1,2,3 \tag{8}$$

where $\theta = 730$ K is the zone-center optical phonon energy for silicon,[23] τ_o is the constant which determines the magnitude of the acoustic phonon scattering, W is the relative coupling strength of the holes to the optical phonon mode compared to the acoustic phonon mode, and $n = (e^{\theta/T} - 1)^{-1}$ is the number of optical phonons. The first term in the brackets in equation (8) corresponds to optical phonon absorbtion while the second term in the brackets corresponds to optical phonon emission and is included only when this is energetically possible ($x > \theta/T$).

Scattering by ionized impurities with a screened coulomb potential has been considered using the theory of Brooks,[24] Herring, and Dingle.[25] Relaxation times for several different impurity potentials have been calculated by Sclar[26] who has considered the approximations involved and the range of validity for the different theories. Barrie[6] has considered

the modifications required due to the non-parabolic band structure.

The relaxation time is:

$$\frac{1}{\tau_{ii}^{ion}} = \frac{N_I \pi q^4 \gamma_i'(x) \quad (kT\gamma_i(x))^{-3/2}}{\kappa^2 (2m_i^*)^{1/2}} [\ln(b_i + 1) - \frac{b_i}{b_i + 1}] \quad i = 1,2,3 \quad (9)$$

$$= \frac{1.764\times10^{-2} N_I \gamma_i^{-3/2}(x) \quad \gamma_i'(x) \quad T^{-3/2}}{(m_i^*/m_e)^{1/2}} [\ln(b_i + 1) - \frac{b_i}{b_i + 1}] ,$$

where $$b_i = \frac{2\kappa m_i^* (kT)^2 \gamma_i(x)}{\pi \hbar^2 q^2 p'} = \frac{5.014\times10^{14}}{p'} \frac{m_i^*}{m_e} T^2 \gamma_i(x) \quad , \quad (10)$$

$$p' = p + (p + N_d)[1 - (p + N_d)/N_a] \quad , \quad (11)$$

and $N_I = 2N_d + p$. N_a and N_d are the acceptor and donor concentrations respectively, p is the hole density, q is the magnitude of the electronic charge, and κ is the dielectric constant of silicon which we have taken as 11.7 in evaluating the above expressions.

Scattering by neutral impurities in semiconductors has been considered by Erginsoy[27] who analyzed the analogous problem of electron scattering by hydrogen atoms. Using a scaled Bohr radius he obtained

$$\frac{1}{\tau_N} = \left(\frac{\kappa \hbar^2}{m^* q^2}\right) \frac{20 \hbar}{m^*} N_N \quad , \quad (12)$$

where $N_N = N_a - N_d - p$ is the density of neutral impurities. Brooks[28] has suggested the use of the geometric mean mass for evaluating the scaled Bohr radius term while an effective mass appropriate to the mobility evaluation should be used for the other effective mass in the above equation. In evaluating the scaled Bohr radius, we have used the

density of states effective mass (here taken as $.59m_e$) and for the mobility mass we have used the appropriate energy dependent effective mass. Since acceptors in silicon are not strictly hydrogenic, we have also included an adjustable parameter, A, in the relaxation time for neutral scattering. This adjustable parameter has previously been found necessary in analyzing the mobility of deep impurities (copper) in germanium[29] and also for n-type impurities in silicon.[30] We thus have:

$$\frac{1}{\tau_{ii}^{N}} = \frac{2.423 \ \ 10^{-6} \ N_N}{A(m_i^*/m_e) \ \gamma_i'(x)} \quad i = 1,2,3 \ . \tag{13}$$

Having obtained relaxation times for the various scattering processes here considered, we must combine them appropriately to obtain the mobility. Approximate methods such as computing the mobility for each scattering process and inversely adding the partial mobilities can cause considerable error.[31] We have inversely added the relaxation times for the different scattering processes to obtain a combined relaxation time

$$\tau_{ij} = [\textstyle\sum_a 1/\tau_{ij}^a]^{-1} \quad , \tag{14}$$

where a denotes the different scattering processes. The mobility is calculated separately for each band and then summed after being weighted by the hole density in a given band. Thus,

$$\mu = \sum_{i=1}^{3} p_i \ \mu_i / \sum_{i=1}^{3} p_i \quad , \tag{15}$$

where μ is the total mobility and μ_i is the mobility in band i. The

hole density in band i is given by

$$p_i = \frac{2}{(2\pi)^3}\int_0^\infty f_o(E)\, d^3k_i \qquad i = 1,2,3 \quad . \tag{16}$$

where $f_o(E)$ is the equilibrium Boltzmann distribution. Performing the angular integration in equation (16) and using the dispersion relation, equation (4), to change from an integral over all k to an integral over the energy (in dimensionless notation), we obtain for the mobility

$$\mu = \sum_{i=1}^{3} m_i^{*3/2} I_i \mu_i \Big/ \sum_{i=1}^{3} m_i^{*3/2} I_i \qquad i = 1,2,3 \quad , \tag{17}$$

where

$$I_i = \int_0^\infty e^{-x} \gamma_i^{1/2}(x)\gamma_i'(x)dx \qquad i = 1,2, \tag{18a}$$

and

$$I_3 = \frac{\pi^{1/2}}{2} e^{-\Delta/kT} \quad . \tag{18b}$$

With the inclusion of interband scattering as given by Bir et al.,[20] we have written the mobility of the individual bands as:

$$\mu_i = q\left\langle \frac{1}{\delta}\left(1 + \frac{m_i^*(E)\tau_{jj}}{m_j^*(E)\tau_{ij}}\right)\frac{\tau_{ii}}{m_i^*(E)}\right\rangle_i \qquad i \neq j, \quad i = 1,2 \quad , \tag{19a}$$

$$\mu_3 = q\left\langle \frac{\tau_{33}}{m_3^*}\right\rangle_3 \quad , \tag{19b}$$

where

$$\delta = 1 - \frac{\tau_{11}\tau_{22}}{\tau_{12}\tau_{21}} \quad , \tag{20}$$

and $\langle A(x)\rangle_i$, the average over the Boltzmann distribution, is given by[7,32]

$$\langle A(x)\rangle_i = \int_0^\infty A(x)\gamma_i^{3/2}(x)e^{-x}dx \Big/ \int_0^\infty \gamma_i^{3/2}(x)e^{-x}dx \qquad i = 1,2 \tag{12a}$$

For the parabolic split-off band we have the familiar result

$$\langle A(z)\rangle_3 = \frac{4}{3\pi^{1/2}} \int_0^\infty A(z) z^{3/2} e^{-z} dz \quad , \tag{21b}$$

where $z = x - \Delta/kT$. We have explicitly denoted the energy dependence of the effective mass by $m_i^*(E)$ $(= m_i^* \gamma_i'(x))$ in the mobility expressions for the light and heavy holes. In the cases where there are ratios of effective masses (the parenthesized term in equation (19a) and in equation (7d)), we have also considered the energy dependent $m_i^*(E)$. However, we have found that neglecting the energy dependence of the ratios of effective masses in these terms resulted in a negligible difference (a maximum of 0.3% at 300 K) in the lattice scattering limited mobility.

Several parameters in the relaxation times for the different types of scattering remain to be determined. These parameters will be obtained from a mobility analysis by fitting the mobility theory to the experimental data. The numerical fitting process is discussed in the following chapter and the determination of the parameters from the experimental data is discussed in Chapter V.

Having obtained suitable expressions for an analysis of the mobility, we now turn to an analysis of the carrier concentration data as a function of temperature. Obtaining an accurate and valid determination of the carrier concentration from the measured Hall coefficient requires careful experimental technique. We shall defer a discussion of these points to the following chapter and here briefly present our method for

analyzing the carrier concentration data.

For the range of temperatures measured in these experiments the carrier concentration is determined by the impurities present in the silicon samples. The concentration of thermally excited holes, p, can be expressed in terms of the acceptor density, N_a, the donor density, N_d, and the density of states in the valence band, N_v, as[33]

$$\frac{p(p + N_d)}{(N_a - N_d - p)} = \frac{N_v \exp(-E_a/kT)}{g + \sum_i g_i \exp(-E_i/kT)} \quad , \tag{22}$$

where E_a is the acceptor's activation energy, g is the ground state degeneracy, and g_i and E_i are respectively the degeneracies and separation in energy from the ground state of the excited states. We have included the first three excited states and taken their energies, as shown in Figure 3, to be 30.42 meV, 34.52 meV, and 38.39 meV above the ground state.[13] We have used a degeneracy of 4 for the ground state and the three excited states.[14,15] Although for completeness we have included the effects of the excited states, this will have a very minor influence on the carrier concentration due to the large separation between the ground state and the excited states.[34] By fitting equation (22) to the experimental data (p as a function of T), the parameters N_a, N_d, N_v, and E_a can be determined.

The density of states in the valence band requires additional comment. The density of states is given by

$$N_v = 2(2\pi m_d^* kT/h^2)^{3/2} \quad , \tag{23}$$

where m_d^* is the density of states effective mass. In certain cases we have taken $N_v = 2.19 \times 10^{15} T^{3/2}$ corresponding to a density of states effective mass of .591 m_e. However, the non-parabolic band structure and the corresponding energy dependent effective masses imply that the density of states in the valence band will have an additional temperature dependence. Barber[35] has calculated the temperature dependence of the density of states effective mass using a simplified model of the valence band structure. We have obtained results similar to those of Barber using the valence band structure described herein. The resulting temperature dependence of the effective mass is shown in Figure 4. These values have been fitted to a polynomial in the temperature to obtain $m_d^*(T)$ for which the explicit polynomial expansion is given in Appendix II. This additional temperature dependence has been included for comparison in the density of states of the valence band in some of our analyses of the carrier concentration as a function of temperature.

CHAPTER IV

EXPERIMENTAL METHODS

A. Sample Preparation

The boron-doped silicon used in this study was commercially grown material part of which was obtained through the courtesy of P. Norton (Bell Laboratories), J.Stannard (Naval Research Laboratories), and A. Honig (Syracuse University). Most crystals were grown by the float-zone technique with the growth direction along the <111> crystallographic axis. The crystal orientation was determined by Laue back-reflection x-ray photography. Sample slices were cut from the crystal perpendicular to the direction of growth. Bridge shaped samples suitable for Hall measurements were cut from the slices. The samples were oriented for the Hall measurements such that the magnetic field was in the growth direction, <111> , and the electric field was along the <110> axis. Sample Si:B-8 was oriented such that the magnetic and electric fields were parallel to the <001> and the <100> directions, respectively.

Contacts were made to the etched samples by aluminum spot welds.[37] These areas were then rhodium plated and leads were attached to the rhodium plating with indium solder. Contacts made in this manner, although somewhat mechanically fragile, were electrically suitable for the currents and voltages employed in the Hall effect measurement. The samples were mounted with General Electric No. 7031 varnish on a sapphire plate which was soldered to the cold finger of a helium research dewar.

B. Measurement Apparatus

Hall measurements were performed by standard potentiometric methods when the sample impedance was low. For sample impedances greater than 10^5 ohms, a Keithley Model 610B electrometer with an input impedance of 10^{14} ohms was used. An accuracy of 1% was obtained for the electrometer measurement by using a Keithley Model 160 digital voltmeter to display the unity gain output of the electrometer. Using a Honeywell Model 2784 potentiometer with a Leeds and Northrup Model 9834 electronic null detector, voltages could be resolved to better than one microvolt in the low sample impedance region. The working voltage for the potentiometer was provided by a Honeywell Model 2890 guarded D.C. power supply. The matchbox and all connections were carefully guarded and isolated from ground to reduce electrical pickup. This arrangement is shown in Figure 5. The sample isolation from ground was better than 2×10^{12} ohms. Measurements were limited to sample impedances of less than 10^{10} ohms due to the prohibitively long RC risetime of the measured voltages at higher impedances.

The magnetic field for the Hall measurements was provided by a Varian (V4004) 4 inch electromagnet with a current regulator (V2301A) and a magnet power supply (V2300A). Magnetic fields as high as 20 kilogauss could be obtained with a one-half inch pole separation. The magnetic field strength was monitored by a Rawson Model 820 rotating coil fluxmeter with a stated accuracy of 0.1% when used with an external galvanometer.

The temperature was measured by calibrated platinum resistance and carbon resistance thermometers. The carbon resistor was an Allen-

Bradley 100 ohm, 1/10 watt model TR which was calibrated between 2 K and 100 K with a Cryocal 1000-1.5-100 germanium resistance thermometer mounted in place of the sample. A Rosemount Engineering Model 118LX platinum resistance thermometer was purchased with a factory calibration. This calibration agreed with the germanium resistance thermometer where a comparison between the two was possible (up to 100 K). The carbon resistance thermometer was used to measure the temperature below 30 K, while above 30 K the platinum resistance thermometer was used.

C. Measurement Theory

Galvanomagnetic effects in semiconductors have been discussed in detail by Beer.[37] Putley[38] has discussed the Hall effect primarily emphasizing the experimental aspects. The Hall coefficient, R, is defined in terms of the measured quantities as:

$$R = V_H \cdot t \cdot 10^8 / i\,B \quad cm^3 \quad coulomb^{-1} \tag{24}$$

where V_H is the Hall voltage, t is the sample thickness in centimeters, i is the current, and B is the magnetic flux density in gauss. The geometry is such that the current is along the length of the sample and perpendicular to the magnetic field. The magnetic field is parallel to the sample thickness. The current carriers are deflected in the magnetic field due to the Lorentz force giving rise to the transverse Hall voltage. The Hall mobility is defined as the ratio of the Hall coefficient and the resistivity ρ, where ρ is in ohm-cm. Thus,

$$\mu_H = R/\rho \quad cm^2/\text{Volt sec.} \tag{25}$$

As a Hall measurement requires the use of both electric and magnetic fields, the effects of these fields upon the measurement must be

considered. Due to the charge carriers' random motions while in thermal equilibrium with the crystal lattice, the carriers will have a distribution in energy characteristic of the thermal equilibrium conditions. In this equilibrium distribution the carriers will have an average thermal energy on the order of kT. When an electric field is applied to the sample, the carriers will acquire a drift velocity and thus gain energy from the electric field. For the carriers' energy distribution to remain unchanged, the energy gained from the electric field must be small compared to the average thermal energy. This requires that $(\mu E)^2 m^*/2 \ll kT$. For p-type silicon this requirement must be satisfied for both the light and heavy holes. As the mobility of the light holes is larger than that of the heavy holes, the light holes will provide the more restrictive requirement on the electric field. For an electric field of one volt per centimeter and temperatures of 10 and 100 K, the light hole mobility must be less than 4.4×10^6 and 1.4×10^7 cm^2/V sec, respectively. As the mobility depends on the density of impurities, the allowable electric field strength will vary from sample to sample. Pure samples at low temperatures will provide the most stringent limitation. Our Hall measurements have in general been made at electric fields of less than 0.1 volts/cm which should have a negligible effect on the carriers' energy distribution. Several samples have been checked over a range of electric field strengths to be certain that the electric field was not large enough to influence the measurement.

The magnetic field dependance of the Hall coefficient has received considerable experimental and theoretical attention. An excellent review

of this subject has been given by Beer in Galvanomagnetic Effects in Semiconductors.[37] For valence semiconductors such as p-type germanium and silicon, a successful theory must take into account the degenerate coupled bands, the anisotropic nature of the bands, and the inclusion of interband scattering. For p-type silicon the non-parabolicity of the bands should also play an important role. Several detailed treatments of galvanomagnetic effects have been given, notably those of Bir and Pikus[39] and Lawaetz.[40] However, the numerical calculations of Lawaetz still do not agree with the experimental value of the Hall factor, r, at 77 K in p-type germanium[41]. The Hall factor is defined by $r = R(0)/R(\infty)$ where $R(0)$ and $R(\infty)$ are the values of the Hall coefficient as the magnetic field approaches zero and infinity, respectively.

For sufficiently high magnetic fields several simplifications occure in the magnetic field dependence of the Hall coefficient. This regime is known as the high-field limit and is reached when the product μB becomes greater than 10^8 $cm^2 gauss/Volt\ sec$.[42] In the high-field limit the Hall coefficient is simply related to the carrier concentration by[43]

$$R = \frac{1}{pq} . \qquad (26)$$

We have been able to satisfy the high-field limit for several of our samples between 4 K and 120 K. It should be noted that in the low field limit the Hall coefficient is not simply related to the carrier concentration because the Hall factor, r, must be taken into account. The conductivity, σ, is given by the expression

$$\sigma = pq\mu \qquad (27)$$

This mobility, defined in terms of the conductivity, has been termed

the conductivity or drift mobility. By a comparison between this expression for the drift mobility and the previously given expression for the Hall mobility, we see that when the Hall coefficient is measured in the high field limit, and thus simply related to the carrier concentration, the drift mobility and the Hall mobility are equal. As the mobility calculated from the expressions given in Chapter III is the drift mobility, the use of the high-field limit in the Hall coefficient measurement will enable us to compare the experimental and calculated mobilities.

Although the high-field limit considerably simplifies the determination of the carrier concentration, excessively high magnetic fields can cause problems due to the quantization of the hole orbits in a magnetic field. A review of high magnetic field effects has been given by Adams and Keyes.[44] The quantization of the particle motion in a magnetic field will create Landau levels within the band. The Landau levels will modify the density of states in the valence band which could affect the interpretation of experimental data.[45] Neglecting coupling between the bands, for p-type silicon there will be two sets of levels corresponding to the light and heavy hole bands. The spacing between Landau levels is given by $\hbar\omega_i$ where ω_i is the cyclotron frequency of the band under consideration. For quantum effects to be negligible the thermal energy must be large compared to the separation between Landau levels, or $kT \gg \hbar\omega_i$. As the separation between levels is larger for the light hole band than the heavy hole band, the light holes will provide the more restrictive condition. A field of 10 kilogauss will correspond to a temperature of 9.1 K for the light hole band. Also

important at high magnetic fields is another effect which has been termed "magnetic freeze out". Yafet, Keyes and Adams[46] predicted this effect from the theory of hydrogen atoms in strong magnetic fields. The effect occurs because in a strong magnetic field the bound state wave-functions are more strongly localized than at zero magnetic field. Due to the more localized charge distribution, the coulomb binding energy of the impurity state is increased. Thus, at a fixed temperature the concentration of thermally excited charge carriers will be smaller and the Hall coefficient will be effectively increased. This of course gives rise to the terminology "magnetic freeze out". Experimentally we have not observed any variations in the Hall coefficient which could be attributed to magnetic quantization.

The expressions for carrier concentration and mobility given in Chapter III have been used to determine the impurity parameters for our material. The carrier concentration expression, equation (22), can be solved for p to obtain:

$$p = [(N_d - E_k) - \sqrt{(N_d+E_k)^2 - 4(N_a - N_d)E_k}\,]/2 \qquad (28)$$

where $E_k = N_v \exp(-E_a/kT)/(g + \Sigma g_i \exp(-E_i/kT))$. We have fit the carrier concentration as a function of temperature data to the solution for p given above. The four parameters N_a, N_d, E_a, and N_v were permitted to vary such that the least squares differences between the calculated and experimental values of p were minimized. As the carrier concentration varied by several orders of magnitude over the temperature interval studied, the differences in the logarithms of p were compared. Initial values of the parameters, required as input data for the fitting

program,[47] were obtained from a graphical analysis of the Hall data. The program then tries to improve the fit in successive iterations by using the partial derivatives with respect to each parameter to adjust the four parameters optimally. After the program has converged on a set of parameters, statistics are calculated to evaluate the results.

As the carrier concentration freezes out exponentially with temperature, accurate thermometry is very important for an accurate determination of the impurity parameters from the carrier concentration as a function of temperature data. However, for mobility with its power law rather than exponential dependence on temperature, the thermometry will not be as crucial for an accurate determination of the parameters. Thus, mobility analysis can provide an important cross check for the carrier concentration analysis. As with the carrier concentration data, the calculated and experimental values of the mobility were compared by the fitting program and the parameters were adjusted to give the best least squares fit. Several parameters, in different combinations, have been allowed to vary in our analysis of the mobility. These include the constant r_0 which controls the magnitude of the acoustic phonon scattering contribution to the mobility, the coupling constant W, the donor density N_d, the scale factor multiplying the Erginsoy equation A, and another scale factor, G, to account for any error in measuring the sample dimensions. The dimensional factor G will be a number close to unity multiplying the calculated mobility. Although the sample thickness could be measured quite well, the sample width and distance between resistivity arms was only known to within about

five percent. For pure samples the contribution of ionized impurity scattering can be comparable to the geometrical measurement errors. For this reason we have included this adjustable parameter G. The determination of these parameters from the experimental data will be discussed in Chapter V.

One final comment concerning the mobility analysis is necessary. The fitting program uses the partial derivatives of the mobility with respect to the variable parameters as a guide in adjusting the parameters to obtain an optimum fit. However, the complexity of the mobility expression given in Chapter III does not readily allow one to differentiate it with respect to the parameters. For the purpose of obtaining derivatives we have used the approximate expression:

$$\mu = [\sum_{\alpha}(1/\mu)_{\alpha}]^{-1} \qquad (29)$$

where α denotes the different scattering processes. Although this is inaccurate for the calculation of the mobility, it is sufficient for the purpose of providing partial derivatives for the fitting program.

CHAPTER V

EXPERIMENTAL RESULTS

A. Carrier Concentration

The samples measured in this study have covered a range of impurity densities between 10^{13} cm^{-3} and 10^{17} cm^{-3}. The carrier concentration as a function of reciprocal temperature, for four representative samples with acceptor densities of approximately 10^{13} cm^{-3}, 10^{14} cm^{-3}, 10^{15} cm^{-3}, and 10^{16} cm^{-3}, is shown in Fig. 6. The experimental data are given by the coded points while the solid line is the result obtained by fitting the data for carrier concentration as a function of temperature to equation (22). The parameters determined from the fit to equation (22) for these samples as well as the other samples measured in this work are given in Table II. The parameters N_a, N_d, and E_a have been allowed to vary in fitting the experimental data while the density of states in the valence band, N_v, has been either fixed or also allowed to vary. As N_v is given by $4.83\times10^{15}(m_d^*/m_e)^{3/2}T^{3/2}$ cm^{-3}, we have listed in Table II the value of m_d^* corresponding to a given value of the density of states. For samples in which the exhaustion region was reached at relatively low temperatures, such as Si:B-14, we have found very little change in the value of m_d^* when the density of states was allowed to vary. For samples where the exhaustion region could not be reached, such as Si:B-7, this was not necessarily the case.

Samples Si:B-3 and Si:B-6 exhibited a region at low temperatures where impurity-hopping conduction dominated the conduction due to free carriers in the valence band. Data from this region has not been used

in the carrier concentration analysis. Several other samples were measured, particularly ones with high room temperature resistivities (3,000 to 10,000 Ω-cm), which showed large inhomogeneities in impurity density from one end of the Hall bridge to the other. We have not used these samples for further analysis, and they are not included in Table II.

As discussed in Chapter III, the density of states of the valence band has an additional temperature dependence due to the temperature dependence of the density of states effective mass as shown in Fig. 4. We have also fit to equation (22) the carrier concentration as a function temperature data taking into account this additional temperature dependence. These results are presented in Table III. The parameters thus obtained are very similar to those obtained using a temperature independent effective mass. However, the trend, except for the closely compensated samples Si:B-2 and Si:B-14, is to lower values of N_a and N_d by a few percent. For the closely compensated samples, N_a and N_d increase by a few percent when analyzed using a temperature dependent effective mass. This behavior can be qualitatively understood using approximate expressions for the carrier concentration for the cases of uncompensated and closely compensated samples.[48] When the density of compensating donors is very much less than the carrier concentration, the carrier concentration is approximately given by

$$p \approx (N_a N_v/g)^{1/2} e^{-E_a/2kT} , \qquad (30)$$

where g is the ground state degeneracy and we have neglected the influence of the excited states. For an analysis using the temperature dependent effective mass, the density of states of the valence band at a

given temperature will be larger than for an analysis using a temperature independent effective mass. In order to calculate from equation (30) the same carrier concentration for a larger density of states the value of N_a must be correspondingly reduced which agrees with a comparison of Tables II and III for the relatively uncompensated samples. For very closely compensated samples the carrier concentration is now approximately given by

$$p \simeq \frac{(N_a - N_d)}{1+(N_d/N_v g^{-1})e^{E_a/kT}}. \qquad (31)$$

In the exhaustion region p will be determined by the difference $N_a - N_d$. N_d will be determined as the carrier concentration begins to freeze out and the denominator in equation (31) becomes larger than one. Here, for a larger value of N_v we must have a correspondingly larger value of N_d to obtain a given carrier concentration. Thus N_a and N_d will increase for the closely compensated samples when the temperature dependent effective mass is used in the carrier concentration analysis.

Also shown in Tables II and III is the standard deviation of the fit to the carrier concentration data. In most, but not all, samples the standard deviation is slightly improved when analyzed with the temperature dependent effective mass. However, as the differences between the parameters N_a and N_d for the two cases are at most ten percent, we have concluded that the additional temperature dependence of the density of states in the valence band due to the temperature dependence of the effective mass does not appreciably alter the determination of these parameters from the temperature dependence of the carrier

concentration.

B. Mobility

The mobility for four representative samples is shown in Figs. 7 and 8. The experimental data are shown by coded points and the solid lines are fits to this data using the mobility theory formulated in Chapter III. The mobility theory has been fit to the experimental data by adjusting several parameters. These parameters are: τ_o, the magnitude of the relaxation time for scattering by acoustic phonons; N_d, the density of compensating donors; W, the coupling constant of the holes to the optical phonon mode relative to the acoustic phonon mode; A, the factor multiplying the magnitude of the relaxation time for neutral impurity scattering; and G, a scale factor used to account for measurement errors in the sample dimensions. We felt the acceptor density, N_a, was known with enough precision from the carrier concentration analysis so that its value was not permitted to vary in the analysis of the mobility. The determination of the above parameters from an analysis of the temperature dependence of the mobility will be discussed in the following subsections.

(1) Lattice Scattering by Acoustic Phonons

In pure samples where impurity scattering is relatively unimportant, scattering by acoustic and optical phonons will dominate the mobility. We have determined the lattice scattering constant, τ_o, by fitting the mobility theory to our three purest samples over a temperature range of approximately 25 K to 80 K. We have not used data above 80 K so that any contribution to the mobility due to optical phonon scattering could be neglected. This has allowed us to fix the parameter

controlling the contribution of optical phonon scattering, W, and ignore it in fitting the mobility over this restricted temperature interval. As relatively pure samples have been used, the neutral impurity scattering factor, A, has also been fixed. The geometrical scale factor, G, has been fixed at 1.0 for these fits, thus assuming perfect geometry for these three samples. The remaining parameters, τ_o and N_d, were allowed to vary to obtain the best least squares fit to the mobility data. The results of these fits are given in Table IV. The values for the magnitude of the acoustic phonon scattering relaxation time, τ_o, agree quite well with one another. From these fits we have chosen the value, $\tau_o = 5.25 \times 10^{-9}$ sec as most representative and taken its value as fixed when fitting less pure samples.

The differences of a few percent between the values of τ_o as seen in Table IV could easily be due to differences in the geometrical error for the three samples. To check this we have fixed the value of τ_o at 5.25×10^{-9} sec and refit samples Si:B-1 and Si:B-14 over the same temperature range with N_d and G variable. These results are given in Table V. The resulting values of G agree quite closely with the corresponding differences in τ_o. For Si:B-14 , G decreased by 1 percent corresponding to the 1.5 percent decrease in τ_o between Si:B-8 and Si:B-14 , while for Si:B-1 , G increased by 3 percent corresponding to the 2.7 percent increase in τ_o between Si:B-8 and Si:B-1. Thus, the differences in τ_o can be readily accounted for by the geometrical measurement differences between the samples. Since the dimensional measurement errors for these samples are only a few percent, the determination of τ_o for these samples is correspondingly accurate.

(2) Lattice Scattering by Optical Phonons

To determine the parameter W, the relative coupling strength of the holes to the optical phonon mode compared to the acoustic phonon mode, requires mobility data at higher temperatures where optical phonon scattering contributes significantly to the mobility. However, at higher temperatures the high-field limit, $\mu B >> 10^8$ cm^2 Gauss/Volt sec, required for a rigorous interpretation of the Hall effect measurement could not be satisfied with our available magnetic field strengths. This complicates the analysis of the mobility in that the Hall factor, which may no longer be equal to unity, must be taken into account. Rather than attempt to calculate the Hall factor, which varies with temperature and the predominate type of scattering, we have obtained the drift mobility in the following manner. The parameters determined from the carrier concentration analysis have been used to calculate the carrier concentration by means of equation (22) for temperatures above the high-field limit. As these parameters were determined from data measured in a region where the high-field limit was valid, when used in equation (22) the carrier concentration should be accurately computed at higher temperatures. Thus, at higher temperatures, we have measured the resistivity, ρ, and obtained the drift mobility from $\mu = 1/pq\rho$, where p is the calculated carrier concentration.

Mobility data has been obtained in this manner for samples Si:B-8 and Si:B-14 where the resistivity has been measured for temperatures up to 400 K and 300 K, respectively. Above 300 K for Si:B-8 corrections have been made to take account of the change in resistivity due to intrinsic conduction.[49] This data has been fit with the parameters N_d,

W, and G variable. The data for these samples over the entire temperature range is shown by the coded points in Figs. 9 and 10 where the solid line is the fit to the mobility theory. The parameters determined from these fits are given in Table VI. We have obtained values for W of 2.00 and 1.78 for Si:B-8 and Si:B-14, respectively.

(3) Ionized Impurity Scattering

At low temperatures scattering by ionized and neutral impurities can control the mobility. As the number of ionized impurities is directly related to the density of compensating donors ($N_I = 2N_d + p$), one can determine N_d from the contribution of ionized impurity scattering to the mobility. As N_d has also been determined from the carrier concentration analysis, a comparison of the values obtained provides evidence as to the validity of the mobility analysis. This comparison is given in Table VII for several of the samples studied. For some of the samples listed in Table VII the parameters N_d, A, and G were varied in the mobility fit. However, for other samples with marginal amounts of neutral impurity scattering, it was found that A, the parameter modifying the neutral impurity scattering strength, would become unreasonably large or small when allowed to vary. This is because the mobility in these samples was not particularly sensitive to the amount of neutral impurity scattering and the computer apparently allowed A to vary considerably in order to account for small differences between the calculated and experimental mobilities. Consequently, for these samples we have varied N_d and G and fixed A at several different values in order to observe the effect of A on the value of N_d obtained from the mobility analysis.

As can be seen from Table VII, the values of N_d obtained from the

carrier concentration analysis and the mobility analysis are in good agreement. For the purer samples (Si:B-8 and Si:B-14), the choice of different values of A has a negligible effect on the determination of N_d since neutral impurity scattering is very weak in these samples. The fits to the moderately doped samples (Si:B-4 and Si:B-5) are more strongly affected by the choice of A. For these samples a choice of A near 4 gives the best agreement for the values of N_d determined from the mobility and carrier concentration analyses. The three remaining samples are more heavily doped and deserve additional comment. As the mobility was quite low in these samples, the high-field limit could not be reached over most of the temperature interval studied. In addition, Si:B-3 and Si:B-6 exhibited impurity-hopping conduction at low temperatures. For these samples data below 35 K has been excluded from the mobility analysis. Since the high-field limit could not be reached, the Hall factor will affect the temperature dependence of the mobility. As neutral impurity scattering is quite strong in these samples, any temperature dependence of neutral impurity scattering not accounted for in the Erginsoy formulation could also affect the mobility analysis. For these reasons, the analysis of these samples cannot be considered as reliable as the analysis of the purer samples. However, even with these limitations, the values of N_d obtained from the carrier concentration analysis and the mobility analysis are in reasonable agreement.

(4) Neutral Impurity Scattering

Throughout this work we have found it necessary to include the adjustable parameter A to modify the scattering time by neutral impurities. For the samples doped on the order of 10^{16} cm^{-3}, we see from

Table VII that the fitted values of A are between 2 and 3. For the samples with about 10^{15} cm^{-3} acceptors, a value of A near 4 gives the best agreement with the value of N_d determined from the carrier concentration analysis. As mentioned in the previous section, the interpretation of the experimental data for the more heavily doped samples is complicated by the need to take into account the Hall factor. Also, the different values of A obtained for the different samples lead us to feel that the value of A determined from the mobility analysis for a given sample cannot be considered particularly reliable.

In order to demonstrate the influence of A on the mobility, we have calculated the mobility with A = 2 and A = 6 using the parameters of Si:B-5 with N_d fixed at 2.05×10^{12} cm^{-3} . The calculated mobilities along with the experimental data of Si:B-5 are presented in Fig. 11. The experimental data points below 20 K have been obtained from photo-Hall measurements using 300 K background radiation to photo-excite the carriers. The validity of a comparison with theory for this low temperature data requires that two conditions be satisfied. The Born approximation used in calculating the ionized impurity scattering contribution to the mobility requires that $|\vec{k}a| >> 1$ where $\vec{k}$ is the carrier wavevector and a is the scattering length.[26] For silicon $|\vec{k}a| = 1.4\times10^{7}T(m^{*}/m_e p')^{1/2}$, where p' is given by equation (11). Taking the density of photo-excited carriers as 10^{9} cm^{-3} and N_a and N_d from the Hall fit for Si:B-5, we obtain for the more stringent case of the light holes: $|\vec{k}a| = 3.8T$. Thus, the above requirement is satisfied for the experimental data shown in Fig. 10. A second requirement is that the thermalization time of the photo-excited carriers be much less than the carrier lifetime. If, on the

contrary, the thermalization time is longer than the carrier lifetime, the carrier distribution will be "hot", corresponding to the energy distribution of the incident radiation used to photo-excite the carriers in the photo-Hall measurement. A mobility measurement under such conditions cannot be compared to the calculated mobility which assumes a thermal carrier distribution. From the energy loss rate due to acoustic phonon emission,[50] we can estimate the thermalization time for the more restrictive case of the heavy holes to be $3.5\times10^{-10}\ T^{-1/2}$ sec.[51] The carrier lifetime may be determined from the recombination cross section for holes at ionized boron impurities[52] by $\tau = (N^{-}\langle v\rangle\sigma)^{-1}$, where N^{-} is the density of negatively ionized boron impurities, $\langle v\rangle$ is the average thermal velocity, and σ is the recombination cross section. At 10 K we obtain a carrier lifetime for Si:B-5 of approximately 3×10^{-8} sec and a thermalization time of 10^{-9} sec. Thus, the experimental photo-Hall data for Si:B-5 satisfy both of the above restrictions. The experimental points shown in Fig.11 lie between the curves corresponding to A = 2 and A = 6. This is consistant with the results given for this sample in Table VII.

C. Mobility Analysis Assuming a Parabolic Band Structure

The results presented in the previous sections of this chapter have been based upon an analysis of the mobility using the formulation given in Chapter III which took account of the non-parabolicity of the silicon valence band. For the parameters determined from the mobility analysis, good agreement between the experimental and calculated mobilities has been obtained. However, one could ask if similarily good agreement, perhaps with a different set of parameters, could be obtained by a mobility analysis which ignores the valence band non-parabolicity and assumes

parabolic valence bands. The following section will demonstrate that indeed this is not the case.

The mobility formulation described in Chapter III is easily reduced to the parabolic case by the replacement of $\gamma(E)$ by E and $\gamma'(E)$ by 1. We have reanalyzed the experimental mobility data of samples Si:B-8 and Si:B-14 assuming a parabolic band structure. The experimental data shown by the coded points along with the parabolic mobility fit to this data shown by the solid line is presented in Figs. 12 and 13 for samples Si:B-8 and Si:B-14, respectively. The parameters as determined from these fits are given in Table VIII. To facilitate a comparison between the parabolic and non-parabolic mobility fits, we have plotted the percentage error between the calculated and experimental mobilities for the two cases for Si:B-8 and Si:B-14 in Figs. 14 and 15, respectively. For both samples the error for the parabolic mobility fits is considerably larger than for the non-parabolic mobility fits. This is strong evidence as to the importance of the valence band non-parabolicity in determining the temperature dependence of the mobility.

Further evidence as to the importance of the non-parabolic description comes from an examination of the parameters as determined from the different mobility fits. For Si:B-14 the value of N_d obtained from the parabolic mobility fit was 2.2×10^{12} cm^{-3} while the non-parabolic mobility fit gave 1.39×10^{13} cm^{-3}. As seen in Table VII, the value of N_d determined from the carrier concentration analysis agrees very closely with the value determined from the non-parabolic mobility fit. Thus, not only is the fit to the experimental data better for the non-parabolic case, but also a considerably more realistic value of the parameter N_d is

obtained by the non-parabolic mobility analysis. Similar considerations hold for Si:B-8.

In order to observe more closely the differences between the parabolic and non-parabolic models, we have plotted in Fig. 16 the lattice scattering limited mobility for the two cases with $\tau_o = 5.25 \times 10^{-9}$ sec and W = 2.0. As expected for the parabolic case, we observe a $T^{-3/2}$ temperature dependence for the mobility up to approximately 100 K where optical phonon scattering begins to contribute to the mobility. Since in the non-parabolic case the effective mass increases with temperature and the acoustic phonon scattering time becomes shorter than in the parabolic case, we observe a more rapid decrease in the mobility than a $T^{-3/2}$ temperature dependence.

We are now in a position to understand better the differences in the parameters as determined from the parabolic and non-parabolic mobility fits. As exemplified by Si:B-14, the calculated mobility near 100 K for the parabolic case is considerably larger than the experimental mobility even though the experimental mobility is primarily dominated in this temperature region by lattice scattering. Thus, for the parabolic case the parameter τ_o must be lowered relative to the non-parabolic value of τ_o to obtain agreement with the experimental mobility as to the magnitude of lattice scattering limited mobility. Such a change in τ_o is observed by comparing Tables VI and VIII. At higher temperatures the parameter W must be increased considerably for the parabolic case to increase the relative contribution of optical phonon scattering and thus lower the mobility to obtain agreement with the experimental mobility near room temperature. The value of W was determined to be near 2.0 for

the non-parabolic case while a value of 6.0 was found for the parabolic case. Since the value of τ_o was reduced for the parabolic case, at low temperatures the lattice scattering contribution to the mobility will be large and consequently the calculated mobility will be too small. Thus, the amount of ionized impurity scattering must be decreased for the parabolic case to raise the mobility to near the experimental value at low temperatures. This results in a value of N_d which is much smaller for the parabolic mobility fits than for the non-parabolic mobility fits as can be seen from Tables VI and VIII.

With the above differences in the parameters as determined from the parabolic and non-parabolic mobility fits and the poor agreement in determining the temperature dependence of the mobility for the parabolic case as seen in Figs. 14 and 15, we must conclude that the inclusion of the non-parabolicity of the valence band is necessary for an accurate description of the temperature dependence of the mobility.

D. Influence of the Split-off Band on the Mobility

In the formulation of the mobility theory in Chapter III we included the contribution to the mobility of the split-off band. It is clear from equations (17) and (18b) that at low temperatures this band cannot play a major role in determining the mobility due to the exponential factor $e^{-\Delta/kT}$ multiplying the split-off band's contribution to the mobility. We have calculated the lattice scattering limited mobility for a two-band model and compared it with the mobility calculated including the third split-off band. The lattice scattering limited mobility for the three-band model has been plotted already (for the non-parabolic case) in Fig. 16. The calculated two-band mobility is lower than the three-band

mobility by 12.8% at 300 K, by 5.4% at 200 K, and by 2.1% at 150 K. At lower temperatures the difference rapidly becomes negligible. However, near room temperature the split-off band's contribution to the mobility is significant.

It is of interest to consider what effect a mobility analysis using two bands would have on the determination of the parameter W. As the contribution of the split-off band becomes noticeable only at high temperatures, the other parameters which are primarily determined from low temperature data would be unaffected by an analysis neglecting the split-off band. However, as W in part controls the magnitude of the mobility above 100 K, its determination will be affected by the number of bands included in the mobility analysis. For the parameters $\tau_o = 5.25 \times 10^{-9}$ sec and W = 2.0 (determined from fitting the three-band mobility theory to the experimental data of Si:B-8), we have obtained a lattice scattering limited mobility (see Fig. 16) of 475 cm^2/Volt sec at 300 K. For a two-band mobility calculation a coupling constant of W = 1.5 was required to give a 300 K mobility of 479 cm^2/Volt sec. Thus, W is lowered for a two-band mobility calculation relative to a three-band mobility calculation in order to obtain agreement with the room temperature mobility.

CHAPTER VI

COMPARISON WITH OTHER WORK

The activation energy of the boron acceptor in silicon as determined from the carrier concentration analysis is in good agreement with other electrical optical measurements.[53,54,55] For our purer samples, the small changes in the density of states of the valence band when this parameter was allowed to vary indicates that our use of four for the ground state degeneracy is correct. If the ground state degeneracy were different from four, the density of states would change accordingly when this parameter was fit to the carrier concentration data. A ground state degeneracy of four is in agreement with the splitting of the ground state under uniaxial stress as determined by optical absorption.[15]

There has been very little work done in the analysis of mobility incorporating all the relevant types of scattering over wide ranges of temperatures and impurity densities. Several pure samples ($N_a = 10^{13}$ cm^{-3}) have been measured by L. Elstner[56] who obtained an acoustic-phonon-limited mobility for temperatures below 50 K of $1.4\times10^{7}\ T^{-1.51}$ cm^2/Volt sec. Above 50 K a steeper temperature dependence was observed. This is in reasonable agreement with our value for the lattice mobility of $1.6\times10^{7}\ T^{-1.54}$ cm^2/Volt sec corresponding to $\tau_o = 5.25\times10^{-9}$ sec which has been obtained from the fits to our experimental data with τ_o as an adjustable parameter as given in Table IV.

The drift mobility at 300 K has been measured by several experimenters. Prince,[57] Ludwig and Walters,[58] and Cronmeyer[59] have obtained mobilities of 495, 475, and 504 cm^2/Volt sec, respectively. By fitting the mobility theory to our experimental data for samples Si:B-8 and

Si:B-14, we have obtained lattice-scattering-limited mobilities at 300 K of 475 and 505 cm^2/Volt sec corresponding to optical phonon coupling constants of 2.00 and 1.78 respectively.

A relative coupling constant of the holes to the optical phonon mode compared to the acoustic phonon mode of 2.00 and 1.78 has been obtained by us from the mobility analyses of Si:B-8 and Si:B-14, respectively. Asche and Borzeszkowski[3] obtained reasonable agreement with the data of Elstner[56] in calculating the mobility for a non-parabolic band structure using a relative coupling constant of 2.5. However, their calculated 300 K mobility (from Fig. 7 of Ref. 3) was approximately 420 cm^2/Volt sec which is somewhat lower than our room temperature mobilities as given in the preceeding paragraph for the above coupling constants. This indicates that a smaller coupling constant would allow Asche and Borzeszkowski[3] to obtain better agreement with room temperature drift mobilities.

Wiley and DiDomenico[60] have computed the mobility for parabolic bands. Their procedure was to fix the relative coupling constant at 2 and adjust the magnitude of the acoustic phonon scattering time to obtain agreement with a mobility at 300 K of 350 cm^2/Volt sec. Although a coupling constant of 2 agrees with our value for the non-parabolic mobility analysis, it is in disagreement with our results when we attempted to fit a parabolic model to our mobility data. For our parabolic analysis we required a coupling constant near 6 to obtain agreement with our high temperature data. The reason for this difference becomes clear if we look at the acoustic mobility obtained by Wiley and DiDomenico. Their mobility for scattering by acoustic phonons (from

Eq. 11 and Table I of Ref. 60) is $4.2 \times 10^6 \, T^{-1.5}$ cm^2/Volt sec which is considerably lower than our result and the acoustic mobility obtained by Elstner.[56] If Wiley and DiDomenico's acoustic mobility were raised to obtain agreement with the experimental mobility at low temperatures, a larger coupling constant would be required by them to obtain agreement with the room temperature mobility. This should yield results closer to ours obtained for a parabolic band structure. Mobility in parabolic bands has recently been considered by Costato et.al.[16] who have obtained results similar to those of Wiley and DiDomenico.[60] Both Costato et. al.[16] and Wiley[61] have pointed out the necessity of considering the valence band non-parabolicity when interpreting the hole mobility in silicon.

CHAPTER VII

SUMMARY

The analysis of the carrier concentration and mobility as a function of temperature has been shown to be a useful tool for the characterization of impurity parameters in p-type silicon. Good agreement for the density of compensating donors has been obtained from the two analyses. This must be largely due to the accuracy of the Brooks, Herring, and Dingle formulation of ionized impurity scattering as well as the correctness of the non-parabolic approach to the analysis of hole mobility in silicon. The donor and acceptor densities as determined from the carrier concentration analysis have exhibited a systematic although minor variation due to the additional temperature dependence of the valence band density of states with the inclusion of temperature dependent effective masses.

The temperature dependence of the mobility has been substantially accounted for by including the valence band non-parabolicity and the relevant types of scattering in the mobility analysis. The parameters as determined from the mobility analysis, particularly the amount of ionized impurity scattering and the relative contribution of optical phonon scattering, have been found to change considerably when analyzed assuming a parabolic rather than a non-parabolic valence band structure. The agreement with the temperature dependence of the experimental mobility data and the agreement with the carrier concentration analysis for the donor density has been significantly improved by the non-parabolic rather than parabolic mobility analysis.

Appendix I

POLYNOMIAL EXPANSIONS FOR THE $\gamma_i(E)$

Using the spherically averaged valence band structure as given in Fig. 1, we have fit k^2 to a polynomial in powers of the energy E. Thus,

$$k_i^2 = \sum_{n=0}^{m} \alpha_{in} E^n \quad . \tag{I.1}$$

Although a constant term (α_o) has been included in the polynomial expansions, numerically this has not altered their limiting behavior over the energy range here considered. The values of k^2 are calculated to an accuracy of better than 0.1% in all cases. From the dispersion relation, equation (4), we have

$$k_i^2 = \frac{2m_i^*}{\hbar^2} \gamma_i(E) \quad . \tag{I.2}$$

Thus,

$$\gamma_i(E) = \sum_{n=0}^{m} \alpha'_{in} E^n \quad , \tag{I.3}$$

where

$$\alpha'_{in} = \frac{\hbar^2}{2m_i^*} \alpha_{in} \quad . \tag{I.4}$$

We have divided the energy range considered into four intervals. For the energy in eV and k^2 in cm^{-2}, the coefficients α_{in} are:

Light Hole Band (i=1)

$10^{-6} \leq E \leq 10^{-3}$ eV

$$\alpha_0 = 8.3986018384 \times 10^{5}$$
$$\alpha_1 = 4.0114088474 \times 10^{14}$$
$$\alpha_2 = 2.1706358117 \times 10^{15}$$
$$\alpha_3 = -4.2108560228 \times 10^{17}$$
$$\alpha_4 = 3.1328296107 \times 10^{20}$$

$10^{-3} < E \leq 2 \times 10^{-2}$ eV

$$\alpha_0 = -1.5217785981 \times 10^{8}$$
$$\alpha_1 = 4.0124984119 \times 10^{14}$$
$$\alpha_2 = 1.9808272516 \times 10^{15}$$
$$\alpha_3 = 3.3884004554 \times 10^{16}$$
$$\alpha_4 = 4.4890798898 \times 10^{17}$$

$2 \times 10^{-2} < E \leq 10^{-1}$ eV

$$\alpha_0 = -6.5562268877 \times 10^{11}$$
$$\alpha_1 = 5.5307508141 \times 10^{14}$$
$$\alpha_2 = -1.0579054256 \times 10^{16}$$
$$\alpha_3 = 5.0976268797 \times 10^{17}$$
$$\alpha_4 = -7.8252633691 \times 10^{18}$$
$$\alpha_5 = 5.42[illegible] \times 10^{19}$$
$$\alpha_6 = -1.4418985467 \times 10^{20}$$

$10^{-1} < E \leq 1$ eV

$$\alpha_0 = -1.5655203163 \times 10^{13}$$
$$\alpha_1 = 9.0144277063 \times 10^{14}$$
$$\alpha_2 = -3.9222961582 \times 10^{13}$$
$$\alpha_3 = 4.3293879689 \times 10^{13}$$
$$\alpha_4 = -1.7284317452 \times 10^{13}$$

Heavy Hole Band (i=2)

$10^{-6} < E \leq 10^{-3}$ eV

$\alpha_0 = 1.0172944856 \times 10^{7}$

$\alpha_1 = 1.3195281939 \times 10^{15}$

$\alpha_2 = 1.6680196336 \times 10^{16}$

$\alpha_3 = -1.4896411036 \times 10^{19}$

$\alpha_4 = 8.6749489378 \times 10^{21}$

$10^{-3} < E \leq 2 \times 10^{-2}$ eV

$\alpha_0 = -8.0235703300 \times 10^{8}$

$\alpha_1 = 1.3212303419 \times 10^{15}$

$\alpha_2 = 9.2707769617 \times 10^{15}$

$\alpha_3 = 1.5232384239 \times 10^{17}$

$\alpha_4 = -3.1297707692 \times 10^{18}$

$2 \times 10^{-2} < E \leq 10^{-1}$ eV

$\alpha_0 = 2.4165450859 \times 10^{11}$

$\alpha_1 = 1.2228752957 \times 10^{15}$

$\alpha_2 = 1.7976342350 \times 10^{16}$

$\alpha_3 = -1.4155388985 \times 10^{17}$

$\alpha_4 = 4.3741658465 \times 10^{17}$

$10^{-1} < E \leq 1$ eV

$\alpha_0 = -2.7105936976 \times 10^{13}$

$\alpha_1 = 2.3038823189 \times 10^{15}$

$\alpha_2 = 1.1462382301 \times 10^{14}$

$\alpha_3 = -1.2268956892 \times 10^{14}$

$\alpha_4 = 4.7434174345 \times 10^{13}$

Appendix II

POLYNOMIAL EXPANSION FOR THE DENSITY OF STATES EFFECTIVE MASS

The density of states in the valence band is given by[64]

$$N_v = p/F_{1/2}(\eta) \quad ,$$

where $F_{1/2}(\eta)$ is the Fermi-Dirac integral of order 1/2, η is the reduced Fermi level, and $p = \sum_{i=1}^{3} p_i$ where the p_i have been given by equation (16). The density of states has been given in equation (23) as

$$N_v = 2(2\pi m_d^* kT/h^2)^{3/2} \quad .$$

Solving for m_d^* and evaluating the integrals, we obtain

$$m_d^{*3/2} = \frac{2}{\pi^{1/2}} \sum_{i=1}^{3} m_i^{*3/2} I_i \quad ,$$

where the I_i have been given by equations (18a) and (18b). The integrals I_i have been solved numerically and m_d^* has been graphed in Fig. 4. We have fit m_d^* to a polynomial in the temperature such that

$$m_d^* = \sum_{n=1}^{n'} a_n T^n \quad ,$$

where for T in Kelvins and m_d^* in units of the electron mass, the a_n are

$a_0 = 5.5709558588\times10^{-1}$, $a_1 = 8.1556310156\times10^{-4}$, $a_2 = 4.4332221749\times10^{-6}$, $a_3 = -3.8018360141\times10^{-8}$, $a_4 = 1.4418210956\times10^{-10}$, $a_5 = -3.1693725411\times10^{-13}$, $a_6 = 3.8394932962\times10^{-16}$, and $a_7 = -1.9715702458\times10^{-19}$.

APPENDIX III

NUMERICAL CALCULATION OF THE MOBILITY

The mobility is calculated following the formulation given in Chapter III. The numerical integrations have been performed using Simpson's rule. The techniques used in and the accuracy of these numerical calculations has been discussed previously.[30,41] Subroutines BANDX and BANDT evaluate the $\gamma_i(x)$ at a given energy and temperature to use as required in computing the mobility in subroutine FUN. These subroutines are listed below.

```
      SUBROUTINE BANDT(X,GAMMA,DGAMMA,LIMIT1,LIMIT2,LIMIT3,
     &                 INTG1,INTG2,NORM1,NORM2)
      REAL INTG1,INTG2,NORM1,NORM2
      DOUBLE PRECISION DINTG1,DINTG2,DNORM1,DNORM2
      DOUBLE PRECISION GAMMA(8,7),DGAMMA(8,7),T(7)
      REAL LIMIT1,LIMIT2,LIMIT3
      REAL XT
      DIMENSION X(48)
C     THE SUBROUTINE BANDT EVALUATES, FOR A GIVEN T, THE COEFFICIENTS
C     GAMMA(I,J)FOR THE POLYNOMIAL EXPANSION OF
C     GAMMA(EPS)=GAMMA(I,J)* EPS**(N+1-J) SUMMED FROM J=1,N
C     THE INDEX I=1,2,3,4 IS FOR DIFFERENT ENERGY REGIONS FOR THE
C     LIGHT HOLE BAND, I=5,6,7,8 THE HEAVY HOLE BAND
      GAMMA(1,1)= 4.0914352291D-07
      GAMMA(1,2)=-2.7857324061D-06
      GAMMA(1,3)= 4.6525738890D-04
      GAMMA(1,4)= 9.6856587146D-01
      GAMMA(1,5)= 2.4249262850D-05
      GAMMA(2,1)= 7.1533045594D-10
      GAMMA(2,2)= 4.2[illegible]
      GAMMA(2,3)= 4.2[illegible]
      GAMMA(2,4)= 9.3[illegible]
      GAMMA(2,5)=-4.3[illegible]
      GAMMA(3,1)=-1.7[illegible]
      GAMMA(3,2)= 7.5[illegible]
      GAMMA(3,3)=-1.2[illegible]
      GAMMA(3,4)= 9.6[illegible]
      GAMMA(3,5)=-2.[illegible]
      GAMMA(3,6)=-1.[illegible]
      GAMMA(3,7)=-1.[illegible]
      GAMMA(4,1)=-2.[illegible]
      GAMMA(4,2)= 0.[illegible]
      GAMMA(4,3)=-5.[illegible]
      GAMMA(4,4)= 2.[illegible]
      GAMMA(4,5)=-4.[illegible]
      GAMMA(5,1)= 4.[illegible]
      GAMMA(5,2)=-6.[illegible]
      GAMMA(5,3)= 1.[illegible]
      GAMMA(5,4)= 0.[illegible]
      GAMMA(5,5)= 0.[illegible]
      GAMMA(6,1)=-1.[illegible]
      GAMMA(6,2)= 8.[illegible]
      GAMMA(6,3)= 7.[illegible]
      GAMMA(6,4)= 1.[illegible]
      GAMMA(6,5)=-7.[illegible]
      GAMMA(7,1)= 1.[illegible]
      GAMMA(7,2)=-7.[illegible]
      GAMMA(7,3)= 1.[illegible]
      GAMMA(7,4)= 0.[illegible]
      GAMMA(7,5)= 9.[illegible]
      GAMMA(8,1)= 2.[illegible]
      GAMMA(8,2)=-4.[illegible]
      GAMMA(8,3)= 7.[illegible]
      GAMMA(8,4)= 1.[illegible]
      GAMMA(8,5)=-2.[illegible]
      T(1)=X(1)
      DO 10 I=2,7
      IM1=I-1
   10 T(I)=T(IM1)*T(IM1)
      DO 22 I=1,8
```

```
      N=4
      IF(I.EQ.3) N=6
      DO 30 J=1,7
      IF(J.EQ.N) GO TO 25
      NMJ=N-J
      GAMMA(I,J)=GAMMA(I,J)*T(NMJ)
      DGAMMA(I,J)=(NMJ+1)*GAMMA(I,J)
      GO TO 30
   25 NP1=N+1
      GAMMA(I,NP1)=GAMMA(I,NP1)/T(1)
      DGAMMA(I,N)=GAMMA(I,N)
      GO TO 32
   30 CONTINUE
   32 CONTINUE
      RK=8.61707E-05
      KT=RK*X(1)
      LIMIT1=1.0E-03/KT
      LIMIT2=2.0E-02/KT
      LIMIT3=1.0E-01/KT
C     CALCULATION OF INTEGRALS NEEDED IN SUBROUTINE FUN
      DINTG1= 8.8469106654D-01      +1.2427729615D-03*T(1)
     $        +1.2353398559D-05*T(2)+3.6937544702D-08*T(3)
     $        -6.2704747326D-10*T(4)+2.3337430490D-12*T(5)
     $        -3.7709451039D-15*T(6)+2.3108211276D-18*T(7)
      DINTG2= 8.8491475600D-01      +2.9966913409D-03*T(1)
     $        +1.3974670697D-05*T(2)-1.2312794460D-07*T(3)
     $        +5.3257331559D-10*T(4)-1.2280155299D-12*T(5)
     $        +1.5120564979D-15*T(6)-7.7439913461D-19*T(7)
      DDGDM1= 1.3283963579D+00      +1.8843754534D-03*T(1)
     $        +1.9917421079D-05*T(2)+5.5395956689D-08*T(3)
     $        -9.4066959059D-10*T(4)+3.4326795088D-12*T(5)
     $        -5.6551794465D-15*T(6)+3.4693652240D-18*T(7)
      DDGDM2= 1.3285394749D+00      +3.3224354570D-03*T(1)
     $        +1.9911430251D-05*T(2)-1.8474033749D-07*T(3)
     $        +7.9903746093D-10*T(4)-1.7656033170D-12*T(5)
     $        +2.1633464024D-15*T(6)-1.1044992767D-18*T(7)
      INTG1=SNGL(DINTG1)
      INTG2=SNGL(DINTG2)
      DDGDM1=SNGL(DDGDM1)
      DDGDM2=SNGL(DDGDM2)
      RETURN
      END
```

```
      SUBROUTINE RANDY(EPS,GAMMA,DGAMMA,LIMIT1,LIMIT2,GAM1,GAM2,
     2 DGAM1,DGAM2,GAM,DGAM,TIC,TAC,LIMIT3)
      DOUBLE PRECISION H8(7),H88(7),DH8(7),DH88(7)
      DOUBLE PRECISION GAMMA(8,7),DGAMMA(8,7)
      REAL LIMIT1,LIMIT2,LIMIT3
      DIMENSION GAM(4),DGAM(4)
C     THE SUBROUTINE RANDY EVALUATES THE POLYNOMIAL EXPANSION OF
C     GAMMA(EPS) FOR A GIVEN VALUE OF EPS
      M=0
   10 CONTINUE
      M1=5
      M2=5
      IF(EPS.GT.LIMIT3) GO TO 18
      IF(EPS.GT.LIMIT2) GO TO 20
      IF(EPS.GT.LIMIT1) GO TO 22
      GO TO 24
   18 L1=4
      L2=8
      GO TO 30
   20 L1=3
      L2=7
      M1=7
      GO TO 30
   22 L1=2
      L2=6
      GO TO 30
   24 L1=1
      L2=5
   30 CONTINUE
      H8(1)=GAMMA(L1,1)
      H88(1)=GAMMA(L2,1)
      DH8(1)=DGAMMA(L1,1)
      DH88(1)=DGAMMA(L2,1)
      M1M1=M1-1
      M2M1=M2-1
      DO 32 I=2,M1
   32 H8(I)=H8(I-1)*EPS+GAMMA(L1,I)
      DO 34 I=2,M2
   34 H88(I)=H88(I-1)*EPS+GAMMA(L2,I)
      DO 36 I=2,M1M1
   36 DH8(I)=DH8(I-1)*EPS+DGAMMA(L1,I)
      DO 38 I=2,M2M1
   38 DH88(I)=DH88(I-1)*EPS+DGAMMA(L2,I)
      IF(M) 42,44,46
   42 GAM(3)   =SNGL(H8(M1))
      GAM(4)   =SNGL(H88(M2))
      DGAM(3)  =SNGL(DH8(M1-1))
      DGAM(4)  =SNGL(DH88(M2-1))
      GO TO 70
   44 GAM1     =SNGL(H8(M1))
      GAM2     =SNGL(H88(M2))
      DGAM1    =SNGL(DH8(M1-1))
      DGAM2    =SNGL(DH88(M2-1))
      GO TO 50
   46 GAM(1)   =SNGL(H8(M1))
      GAM(2)   =SNGL(H88(M2))
      DGAM(1)  =SNGL(DH8(M1-1))
      DGAM(2)  =SNGL(DH88(M2-1))
      GO TO 60
   50 EPS=TAC



      M=1
      GO TO 10
   60 IF(TIC) 70,70,61
   61 EPS=TIC
      M=-1
      GO TO 10
   70 CONTINUE
      RETURN
      END
```

```
      SUBROUTINE FUN(NO,NX,P,X,YC,DFDP)
C     ANALYTIC INTEGRATION FOR NEUTRAL,IONIZED, AND LATTICE SCATTERING
C     Y(1) IS THE TEMPERATURE, Y(2) IS THE HOLE CONCENTRATION
C     ASSUMED CONCENTRATION IS KEPT FIXED IN THE FITTING
C     P(1-3) ARE FOR NEUTRAL SCATTERING, DONOR AND ACCEPTOR CONCENTRATION
C     P(4) IS A FACTOR TO NORMALIZE THE MOBILITY DUE TO INACCURACIES
C     IN THE SIMPLE DIFFUSION MEASUREMENTS.  P(4) SHOULD BE CLOSE TO 1.0
C     P(5) IS A CONSTANT WHICH CONTROLS THE OVERALL MAGNITUDE
C     OF THE LATTICE SCATTERING TIME
C     P(6) IS THE RELATIVE COUPLING STRENGTH OF THE ACOUSTIC TO OPTICAL PHONONS
      DIMENSION P(48),Y(48),DFDP(48)
      REAL LAMDA,LAMDA3
      REAL NA(3),ND(3),NORM,NORM2
      REAL MOBL,MOBL2
      DIMENSION GAMMA(3),DGAM(3)
      DIMENSION GAMMA(8,7),DGAMMA(8,7)
C     DEFINE CONSTANTS
      PI=3.1415926
      SQRTPI=1.772454
      Q=1.E-19
      BOLTZ=8.616E-5
      EMASS=9.11E-31
      TEMP=Y(1)
      HBAR=1.054E-34
      EPS0=8.854E-12
      EPS=EPS0*16.5
      ALPHA=HBAR**2/(2.*EMASS*Q*BOLTZ)
      BETA=(Q**3/(8.*PI*EPS))**2*3.
      GAMMA(1)=1.5
      GAMMA(2)=-.5
      GAMMA(3)=1.5
      DGAM(1)=0.
      DGAM(2)=0.
      DGAM(3)=0.
      NORM=P(1)/1.E22
      NORM2=P(2)/1.E22
      MOBL=1.E4/Y(1)
      MOBL2=P(5)*1.E-4*MOBL
      DO 10 I=1,NO
C     INTEGRATION BY SIMPSON'S RULE
C     THE INTEGRATION IS DIVIDED INTO TWO REGIONS, THE INTEGRATION
C     FROM 0 TO P(1)/P(2) IS DONE IN 100 STEPS AND FROM P(1)/P(2) TO P(1)/P(2)
C     + 6.*KT/Q, THE FIRST 6 KT/Q INTERVAL IN UNITS OF KT FOR
C     THE SECOND REGION )
      N1=50
      N2=50
      XMIN=.2500
      XMAX=.0000
      IF(I
C     CALCULATE THE ONE OF VARIOUS SCATTERING MECHANISMS
      IF(P(3)
      XL=(P(1)-P(3)*(EXP(P(1)/(P(3)*BOLTZ*TEMP))-1.)-P(2))/(P(3)*BOLTZ*TEMP)
      IF(XL.GT.80.)XL=80.
      EXPXL=EXP(XL)
      XMIN=(P(3)*BOLTZ*TEMP*LOG(1.+EXPXL)+P(2))/(P(3)*BOLTZ*TEMP)
      XMAX=(P(3)*BOLTZ*TEMP*LOG(1.+EXP(XL-6.*Q/(BOLTZ*TEMP)))+P(2))/(P(3)*BOLTZ*TEMP)
      DX1=(XMIN-.2500)/N1
      DX2=(XMAX-XMIN)/N2
      SUM=0.
      DO 20 J=1,N1
      X=.2500+(J-1)*DX1
      IF(X.LT.1.E-10)X=1.E-10
      SUM=SUM+DX1*(X**(GAMMA(I)+1.5)*EXP(-X)/(X+P(2)/P(3)))
      DO 30 J=1,N2
      X=XMIN+(J-1)*DX2
      SUM=SUM+DX2*(X**(GAMMA(I)+1.5)*EXP(-X)/(X+P(2)/P(3)))
      DFDP(I)=SUM*EXPXL/DENOM
      DENOM=DENOM+DFDP(I)
      DFDP(I)=1./(P(I)**2)*DFDP(I)
      IF(I.EQ.1)DFDP(I)=-.586
      IF(I.EQ.2)DFDP(I)=-3.119*P(I)
```

```
      TLO21=TLO12*EM1252
      TLO22=TLO21/1.61
C     LATTICE - OPTICAL PHONONS
      T0C=230./X(1)
      IF(T0C.GT.100.) T0C=100.
      T00=230.*X(6)*SQRT(X(1))/X(5)
      T0=1.0/(EXP(T0C)-1.0)
      T00=T00*(T0C+1.0)
      T0D=T0D*T0D
      CALL RANDOT(X,GAMMA,DGAMMA,LIMIT1,LIMIT2,LIMIT3,
     F                    INTG1,INTG2,NOPM1,NOSM2)
C     SETUP INTEGRATION LOOP
      M=1
      M2=1
      N=N1-1
      L=L1
      H=H1
      Q=M2/M1
      TSUM1=0.0
      TSUM2=0.0
      TSUM3=0.0
   10 CONTINUE
      ESUM1=0
      ESUM2=0
      ESUM3=0.0
      QSUM1=0
      QSUM2=0
      QSUM3=0.0
   20 CONTINUE
      DO 100 I=L,N
C     EPS IS THE SCALED ENERGY IN UNITS OF KT FOR EACH INTERVAL
      EPS=I*H
      T1C=EPS+T0C
      T2C=EPS-T0C
      EPP=-EPS
      CALL RANDX(EPS,GAMMA,DGAMMA,LIMIT1,LIMIT2,GAM1,GAM2,
     2   DGAM1,DGAM2,GAM,DGAM,T1C,T2C,LIMIT3)
      EPP=-EPS
C     ANHARMONIC
      T1=T0C/DGAM1
      T2=T00/DGAM2
C     IMPURITY
      B0M1=B0M1*GAM1
      B0M2=B0M2*GAM2
      B0M3=B0M3*EPS
      T11=(1.+B0M1*(1.-B0M1/(B0M1+1.)))*B0M1*DGAM1/GAM1**1.5
      T12=(1.+B0M2*(1.-B0M2/(B0M2+1.)))*B0M2*DGAM2/GAM2**1.5
      T13=(1.+B0M3*(1.-B0M3/(B0M3+1.)))*B0M3/EPS**1.5
C     ACOUSTIC PHONONS
      T1=T1*(1.-DGAM1*SQRT(GAM1)
      T2=T2*(1.-DGAM2*SQRT(GAM2)
      T12=T12*T12/T11
      T22=T22*T22/T21
      T3=T3*(EPS)
C     SUBTRACT ANNIHILATION EMISSION IF NOT POSSIBLE
C     IF(EPS-T0C*X/T.LT.0.)GO TO
      T1M1=T1*(1.-SQRT(GAM(1))*DGAM(1)
      T1M2=T12*(1.-SQRT(GAM(3))*DGAM(3)
      T2M2=T22*(T2C
      IF(T1C) 35,35,30
```

```
C     OPTICAL PHONON EMISSION IS POSSIBLE
C     IF ESPS=THETA/T IS POSITIVE
   30 TOP1=TOP1+TOPP*SQRT(GAM(2))*DGAM(2)
      TOP2=TOP2+TOPP*SQRT(GAM(4))*DGAM(4)
      TOP3=TOP3+TOPP*SQRT(TIC)
   35 CONTINUE
C     TOTAL THE INVERSE SCATTERING TIMES AND INVERT TO GET
C     INTRAAND SCATTERING TIMES
      T1=1.0/(TM1*TL1+TOP1)
      T2=1.0/(TM2*TL2+TOP2)
      T3=1.0/(TM3*TL3+TOP3)
C     INTERBAND SCATTERING TERMS
      DELTA=1.0-TL1**2*TL2*TL2*(DGAM1/DGAM2)**2.5
      CROSS1=1.0+T2**2*TL12*EM12*DGAM1/DGAM2
      CROSS2=1.0+T1**2*TL21*(DGAM1/DGAM2)**1.5/EM12
      SUM1=CROSS1*T1*G1*1.5*EXP(ESP)/(DELTA*DGAM1)
      SUM2=CROSS2*T2*G2*1.5*EXP(ESP)/(DELTA*DGAM2)
      SUM3=T3*ESP**1.5*EXP(ESP)
      IF(M) 150,40,50
   40 ESUM1=ESUM1+SUM1
      ESUM2=ESUM2+SUM2
      ESUM3=ESUM3+SUM3
      M=1
      GO TO 100
   50 ESUM1=ESUM1+SUM1
      ESUM2=ESUM2+SUM2
      ESUM3=ESUM3+SUM3
      M=0
  100 CONTINUE
      M=-1
      L=N+1
      DO 20
C     FINISH SUBTOTALS ACCORDING TO SIMPSONS RULE AND COMPUTE MOBILITY
  110 TSUM1=DX*((SUM1+0.5*SUM1)*4.+ESUM1*2.)/3.)/EM1+TSUM1
      TSUM2=DX*((SUM2+0.5*SUM2)*4.+ESUM2*2.)/3.)/EM2+TSUM2
      TSUM3=DX*((SUM3+0.5*SUM3)*4.+ESUM3*2.)/3.)/EM3+TSUM3
      IF(M) 200,200,160
  150 M2=-1
      M=1
      L=12
      N=M2-1
      E=0.0
      DO 10
  200 CONTINUE
      WOM1=EM133*TSUM1/WOOM
      WOM2=EM233*TSUM2/WOOM2
      WOM3=EM333*TSUM3/3.
      WOOM=(WOM1+WOM2+WOM3)/(EM132*INTG1+EM232*INTG2+
     *  EM332*INTG3)**2/2.
C     PRINT RESULTS AND FIND DERIVATIVES
      WRITE(1,5,ERR=*)X(2),Y(2)
      WRITE(1,5,ERR=*)X(1),Y(1)
      WRITE(1,5,ERR=*)(X(2)**2.*P(2)+(ALOG(1./3.*ESP01/EM1)-1.))
      WRITE(1,5,ERR=*)
    5 FORMAT(1X,E15.6)
      UL=(1.0+P(4)*A)*X(1)**1.5)
      DY=(UM-UL)*(UM-UL)
      DX=UM-UL
      DERP(1)=DERP(1)/(UM-UL)*(UL-UM)/(UM*UD)
      DERP(2)=DERP(2)/(UM-UL)*(UM-UL)/(UM*UD)
      DERP(3)=UL/(UM-UL)*(UM-UL)/(UM*UD)
      DERP(1)=DERP(1)/(P(1)*YC)
      DERP(2)=(DERP(2)-X(2))*DERP(2)*(-2.)/(X(2)+2.*P(2))/YC
      DERP(3)=0.0
      DERP(4)=1.0
      DERP(5)=DERP(5)/(P(5)*YC)
      DERP(6)=DERP(6)*(-1.)/((1.+P(6)*A)*YC)
      WRITE(1,5,ERR=*)(1.0/UL+1.0/UL)/UL
C     CORRECT TO METHOD OF LOG FOR COMPARISON WITH MEASURED MOBILITY
      YC=ALOG(YC)
      DERP(4)=
      END
```

Table I. Constants used in evaluation of secular equation (Eq. (2) of text).

Quantity	Value	Units
μ	1/5 [a]	
q	1/105 [a]	
Δ [b]	.044	eV
A [c]	-4.27	$\hbar^2/2m_e$
B [c]	-0.63	$\hbar^2/2m_e$
N [c]	-8.75	$\hbar^2/2m_e$

[a] spherically averaged value

[b] Ref. (64)

[c] Ref. (65)

Table II. Results of carrier concentration analysis with temperature independent effective mass.

Sample	N_a (cm^{-3})	N_d (cm^{-3})	E_a (meV)	m_d^*/m_e	Stand. Dev. of Fit (10^{-2})
Si:B-1	1.32×10^{14}	8.30×10^{12}	44.2	.59[a]	1.0
	1.35×10^{14}	8.32×10^{12}	43.9	.53	0.5
Si:B-2	5.40×10^{13}	4.67×10^{13}	43.2	.59[a]	2.2
Si:B-3	5.82×10^{16}	2.45×10^{15}	41.1	.59[a]	0.9
	7.61×10^{16}	2.27×10^{15}	41.1	.47	0.7
Si:B-4	1.24×10^{15}	7.48×10^{12}	45.0	.59[a]	1.4
	1.15×10^{15}	7.57×10^{12}	45.2	.66	1.2
Si:B-5	1.48×10^{15}	2.14×10^{12}	44.9	.59[a]	1.4
	1.43×10^{15}	2.08×10^{12}	45.0	.62	1.4
Si:B-6	3.36×10^{17}	2.34×10^{14}	44.3	.59[a]	3.5
Si:B-7	1.76×10^{16}	1.91×10^{13}	45.4	.59[a]	2.8
	1.30×10^{16}	7.69×10^{12}	49.0	1.16	2.0
Si:B-8	1.54×10^{14}	4.99×10^{12}	45.3	.59[a]	1.8
	1.48×10^{14}	5.13×10^{12}	45.8	.71	0.7
Si:B-14	2.14×10^{13}	1.26×10^{13}	44.8	.59[a]	0.5
	2.10×10^{13}	1.22×10^{13}	44.7	.61	0.5

[a] value fixed

Table III. Results of carrier concentration analysis for temperature dependent effective mass.

Sample	N_a (cm^{-3})	N_d (cm^{-3})	E_a (meV)	$m_d^*(T)/m_e$	Stand. Dev. of Fit (10^{-2})
Si:B-1	1.30×10^{14}	7.86×10^{12}	44.3	.56[a]	1.5
	1.34×10^{14}	7.97×10^{12}	44.7	.48	0.6
Si:B-2	5.86×10^{13}	5.07×10^{13}	42.9	.56[a]	2.1
Si:B-4	1.18×10^{15}	7.14×10^{12}	45.0	.56[a]	1.2
	1.11×10^{15}	$7.2. \times 10^{12}$	45.1	.61	1.1
Si:B-5	1.39×10^{15}	2.05×10^{12}	44.8	.56[a]	1.3
	1.37×10^{15}	2.00×10^{12}	44.9	.59	1.3
Si:B-7	1.57×10^{16}	1.88×10^{13}	45.1	.56[a]	1.6
	1.27×10^{16}	8.68×10^{12}	48.2	.96	1.3
Si:B-8	1.51×10^{14}	4.84×10^{12}	45.3	.56[a]	1.4
	1.47×10^{14}	4.92×10^{12}	45.6	.64	0.8
Si:B-14	2.27×10^{13}	1.40×10^{13}	44.5	.56[a]	0.5
	2.10×10^{13}	1.22×10^{13}	44.5	.52	0.5

[a] value fixed

Table IV. Results of mobility fits used to determine the lattice scattering parameter τ_o.

Sample	τ_o (sec) (10^{-9})	N_d (cm^{-3})	W^a	A^a	G^a	Stand. Dev. of Fit (10^{-2})	Temperature Range (K)
Si:B-8	5.25	4.45×10^{12}	2.0	2.0	1.0	1.2	25-80
Si:B-14	5.17	1.39×10^{13}	2.0	2.0	1.0	1.6	25-80
Si:B-1	5.39	3.17×10^{12}	2.0	2.0	1.0	1.0	25-80

[a]value fixed

Table V. Mobility fits used to investigate influence of G on the determination of τ_o.

Sample	τ_o^a (sec) (10^{-9})	N_d (cm^{-3})	W^a	A^a	G	Stand. Dev. of Fit (10^{-2})	Temperature Range (K)
Si:B-14	5.25	1.40×10^{13}	2.0	2.0	0.99	0.5	25-80
Si:B-1	5.25	4.01×10^{12}	2.0	2.0	1.03	1.6	25-80

[a]value fixed

Table VI. Results of mobility fits used to determine W.

Sample	τ_o^a (sec) (10^{-9})	N_d (cm^{-3})	W	A^a	G	Stand. Dev. of Fit (10^{-2})	Temperature Range (K)
Si:B-8	5.25	4.09×10^{12}	2.00	2.0	0.99	1.3	25-400
Si:B-14	5.25	1.34×10^{13}	1.78	2.0	0.98	1.1	25-300

[a] value fixed

Table VII. Comparison of compensation density as determined from mobility and carrier concentration analysis.

Sample	N_a	N_d from carrier concentration analysis (cm^{-3})	N_d from mobility analysis (cm^{-3})	A	G	Stand. Dev. of Fit (10^{-2})
			6.11×10^{12}	2.0[a]	0.98	0.8
Si:B-4	1.18×10^{15}	7.14×10^{12}	7.05×10^{12}	4.0[a]	0.98	0.8
			7.37×10^{12}	6.0[a]	0.98	0.8
			1.54×10^{12}	2.0[a]	0.95	1.2
Si:B-5	1.39×10^{15}	2.05×10^{12}	2.19×10^{12}	4.0[a]	0.94	0.9
			2.43×10^{12}	6.0[a]	0.94	0.8
Si:B-8	1.51×10^{14}	4.84×10^{12}	4.27×10^{12}	2.0[a]	0.99	1.3
			4.37×10^{12}	4.0[a]	0.99	1.3
Si:B-14	2.27×10^{13}	1.40×10^{13}	1.39×10^{13}	2.0[a]	0.99	1.4
			1.39×10^{13}	4.0[a]	0.99	1.4
Si:B-3	5.86×10^{16}	2.45×10^{15}	1.32×10^{15}	3.3	0.88	1.5
Si:B-6	3.36×10^{17}	2.34×10^{14}	4.57×10^{14}	2.0	0.98	3.4
Si:B-7	1.57×10^{16}	1.88×10^{13}	2.60×10^{13}	2.2	0.94	2.1

[a]value fixed

Table VIII. Results of mobility fits assuming a parabolic band model.

Sample	τ_o (sec) (10^{-9})	N_d (cm^{-3})	W	A	G	Stand. Dev. of Fit (10^{-2})
Si:B-8	3.09	4.7×10^{9} [a]	5.98	2.0[b]	1.0[b]	9.1
Si:B-14	2.95	2.3×10^{12}	5.99	2.0[b]	1.0[b]	5.8

[a] parameter did not converge to required confidence level

[b] value fixed

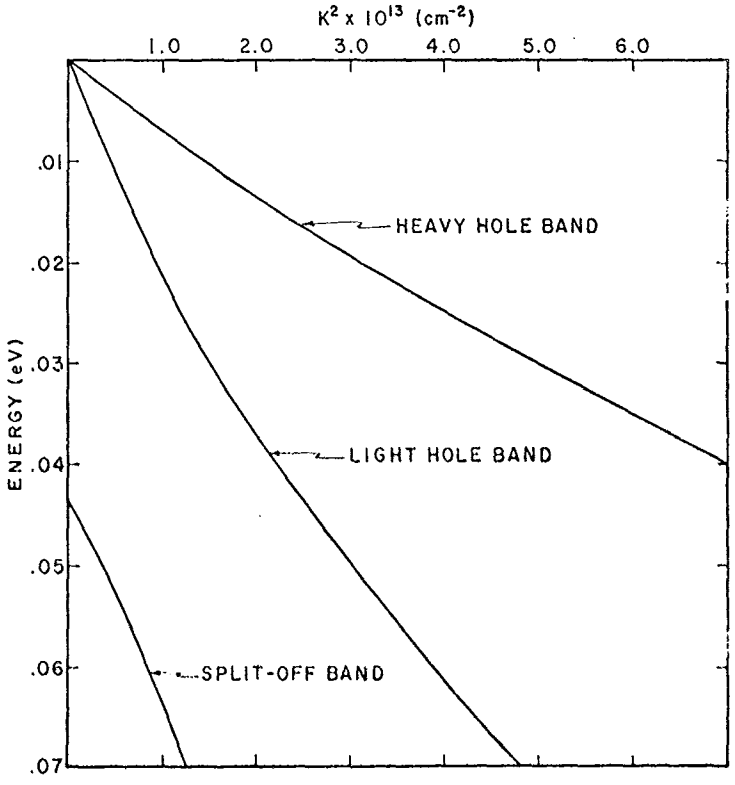

FIG. 1. Spherically averaged valence band structure of silicon as calculated from equation (2) with the parameters of Table I.

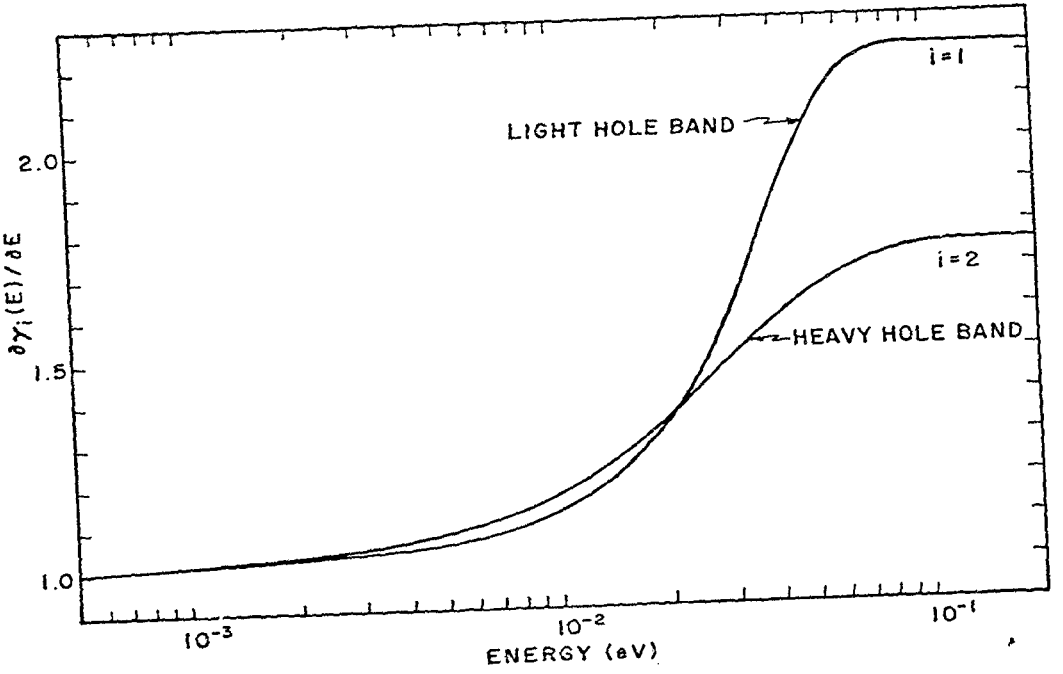

FIG. 2. Change in slope of E versus k^2 curve of Fig. 1 for the light and heavy hole bands as a function of the energy. A constant slope in the limit of low energy is clearly evident.

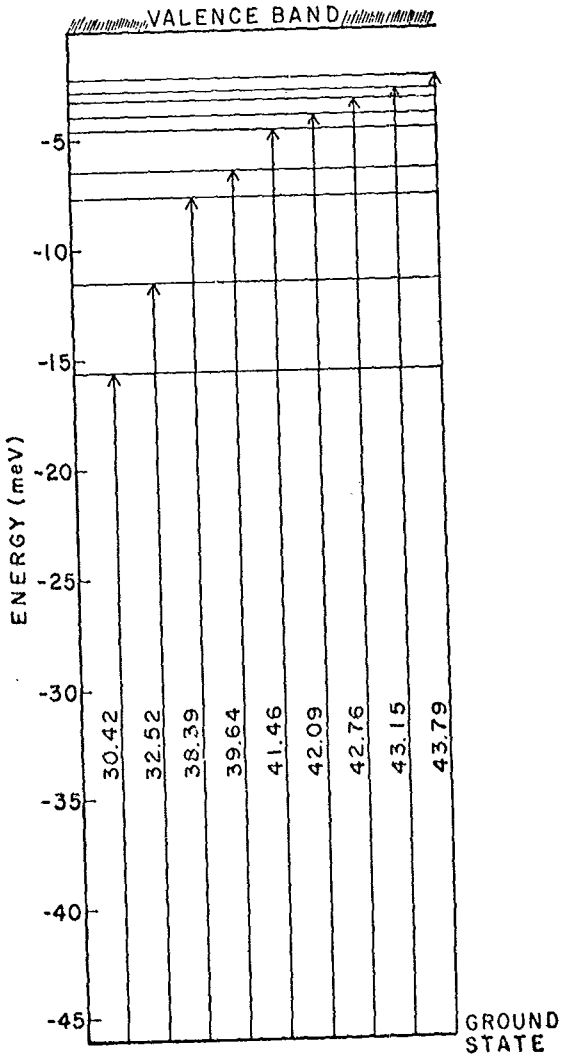

FIG. 3. Energy differences between the ground state and the excited states for boron-doped silicon (after Colbov, Ref. 13).

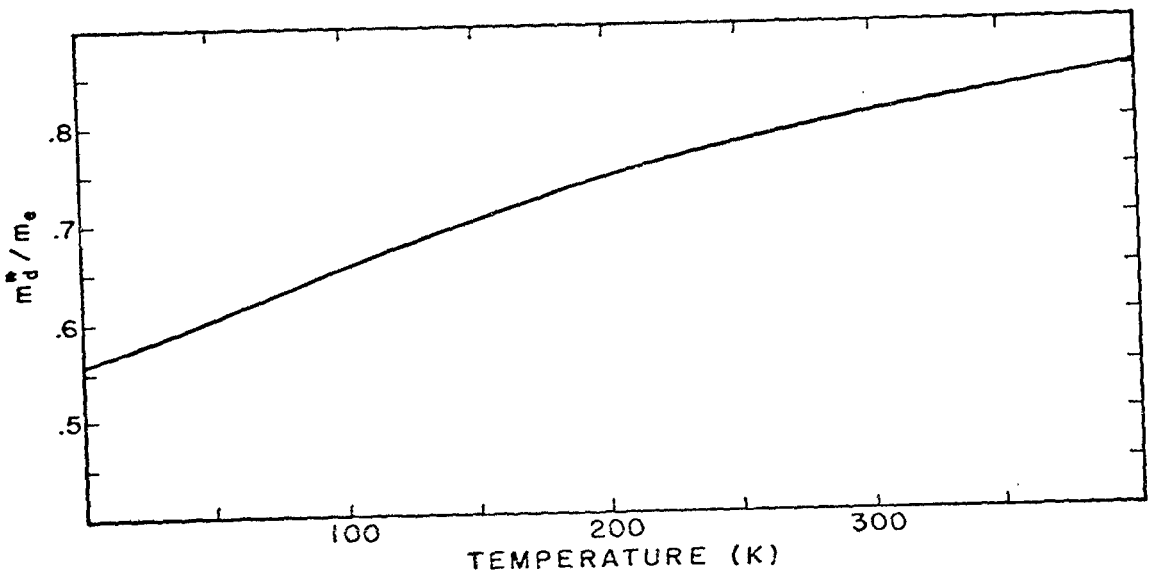

FIG. 4. Temperature dependence of density of states effective mass due to the non-parabolic valence band structure of silicon.

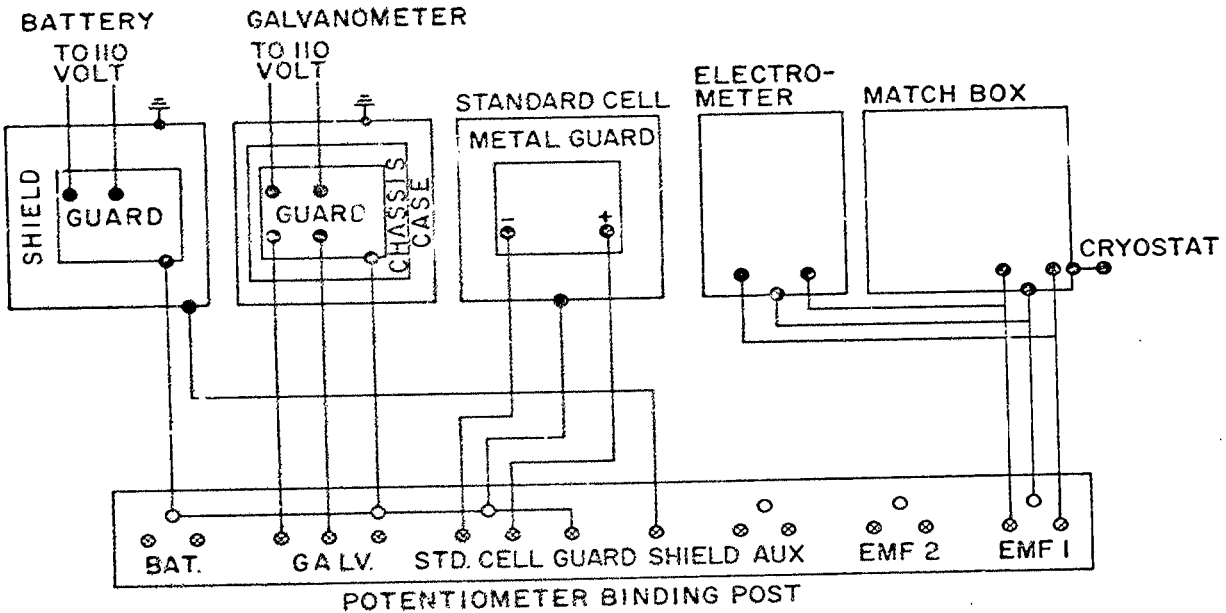

FIG. 5. Arrangement of Hall and resistivity measurement apparatus.

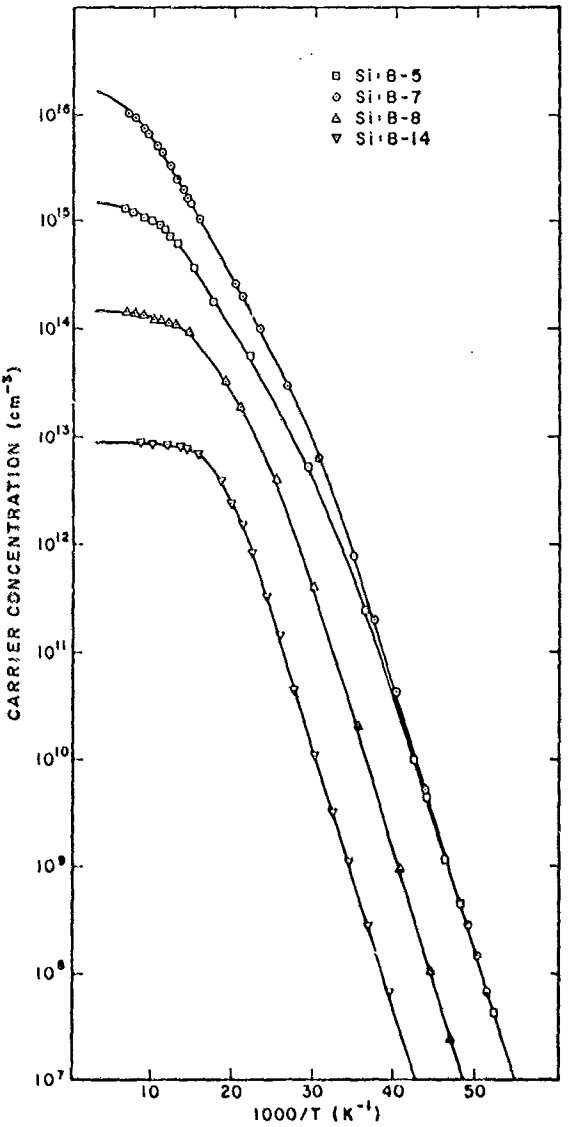

FIG. 6. Carrier concentration as a function of reciprocal temperature for four representative samples. Solid lines are computed curves fit to the data shown by coded points.

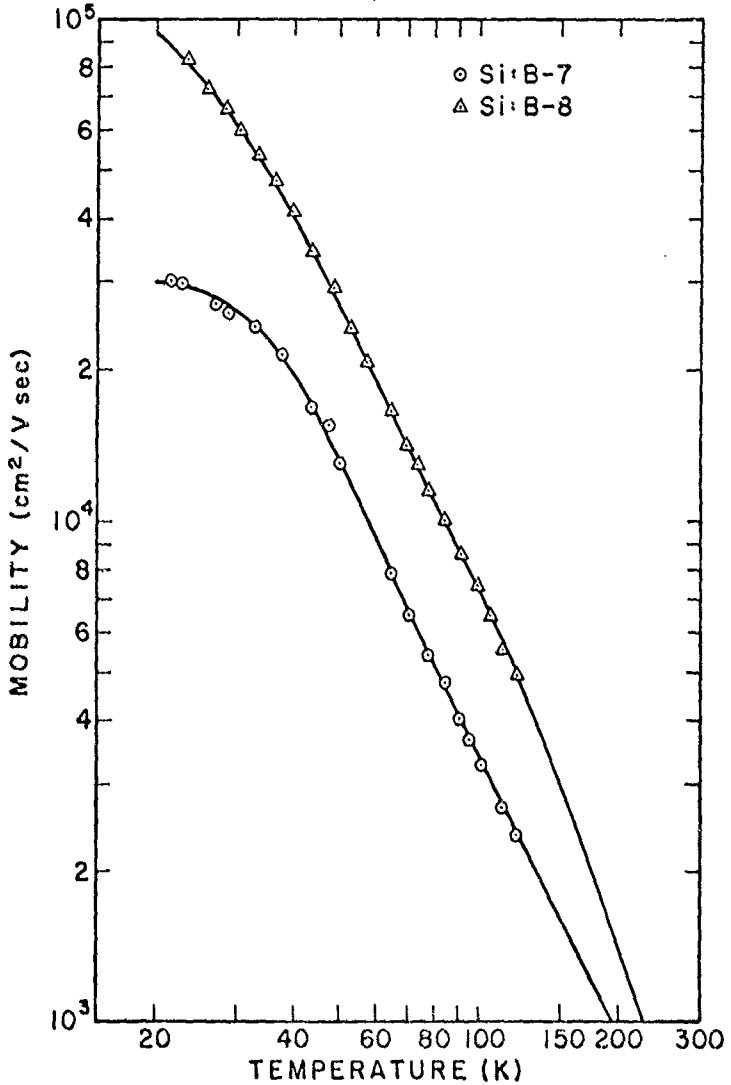

FIG. 7. Mobility as a function of temperature for Si:B-7 and Si:B-8. [illegible] curves fit to the data shown by coded points.

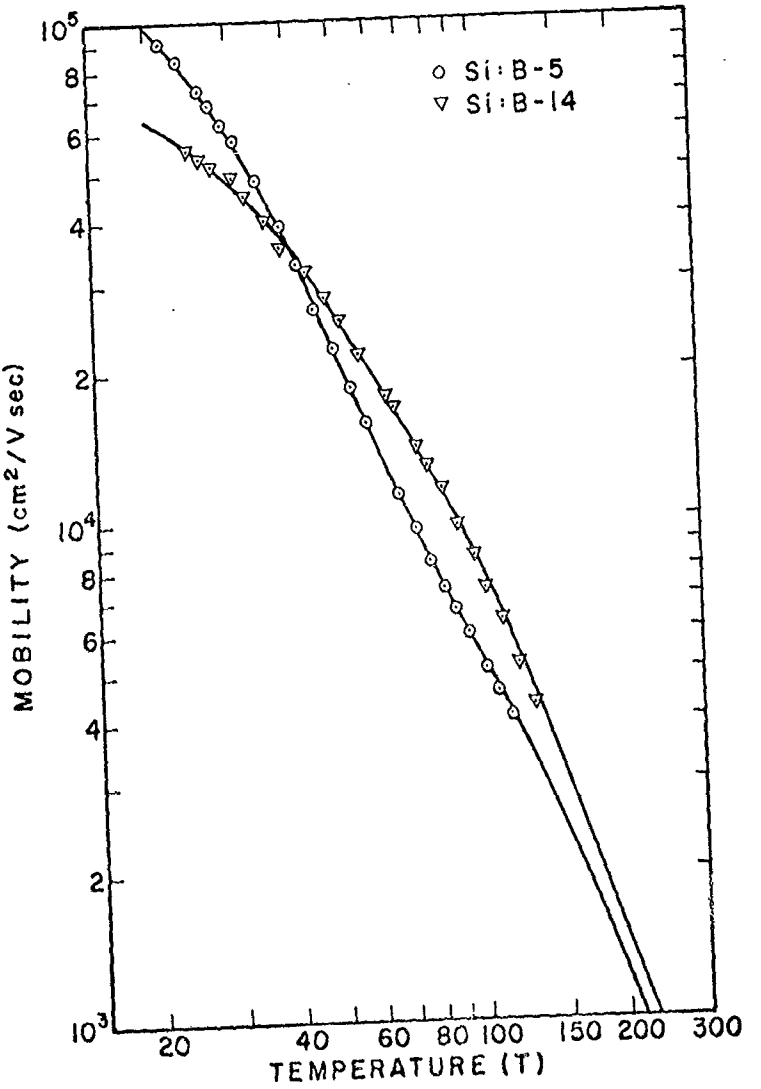

FIG. 8. Mobility as a function of temperature for Si:B-5 and Si:B-14. Solid lines are computed curves fit to the data shown by coded points.

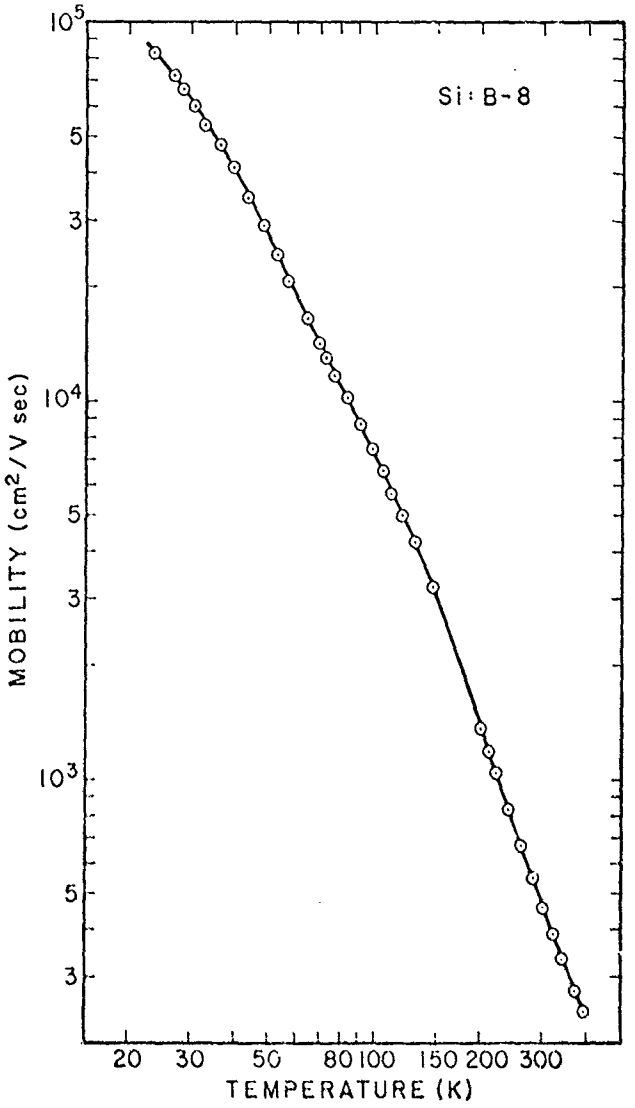

FIG. 9. Mobility as a function of temperature for Si:B-8. Mobility data points above 130 K have been obtained from the measured resistivity and the calculated carrier concentration (see text). Solid lines are computed curves from the fit given in Table VI to the data shown by

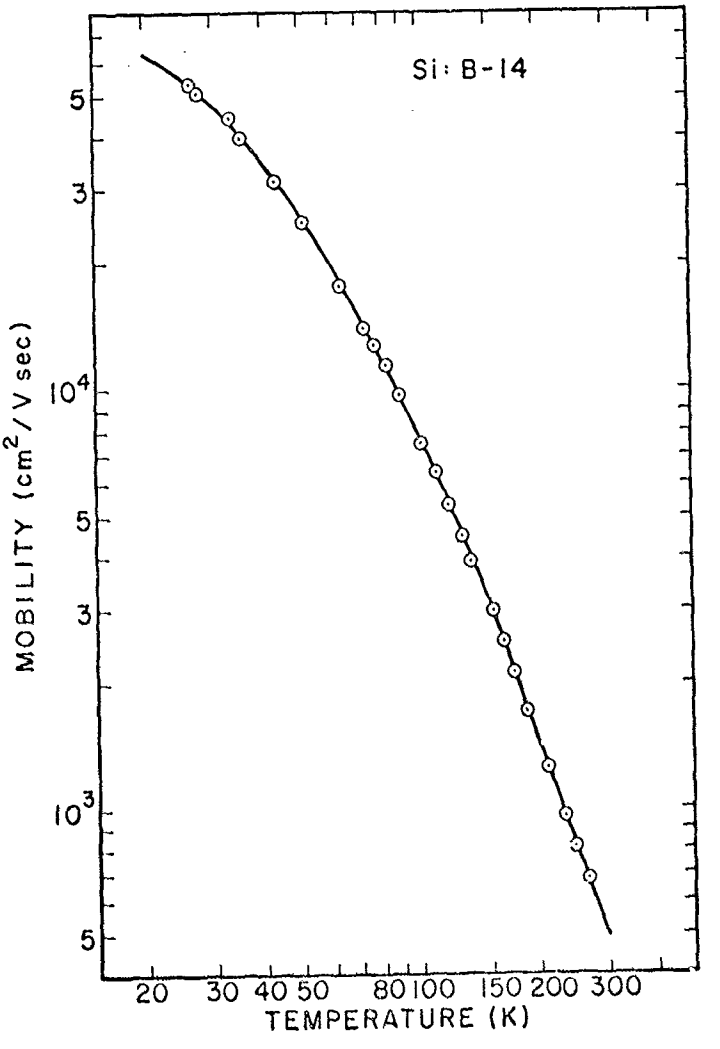

FIG. 10. Mobility as a function of temperature for Si:B-14. Mobility data points above 120 K have been obtained from the measured resistivity and the calculated carrier concentration (see text). Solid lines are computed curves from the fit given in Table VI to the data shown by coded points.

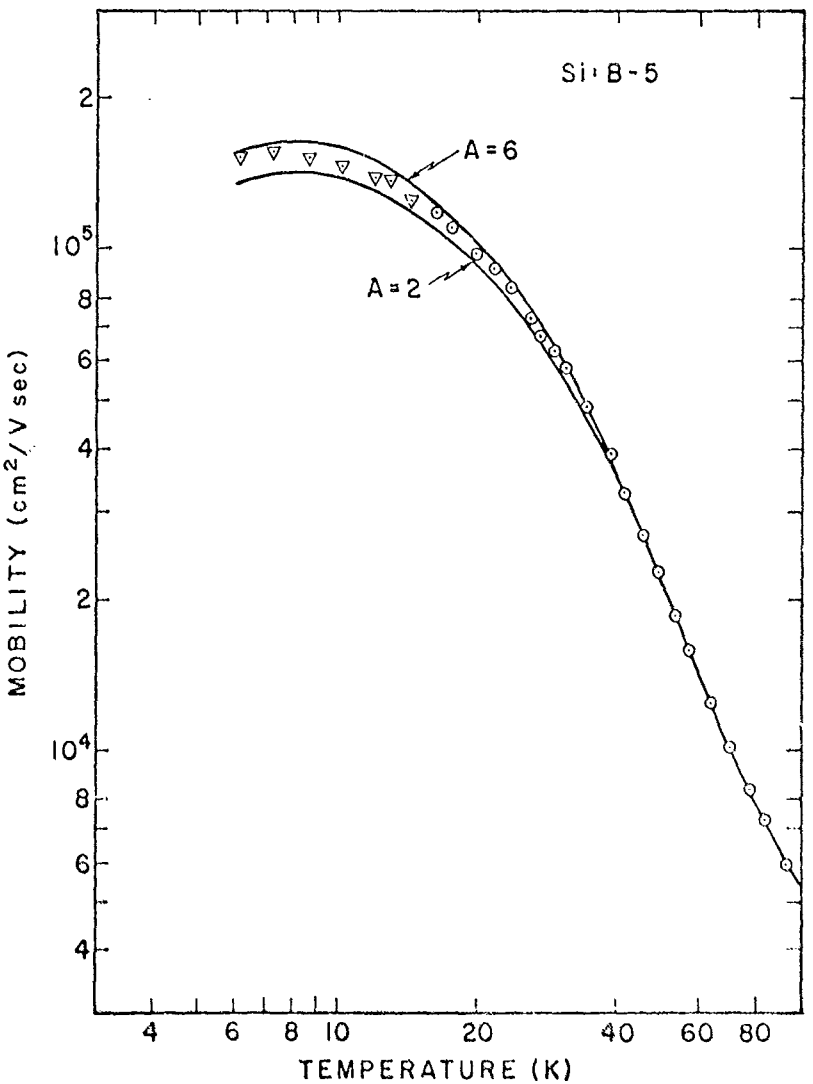

FIG. 11. Influence of the neutral impurity scattering parameter, A, on the calculated mobility compared with the experimental mobility data of Si:B-5. Below 20 K the mobility data was obtained from Hall

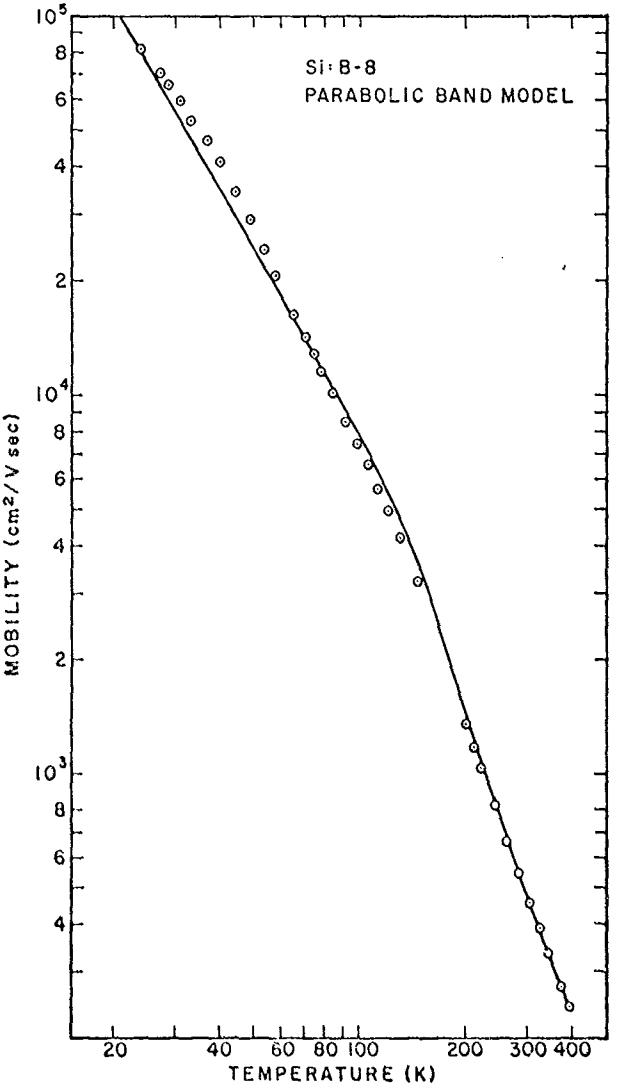

FIG. 12. Mobility fit (solid line) assuming a parabolic valence band structure to the experimental data (coded points) of Si:B-8. The parameters determined from this fit are given in Table VIII.

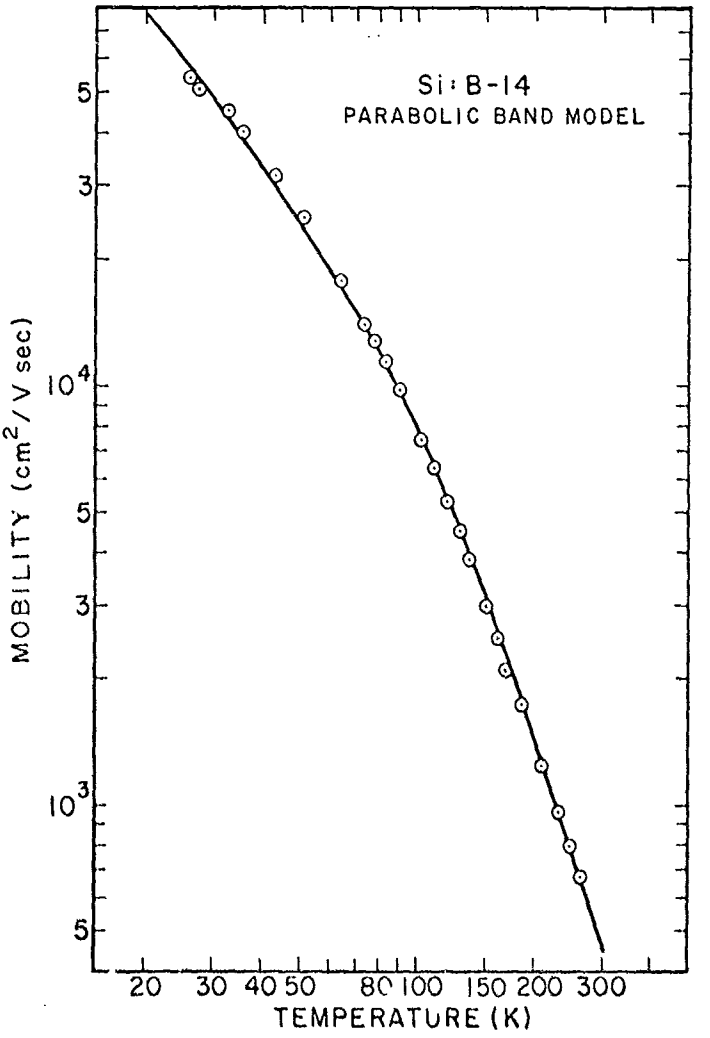

FIG. 13. Mobility fit (solid line) assuming a parabolic valence band structure to the experimental data (coded points) of Si:B-14. The parameters determined from this fit are given in Table VIII.

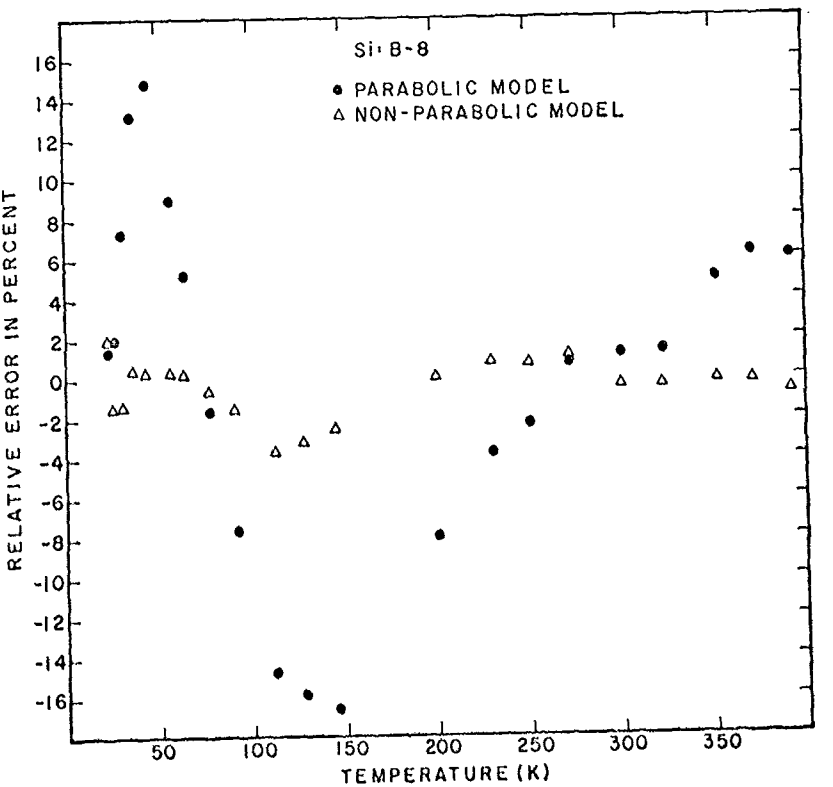

FIG. 14. Relative error in percent for the parabolic and non-parabolic mobility fits to the data of Si:B-8. The parabolic and non-parabolic fits have been graphed in Figs. 12 and 9, respectively. Relative error is defined as Error = $[(\mu_E - \mu_c)/\mu_E] \cdot 100$, where μ_E is the measured mobility and μ_c is the calculated mobility. The parameters for the calculated mobility are given for the parabolic and non-parabolic cases in Tables VIII and VI, respectively.

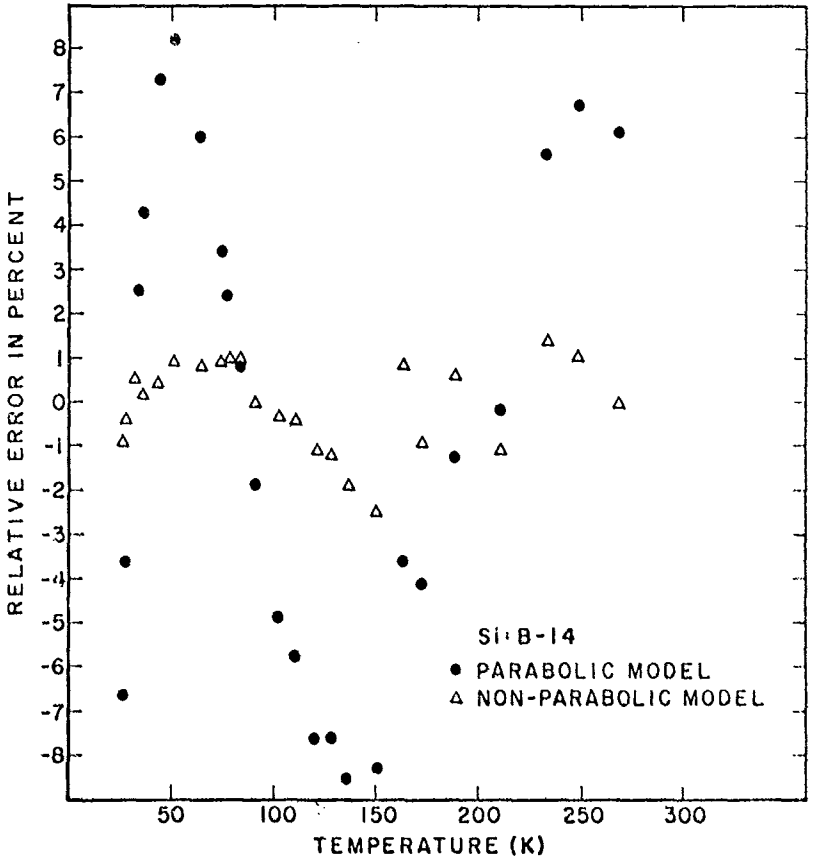

FIG. 15. Relative error in percent for the parabolic and non-parabolic mobility fits to the data of Si:B-14. The parabolic and non-parabolic fits have been graphed in Figs. 13 and 10, respectively. The relative error is defined as in the caption to Fig. 14. The parameters for the calculated mobility are given for the parabolic and non-parabolic cases in Tables VIII and VI, respectively.

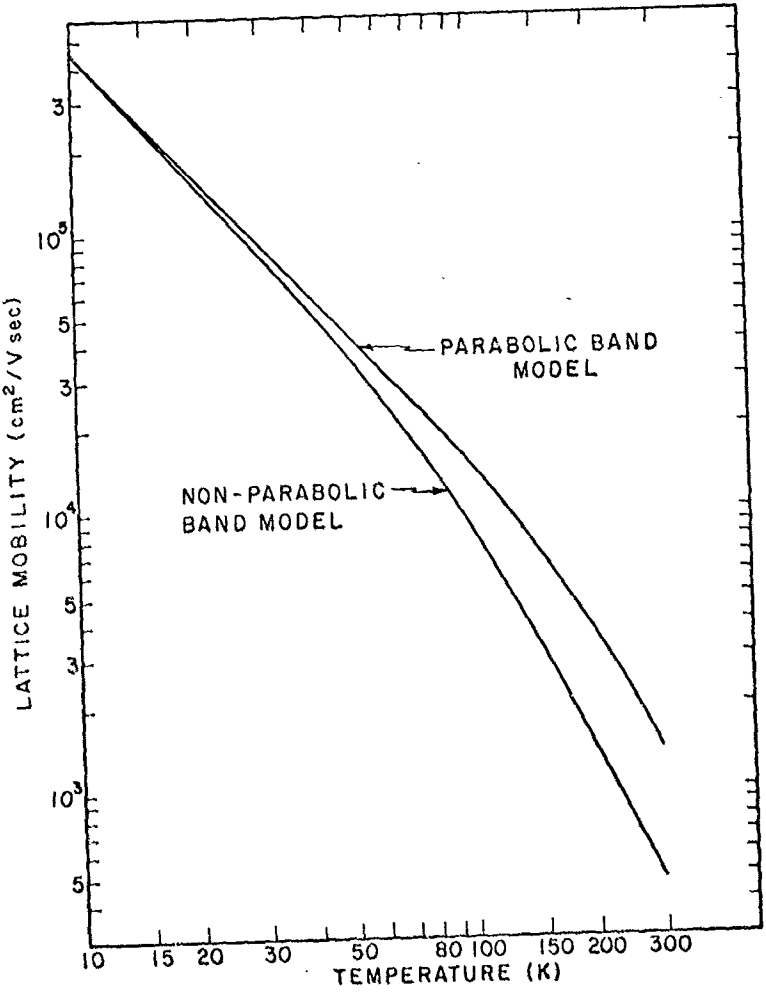

FIG. 16. Lattice-scattering-limited mobility assuming parabolic and non-parabolic valence band structures. The following parameters have been used: $N_a = 1\times10^{10}$ cm^{-3}, $N_d = 1\times10^{7}$ cm^{-3}, $\tau_o = 5.25\times10^{-9}$ sec, W = 2.0, A = 1.0, and Q = 1.0.

REFERENCES

1. E.O.Kane, J. Phys. Chem. Solids 1, 82 (1956).
2. K.Ya-Shtivel'man, Fiz. Tverd. Tela 2, 499 (1960) [Sov. Phys.-Solid State 2 , 464 (1960)].
3. M.Asche and J. Borzeszkowski, Phys. Status Solidi 37, 433 (1970).
4. J. Borzeszkowski, Phys. Status Solidi B 61 , 607 (1974).
5. G. Dresselhaus, A.F. Kip, and C. Kittel, Phys. Rev. 98, 368 (1955).
6. R. Barrie, Proc. Phys. Soc. London B69 , 553 (1956).
7. L. Sosnowski, in Proceedings of the Seventh International Conference on the Physics of Semiconductors, Paris, 1964 (Dunod, Paris, 1964) p. 341.
8. D.Schecter, J. Phys. Chem. Solids 23 , 237 (1962).
9. K.S.Mendelson and D.R.Shultx, Phys. Status Solidi 31, 59 (1969).
10. N.O.Lipari and A.Baldereschi, Phys. Rev. Lett. 25 , 1660 (1970).
11. A.Baldereschi and N.O.Lipari, Phys. Rev. B 9 , 1525 (1974).
12. M.Jaros and M.F.Ross, J. Phys. C Solid State Phys. 6, 1753 (1973).
13. K.Colbow, Can.J.Phys. 41, 1801 (1963).
14. M.W.Skoczylas and J.J.White, Can. J. Phys. 43 , 1388 (1965).
15. A.Onton, P.Fisher, and A.K.Ramdas, Phys. Rev. 163, 686 (1967).
16. M.Costato, G.Gagliani, C.Jacoboni, and L.Reggiani, J.Phys. Chem. Solids 35 , 1605 (1974).
17. P.Lawaetz, Phys. Status Solidi 11, K117 (1965).
18. J.M.Radcliffe, Proc. Phys. Soc. London A68 , 675 (1955).
19. W.Zawadzki and W.Szymanska, Phys. Status Solidi B 45, 415 (1971).
20. G.I.Bir, E.Normantas, and G.E.Pikus, Fiz. Tverd. Tela 4, 1180 (1962) [Sov. Phys.-Solid State 4 , 867 (1962).
21. The evaluation of the acoustic phonon scattering times as given in

Ref. 20 requires a knowledge of the inverse mass band parameters (listed in Table I), the elastic constants of silicon [J.J.Hall, Phys. Rev. 161 , 756 (1967)], and the deformation potential constants a, b, and d (in the notation of Ref. 39). For the deformation constants we have used b = 2.4 ev, d = -53 ev, and $\Xi d + \frac{1}{3}\Xi\mu - a = 3.8$ ev [I.Balslev, Phys. Rev. 143, 636 (1965)] and determined a = -6.4 ev from values of Ξd and Ξμ given by [R.Ito, H.Kawamura, and M.Fukai, Phys. Lett. 13, 26 (1964)].

22. E.Conwell, J. Phys. Chem. Solids 8, 234 (1959).

23. B.N.Brockhouse, Phys. Rev. Lett. 2, 256 (1959).

24. H.Brooks, Phys. Rev. 83 , 879 (1951); in Ref. 28.

25. R.B.Dingle, Phil. Mag. 46, 831 (1955).

26. N.Sclar, Phys. Rev. 104, 1548 (1956).

27. C. Erginsoy, Phys. Rev. 79, 1013 (1950).

28. H.Brooks, in Advances in Electronics and Electron Physics,edited by L.Marton (Academic, New York, 1955), Vol. 7, p. 85.

29. P.Norton and H. Levinstein, Phys. Rev. B 6, 470 (1972).

30. P.Norton, T. Braggins, and H. Levinstein, Phys. Rev. B 8, 5632 (1973).

31. P.P.Debye and E.M.Conwell, Phys. Rev. 93, 693 (1954).

32. D.Matz, J. Phys. Chem. Solids 28, 373 (1967).

33. J.S.Blakemore, Semiconductor Statistics (Pergamon, New York, 1962), p. 139.

34. Ref. 33, p. 146.

35. H.D.Barber, Solid State Elect. 10, 1039 (1967).

36. J.M.Flores, Rev. Sci. Inst. 35, 112 (1964).

37. A.C.Beer, Galvano magnetic Effects in Semiconductors (Academic, New York, 1963.)

38. E.H.Putley, The Hall Effect and Semiconductor Physics (Dover, London, 1968).

39. G.L.Bir and G.E.Pikus, Fiz Tverd. Tela 2, 2287 (1960).
[Sov. Phys.- Solid State 2, 2039 (1961)].

40. P.Lawaetz, Phys. Rev. 174, 867 (1968).

41. P.Norton, Ph D. dissertation (Syracuse University, 1970), (unpublished).

42. R.Willardson, T.Harman, and A.Beer, Phys. Rev. 96, 1512 (1954).

43. J.Swanson, Phys. Rev. 99, 1799 (1955).

44. E.N.Adams and R.W.Keyes, in Progress in Semiconductors, edited by A.F.Gibson (Wiley, New York, 1962), vol. 6, p. 85.

45. Ref. 33, p. 48 ff.

46. Y.Yafet, R.W.Keyes, and E.N.Adams, J. Phys. Chem. Solids 1, 137 (1956).

47. W.Daniels, Jr., University of Maryland Technical Report No. 579, (unpublished).

48. Ref. 33, p. 135.

49. Ref. 33, p. 108.

50. P.Norton and H. Levinstein, Phys. Rev. B 6, 478 (1972).

51. We have evaluated the thermalization time using equation (8) of Ref. 50 assuming a carrier injection energy large compared to the average thermal energy. A deformation potential of E_1 = 9.1 eV and an effective mass of .537 m_e have been used.

52. T.Braggins (unpublished measurements).

53. F.Morin, J.Maita, R.Shulman, and N.Hannay, Phys. Rev. 96, 833 (1954).

54. E.Burstein, G.Picus, B.Henvis, and R.Wallis, J. Phys. Chem. Solids 1 , 65 (1956).

55. H.Brooktowski and R.Kaiser, J. Phys. Chem. Solids 4, 148 (1958).

56. L.Elstner, phys. Status Solidi 17, 139 (1966).

57. M.B.Prince, Phys. Rev. 93, 1204 (1954).

58. G.W.Ludwig and R.L.Watters, Phys. Rev. 101, 1699 (1956).

59. D.Cronemeyer, Phys. Rev. 105, 522 (1957).

60. J.D.Wiley and M.DiDomenico,Jr., Phys. Rev. B 2, 427 (1970).

61. J.D.Wiley, Solid State Comm. 8 ,1865 (1970).

62. S.Zwerdling, K.J.Button, B.Lax, and L.M.Roth, Phys. Rev. Lett. 4, 173(1960).

63. I.Balslev and P.Lawaetz, Phys. Lett. 19, 5 (1965).

64. Ref. 33, p. 81.

PART II

ABSORPTION EDGE SHIFT IN HEAVILY DOPED LEAD-TIN TELLURIDE

CHAPTER I

INTRODUCTION

The lead-tin telluride ((Pb,Sn)Te) alloy system has been studied extensively by many investigators in the past ten years. A summary of the important results is given in two excellent review articles[1,2] which also discuss the possible applications of this material. (Pb,Sn)Te is a narrow gap semiconductor and is sensitive to the infrared spectrum of the electromagnetic radiation. Since the energy gap depends on the composition and temperature, both diode lasers and photon detectors with maximum sensitivity at any desired wavelength between 5 and 30 micrometers can be fabricated.

This study is concerned with impurity diffusion in (Pb,Sn)Te and the effect of these diffused impurities on its optical and electrical properties. By using light sensitive diffused lead-tin telluride detectors, we were able to examine the behavior of the fundamental absorption edge as a function of impurity concentration, the content fractional amount of SnTe in the crystal, and the temperature. Our results indicate three different behaviors corresponding to three types of impurities: cadmium, antimony, and a mixture of cadmium and indium. Cadmium diffusion may result in a material with carrier concentration as low as 10^{17} per cm^3. For (Pb,Sn)Te with carrier density below 10^{18} per cm^3 there is essentially no change in the energy gap. If, however, as a result of the diffusion the carrier concentration is higher, such as in the case of antimony diffusion, there is a considerable shift in the fundamental

absorption edge. Then the material is no longer sensitive to lower energy radiation. We compared the two cases by measuring the spectral response of two types of photodiodes: one was made by diffusing Sb and the other by diffusing Cd into (Pb,Sn)Te. A similar displacement of the absorption edge had been observed in data obtained from transmission measurements.[3] These transmission results, which had been performed earlier in our laboratory, revealed that in undiffused, unannealed (Pb,Sn)Te, where excess of tellurium is a source of high carrier density, there is an obvious shift in the absorption edge. A model proposed by Burstein[4] was used to explain this anomalous behavior. It is suggested that for small gap materials with a small effective mass and high carrier concentration, the Fermi energy, E_f, moves to either the conduction or the valence band, depending whether it is n-type or p-type semiconductor. Since we are dealing with a direct gap semiconductor, the photon energy, hν, required to excite electron hole pair in such a degenerate material is greater than the energy gap E_g. Here h is Planck's constant and ν is the photon frequency. For (Pb,Sn)Te it is given by

$$h\nu = E_g + 2(E_f - \gamma k_B T) \tag{1.1}$$

where γ depends only on the absorption coefficient, k_B is Boltzmann's constant, and T is the absolute temperature. We used Kane's nonparabolic band model[5] in calculating the Fermi level and showed that this model is in agreement with the experimental results. The experimental values of hν for two samples have been fit to the calculated ones using a digital computer, and values for γ and the effective mass, m^*, were obtained.

A different type of diffused (Pb,Sn)Te produced an even more pronounced change in its absorption spectra. In this case the diffusion of cadmium-indium alloy produced material with higher resistivity, lower carrier density, and larger energy gap than ever reported before. This is probably due to some change in the compound itself rather than just in its doping level. It was observed that although the crystalline structure remains essentially the same, the unit cell expands as a result of the diffusion. X-ray examination and microprobing indicate microscopic centers of impurity. The effect is more pronounced as the diffusion temperature is increased. The temperature dependence of the Hall coefficient and mobility of various Cd-In diffused samples were studied in an effort to characterize the phenomenon.

In the next chapter we present background information on lead-tin telluride. We discuss its energy band structure and its phase diagram since these are important for the understanding of our study. The phase diagram explains why the physical properties of the material depend to a large degree on the technique and condition of its preparation. This critical dependency is our reason for choosing to devote a significant part of the study to crystal growth. The last two sections of chapter 2 contain the basic theory of impurity diffusion in semiconductors and of p-n junctions.

Chapter III describes the experimental techniques which were used in this study. Crystal growth methods and evaluations by x-ray are described in detail, followed by diffusion and diode fabrication procedures. The electrical and optical setups which we used, as well as the measurement techniques, are also discussed in that chapter. Our experi-

mental results and calculations are presented and compared in chapter IV

Chapter V summarizes the results of our measurements and discusses the conclusions we have drawn from them.

CHAPTER II

BACKGROUND AND THEORY

A. Material Properties

Lead-tin telluride is an alloy system composed of two IV-VI compounds, PbTe and SnTe.[1,6] In general this mixed alloy has similar properties to lead salt compounds, and is referred to as a pseudobinary alloy system. The lead salts which include sulfur, selenium, or tellurium are called lead chalcogenides and their chemical bonds are mixtures of ionic and covalent bonds.[7] Both PbTe and SnTe have a face center cubic crystal structure and their lattice constants differ by only two percent.[8,9] The ordering of the atoms along any principal axis is: metal, Te, metal, Te... When PbTe and SnTe are mixed and reacted properly, the pseudobinary $Pb_{1-x}Sn_xTe$ alloy is obtained. These alloys exhibit complete solid solubility for any composition.[1] The resulting compound also has a NaCl crystal structure but the metal atoms are either lead or tin depending on the fractional content of SnTe, x, in the alloy.[2] It was found that when varying the alloy fraction, x, the melting point of the system changes as shown in figure 1.[10,11] The lattice constant and the density of $Pb_{1-x}Sn_xTe$ are found to be an almost linear function of x.[8,9]

1. Band Structure

The minimum energy gap of this system occurs at the L(111) point of the Brillouin zone face.[12] Within the first zone there are eight equivalent half ellipsoidal constant energy surfaces with major axes in the <111> directions. The energy gap of the lead salts increases with temperature.[12] In most other semiconducting materials, including SnTe

the band gap decreases with temperature.[13] The energy gap of the (Pb,Sn)Te mixed system varies strongly with both the alloy fraction and the temperature as shown in figure 2. These energy gap or composition curves are deduced from experimental results of many investigators.[12] However, although many independent experiments support these curves, they were all done on $Pb_{1-x}Sn_xTe$ samples with fractional SnTe constant, x, smaller than 0.35 or on pure SnTe. For alloy composition with corresponding $0.35 < x < 1$ the homogeneity range is shifted far into the metal deficient region (as discussed later) and it is impossible to obtain material with hole concentration of less than 10^{19} per cm^3. Due to the high free carrier concentration, meaningful optical measurements cannot be performed. For material with SnTe content less than 35 percent, the energy gap was determined by optical absorption measurements,[2,14-18] detector response cutoff[19,20] and laser emission.[12,21,22] Tunneling experiments were used for the determination of SnTe energy gap.[13]

The unusual behavior of the energy gap as a function of the alloy composition was explained by Dimmock, Melngailis and Strauss[12,35] (DMS). Their band structure model suggests a band inversion at some intermediate alloy composition. For PbTe the L_6^+ energy state is the valence band edge while the L_6^- is the conduction band. When alloying with SnTe, the two states approach each other as shown schematically in figure 3. As the percentage of SnTe is increased in the alloy, the separation between the two bands, E_g, decreases and becomes zero at some intermediate composition. On further increasing the SnTe content,

the L_6^+ state becomes higher than the L_6^- and the two bands interchange their rolls: the L_6^+ state is now the conduction band and the L_6^- is the valence band.

Looking again at figure 2 we see that the temperature coefficient of the energy gap, dE_g/dT, changes sign at the inversion point. All experimental results, performed on $Pb_{1-x}Sn_xTe$ with $x \leq .35$ and on SnTe, for direct determination of the energy gap by optical measurements, are in full agreement with the DMS band inversion model. As mentioned earlier, due to its prohibitive high hole density, no direct measurements could verify this model on material with composition in the crossover region. The only experimental support for this composition region comes from measurements of the electrical resistivity as a function of temperature. These measurements, which were done first by Dixon and Bis,[23] show that at a composition near the expected crossover, the temperature variation of the resistivity shows a distinct break in an otherwise almost linear dependency. This break corresponds to the change in sign of the temperature coefficient of the energy gap, dE_g/dT, at the inversion point. We have made similar measurements on a bulk crystal with $x = .44$ and obtained similar results which are presented in figure 4. The changes in the slopes, or the breaks in the resistivity-temperature curves, take place at different temperatures due to the change in the composition of the sample as expected from the DMS model.

Theoretical calculation of the energy states show that for the empty lattice model of the IV-VI compounds one would expect the L_6^+ state to be of higher energy than the L_6^-. Although this is true for the case

for some compounds, just the opposite occurs in the lead chalcogenides. The reason is due to the importance of the relativistic correction on the L_1 level.[24] The L_6^+ state originates from the L_1 level when energy splitting due to spin-orbit interaction is taken into account. The L_1 state has an S-type symmetry around the lead atom. This heavy atom is the source for the significance of the relativistic correction to the extent of inverting the normal order of the L_1 and the L_2^1 levels. As the fraction of the lead atoms decreases and is replaced by much lighter tin atoms, the relativistic correction becomes less important.

A chemical approach was used by Wemple[25] for explaining the energy gap variation and the band inversion in lead-tin telluride. He proposed that the possible basis for the energy variation at the L point is the variation with composition of the electronegativity difference, C, of two neighboring atoms. In fact, he showed that with some approximations C is proportional to the difference between the number of valence electrons of the two atoms. In this case, since we are dealing with a mixture of ionic and covalent bonds, C depends on the charge distribution around the two atoms. When the content of SnTe in the alloy increases, the charge distribution changes in such a way that the cations and anions tend to change their role in a manner similar to the valence and conduction bands. At the crossover point ($x \approx 0.65$ at 300K) the electronegativity difference and hence the ionicity fall to zero and the material shows metallic physical properties.

Many detailed calculations of the temperature dependence of E_g based on theoretical determination of the band structure[26] and the

experimental results[2,17] have been reported. Within the temp range of 50-300K, dE_g/dT is almost constant with reported values $(3.8 \pm .5) \times 10^{-4}$ eV/K. Tauber et al.[17] observed that the temp coefficient approaches zero at te eratures close to 400K ... gested the existence of a second valence band. This seco... not move with temperature and .t temperatures lower than ... than the first valence band and therefore its contribution ... absorption process is not evident. Upon increasing the t..., first valence band moves below the second one and the observa... tions are between the latter and the conduction band.

Lockwood[3] used transmission measurements and diode r... to plot the optical gap variation with temperature. His de... ments at low temperature (2-80K) show consistent decrease ... pared to the linear region. In a few samples he observed ... temperature coefficient at temperatures below 25K.

2. Phase Diagram

The physical properties of lead chalcogenides are ... large degree by their respective phase diagrams[27] (temperat... composition relations). Even when starting with pure ... both, the nature of conduction and the carrier concentra... the condition of crystal preparation. According to the ph... the temperature and the pressure which exist during the p... the material effect the proportion of its components a... degree of deviation from stoichiometry.[27,28] The type ... of charge carriers, then, are determined by the crystal ...

Also, if the phase diagram is known, the carrier concentration may be adjusted or even inverted by excess metal (or excess Te) saturation under controlled temperature and pressure.[10] This process is called annealing and will be discussed in the next chapter.

The upper portion of figure 5 shows the temperature-composition projection for a PbTe system. The compound exhibits very small deviation from stoichiometry, and on this scale it is represented by a single line at 50 atomic percent Te. A detailed examination of the deviation from stiochometry can be obtained from the lower part of figure 5. The phase diagram of PbTe and $Pb_{0.87}Sn_{0.13}Te$ in the vicinity of 50 atomic percent Te is presented on an expanded scale. It is important to observe that the homogeneity ranges for both compounds include the stoichiometric composition only at temperatures below the maximum (respective) melting points. At this temperature the compound is always Te-rich. As x increases, the melting temperature of $Pb_{1-x}Sn_xTe$ along with the homogeneity range shift toward the Te-rich side of the diagram as seen, also, from the experimental results in figure 6. The crossover temperature from p-type to n-type decreases too. In fact, for x larger than about 0.33 it is practically impossible to obtain n-type material by self annealing. The farther the crystal is from stoichiometric composition, the greater is the metal deficiency. This is a source for more lattice point defects[27] which are always ionized and contribute free charge carriers to the electrical conduction mechanism.

The annealing technique[10,28,29] involves an equilibrium condition between the sample and metal rich powder of the same composition,

at a desired temperature. This is done in an evacuated quartz ampoule. The sample and the powder are in quasi equilibrium iwth the vapor phase. Since there is only one degree of freedom in this closed system, fixing the temperature would fix the equilibrated composition of each phase. The phase diagram, then, can tell us at what temperature we should anneal in order to obtain the desired carrier density for a given composition. Carrier concentrations as low as 10^{15} per cm^3 have been reported[27] using this method. Our experience shows no difficulties in annealing material to a carrier density of the order of 10^{16} per cm^3.

B. Charge Carriers Statistics

In an intrinsic semiconductor the conduction mechanism is dominated by electrons which are thermally excited from the valence band to the conduction band.[30] The density of the conduction band electron, n, and the valence band holes, p, in such a material, depend on the nature of these bands, their separation (for forbidded gap) and the temperature. We wish to find expressions of the electron density as a function of the band parameters and the temperature. We will consider two cases: the first is the most common and simple situation of parabolically spaced constant-energy-surface in k-space, and then the nonparabolic energy wave vector dispersion relation. The second case is common in narrow gap semiconductors such as lead-tin telluride and therefore is of special interest for us. The hole density can be calculated in a similar way.

In general the number of free electrons present per unit volume

is given by[30]

$$n = \int_{E_c}^{\infty} f(E)g(E)dE \tag{2.1}$$

where g(E)dE is the number of states available in an energy range dE, and f(E) is the probability of occupancy for a state of energy E. We use of course Fermi-Dirac statistics and f(E) is the well known Fermi-Dirac distribution function

$$f(E) = \frac{1}{1+\exp[(E-E_f)/k_BT]} . \tag{2.2}$$

The integral (2.1) is evaluated from the bottom of the conduction band. It is simple to show[30] that the number of states per unit volume within an infinitesimal range of energy or wave-vector, k, is

$$g(E)\cdot dE = g(k)\cdot dk = (\frac{k}{\pi})^2 dk \quad . \tag{2.3}$$

Using equations (2.2) and (2.3) in equation (2.1) we get

$$n = \frac{1}{\pi^2}\int_0^{\infty} \frac{k^2 dk}{1+\exp[(E-E_f)/k_BT]} \quad . \tag{2.4}$$

This integral can be used to evaluate the electron density if the energy-wave vector dispersion relation is known.

For a spherical constant-energy-surface the parabolic E-k relation is

$$E = \frac{h^2}{2m^*} k^2 \tag{2.5}$$

where E is measured from the bottom of the conduction band and $m^* = (m_x^* m_y^* m_z^*)^{1/3}$ is the density-of-states (scalar) effective mass. From equation (2.5) we get

$$k^2 dk = \frac{1}{2} \left(\frac{8\pi^2 m^*}{h^2}\right)^{3/2} E^{1/2} dE \tag{2.6}$$

which is substituted in equation (2.4) to give

$$n = 4\pi \left(\frac{2m^*}{h^2}\right)^{3/2} \int_0^\infty \frac{E^{1/2} dE}{1+\exp[(E-E_f)/k_B T]} . \tag{2.7}$$

It is convenient to use dimensionless notations, $x = E/k_B T$ and $\eta = E_f/k_B T$, and then equation (2.7) becomes

$$n = 4\pi \left(\frac{2m^* k_B T}{h^2}\right)^{3/2} \int_0^\infty \frac{x^{1/2} dx}{1+\exp(x-\eta)} \tag{2.8}$$

$$= N_c F_{1/2}(\eta)$$

where

$$N_c = 2\left(\frac{2\pi m^* k_B T}{h^2}\right)^{3/2} \tag{2.9}$$

and

$$F_{1/2}(\eta) = 2\pi^{-1/2} \int_0^\infty \frac{x^{1/2} dx}{1+\exp(x-\eta)} . \tag{2.10}$$

In a similar manner we can show that the hole density is

$$p = N_v F_{1/2}(-\epsilon, -\eta) \tag{2.11}$$

where N_v is the same expression as N_c of equation (2.9) but here the hole effective mass, rather than the electron effective mass, is used. $\varepsilon = E_g/k_BT$ is the dimensionless energy gap.

For an intrinsic semiconductor, where η is negative, the Fermi-Dirac integrals can be replaced by their limited forms so that the intrinsic carrier concentration is obtained

$$n_i^2 = np = N_c N_v \exp(\varepsilon) \tag{2.12}$$

or in conventional energy units

$$n_i = (N_c N_v)^{1/2} \exp(-E_g/2k_BT) \ . \tag{2.13}$$

Next we proceed to calculate the electron density for the non-parabolic band structure. The dispersion relations for small gap semiconductors has been given by Harman et al.[31] who used the Kane band model.[5] With additional restrictions that $m^* << m$ and $E << E_g$ (small gap) the following relationships are obtained:

$$k^2 = \left(\frac{8\pi^2 m^*}{h^2}\right)\left(1 + \frac{E}{E_g}\right)E \tag{2.14}$$

$$\frac{dE}{dk} = \left(\frac{h^2 E\left(1 + \frac{E}{E_g}\right)}{2\pi^2 m^*\left(1 + \frac{2E}{E_g}\right)}\right)^{1/2} \ . \tag{2.15}$$

We use these results in equation (2.4), as we did in the parabolic case and we get

$$n = 4\pi\left(\frac{2m^*}{h^2}\right)^{3/2} \int_0^\infty \frac{E^{1/2}\left(1 + \frac{E}{E_g}\right)^{1/2}\left(1 + \frac{2E}{E_g}\right)}{1+\exp[(E-E_f)/k_BT]} \, dE \ . \tag{2.16a}$$

For large band gap $E \to \infty$, this expression becomes identical to the parabolic expression (2.7). Again we make use of the dimensionless notations and rewrite equation (2.16a) as:

$$n = [2\left(\frac{2\,m^{*}k_{B}T}{h^{2}}\right)^{3/2}][2\pi^{-1/2}\int_{0}^{\infty}\frac{x^{1/2}(1+\frac{x}{\varepsilon})^{1/2}(1+\frac{2x}{\varepsilon})}{1+\exp(x-\eta)}\,dx]. \quad (2.16b)$$

We shall use the last expression in section D of chapter VI to extract the Fermi level for given n, E_g and T. The intrinsic carrier density for lead-tin telluride was shown[1] to be

$$n_i = 2.9\times10^{15}(TE_g)^{3/2}\exp - (E_g/1.72\times10^{-4}T) \quad (2.17)$$

C. Diffusion and p-n Junction

Impurity diffusion and isothermal annealing have been used successfully to reduce the carrier concentration[10,19] of as-grown lead-tin telluride, and to form p-n junction.[20,32]

1. Diffusion in Semiconductors

Diffusion is the transport of an impurity in some host material due to thermal motion.[33] If there exists a concentration gradient of the impurity, the diffusion process will be such that a net flow of the impurity atoms will tend to even out this gradient. In a one dimensional model we can express the net diffusion current, J, as

$$J_x = - D\,\frac{\partial N(x,t)}{\partial x} \quad (2.18)$$

where D is the diffusion coefficient and N(x,t) is the impurity

concentration at point x and time t.

The change in concentration in any volume is equal to the net flow into the volume. Thus, the continuity expression in one direction can be written

$$\frac{\partial N(x,t)}{\partial t} = -\frac{\partial J_x}{\partial x}$$

or using equation (2.18) for J_x

$$\frac{\partial N(x,t)}{\partial t} = -\frac{\partial^2 N(x,t)}{\partial x^2} . \qquad (2.19)$$

Equations (2.18) and (2.19) are known as Fick's laws.

Diffusion in solids occurs by a number of possible atomic mechanisms[33] all involving a series of jumps, made by the diffusing atoms, from one lattice site to another. We will discuss the three most common mechanisms: Exchange, Vacancy, and Interstitial. In the first possible diffusion process, the Exchange mechanism, two or more neighboring atoms interchange their sites. This process requires high activation energy and thus is unlikely to be significant for diffusion in close packed crystals. Another process is called Vacancy mechanism. This involves propagation of atoms via defects or vacant lattice sites which exist in all crystals. Here the energy involved is not high but still not as low as in the third process, the Interstitial mechanism. Diffusion by the latter process involves impurity atoms which move through the crystal by jumping from interstitial sites to neighboring interstital positions.

Fick's first law, equation (2.18), relates the diffusion current, J, to the impurity concentration gradient and to the diffusion coefficient D. The diffusion rate in solids depends also on the impurity and crystal thermal energy, as well as on material parameters such as structure, composition and imperfections. The temperature dependence of D is generally described by

$$D(T) = E_o \exp(-Q/k_B T) \tag{2.20}$$

where Q is the activation energy of the diffusion and D_o is the diffusion coefficient extrapolated to infinite temperature. This is an Arrhenius equation. If D is determined experimentally for various temperatures, than the slope of a straight line obtained by plotting ln D versus 1/T is equal to $-\frac{Q}{k_B}$.

The solution for Fick's second differential equation when assuming a case of a semi-infinite medium and diffusion from constant source is given by[33]

$$N(x,t) = N_o(1 - \text{erf}\ \frac{x}{2\sqrt{Dt}}) \tag{2.21}$$

where $N_o = N(0,t)$. In chapter IV section C we use our experimental data in the above equation to obtain a few values for the diffusion coefficient D. D_o and Q for our particular system can then be calculated using equation (2.20).

2. The p-n Junction Diode

If donor impurities are introduced into one side and acceptors into the other side of a single crystal of a semiconductor, a p-n junction is

formed. Such a system is illustrated in figure 7(a) where two modes of the impurity concentration profile are shown: the abrupt junction and the linearly graded junction. Due to the density gradient across the junction, holes diffuse to the n side across the junction and electrons to the p side. The region near the junction is then depleted of mobile charges and is called the depletion region or the space-charge region. As a result of the displacement of the free charge in the depletion region, an electric field appears across the junction to counterbalance the diffusion current, since for an open circuit case the net flow must be zero. This is the origin of the potential barrier or the built-in voltage, V_{bi}, of figure 7(c).

When treating the static and dynamic characteristics of the abrupt and the graded junction models, the following results are obtained:[24] the depletion width, d, depends on the built-in voltage, and on the impurity concentration as well as on the dielectric constant of the semiconductor. For a two-sided abrupt junction we have

$$d = \left[\frac{2\epsilon_s}{e}\left(\frac{1}{N_A} + \frac{1}{N_D}\right)V_{bi}\right]^{1/2} \tag{2.22}$$

where ϵ_s is the material permittivity, e is the electron charge, and N_A and N_D are the acceptor and donor impurity concentrations respectively. For the one-sided abrupt junction equation (2.22) becomes

$$d = \left[\frac{2\epsilon_s}{e}\frac{V_{bi}}{N_B}\right]^{1/2} \tag{2.23}$$

where $N_B = N_A$ or N_D.

If the junction is linearly graded then

$$d = \left[\frac{12\epsilon_s V_{bi}}{ea}\right]^{1/3} \tag{2.24}$$

where a is the impurity gradient. The capacitance of the one-sided abrupt junction is

$$C = \left[\frac{\epsilon_s e N_B}{2(V_{bi} \pm V_B)}\right]^{1/2}. \quad pf/cm^2 \tag{2.25}$$

The sign depends on the direction of the applied bias voltage V_B. For the graded junction we have

$$C = \left[\frac{\epsilon_s^2 e\, a}{12(V_{bi} \pm V_B}\right]^{1/3}. \quad pf/cm^2 \tag{2.26}$$

We see that for an abrupt junction C is proportional to $V_B^{-1/2}$ and for graded one it is proportional to $V_B^{-1/3}$.

The current in the diode can be shown to have two major components.[34] One is given by the Shockley equation for diffusion current in the ideal diode

$$J = J_s[\exp(eV/k_BT)-1] \tag{2.27}$$

where J_s is called saturation current and is equal to

$$J_s = |e| n_i^2 \left(\frac{1}{N_A}\frac{\overline{D_n}}{\tau_n} + \frac{1}{N_D}\frac{\overline{D_p}}{\tau_p}\right). \tag{2.28}$$

Here $D_{n(p)}$ and $\tau_{n(p)}$ are the carriers' diffusion coefficient and lifetime respectively.

The second current component is due to thermal generation and recombination of electrons and holes. For reverse bias the dominant

process is electron and hole emission,[53] or generation. For the forward bias case recombination, or capture of electron and hole is the major mechanism. Sah et al.[53] have shown that for both cases, reverse and forward bias, the current is

$$J_s \propto n_i \quad . \tag{2.29}$$

Looking at equations (2.28) and (2.29) we note that when the diffusion current is the dominant, the junction current is proportional to the second power of the intrinsic carrier concentration, n_i. On the other hand, the generation recombination current is linearly proportion to n_i.

The results arrived in this section will be used in chapter IV to obtain information on the types of junction, their width and built-in potential, and on the current mechanism which is dominant in our photodiodes.

D. Photoconductivity and the Photovoltaic Effect

When photons of sufficient energy reach a semiconductor material they can be absorbed thereby generating free electrons and free holes.[36] This process produces free charge carriers in excess of those existing in thermal equilibrium. The excess carriers can either produce a potential difference, as is the case in a photodiode, or they can dominate the conduction mechanism of the material as in photoconductivity. These two cases will be discussed in this section. A device which is sensitive to radiation is called a detector.

Treating only band to band (intrinsic) direct transition, we have a process in which the absorbed photons excite electrons from the

valance band to the conduction band, with no change in the electron's momentum. The conduction band has now an excess of free electrons while the valance band has an excess of free holes. Both types of the photo-generated carriers can diffuse if an electric field is present, until they eventually recombine and return to the original stable state.

If the number of photons incident upon a detector is invariant with wavelength and if it is assumed that in the ideal case each incident photon excites one electron-hole pair (quantum efficient equal one), the spectral response of figure 8(a) is obtained. The wavelength λ_1 is called the threshold and corresponds to the photon whose energy, $h\nu_1$, just equals the energy of the forbidden gap. It is experimentally more convenient, however, to plot the response which is normalized to constant energy. Then with increasing wavelength the number of incident photons is increased linearly, such that the energy flux remains constant. Figure 8(b) shows such an ideal response along with a response of a real detector. The deviation of the latter from the ideal case is discussed next. Figure 9 illustrates the distribution function, the density of states function, and the electron and hole populations for an intrinsic semiconductor. Since the probability of generating electron-hole pair depends on the available states for the excited carriers to occupy, it can be seen that the likelihood of such a transition varies with the photon incident energy: photons with frequencies smaller than the threshold frequency, ν_1 will not have enough energy to excite electrons across the gap and therefore will not be absorbed by this process. When the photon energy is increased to $h\nu_1$, transition is possible but is not very probable.

The most likely transition occurs when the incident photons have energy of $h\nu_2$. As the photon energy is further increased, the transition probability decreases since there are less available states. The reason that the spectral response curve of a non-ideal detector has no absolute cutoff (threshold) but a rather somewhat gradual decrease in the photosignal is due to interactions of photons with lattice vibrations or with impurity states which may be present in the forbidden gap but very close to either of the bands.

We want to establish a criteria by which a reasonable value of the threshold energy can be determined from relative response measurements even if there is no absolute cutoff. Moss[36] showed that when the response has fallen to half of its maximum value the photon energy is equal to the energy gap of the material. The response of the sample in the region of the threshold is written as

$$R(E) = R_o \left[1+\exp(\beta[E_o-E])\right]^{-1} \tag{2.30}$$

where E is the energy, E_o is the energy gap and β is a constant. Assuming that the response is dependent upon the distribution of states from which the photocarriers originate and that there are N(E)dE levels between E and E + dE, then for a given energy E' the response will be proportional to the number of states with E < E'. Hence,

$$R(E) \propto \int_0^{E'} N(E)\,dE \tag{2.31}$$

or by differentiating

$$N(E) = C\,\frac{dR(E)}{dE} \tag{2.32}$$

where C is a constant. We use equation (2.30) for R(E) in the above equation and get

$$N(E) = C\beta \frac{\exp(\beta[E_o - E]}{[1+\exp(\beta[E_o - E])]^2} \quad . \tag{2.33}$$

The density of electrons which were raised to the conduction band due to thermal energy is given by

$$n = \int C' \sqrt{N(E)}\, \exp(-E/2k_B T) dE \tag{2.34}$$

where E is the energy measured from the bottom of the conduction band. Substituting equation (2.33) in equation (2.34) we get

$$n = C \int_{-\infty}^{0} \frac{\exp[\frac{\phi}{2}(\beta + \frac{1}{k_B T})]\, \exp[-\frac{E_o}{2k_B T}]}{1+\exp[\beta\phi]} d\phi$$

where $\phi = E - E_o$.

This integral is put in a standard form from which we obtain

$$n = C \sqrt{\frac{c}{\beta}} \frac{\pi}{\sin(\frac{\pi}{2} - \frac{\pi}{2\beta k_B T})} \exp(-E_o/2k_B T) \tag{2.35}$$

Comparing this with equation (2.13) where we have $n = n_o \exp(-E_g/2k_B T)$ we get $E_g = E$. Then equation (2.30) with $E = F_g$ becomes

$$R(E) = [1+\exp(\beta[E-E_g])]^{-1} = \frac{1}{2} \tag{2.36}$$

which we wanted to show. A different approach[50] will lead us to the same result: We rewrite equation (2.30) as

$$R(\lambda) = [1+\exp(\alpha[E_o - h\frac{c}{\lambda}])]^{-1} \qquad (2.37)$$

Now, as explained earlier, the response depends on the function N(E) which is zero in the gap for the ideal case where there are no states at all in the forbidden band. In reality we expect N(E) to be a continuous function in E, but its value will change most rapidly at the point where $E = E_g$. Therefore $dN(E)/dE$ is maximum at this point and the second derivitive is equal to zero. Now, we define the absorption edge to be the point corresponding to maximum. That is, when plotting the response as a function of the incident wavelength we call the point where the response changes most rapidly with λ the absorption edge and the photon energy associated with it is hc/λ_g. At this point we have

$$\left.\frac{d^2R(\lambda)}{d(h\frac{c}{\lambda})^2}\right|_{\lambda=\lambda_g} = 0$$

which gives $\exp(\alpha[E_o - h\frac{c}{\lambda_g}]) = 1$.

Thus

$$\left.R(\lambda)\right|_{\lambda=\lambda_g} = \frac{1}{2}$$

Again we see the association between the energy gap and the 50 percent cutoff of the spectral response.

Photoconductivity can be observed and measured when the photogenerated carriers change appreciably the material resistivity.[36] The optical sensitivity of a semiconductor depends on the ratio of the number of excess carriers to the number of free carriers at dark, as well as on its mobility, recombination lifetime, and the device noise. The most

common detector noises are Thermal, Generation-recombination, and Current noise. Thermal (or Johnson) noise is due to the random motion of the charge carriers. Generation-recombination noise is due to statistical fluctuation in the number of charge carriers in the semiconductor. The current (or 1/f) noise, however, does not depend on the free carriers at all but rather on other sources such as poor contacts and surface or inhomogeneities of the material.

The photovoltaic effect, in which a potential difference is produced across a junction due to the photo-excited carriers, is discussed next. The absorption mechanism is the same as described above, but the free charge carriers which are generated within or near the depletion region have a good probability to be swept by the junction electric field before they recombine. The built-in field across the junction (as explained in section C(2) of this chapter) is directed such that an excess of electrons in the p side and an excess of holes in the n side will flow toward and across the junction. This diffused reverse current is called minority current. The total current of a photodiode is the sum of the (short circuit) photocurrent, I_p, and the ideal diode current as obtained from Shockley equation (2.27) under applied voltage V.

$$I = I_p - I_s[\exp(eV/k_BT) - 1] \quad . \tag{2.38}$$

The open circuit photovoltage V_{oc}, is obtained by setting $I = 0$ in the above equation. Then

$$V_{oc} = \frac{k_BT}{e} \ln \left(\frac{I_p}{I_s} + 1\right) \quad . \tag{2.39}$$

CHAPTER III

EXPERIMENTAL PROCEDURES

A. Crystal Growth and Sample Preparation

One of the objectives of this study was to improve crystal growth techniques by vapor transport in a closed tube, and to determine the factors influencing the quality of the resulting crystals. As discussed earlier, the material physical properties depend on preparation methods. Many methods of crystal growth for this material have been investigated. Czochralskis,[11] closed tube vapor growth and Bridgman[10] techniques were among the early successful studies reported less than a decade ago. A few years ago, however, larger and better quality crystals were grown by the solid state recrystalization method,[37] as well as by the closed tube vapor transport method with[38] and without[37] seed. We have adopted the latter method using a seed.

In the following sections the detailed procedure for crystal growth, its x-ray evaluation, and sample preparation are described. Back reflection x-ray powder photographs, as well as x-ray topographs were used to characterize crystal composition and structural quality. In the last section the preparation procedure of the samples which we measured is discussed in detail. Both, homogenously diffused samples for Hall and photoconduction measurements, and p-n junction diffused diodes were used in our experiments and therefore their preparation is described.

1. Growth of Single Crystal Lead-Tin Telluride

The closed tube vapor transport technique has proven to yield

high quality single crystals. This process involves vaporaziation of a solid source of lead-tin telluride and the transport of the gas molecules to the other end of the growth ampoule where they condense on an oriented seed. The sublimation process takes place in an evacuated closed quartz tube placed in an almost isothermal zone of the growth furnace at temperature well below the melting point. The source material is homoganous polycrystalline $Pb_{1-x}Sn_xTe$ and the seed is a wafer of a single crystal. The growth technique will be described in detail later following a discussion of the sublimation mechanism of the (Pb,Sn)Te system.

Several studies[40-44] investigated the vaporization nature of this material looking at the solid or at the vapor phase. It was concluded that the system vaporized mostly as molecules of PbTe and SnTe with very similar vapor pressure and effusion rate. Winchell[39] and Sokolov[42] investigated the vapor species of vaporized (Pb,Sn)Te using mass spectrometric methods. Both observed approximately equal amounts of SnTe and PbTe molecules but the latter investigator identified also a one-percent presence of Te_2 and $SnTe_2$ molecules. Northrop[43,44] investigated the thermogravimetrical nature of the vaporization of PbTe, SnTe and $Pb_{1-x}Sn_xTe$ each at 625°, 700° and 825°C. He used an automatic recording balance and was able to determine continuously the weight as a function of time and temperature. Material composition was determined using x-ray and polarographic analyses. From his data he calculated the specific effusion rates which are given below in units of g/cm^2 sec.

PbTe	5.89×10^{-4}
$Pb_{0.90}Sn_{0.09}Te$	5.36×10^{-4}
$Pb_{0.72}Sn_{0.28}Te$	5.97×10^{-4}
$Pb_{0.50}Sn_{0.50}Te$	6.01×10^{-4}
SnTe	6.81×10^{-4}

In addition he calculated the apparent total vapor pressure which is presented in figure 10. These results show a striking similarity in the sublimation nature of the lead-tin telluride components. This feature helps to explain the good results of crystal growth obtained by the closed tube vapor transport method. Similar results were reported earlier by Bates and Weinstein[7] who investigated the sublimation rates of pressed and sintered PbTe and $Pb_{0.5}Sn_{0.5}Te$ commercial thermoelements. Their material, which contained 6% MnTe sublimes in a manner similar to the pure and well reacted source material. Northrop, however, observed that the vaporization of (Pb,Sn)Te is noncongruent. Due to preferential loss of SnTe, there is a continuous decrease of the SnTe/PbTe ratio. For example, one effusion run starts with 28% SnTe and when 2/3 of the source was effused, the residue contained only 18% SnTe. It is also suggested[9] that although PbTe vaporizes congruently, SnTe vaporizes noncongruently. A two-phase Sn-SnTe assemblage is first produced due to a loss of excess Te, and a small amount of pure Sn is formed as a final phase. It is important to remember, however, that all the above effusion studies deal only with one half of the process used for crystal growth i.e. the evaporation of the source. The condensation mechanism is not known to have been

investigated, and therefore will not be discussed here. Next we describe our procedure for growing (Pb,Sn)Te single crystals.

Material Preparation. High purity polycrystalline $Pb_{1-x}Sn_xTe$, with $0 < x < .45$, was prepared as source material for the growth of single crystals. All three elements, 99.9999% purity materials, were obtained from Cominco American (Spokane, Washington). Te, which was received in bar form, is doubly zone refined. Pb and Sn were obtained in both shot and bar forms. Mass spectrographic analysis on these elements as they are received is given in Table 1.

The desired quantities of lead, tin and tellurium were weighed to an accuracy of 0.1 mg, and then placed in a previously cleaned 13 x 15 mm quartz reaction tube. Quartz tubing with 1 mm wall thickness used in this study was obtained from Amersil Quartz Division (Hillside, New Jersey). Prior to use, the quartz was cleaned by immersing it in concentrated electronic grade, $HF:HNO_3$ (1:3 by volume), followed by rinsing with deionized water and electronic grade methanol.

The reaction ampoule was then evacuated to a pressure of less than 1×10^{-5} mm Hg with an oil diffusion pump, then backfilled with purified hydrogen gas to a pressure of about one half atmosphere and sealed.

The chemical reaction took place at a temperature of 1000°-1050°C for about five hours. During the reaction, the oven was rocked to ensure proper mixing of the three elements. The capsule containing the molten (Pb,Sn)Te was then water quenched to reduce segregation of PbTe and SnTe on cooling. It was observed that better results are achieved when the starting material is slightly (1%) metal rich.

Crystal Growth Apparatus. Single crystals with 15 mm diameter and 30 mm length were grown by the closed tube vapor transport technique. Using the polycrystalline charge as source material, the evacuated growth ampoule was placed in a temperature gradient furnace and deposition took place on an oriented single crystal seed at the lower temperature end of the tube.

Most crystals were grown in home made furnaces, although some were grown in a commercial (B.T.U. Engineering Co., Waltham, Mass.) three zone horizontal oven. This 39" long by 2 1/2" bore furnace, equipped with a power supply and temperature controller, was found to be suitable for crystal growing and other high temperature processes. However, home made ovens did not produce inferior results and a description of their construction is given below. The core was an Alundum furnace core (RA 4098, 85.5% Al_2O_3, Norton Co., Worcester, Mass.) with a 1 1/2" bore and 6 to 9 windings per inch. Kanthal (Stamford, Conn.) A-1 gauge 16 wire was used as a resistance heater. The wound core was covered with Sauereisen (Pittsburgh, Pa.) sealing cement, and then wrapped with asbestos sheets, followed by an aluminum sheet. The furnaces were built with three temperature zones which can be adjusted, by using external variable resistance, to obtain the desired temperature profile. Figure 11(a) shows the wiring diagram of such an oven. The furnaces were connected either to a voltage regulator or to a temperature controller. In the first case, temperature stability within 5°C was achieved while in the latter case the temperature did not vary more than one degree from the setting point. Ceramic fire-brick plugs were

used to close the oven ends and stainless steel liner helped to center the capsules inside the oven. Crystals were grown in both vertical and horizontal furnaces, but no conclusion could be drawn in regard to preferable oven orientation.

The growth capsule is constructed from 17 x 19 mm and 15 x 17 mm quartz tubing. A schematic diagram of the chamber is given in figure 12. An eight mm diameter quartz rod served as a heat sink. It is cut and fire polished at both ends. The seed rests on one end of the rod. It is important to make sure that the adjacent surfaces are flat and are in full contact. Otherwise, the heat flow through the quartz cane may be poor and the seed itself may "transport" into a different shape. The seed is cut from a good crystal with the same or lower SnTe composition. Higher content material has lower melting temperature and therefore is not recommended to be used for seed. A Model 716 string saw (South Bay Technology Group, Sherman Oaks, California) with 0.005" wire string is used to cut the seed. The slurry consists of 600 mesh SiC, glycerine and water in a ratio of 7 gm:10 mℓ:2 mℓ. The seed is cut in the (111) orientation and is lapped with a slurry of 600 mesh SiC and soapy water to remove saw marks and reduce seed thickness to about 1 mm. Just before being used, the seed is etched for 5-7 minutes with HBr: 3% Br_2 to remove about 0.2 mm of the surface which is damaged due to lapping. Additional thermal etch is believed to occur when the loaded growth ampoule is placed in the hot furnace. It should be mentioned that seeds which were cleaved from BaF_2 were also used successfully.

After the oven is preheated to the desired temperature, the growth ampoule is placed in it. At the end of the growth period, the oven temperature is lowered to room temperature over 8-15 hours, to prevent a thermal shock.

Growth Runs. More than forty crystals of $Pb_{1-x}Sn_xTe$ have been grown in SnTe content ranging from zero to 45%. The following conclusions based upon the results of these runs could be drawn:

Source Preparation: Figure 13 shows three ways of source preparations. We were unable to conclude that one method is preferred over the others. It was found, however, that breaking of the charge boule into several pieces before insertion into transport tube results in a faster crystal growth rate and better crystal quality. It is believed that the surface of the charge is inhomogeneous and therefore it is important to expose the inside surface. Some charges were transported completely. In such a case, the last-to-grow end of the crystal did not have any facets and its composition was not stoiciometric. Although most of the boule was good quality single crystal, the end section could not be used.

Inner Growth Tube: Good quality quartz tubing was used for the inner chamber of the growth ampoule. Rough inside surface, in the section next to the seed, is a source of defects which propagate and give poor crystals. The exact shape of the section near the seed was not found to be significant, provided that its diameter increases gradually starting from the seed. The size of the hole in the inner tube determines the area of the seed on which deposition occurs. Larger holes would provide better heat flow. Holes with up to 8 mm in diameter have been tried, but 4 to 6 mm

diameter was found to give better and more consistent results.

Seed: High quality seeds are essential for growing good crystals. In some cases defects in the seed were observed to propagate through the crystal even as far as the last-to-grow end. A few seeds were cut in the (100) orientation, but better crystals were obtained when grown in the (111) direction. The seed was never thinner than 0.8 mm when ready to be used, for the following reason: It is believed that initially the seed temperature is higher than that of the charge since its thermal inertia is much smaller. Therefore, some thermal etch of the seed takes place until thermal equilibrium prevails. If the seed is too thin, it would vaporize.

Growth Temperature: Good crystals were obtained when grown in any temperature between 830 to 855°C. The charge temperature did not approach too closely the melting point. As can be seen from the phase diagram in figure 1, the lower the content of SnTe in the charge the higher is the allowed growth temperature. The temperature difference between the charge and the seed, ΔT, could have a significant effect on the vapor transport process. A large temperature difference would produce a very fast growth rate which would cause an increase in crystalline imperfections, while for ΔT too small the growth time would be excessively long. It was observed that a temperature difference of 2 to 6°C between the charge and the seed would give good results. The temperature stability is not believed to be very critical as long as it does not reach values outside the range mentioned in the beginning of this section. In our runs, however, most crystals were grown at a constant temperature. In one case,

the oven was connected directly to the power line and the temperature varied within 15°C during the run. The result was still acceptable.

2. X-ray Evaluation

The as-grown crystal boules were examined in three ways, in addition to electrical and optical characterization. Basic information is obtained from the appearance of the boule. A good crystal has three to five large (20-50 mm^2) facets and since the material has a rock salt structure and a known growth direction one knows by visual inspection whether or not it is single. X-ray Laue photographs were taken to verify the above observation (see figures 14 and 15). An additional criterion for judging crystal quality is the appearance of their surface. Good crystals always have a very shiny appearance.

Determination of Alloy Composition: The percentage of SnTe in the $Pb_{1-x}Sn_xTe$ single crystals was determined by measurements of the lattice constant[9]. These measurements were made by the back reflection focusing method[45] using X-ray powder photographs. The lattice constant of (Pb,Sn)Te is found to vary linearly with composition ranging from 6.327Å, the lattice constant of SnTe, to 6.460Å, the lattice constant of PbTe[9]. An error analysis established that the precision of this technique is 0.2%.

Our radiation source was a General Electric X-ray Diffraction unit with a copper target. The back reflection camera was equipped with a nickel filter which removes the K_β radiation while it transmitted the K_α doublet. The X-ray radiation used then, consists of K_{α_1} (λ = 1.54050Å)

and K_{α_2} ($\lambda = 1.54434\text{Å}$). Both lines were used in calculations and the results were averaged.

The lattice constant, a_o, is linearly proportional to the spacing of any adjacent (hkℓ) planes and is given by

$$a_o = d_{hk\ell}(h^2 + k^2 + \ell^2)^{1/2} \quad . \tag{3.1}$$

Now when Bragg's law is satisfied for a given λ we can write

$$a_o = \frac{\lambda}{2 \sin \theta} (h^2 + k^2 + \ell^2)^{1/2} \tag{3.2}$$

where θ in the Bragg's angle which can be determined experimentally. Differentiating the above equation in respect to θ we get the fractional error as

$$\frac{\Delta a_o}{a_o} = - \Delta\theta \cot \theta \quad . \tag{3.3}$$

An analysis of the experimental source of error yields[45] an extrapolation function

$$\frac{\Delta a_o}{a_o} = \phi \tan \phi \tag{3.4}$$

where ϕ is (90-θ). It is clear that the error approaches zero as ϕ approaches zero. The extrapolation was done on a digital computer using a least-squares technique. Bis and Dixon[9] have shown that when deviations from stiochiometry are taken into account the lattice constant of $Pb_{1-x}Sn_xTe$ is given by

$$a_o(\text{Å}) = 6.460 - 0.133\,x - 1.7 \times 10^{-23} p \qquad (3.5)$$

where p is the carrier density measured at 77K. Our material did not exceed a carrier concentration of 5×10^{19} cm^{-3} and thus the simple linear relationship of Vegard's law was used in calculating the composition.

Many crystals were examined by this method and it was always observed that the percentage of SnTe was less by 0.5 to 1% than what was originally weighed. In addition, there are indications that the part of the source which did not transport contained a few tenths of a percent less SnTe than the part of the crystal that was transported. These results are in agreement with those obtained by the effusion experiments[44] but to a much lesser degree.

Two crystals were examined to determine composition variation along the growth and radial directions. The results are presented in figure 16. It is interesting to note that in the run were the whole source material transported, the crystal content of SnTe decreased continuously along the direction of growth with deviation of about 3% between the first and the last-to-grow ends. In the run where the source was only partially transported, which is usually the case, such a tendency is not observed and the crystal is much more homogeneous. Similar results have been reported by Johnson and Parker[47] who used electron microprobe analysis techniques to determine the Sn content in their crystals.

Crystal and Surface Defects: X-ray topography is a very powerful

technique for revealing structural imperfections in single crystals and was used in this study to evaluate crystal growth and handling methods. Figure 17 shows the arrangement of our Berg-Barrett[48,49] back reflection X-ray topograph camera used in this evaluation. The crystal is set to reflect the characteristic radiation from the line focus, satisfying the Bragg condition. By placing the film close to the sample, geometric resolution of approximately one micron can be obtained.

Using this technique, it was observed that some crystals, although they looked good by visual inspection, had low angle grain boundaries as shown in figure 18. Efforts were made to understand and to eliminate the cause for these lower quality crystals. It is found that these grains are either inherited from poor seeds or are caused by thermal shock during the quenching of the crystal from growth to room temperature. Thus, good seeds and a slow cooling rate assure crystals free of low angle grains.

The topographs also reveal that as-grown crystals usually have some scratches and holes on their surface which can be eliminated by chemical etching. (See figure 19).

It was interesting to determine the depth and extent of damage in the wafer after cutting and lapping. Figure 20 shows a set of topograph pictures which were taken immediately after lapping and then following successive chemical etches to remove layers of damaged surface. It is seen that the marks extend about 90 μm deep.

3. Diffusion Technique and Diode Fabrication

Isothermal annealing and impurity diffusion were carried out on the as-grown lead-tin telluride in order to reduce carrier concentration, when desired, or to form p-n junctions. As discussed earlier, due to metal deficiency, the as-grown crystals are always p-type with a carrier density of about 10^{19} per cc. By diffusing back enough metal atoms we can fill the vacancies and control the carrier density of the material.[27] When the metal source is just metal rich lead-tin telluride, the process is called annealing or self diffusion. Other metals which behave as donors in lead-tin telluride could be used as diffusion sources instead of the metal rich (Pb,Sn)Te.

In this study we have concentrated on metal diffusion using either cadmium, antimony or a mixture of cadmium and indium as source material. The diffusion process was carried out as follows. The crystal was cut to about 1 mm thick slices along the growth direction in a manner similar to that described in the section on seed preparation (section A). The wafers were then cut into 2-3 mm wide strips and after removing about 100 μm of surface material by etching, they were placed in the diffusion ampoules along with the desired source metal. Excess source material was always used so that the amount and depth of the diffusion would be controlled only by the temperature and the duration of the diffusion process. The source was kept physically separated from the sample so that only metal atoms in the vapor phase would be in contact with the sample surface. Figure 21 shows the configurations of two diffusion capsules which were used most frequently.

Before loading the quartz ampoules they were cleaned by etching in the manner described in the crystal growth ampoule section. The loaded ampoule was then connected to an oil diffusion pump which was later cold trapped. It was sealed off when the pressure was reduced to about 1×10^{-5} mm Hg.

The diffusion furnaces, all home made, are similar to those used for crystal growth and were described in section A of this chapter. The diffusion ampoule was placed in the uniform temperature zone of the preheated oven. Diffusions took place at a temperature range of 350-800°C and the duration varied from 20 minutes to 20 hours depending on the particular case. At the end of the diffusion period the capsule was removed from the oven by holding it with a wet asbestos. This was done so that the metal vapor would condense on the quartz wall rather than on the sample. Nevertheless, some surface alloying was not uncommon and was removed by etching with HNO_3. Diffusion depth was determined using sequential etch and thermoelectric microprobe technique. (The surface of the diffused sample is n-type and by etching away this layer, the p-type material is exposed. The thermoelectric microprobe technique enabled us to determine the type of the surface after each etch so we can measure the depth of the n-layer.)

Samples which were prepared for Hall and resistivity measurements or for photoconduction measurements were diffused long enough to ensure uniformity of impurity distribution in the host semiconductor. In each run an extra slice of (Pb,Sn)Te was diffused and used for verifying that a complete n-type conversion had occurred.

Photodiodes were fabricated in the following way: The desired (Pb,Sn)Te sample was prepared for diffusion as described above. Cadmium was diffused at 400-450°C while antimony at 700°C. Junction depths were 10-20 μm but back etching was used for two purposes, removing the alloying layer and making the junction shallower than 5 μm. The geometry of the diode is shown in figure 22. The top part of the device is called mesa and is the sensitive part of it. A few drops of glycol phthalate (wax) were placed on the diffused samples to confine the mesa areas. Additional back etching was used to remove the n-layer completely except under the wax spots. The etch does not attack this type of wax. When etching was completed, the wax was removed with acetone. The samples were then cut into sections so that each contained a mesa. Using a lead-tin eutectic and Divco type K flux, each sample was mounted on a transistor base (TO-5 header was selected) as shown in figure 22. Contacts to the n-type surface were then made by soldering with indium and the same flux. Both electrical contacts were shown to be ohmic and of low resistance. A typical mesa area was 0.4 mm^2. Two typical I-V curves are shown in figure 23.

B. Electrical Measurements

The electrical measurements made during this study consisted of temperature dependence of resistivity and Hall coefficient of homogenous diffused samples, as well as resistance and capacitance of diodes.

1. Hall and Resistivity

Hall measurements of low impedance samples were performed with standard potentiometric methods or with digital nanovoltmeter. We used

Leeds and Northrup Type K-3 7553 universal potentiometer with their 9834 electronic null detector. The digital nanovoltmeter was Keithley 180. A Keithley 610B high input impedance electrometer was used to measure samples with impedance greater than 10^5 ohms. This setup provides better than one microvolt precision for the low impedance measurements and 3% precision when using the electrometer. The magnetic field was produced by Varian V 4004 4" electromagnet and measured with a Rawson 820 rotating coil fluxmeter.

Hall samples had the form of rectangular prism[52] with a typical dimensions of 1.0 x 0.2 x 0.05 cm. The samples were cut and lapped to the approximate desired size and shape and then etched to remove surface damage. Additional etching took place after the diffusion process was completed in order to remove any alloying on the sample surface. At this point electrical contacts were made.

Three procedures were used for contacting to the lead-tin telluride samples. Indium or lead-tin eutectic with Divco type K soldering flux were found to give good ohmic contacts as long as low current was used and the sample did not undergo much thermal cycling. More elaborate contacting procedure was used when measurement required thermal cycling which included liquid helium temperature. A thermocompression welding technique produced excellent contacts. After etching the sample, gold wires, usually 0.002" in diameter, were welded to it using a Hughes MCW/BB micro pulse thermocompression ball bonder. These contacts had good electrical and mechanical properties while requiring only local heating of the sample.[3] X-ray examination revealed very

little mechanical damage near the properly made contact.

After contacting, the sample was cemented to a sapphire plate soldered to the sample mount of a Hofman cryostat. General Electric No. 7031 varnish was used as the bonding agent due to its good thermal conductivity and electrical isolation. The cryostat arrangement is shown in figure 24.

The temperature dependent measurements of electrical and optical properties were carried between 4K and 380K. To cover the large temperature range of our measurements, several coolants were required. The coolants used were:

Liquid helium	4K - 80K
Liquid nitrogen	70K - 180K
A mixture of solid and liquid Freon11	160K - 250K
A mixture of solid and liquid Freon 113	240K - 320K
Ice mixed with water	274K - 370K
Hot water	350K - 380K

Any temperature within the range of a given coolant could be obtained by adjusting the power input to a heater on the sample mount. A calibrated Allen Bradley 0.1 watt resistor was used to monitor temperature below 60K and a Microdot Incorporated platinum resistance thermometer was used for temperatures above 60K. Both sensors were calibrated against a Cryocal germanium resistance thermometer (CR100 - 1.5-100) for temperature between 2K and 100K. The platinum thermometer was also calibrated against a copper-

constantan thermocouple for temperatures greater than 77K.

2. Capacitance and Resistance of the Diodes

Although the major effort of this part of the study was involved with optical measurements on the diodes, two kinds of electrical measurements were carried out as well. Bias dependence of the diodes capacitance and temperature dependence of the zero bias impedance can provide some important information on the nature of the junction. (See discussion in section C of chapter 2.)

Measurements of the capacitance of the diodes was not an easy task. Lead-tin telluride is known to have a very high dielectric constant and therefore the diode capacitance is high. This, plus the fact that our diodes had relatively low zero bias impedance, made it almost impossible to perform any successful capacitance measurements. The only way to reduce the device capacitance and at the same time to increase its resistance is to fabricate a diode with a very small junction area. This can be done when photolithographic procedure is utilized to confine the mesa area. We used the facilites of a microelectronic laboratory to make three mesas each with 2×10^{-4} cm^2 in effective area. These diodes were Cd diffused $Pb_{0.80}Sn_{0.20}Te$ and were made for the sole purpose of capacitance measurements. The wafer with the junction was mounted on an aluminum block which was immersed in liquid nitrogen. Electrical contacts to both the n-type mesa and the p-type base were made by aluminum probes. The device had a 20 KΩ resistance and 231 pF capacitance when measured with no bias at 77K. A Boonton Electronics Corporation Model 71A capacitance meter was used.

This meter has a range of zero to 1000 pF and can provide an instant direct reading.

The resistance of several diodes at zero bias was measured at a temperature range from 4K to room temperature. This was done while the diode was mounted on the cryostat and temperature adjustment was achieved in the same way as for the Hall measurements. The resistance was measured using an A.C. bridge.

C. Optical Measurements

The two major optical measurements were the spectral response of both photoconductive and photovoltaic (Pb,Sn)Te detectors. The main purpose of these measurements was to determine the fundamental absorption edge and its dependency on temperature, carrier density, and impurity diffusion. In addition, time constant measurements of the diodes were made so junction capacitance could be obtained by an independent measurement technique.

1. Photoconductive Response

Due to the low mobility ratio, high carrier concentration and conductivity of our samples diffused with Sb and Cd, it is almost impossible to obtain a good photosignal when using it as a photoconductive detector. While working on the effects of diffusion in (Pb,Sn)Te, we noticed that using a mixture of cadmium-indium source, a diffusion at the right temperature would produce material suitable for photoconduction measurements.

Sample preparation and mounting were similar to the procedure described for the Hall measurements. The same dewar was used but a KRS-5 window was installed in its tail piece. The temperature range of the measurements was from 4K to 120K. At higher temperature the ratio of photosignal to noise was too poor to conduct measurements. A Perkin Elmer Model 13 spectrometer was used in all our spectral response measurements. The dewar position relative to the spectrometer optics is shown in figure 25. The spectrometer is equipped with a Nernest glower source and a thermocouple detector complete with a 13 Hz chopper, amplifier and a strip-chart recorder. The thermocouple detector has a response which is independent of the incident radiation wavelength and is therefore used for normalizing the response of the measured samples. To minimize noise from our sample the beam was chopped at 208 Hz and signal output was amplified by a Princeton Applied Research Model JB5 lock-in amplifier with a narrow band width which was tuned to that frequency. For photoconduction measurements a Perry Model 607 preamplifier was used in conjunction with the JB5 amplifier. The amplified signal was recorded on the spectrometer strip-chart recorder. The sample response was normalized against the thermocouple response in order to cancel out the wavelength dependence of the spectrometer radiation source. The relative response was then obtained.

2. Diode Spectral Response and Time Constant

In section A(3) of this chapter the photodiode fabrication procedure was described. The long leads of the TO-5 header, on which the device was mounted, were cut and the package was mounted on the sapphire

plate of the dewar just as for the photoconective samples. The detector photo-signal was input to a Triod Corp. Geoformer (transformer). From the geoformer the signal was amplified by the two Princeton Applied Research amplifiers. Recording and reducing the photoresponse was done exactly as for the photoconduction measurements.

The shape of the response as a function of wavelength is basically the same as discussed in the previous section although the junction depth and structure may effect it. If the junction is deeper than the diffusion length, some of the excited photocarriers will not reach the junction and thus will not contribute to the photosignal. In some cases the optical gap may not be of the same width in both sides of the junction and the photoresponse is the result of two transition probabilities.

Time constant measurements were made by shining square light pulses from a 10.6 micron laser[51] on the detector, and observing the signal decay. Rise and decay time of the light pulse were less than 0.5×10^{-9} seconds and the measurements were limited, therefore, by the response time of the amplifier used. The CO_2 laser system had a GaAs electro-optic modulator, external to the laser cavity, which was mounted in the transmission line from a high voltage pulser to a 50Ω termination. The direction of polarization of the laser beam was aligned parallel to the applied electric field. The laser output was partially self-polarized by an internal Brewster window. An x-y recorder was used to record the decay trace as shown in figure 26. The bias dependence of the time constant will be discussed in section C of

chapter 4. We will also discuss the meaning of these measurements when taking the device and load resistance into consideration.

CHAPTER IV

RESULTS AND DISCUSSION

Our diffusion results show two types of anomalous behavior in the doped (Pb,Sn)Te. Cd-In diffusion produced a major change in the physical properties of the host material. The lattice parameter increases while the number of free charge carriers and the mobility decrease drastically. The energy gap, which was determined by photoconductivity measurements, shows a big increase as the result of the Cd-In diffusion. Photodiodes were not fabricated by this method since photoconductivity measurements could be performed to determine the optical gap.

Photodiodes are the main tool for studying the effect of Cd and Sb diffusion on the optical properties of (Pb,Sn)Te. We will also discuss the electrical properties of the two kinds of junctions. The last section is devoted to discussion of the Burstein shift in Sb diffused diodes and in degenerate bulk (Pb,Sn)Te.

A. Diffusion Dependence of Crystal Structure

Solid mixtures of cadmium and indium (Cd-In) were prepared by reacting the two metals in the desired quantities. The alloy was used as the diffusion source. It was observed during the early part of our study that Cd-In diffused (Pb,Sn)Te manifests very unusual physical properties. Hall measurements at nitrogen temperature indicate very low free electron concentrations. In fact, as soon as the diffusion temperatures exceeded 700°C, the carrier densities were equal to or lower

than any number previously reported.

In order to characterize the phenomenon we carried out more than two dozens diffusion experiments under different conditions. A representative selection of these samples was used for more careful and complete electrical and optical measurements as a function of temperature. The results will be shown and discussed in the following sections. The dependence of the physical properties of diffused (Pb,Sn)Te on diffusion temperature, content of SnTe in the sample, and composition of the source alloy was determined. The diffusion temperature range was 400-800°C. The $Pb_{1-x}Sn_xTe$ samples were cut from as-grown crystals with $x \approx 0.04$, $x \approx 0.13$, $x \approx 0.14$, and $x \approx 0.24$. The various diffusion sources were: pure cadmium, 1:1 atomic ratio Cd-In, 1:4 Cd-In, and pure indium. In all cases the samples were completely converted into n-type as a result of the diffusions.

The carrier concentrations, n, were calculated from the Hall coefficient, R, measured at 77K using the formula

$$n = 1/eR \qquad (4.1)$$

77K is assumed to be a low enough temperature to maintain only a small fraction of thermally generated carriers and at the same time high enough to avoid a freeze out of extrinsic carriers.

Figure 27 shows the free carrier concentration dependence on the diffusion temperatures for a few samples. It is clear that as the diffusion temperature is increased, the carrier density decreases. The effect is less pronounced in samples with a low SnTe content ($x \approx 0.04$). In general, one would expect heavier doping at higher diffusion tem-

perature. The results presented in figure 27 do not necessarily contradict this notion for the following reason: the number of impurity atoms may have increased with diffusion temperature, yet most of them are electrically inactive. The number of free charge carriers may decrease if some compensation takes place.

In figure 28 we show the dependence of the carrier density on the diffusion source composition. It appears that only the mixture of cadmium and indium source produces the extraordinary low carrier concentration. Diffusion with either metal alone results in much higher value for the free charge density. It should be pointed out that density as low as 4×10^{12} cm^{-2} has been measured for one sample at 77K.

We have utilized our x-ray techniques, as described in section B of chapter III to examine any structural change as a result of this type of diffusion. Back reflection Laue pictures revealed the same NaCl symmetry, but the reflected radiation was of a much lower intensity. However, when the lattice constant parameter was measured, an obvious and consistent expansion was observed. We then looked at the diffusion temperature dependence of this change. The results, which are presented in figure 29, show almost linear increase in the lattice constant as the diffusion temperature is increased. Diffusion at 800°C caused the crystal parameter to increase by half a percent. These results also indicate that the amount of impurity diffused into the crystal must be very high. It probably requires at least a tenth of a percent of foreign atoms, i.e. more than 10^{20} atoms per cm^3, in order to change the lattice constant.

X-ray topograph pictures (figure 30) of the diffused (Pb,Sn)Te were also taken. Two wafers were examined after etching away about 0.2 mm from the surface. One was diffused into the (111) surface and the other into the (100). The x-ray pattern in the first case indicates symmetric round pit clusters. The diffused (100) plane has a different pattern as seen in figure 30. It looks as though there are four parallel channels across the plane. We conclude that the impurity precipitated in some preferred manner according to the crystal symmetry.

A scanning electron microscope with x ray capability was used as an additional tool for examining the change in crystal structure. The micrograph pictures are shown in figure 31. We looked at the (111) surface and were able to detect some In inside the pit and some Cd outside. The detection was done by looking at the x ray spectrum emitted from the spot hit by the electron beam. This technique is very sensitive to elements of impurity larger than a few tens of a percent. Thus, we have an additional technique for estimating the concentration of impurity diffused.

We conclude that although the crystal symmetry remains the same after the In diffusion, there are some significant changes in the crystal seen from lattice constant measurements, x ray topographs, and electron micrographs. The atomic content of the diffused impurity is only about 10^{20} to 10^{21} per cm^3 which is the [illegible] concentration in the crystal examined. There [illegible] further the electrical and optical [illegible] In diffused [illegible] and also some possible [illegible] will be suggested.

X-ray examination of Sb and Cd diffused (Pb,Sn)Te revealed no change in either material structure or lattice constant.

B. Hall and Mobility Change Due to Diffusion

Hall effect and resistivity measurements at 77K were made on every diffused sample. Those samples which were selected for temperature dependance measurements, were mounted on the Hofman cryostat as described in the previous chapter.

The Hall coefficient, R, is defined as:

$$R = \frac{V_H \times t}{I \times B} \times 10^8 \text{ cm}^3 \text{ Coulomb}^{-1} \qquad (4.2)$$

where V_H is the measured Hall voltage, t is the sample thickness parallel to the magnetic field, I is the current through the sample perpendicular to the magnetic field, and B is the magnetic flux density in gauss. The sample resistivity, ρ, is given by:

$$\rho = \frac{V_R}{I} \frac{W \times t}{\ell} \text{ ohm-cm} \qquad (4.3)$$

where V_R is the measured potential difference between two contacts a distance ℓ apart, and W is the sample width. All dimensions are in centimeters, V_R and V_H are in volts, and I is in amperes. The Hall coefficient as a function of reciprocal temperature for four selected diffused samples (see Table 3) is shown in figures 32 and 33. Resistivity of these same samples is shown in figures 34 and 35. For comparison purpose we included another undiffused (Pb,Sn)Te sample.[3] We observe that sample D1,which was diffused at 640°C, has the lowest Hall constant. Its resistivity and Hall coefficient are similar to those of the undiffused sample. The other three samples were diffused at higher temperatures.

Their specific resistance and Hall constant are strongly temperature dependent and they are larger by a few order of magnitude, than the undiffused material.

The Hall mobility is defined as:

$$\mu_H = R/\rho \ cm^2/volt\ sec$$

and is shown in figure 36. It is very clear that the diffusion caused a major decrease in the mobility of the samples. The higher the diffusion temperature, the lower is the mobility. Again, we observe a strong variation with temperature. Samples D2, D3, and D5 show increasing mobility with temperature for a range below 100K. This is the case when the mobility mechanism is dominated by ionized impurity scattering. At higher temperatures the mobility levels off and then there is a sharp decrease with temperature, which is expected when lattice scattering is the major mobility process. The temperature dependence of the mobility of (Pb,Sn)Te was shown to obey the $T^{-5/2}$ law [3] Sample L, the undiffused material, shows such behavior at temperatures greater than 60K The mobility of our diffused samples approach such a slope only at temperatures higher than 320K. This indicates a strong, even if not dominant, impurity scattering effect at lower temperature range.

Hall and resistivity measurements on completely Sb and Cd diffused samples show results similar to unnealed and annealed samples[3] respectively, and therefore are not discussed here

C. Electrical Properties of the Diodes

We have calculated the Diffusion coefficient, D, for the diffusion of cadmium impurity into a $Pb_{0.79}Sn_{0.21}Te$ single crystal. Our calculations are based on eight experimental runs with diffusion temperature range of 400 to 650°C. and diffusion time from 42 to 120 minutes. Starting from equation (2.21) we assume that the Cd density at the junction is much smaller than on the sample surface,($N(x,t) \ll N(0,t)$), and therefore the approximation $D = x^2/t$ can be used. Our calculated values for D as a function of the reciprocal diffusion temperature is shown in figure 37. As discussed in section C of chapter II, the slope of this plot is equal to the diffusion activation energy. For our system it is about 1.1 eV. D_o of equation (2.20) is 0.02 so the diffusion coefficient for Cd diffusion in $Pb_{0.79}Sn_{0.21}Te$ can be written as $D(T) = 0.02 \exp(1.1/k_BT)$.

The dominant current mechanism in the junction can be determined by looking at the temperature dependence of the zero bias resistance of the diode. It is possible to determine whether the resistance is limited by current due to minority carrier diffusion through the junction or by generation recombination processes within the depletion region.

We can simplify equation (2.28) of chapter 2 for the saturation current for the case of lead-tin telluride where $\mu_n \approx \mu_p$ and $\tau_n \approx \tau_p$ to

$$I_s = e\sqrt{\frac{k_BT}{e}}\,\frac{\mu}{\tau}\left(\frac{1}{N_D} + \frac{1}{N_A}\right) n_i^2 \qquad (4.4)$$

where the relation $D = k_B T \mu/e$ was used. The diode resistance under zero bias, R_o, is proportional to the inverse of the current at zero bias, so we conclude that for the diffusion current case R_o follows the temperature dependence of n_i^{-2} which varies as $\exp(E_{go}/k_B T)$ where E_{go} is the energy gap at the absolute temperature. Referring now to the expressions for generation recombination current, equation (2.29) of chapter II, we note that the current has a linear dependence on n_i so the temperature dependence of the zero bias resistance is clearly n_i^{-1}.

Figure 38 shows a plot of the resistance of both Sb and Cd diffused diodes as a function of the inverse temperature. On the same graph the calculated behavior of n_i^{-1} and n_i^{-2} are plotted using equation (2.17). We observe that within the temperature range plotted the dominant current mechanism in the cadmium diffused diode is due to diffusion while in the case of antimony diffused diode it seems that generation recombination current is dominant. It should be stressed however, that nondegenerate statistics was used in developing the current equations and therefore we are not sure to what degree they are valid for the Sb diffusion case.

In figure 39 the inverse square of a cadmium diffused diode capacitance at 77K is plotted versus bias voltage. The linear relation suggests an abrupt junction as seen from equation (2.25). The built-in voltage is obtained by extrapolating the C-V curve to zero capacitance. In our case it is found to be 0.07 volt. The junction width is calculated, using equation (2.23) of the above section, to

be 0.16 μm when a value of 500 was taken for the dielectric constant and 1×10^{17} cm^{-3} for the donor density. We were unable to measure the capacitance of Sb diffused diodes because of their very high capacitance. Results obtained by M. R. Johnson[55] suggest a linear graded junction with grading constant of 1.9×10^{22} cm^{-4} and built-in voltage of 0.26 volt.

The time constant measurements do not represent the real device decay time which is believed to be RC limited. The reason can be explained as follows: The device is connected in parallel to the time constant system load resistance, R_L. The equivalent resistance, R_{eq}, now should be considered in the equation $\tau = RC$. In our case R_L was 50Ω and R_d was about an order of magnitude larger when the diode was reverse biased. In figure 26 we show two typical time decay traces of the same diode at different bias. The bias dependence of the time constant is shown in figure 40. We note that at very small reverse bias the decay becomes slower but then faster as the bias becomes more negative. The reason for that is due to a big increase in diode resistance and a small decrease in its capacitance at low bias. For larger reverse bias, the constant load resistance is dominant but the diode capacitance decreases making the decay time shorter. Similar results had been obtained earlier.[56]

Using the decay time values for reverse bias larger than 0.2 m amp and the diode's resistance, we were able to calculate its capacitance. The values were of the same order of magnitude as obtained by direct capacitance measurements (figure 39).

D. Fundamental Absorption Edge Shift

The last section deals with two types of shifts in the fundamental absorption edge as a result of impurity diffusion. The first one is caused by the Cd-In diffusion and is probably due to some change in the energy band structure in the material. The second is due to the displacement of the Fermi level from the forbidden gap into one of the bands in degenerate material.

1. Energy Gap Increase Due to Cd-In Diffusion

Photoconductivity measurements were carried out on Cd-In diffused (Pb,Sn)Te samples. As discussed earlier, (section C of chapter 3) the optical energy gap can be determined from the spectral response obtained from such measurements. Figure 41 shows the temperature dependence of the energy gap for three diffused samples. The only difference among the three is the diffusion temperature. On the same graph we present the variation of the gap with temperature of an undiffused (Pb,Sn)Te sample with a similar composition. The effect of the diffusion on the gap is striking. At low (<50K) temperatures the optical energy gap is increased by 50 percent, but at temperatures above 60K there is an extremely sharp increase with temperature. The energy gap at 90K is about four times larger than the gap of an undiffused lead-tin telluride.

We can summarize the effect of Cd-In diffusion into lead-tin telluride as follows: When diffusing at temperature above 650°C the lattice parameter expands by up to 0.5 percent while the crystal

symmetry remains the same. Some impurity clusters are observed. The free carrier concentration and the Hall mobility both decrease by a few order of magnitudes while the optical energy gap increases. The big increase in the gap is not likely to be a result of the lattice expansion since a larger lattice increase, caused when the fractional content of SnTe is increased, produces much smaller increase in the gap. A possible explanation can be obtained if we assume that the impurity clusters produce energy barriers along the lattice. These barriers can explain the increase in the optical gap as well as the decrease in the mobility. They can act also as compensation centers which would bring about a reduction in the number of free carriers.

Alternatively, one can treat the whole system as an homogeneous material rather than (Pb,Sn)Te crystal with impurity centers. Since the physical properties change so drastically only at 700°C and higher temperatures, and since the amount of impurity is of the order of a tenth of a percent, a possible chemical reaction may be taking place producing a semiconducting material with different properties.

Although our measurements do characterize the phenomenon of Cd-In diffusion in (Pb,Sn)Te we do not claim to understand it. We have tried, however, to outline two approaches for explaining it.

2. The Burstein Shift in Lead-Tin Telluride

Our spectral response measurements on the photodiodes were aimed to determine the dependence of the absorption edge on crystal composition, temperature and doping techniques. The methods of detector fabrications and measurements were described in the previous chapter.

The antimony diffusion produced junctions with n-type layers with carrier density of 1-3 x 10^{19} per cm^3 while cadmium doping resulted in n-layers with free electron concentration two orders of magnitude lower. The exact carrier density varied with diffusion temperature and substrate composition. Hall measurements on completely diffused samples were used to determine the exact concentration in each case.

Figure 42 shows typical responses of two diodes at three temperatures. One detector was diffused with antimony and the second with cadmium, but in both cases the host materials were from the same crystal. It is readily seen that the spectral response of the Cd diffused diode shifts to shorter wavelength when operating at higher temperatures. This is expected since the energy gap of lead-tin telluride increases with temperature. However, in the case of the Sb diffused detector there is almost no change in the response when the temperature is increased. A comparison reveals that at a low temperature the first one is sensitive to 12-14 μm radiation incident and the second to 6-9 μm. This implies different fundamental absorption edges at low temperatures. Figures 43 and 44 give more complete picture on the temperature dependence of the spectral response. Each figure shows a comparison of the responses of the two types of detectors. It is clear, also, that in figure 44, where the diodes are made of material with higher content of SnTe than those shown in figure 43, the effect is more pronounced. Below some temperature, which varies with the composition of the substrate, cadmium diffused diodes are sensitive to lower energy photon incident than antimony diffused ones.

X-ray determination of the lattice constant before and after diffusion shows no difference in either case. Thus, it is believed that the difference in absorption properties are not due to the crystal structure change but rather to some other fundamental property of the material under study. We compared our data to transmission measurements results obtained by Lockwood[3] on annealed and unannealed (degenerate) samples. It was observed that for a given composition, measurements on a Cd diffused detectorand transmission on an annealed sample yield very similar values for the energy gap which are in agreement with theoretical prediction.

The results obtained from the antimony diffused diodes show basically similar temperature dependency as those obtained from transmission measurements on unannealed samples and they are in disagreement with conventional theoretical predictions.

This anamolous dependence of the optical absorption edge for high carrier concentration material was observed first in indium antimonide.[57] Burstein[4] proposed the following explanation: Due to the small band gap and small electron effective mass in InSb, the Fermi level moves into the conduction band as the donor concentration, N_d, is increased, resulting in a shift of the absorption edge. In other words, the density of states in the conduction band is low enough so that many of the states at the bottom of this band are already filled (see figure 45) and thus unable to accept any optically excited electrons. Only states of higher energy are still available for occupancy by the photo-generated electrons. This effect, which was also

explained by Moss,[58] has also been observed in other small gap semiconductors.[59] We shall use the Burstein model to calculate the displacement of the absorption edge for degenerate lead-tin telluride.

In figure 46 we show a schematic energy-wave vector band diagram for a degenerate n-type material. In the following we measure all energies from the bottom of the conduction band and consider only direct transitions. The minimum energy required to excite an electron from the valence band into the conduction band is

$$\begin{aligned} h\nu &= E - E_o \\ &= \frac{h^2}{2m_e^*} k^2 - (-E_g - \frac{h^2}{2m_h^*} k^2) \end{aligned} \tag{4.5}$$

where ν is the incident photon frequency, E and E_o are energies (see figure 46), and m_e^* and m_h^* are the respective electron and hole density of state effective masses. The above equation can be rewritten as

$$h\nu = E_g + E(1 + \frac{m_e^*}{m_h^*}) . \tag{4.6}$$

The absorption coefficient, α, for degenerate semiconductors is given by[60]

$$\alpha = \alpha_o [1 - \frac{1}{1+\exp([E-E_f]/k_B T)}] \tag{4.7}$$

where α_o is the absorption coefficient for the nondegenerate case. From equation (4.7) we obtain

$$E = E_f - k_B T \ln (\frac{\alpha_o}{\alpha} - 1) . \tag{4.8}$$

Using this expression for E, equation (4.6 becomes

$$h\nu = E_g + [E_f - \gamma k_B T][1 + \frac{m_e^*}{m_h^*}] \qquad (4.9)$$

where we define $\gamma \equiv \ln(\frac{\alpha_o}{\alpha} - 1)$. For (Pb,Sn)Te the effective masses of electrons and holes are almost equals, so

$$h\nu = E_g + 2(E_p - \gamma k_B T) . \qquad (4.10)$$

Equation (4.10) will be used to evaluate the required incident energy for a direct transition at a given temperature. Burstein has taken $\gamma=4$ and thus insured that within the range of $\gamma k_B T$ the absorption exceeds 99% of its full value at temperature T. Alternatively, γ can be taken as an independent variable the value of which can be determined by fitting equation (4.10) to the experimental data.

Expression (4.10) can be evaluated for a given carrier density n and temperature T only if the Fermi level E_f is known. To calculate E_f we use equations (2.16) of chapter II but the right-hand-side is multiplied by a factor of 4 since we need to take into account all eight half equivalent minima in the zone edge of lead-tin telluride. Hence, equation (2.16b) becomes

$$n = [8(\frac{2\pi m^* k_B T}{h^2})^{3/2}][2\pi^{-1/2} \int_0^\infty \frac{x^{1/2}(1 + \frac{x}{\epsilon})^{1/2}(1 + \frac{2x}{\epsilon})}{1+\exp(x-\eta)} dx]. \qquad (2.11)$$

Defining $N_c \equiv 8(\frac{2\pi m^* k_B T}{h^2})^{3/2} = 1.93 \times 10^{16} (\frac{m^*}{m})^{3/2} T^{3/2}$, where m is the electron mass, and denoting by $F(\epsilon,\eta)$ the integral

$$F(\epsilon,\eta) = 2\pi^{-1/2} \int_0^\infty \frac{x^{1/2}(1 + \frac{x}{\epsilon})^{1/2}(1 + \frac{2x}{\epsilon})}{1+\exp(x-\eta)} dx \qquad (4.12)$$

equation (4.11) can be written as

$$n = N_c F(\varepsilon,\eta) \ . \tag{4.13}$$

The integral $F(\varepsilon,\eta)$ has been evaluated by Bebb and Ratliff[61] for $0.01 \leq \varepsilon \leq \infty$ and $-5 \leq \eta \leq 10$. Using these results we can use equation (4.13) to calculate the (reduced) Fermi level η for given n, ε and T.

For η larger than 10 the integral $F(\varepsilon,\eta)$ is no longer equal to n/N_c. However, as T approaches zero, ε approaches infinity and $F(\varepsilon,\eta)$ becomes the familiar Fermi-Dirac integral $F_{1/2}(\eta)$. For $\eta \gg 1$, $F_{1/2}(\eta)$ can be approximated[30] to within 2 percent by

$$F_{1/2}(\eta) = \frac{4}{3}\,\eta^{-1/2}(\eta^2 + 1.7)^{3/4} \ . \tag{4.14}$$

For this range of T and η we can rewrite equation (4.13) as

$$n = N_c\,\frac{4}{3}\,\eta^{-1/2}(\eta^2 + 1.7)^{3/4} \tag{4.15}$$

Neglecting 1.7 compared to η^2 in the above expression we solve for η and get

$$\eta = 1.68 \times 10^{-11}\ n^{3/2}/(\frac{m^*}{m})T \ . \tag{4.16}$$

Equation (4.16) is then used to obtain the reduced Fermi levels at low temperatures.

The experimental values of the absorved radiation, hv, for two transmission samples (number 9 and number 10) have been fit to equa-

tion (4.10) using a general least-square technique on a digital computer. The values for E_g were obtained from similar optical measurements on non-degenerate material, and the carrier density n was obtained from Hall measurements. The fitting program is given n, E_g, T and initial estimate for γ and m^*. The parameters obtained by use of the fitting program for sample number 9 were $\gamma = 5.057$ and $m^* = 0.04932m$. For sample number 10 we got $\gamma = 6.77$ and $m^* = 0.0235m$. The values of the effective mass of (Pb,Sn)Te reported in the literature are of the order of $0.04m$.[2]

In figure 47 we present the calculated Fermi level as function of electron concentration for sample number 9 at three chosen temperatures. Figures 48 and 49 show the experimental and the calculated absorption edge shifts for both samples. Figure 50 presents the calculated optical energy gap $h\nu$ dependence on carrier concentration at three given fixed temperatures. Here we calculated $h\nu$ for $Pb_{1-x}Sn_xTe$ with E_g corresponding to $x = .17$. m^* and γ were taken from our values for sample number 9.

CHAPTER V

SUMMARY

We have investigated the effect of impurity diffusion in lead-tin telluride on its physical properties. Three types of metal impurities were studied: antimony, cadmium, and a mixture of cadmium and indium. When Cd-In alloy was used as the diffusion source, we observed a drastic change in the electrical and optical properties of the host (Pb,Sn)Te, as well as an expansion of its unit cell. We have measured the temperature dependence of the Hall coefficient and the resistivity of the diffused material, and observed a big increase in both physical quantities and in their variation with temperature. At 77K, for example, the Hall coefficient and the resistivity each increased by up to 6 order of magnitude, depending on the diffusion temperature. The optical energy gap of the Cd-In diffused samples was found to increase by a factor of two, and the lattice constant expanded by half of a percent. We looked at the diffusion temperature dependence of this phenomenon and noticed that diffusion below 700°C does not produce it, but at 700°C it is very pronounced. Further increase in the temperature (up to 800°C) has a relatively small effect. We believe that the system undergoes some kind of intrinsic change, probably due to some chemical reaction, and therefore cannot be treated as conventionally doped (Pb,Sn)Te. Although we were able to characterize the physical changes, further investigation is required in order to provide an explanation as to why they occur.

Cadmium and antimony were used to diffuse p-n junctions on which electrical and optical measurements were carried out. We have found that the diffusion coefficient of Cd in $Pb_{0.79}Sn_{0.21}Te$ is $D(T) = 0.02 \exp(1.1/k_BT)$. The p-n junction which is produced by such a diffusion is an 0.16 μm abrupt junction with a built-in voltage of 0.07 volts. The shift in the spectral response of Sb diffused diodes, which we observed, is believed to be the same as observed in transmission measurements on degenerate (Pb,Sn)Te. Using a model proposed by Burstein[4] we were able to calculate the expected shift of the absorption edge and to show that the theoretical results are in agreement with the experimental data. A fitting procedure of the calculated and the experimental results yields a hole effective mass of about 0.04m.

Table 1

Mass Spectrographic Analysis of the Elements
(Parts per Million, Atomic)

Element	Lead		Tin	Tellurium
	EM 3422	EM 3337	EM 3381	EM 3387
Bi	.1	.1		
Ca	.1	.2	.1	.1
Cu	<.1	<.1	.1	.1
Fe	.1	.2	.2	.1
Mg	<.1	<.1	<.1	<.1
Si	.1	.1	.1	.2
Ag	<.1	<.1		<.1
Al	ND	.1		.1
Pb			.2	<.1

Table 2

Growth Runs

Run Number	Charge Composition (%)	Growth Temperature (°C)	ΔT (°C)	Growth Time (Days)	Crystal Length (mm)	Remarks
3	20	863±2	5	16		N.G.
4	20	843±2	5	16	18	G
5	15	848±4	7	14	30	A.T.
6	15	843±8	5	6	14	G
7	15	842±2	5	10		N.G.
8	15	840±2	5	18		N.G.
S9	10	845±8	5	18	8	hillocks
9	10	848±2	5	26	30	G
S10	18	840±2	5	10	10	G
10	18	840±5	5	25	15	G
11	10	848±3	6	19	25	A.T.
S12	22	850±1	3	13	10	G
12	22	834±5	5	18	17	G
S13	22	837±5	5	20	26	G
13	22	845±5	5	21	15	G
14	22	848±3	3	26	25	G
15	20	845±1	3	30	28	G
16	20	839±2	4	37	20	G
17	25	840±1	3	24	25	G
18	45	807±3	6	28	20	G
S19	0	875±1	3	21	10	G
19	0	865±1	7	28	31	G
20	20	845±5	7	21	30	A.T.
S21	28	845±5	7	17	10	G
21	28					G
S22	0	865±1	5	28	15	G
22	0	865±3	5	21	21	G
23	10					G
S24	5					G
24	5					G
S25	15	836±3	8	22	30	G
25	15	838±3	7	30	35	G
S26	19	834±1	3	30	24	G
26	19	830±2	5	21	20	G
S27	2	815±2	3	30	15	N.G.
27	2	850±3	5	30		A.T.
S28,28	23					G
S29,29	31	853±2	5			G
SS30,S30,30	23					G
SS31,S31,31	22					G
S32	23	840±1	4	22	25	G
32	23	850±1	4	21	30	G
33-39	22					

G-Good; N.G.-No Good; A.T.-All Charge Transported

Table 3

Samples Diffused With Cd-In

Sample	x	Cd:In Ratio	Diffusion Temperature	n_{77K}	R_{77K}	ρ_{77K}	μ_{77K}
D1	.14	1:4	640°C	5×10^{17}	1.25×10^{1}	1.80×10^{-3}	6.9×10^{3}
D2	.14	1:4	700°C	3×10^{14}	2.08×10^{4}	9.76×10^{0}	2.1×10^{3}
D3	.14	1:4	750°C	3×10^{14}	2.02×10^{4}	1.01×10^{1}	2.0×10^{3}
D4	.14	1:4	800°C	3.6×10^{14}	1.70×10^{4}	2.31×10^{1}	7.3×10^{1}
D5	.24	1:1	700°C	4×10^{12}	1.60×10^{6}	3.72×10^{2}	4.3×10^{3}
L *	.10			6.4×10^{17}	6×10^{0}	7×10^{-4}	4×10^{4}

* Sample L is an undiffused (Pb,Sn)Te which is included for comparison. It was prepared and measured by Lockwood.[3]

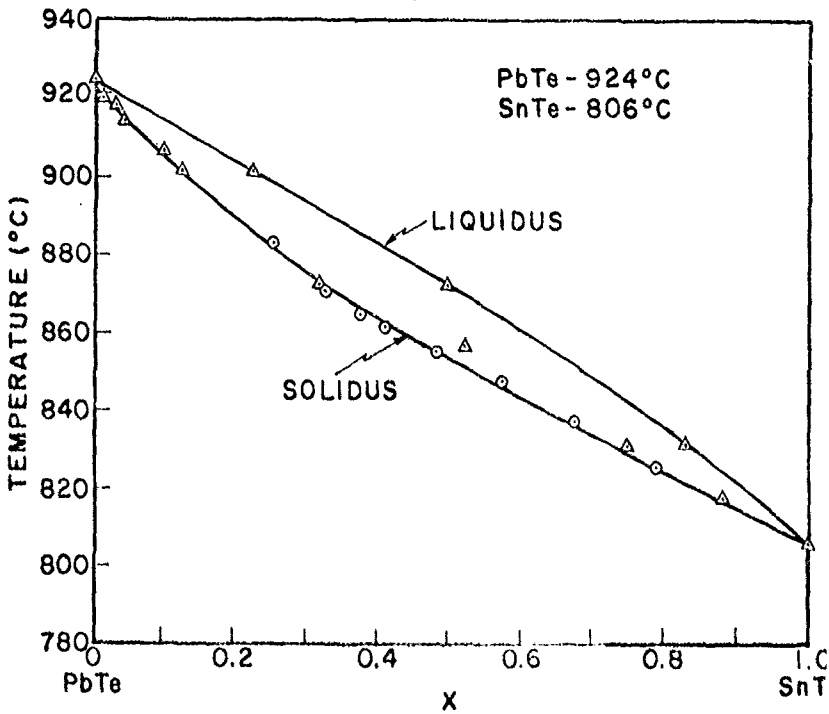

Figure 1. Temperature-composition pseudobinary phase diagram for $Pb_{1-x}Sn_xTe$.[7]

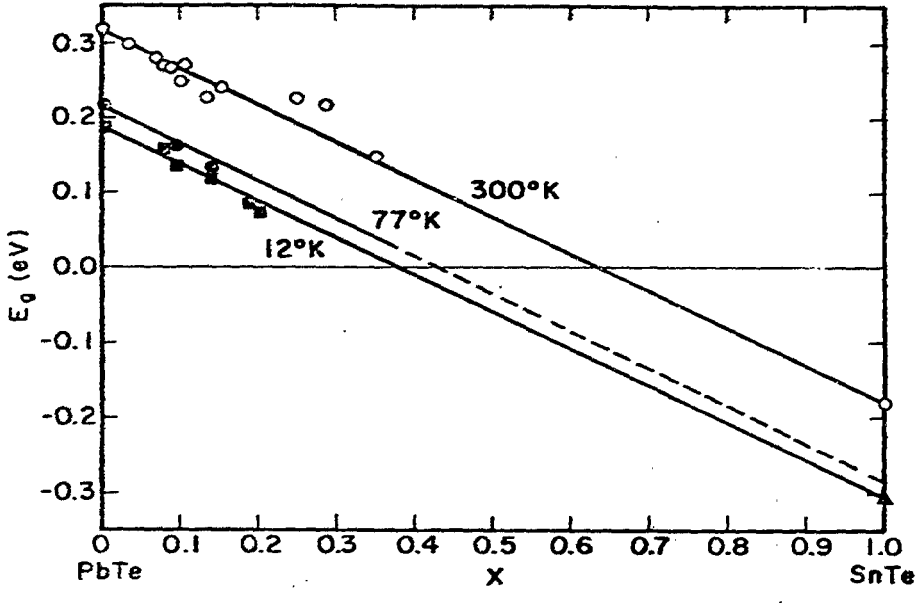

Figure 2. Energy gap as a function of composition and temperature for $Pb_{1-x}Sn_xTe$.[1] The band inversion occurs at $E_g = 0.0$.

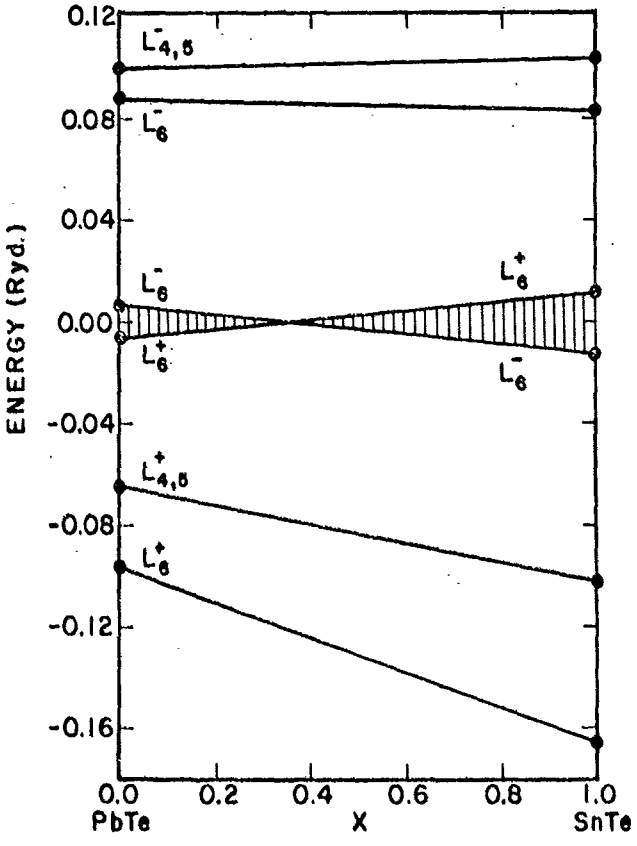

Figure 3. Position of the energy bands in the vicinity of the energy gap at the L point of alloy composition in $Pb_{1-x}Sn_xTe$.[35]

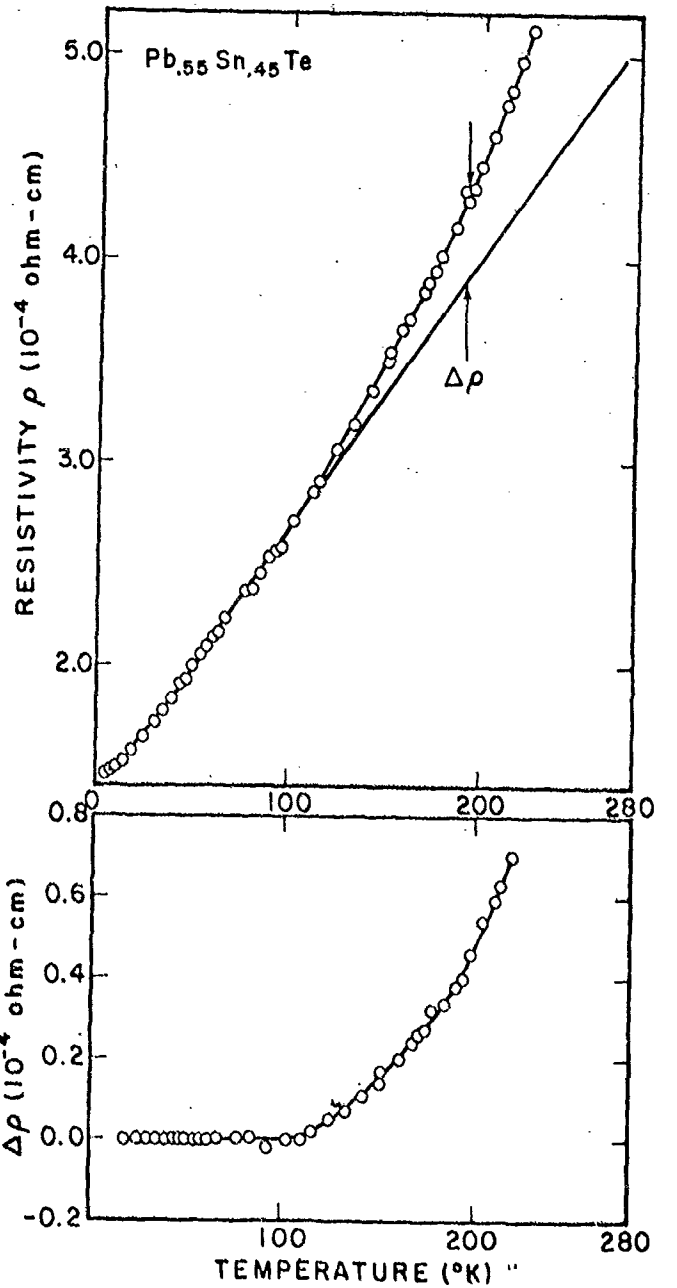

Figure 4. Resistivity as a function of temperature for $Pb_{0.56}Sn_{0.44}Te$. The break in the slope is due to the reversal in sign of dE_g/dT at the band inversion.

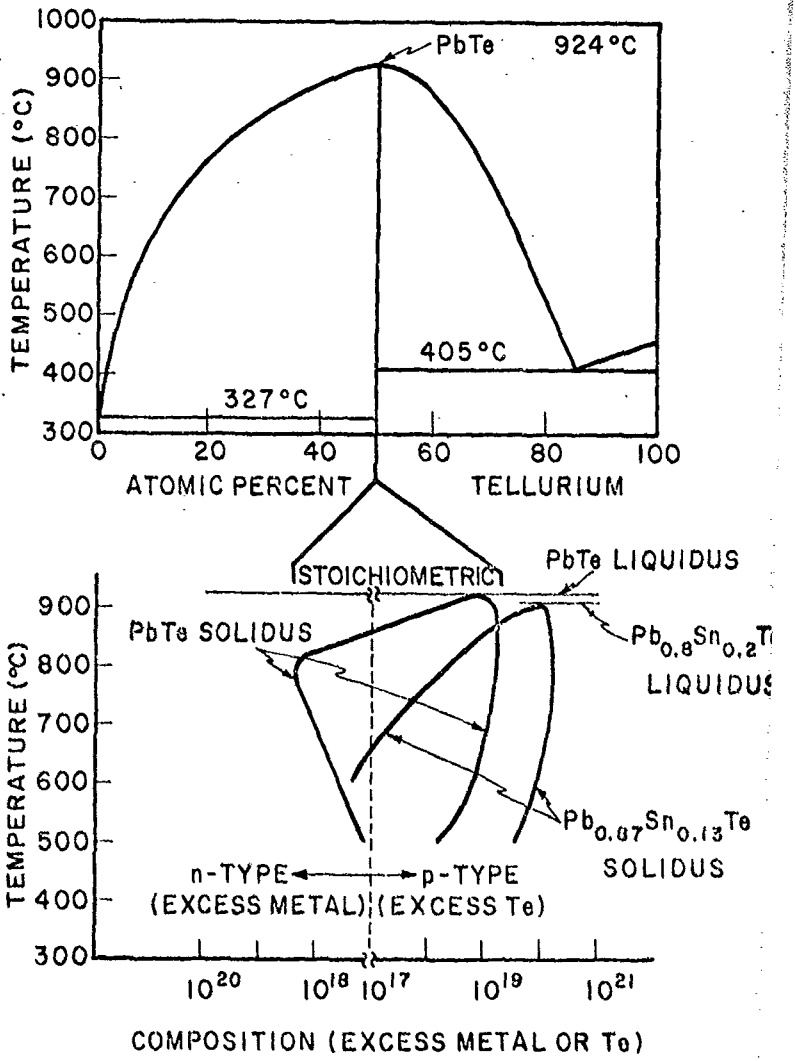

Figure 5. Temperature-composition phase diagram for Pb-Te binary system. The lower diagram in an expansion in the vicinity of the stoichiometric composition.[27]

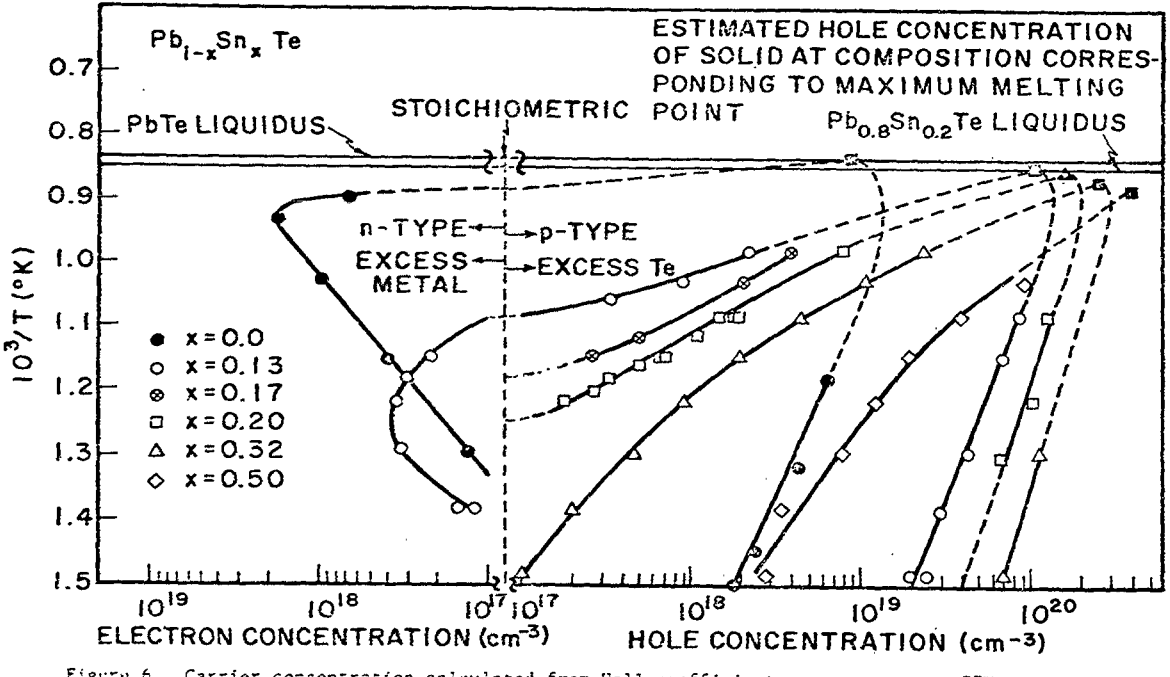

Figure 6. Carrier concentration calculated from Hall coefficient measurements at 77K as a function of isothermal annealing temperature for several $Pb_{1-x}Sn_xTe$ alloying compositions.[27]

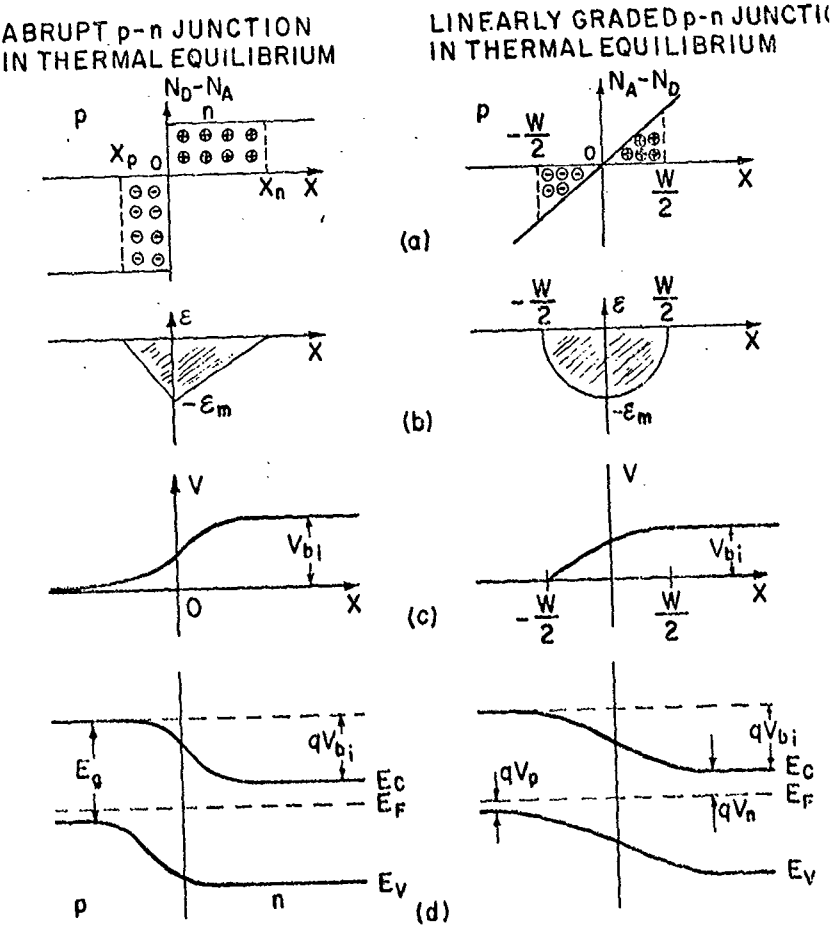

Figure 7. Schematic diagram of (a) impurity distribution, (b) field distribution, (c) potential, and (d) energy for abrupt and graded p-n junctions in thermal equilibrium.[34]

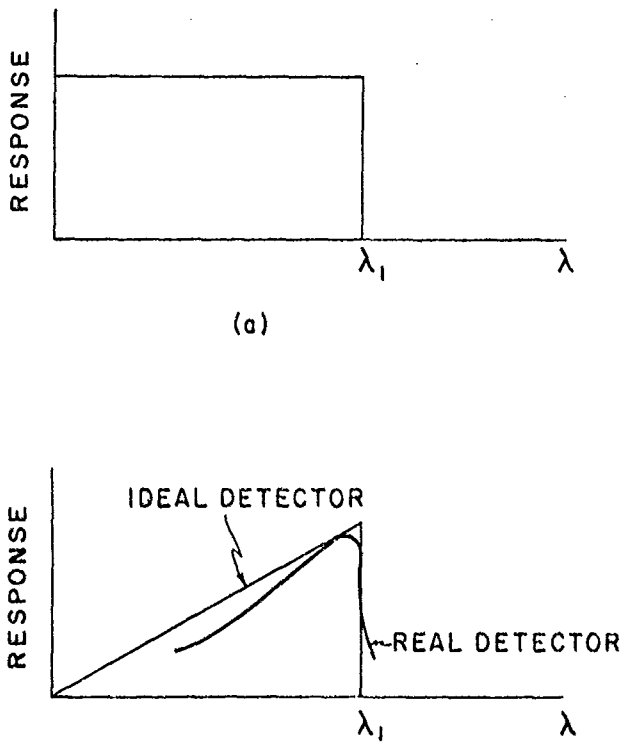

Figure 8. Relative spectral response of a photon detector with (a) constants number of incident photons and (b) constant energy incident flux.

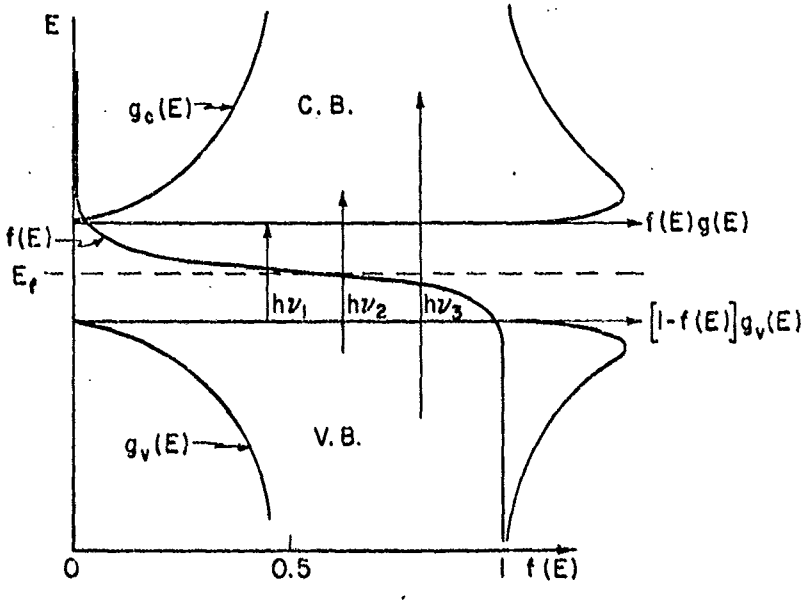

Figure 9. Schematic band diagram for semiconductor. The density of states and the probability functions are shown along with some possible optical transitions.

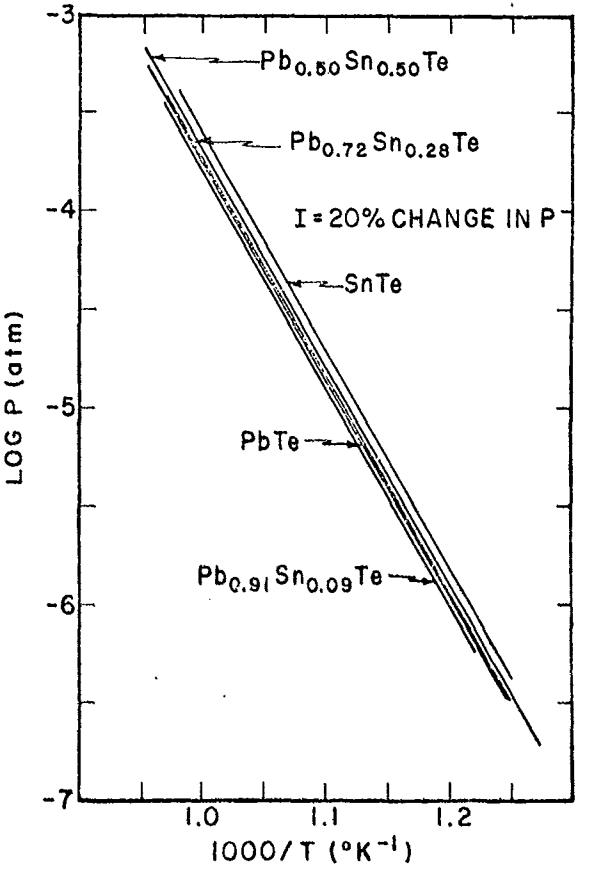

Figure 10. Calculated total vapor pressure for (Pb,Sn)Te alloys.[43]

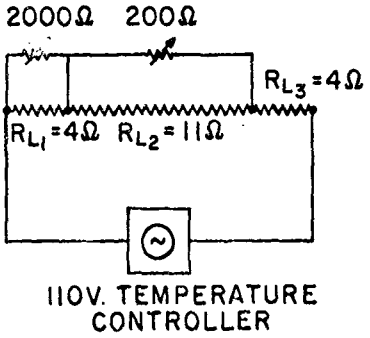

(a)

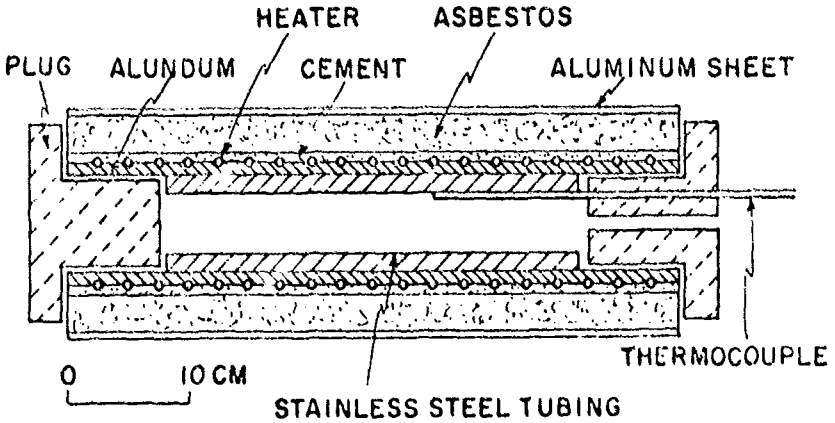

(b)

Figure 11. Home made crystal growth oven configuration. (a) Wiring diagram. (b) Furnace cross section.

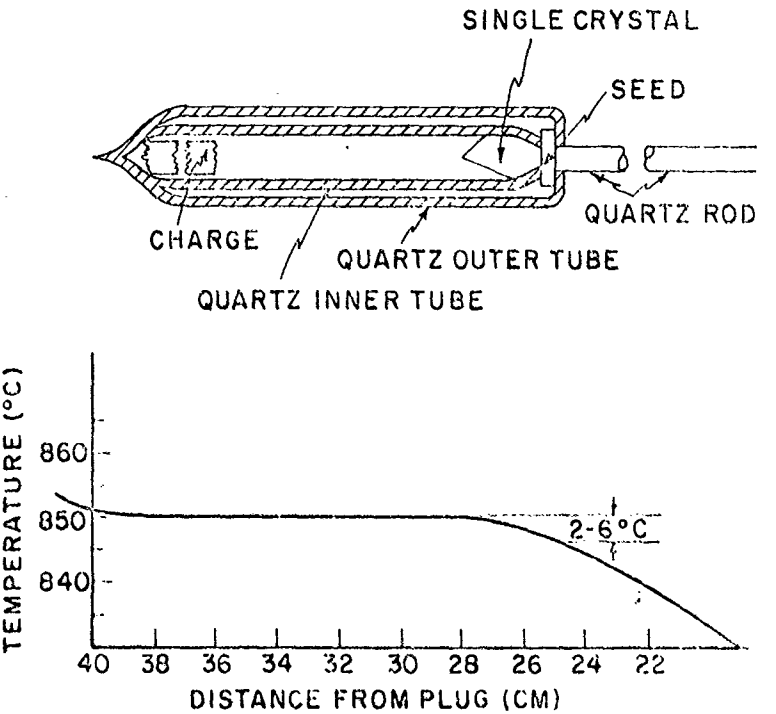

Figure 12. Growth ampoule and temperature profile for vapor transport growth of (Pb, Sn)Te.

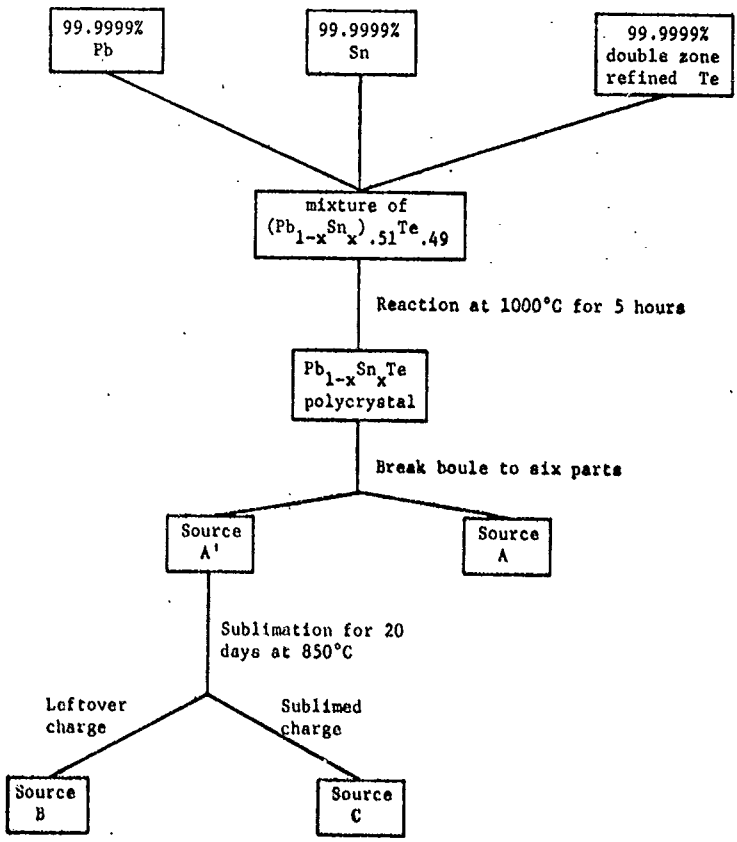

Figure 13. Source preparation diagram

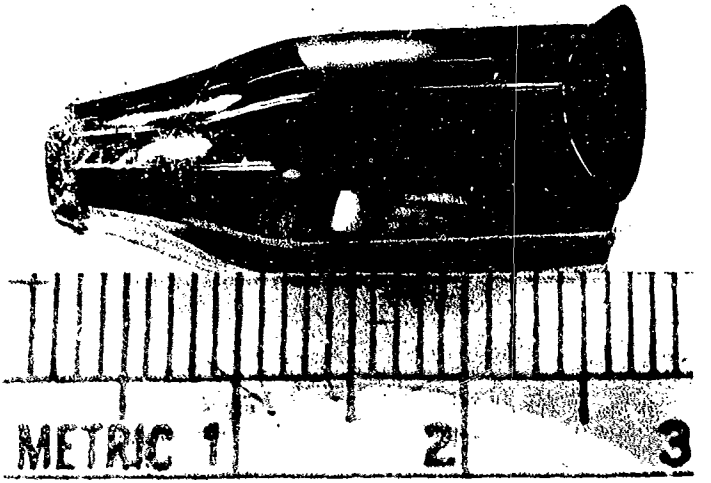

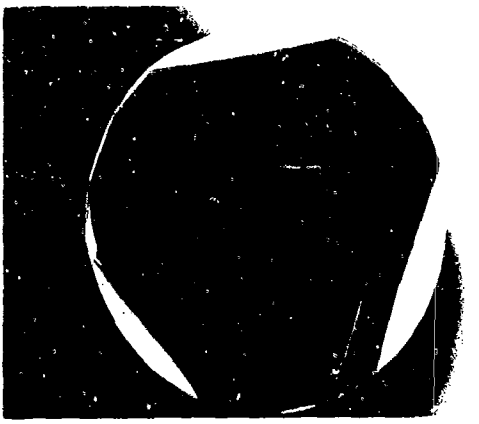

Figure 4. A typical (Pb,Sn)Te crystal.

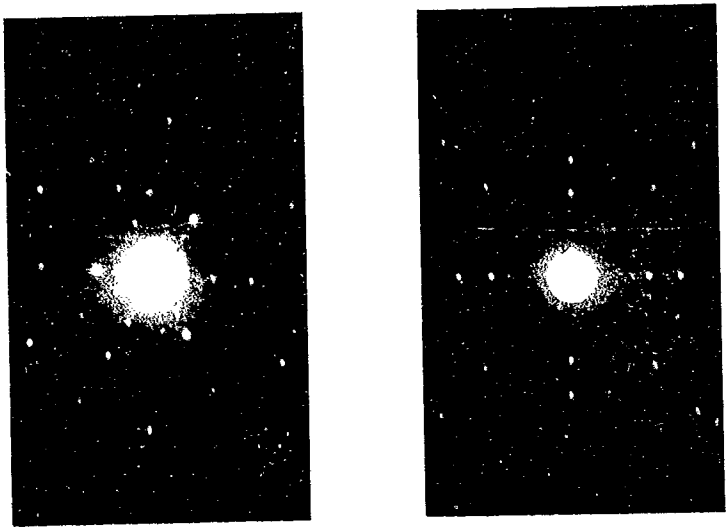

(a) (b)

Figure 5. Laue photographs of (a) (111) facet and (b) (100) facet.

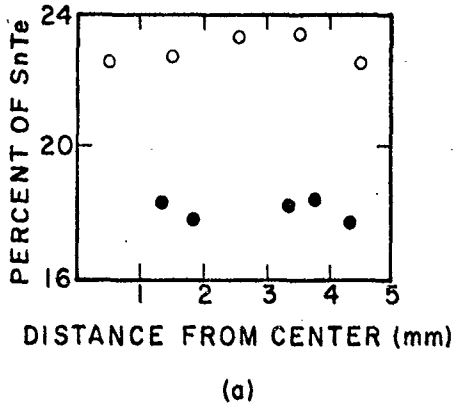

(a)

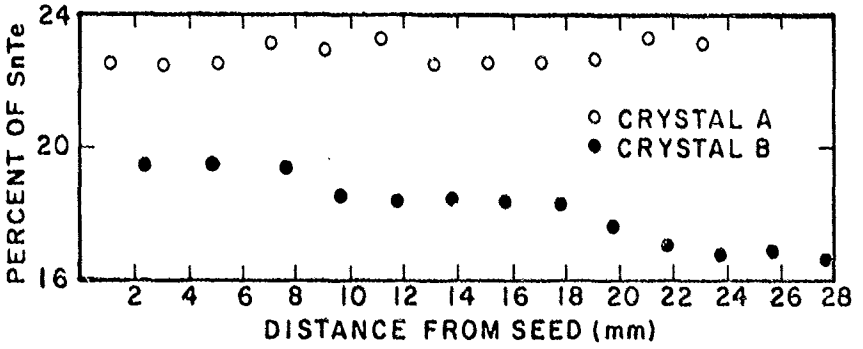

(b)

Figure 16. SnTe content in two (Pb,Sn)Te crystals. (a) crosswise and (b) lengthwise. The source of crystal B was completely transported.

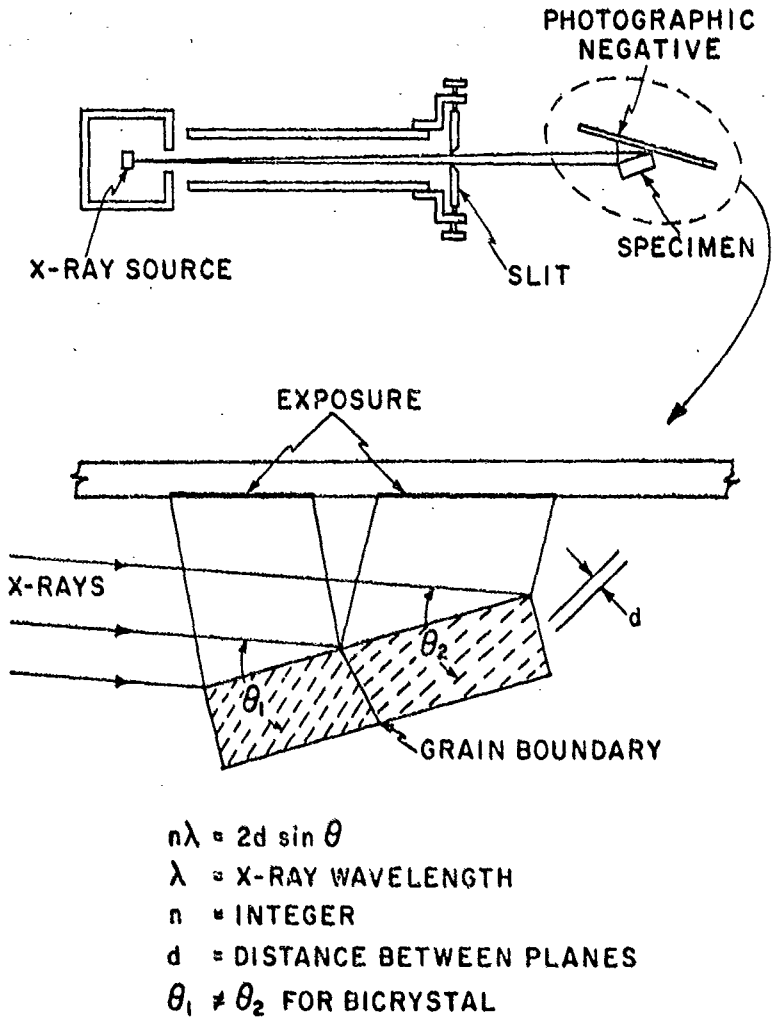

Figure 17.Berg-Barrett Back Reflection X-Ray camera geometry.

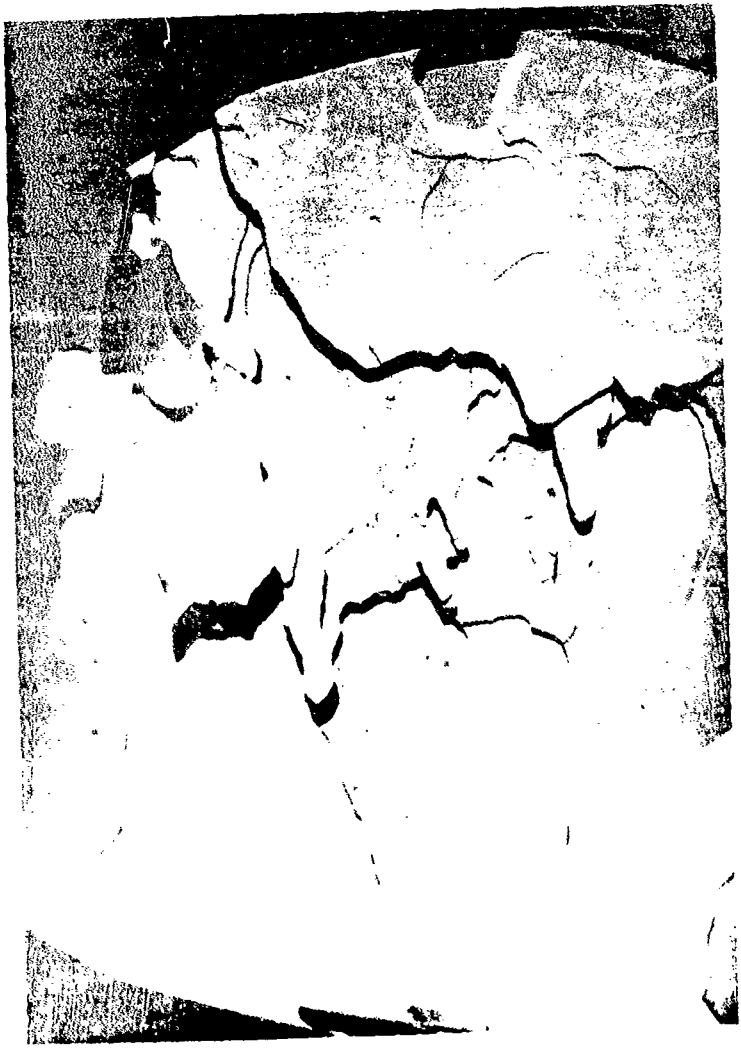

...pograph (X25) reveals low angle boundaries

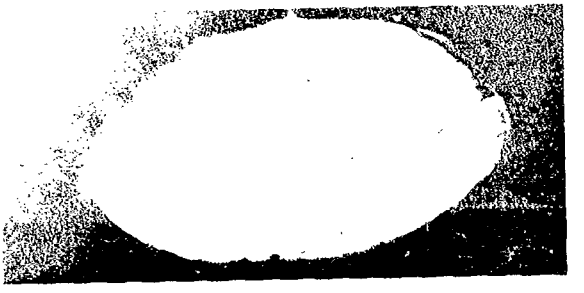

(a)

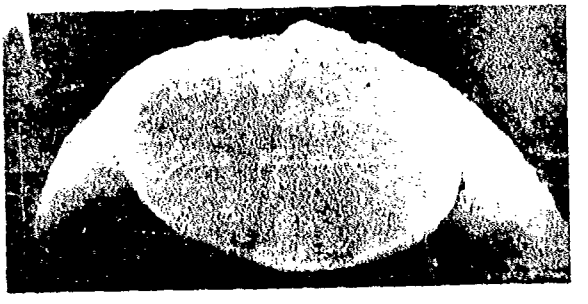

(b)

Figure 7. [illegible] topographs (X12) of (100) facet. (a) [illegible] (b) after surface was etched.

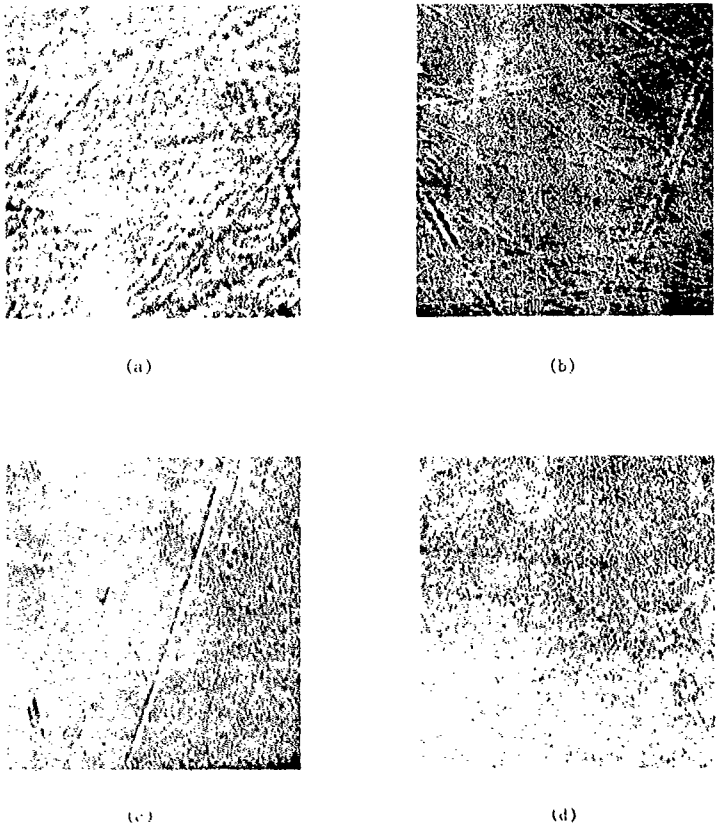

Figure 2. [illegible] topographs (X20) of a lapped water [illegible] surface [illegible] etched to remove (a) 20 μm, (b) 45 [illegible], (c) 70 μm, [illegible]

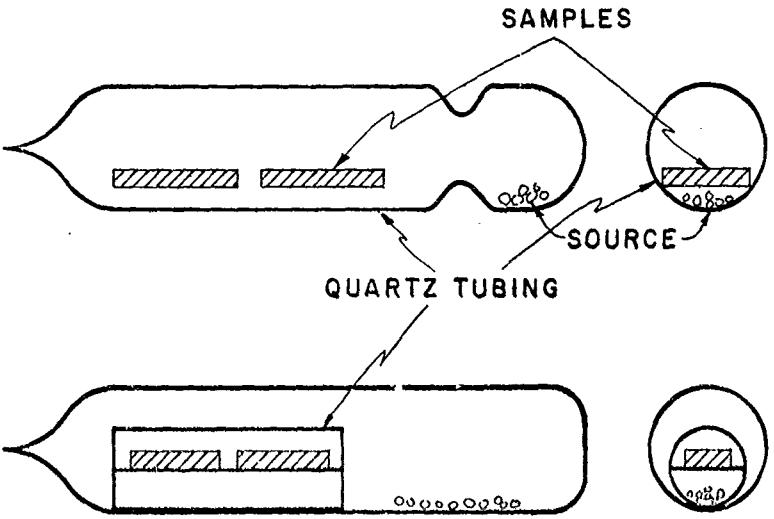

Figure 21. Schematic diagram of two commonly used diffusion ampoules.

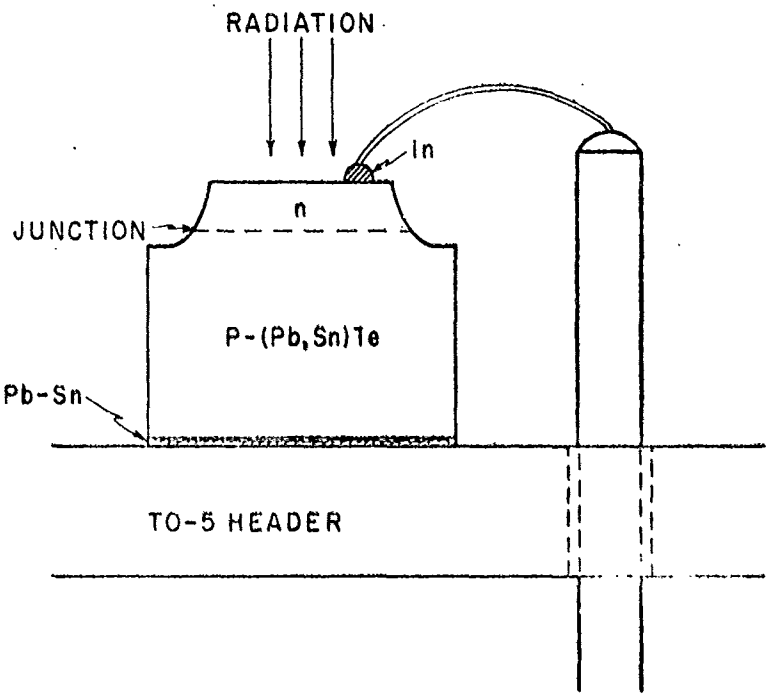

Figure 22. Schematic diagram of (Pb,Sn)Te photodiode.

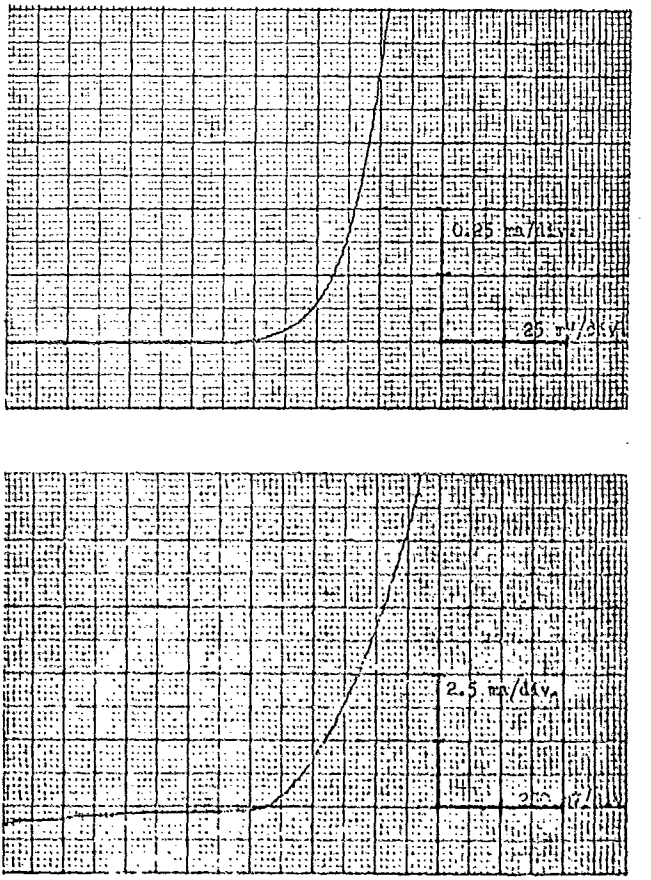

Figure 23. Two typical I-V curves of Lead-Tin Telluride diodes.

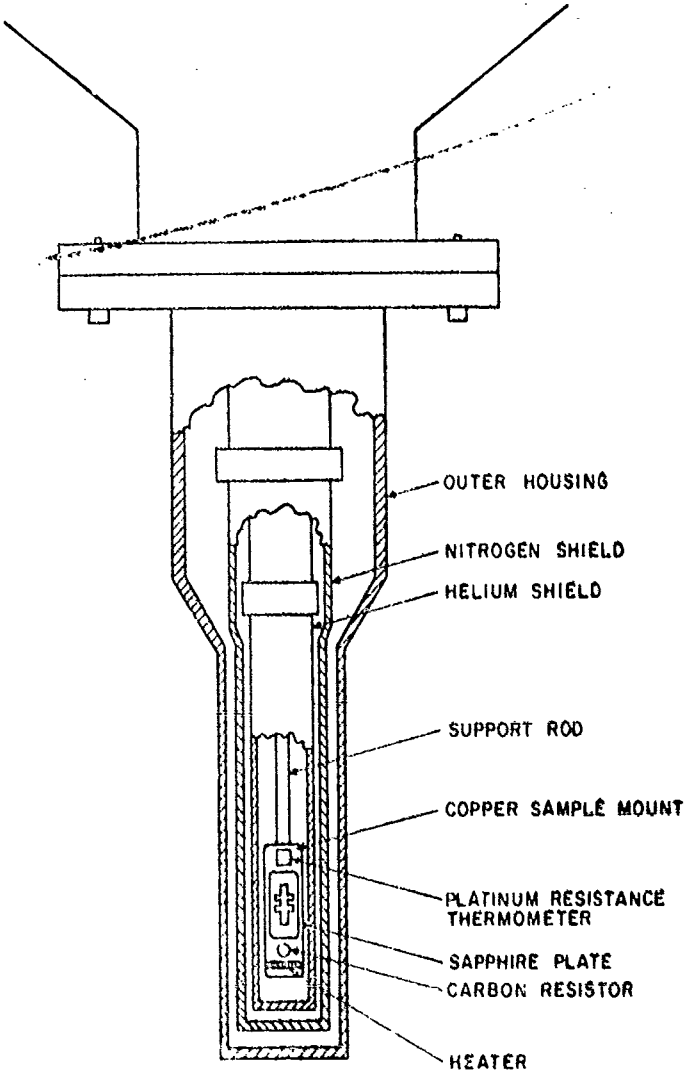

Figure 24. Hofmann Cryostat

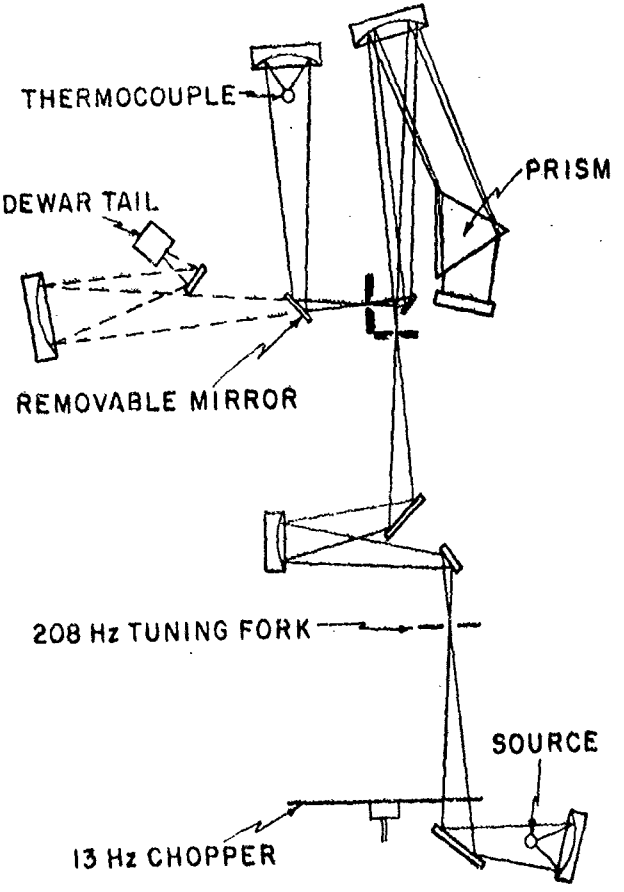

Figure 25. Optics of the Perkin-Elmer Model 13 spectrometer.

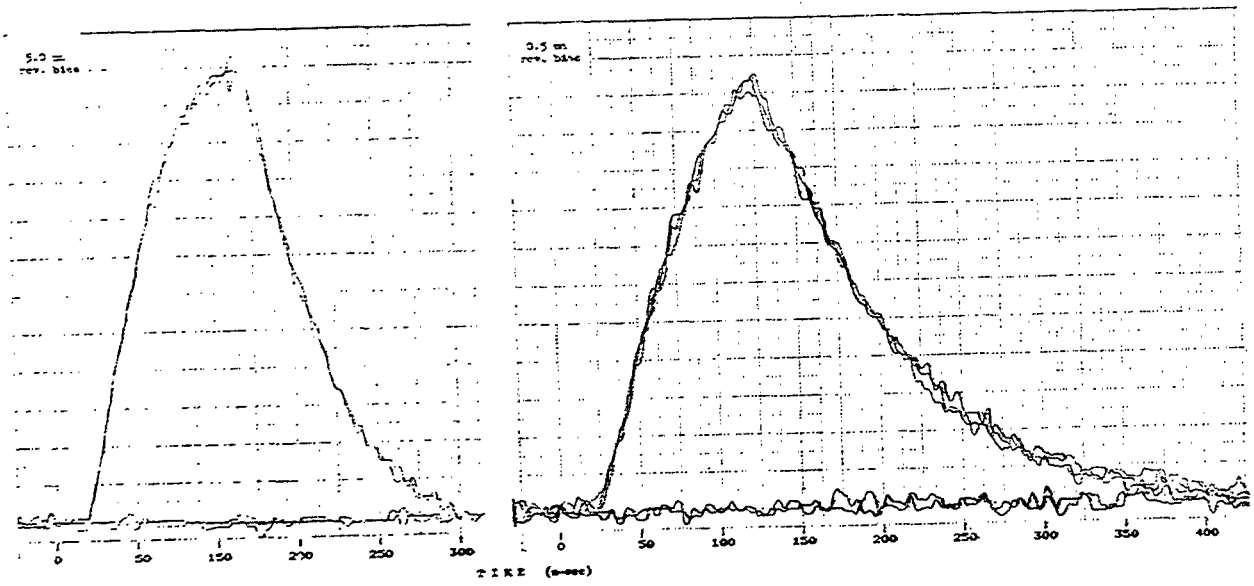

Figure 26. Two traces of time response of a (Pb,Sn)Te detector. The decay is faster when the reverse bias is higher.

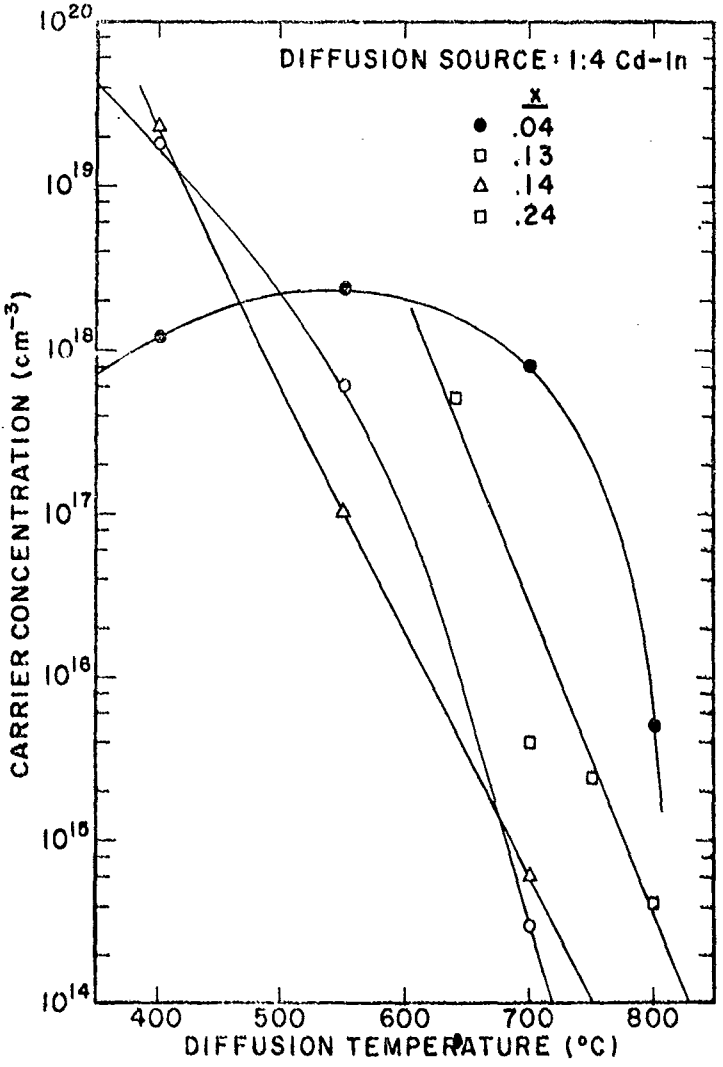

Figure 27. Carrier concentration at 77K as a function of diffusion temperature.

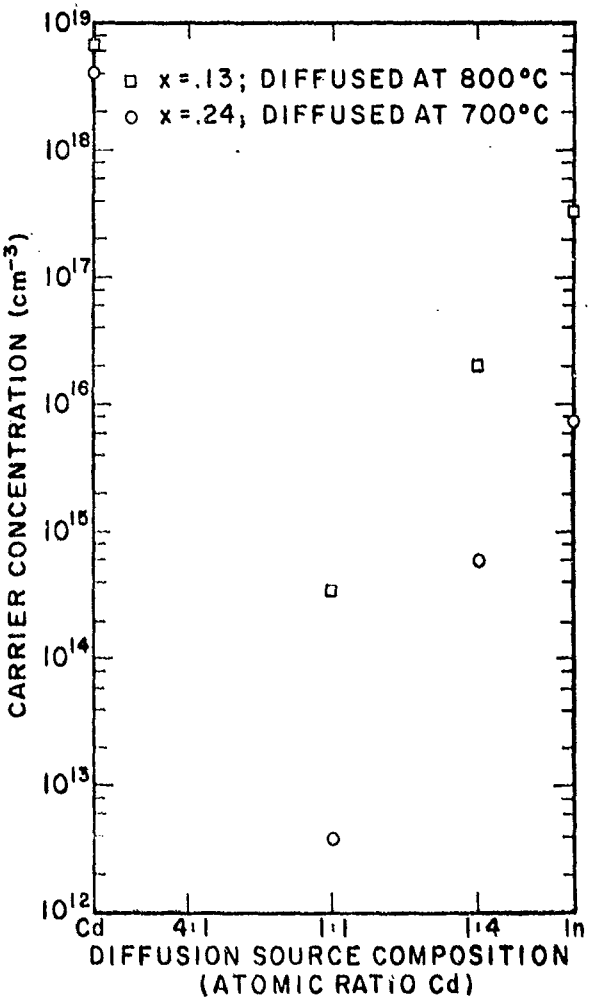

Figure 28. The dependence of the carrier concentration (at 77K) on the diffusion source composition.

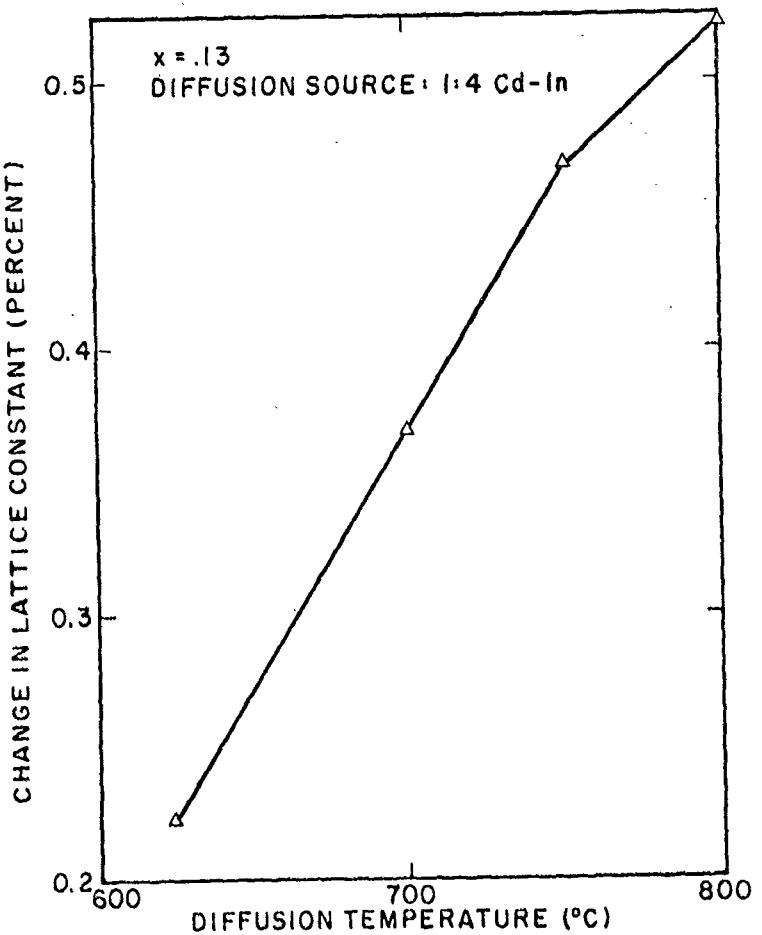

Figure 29. Change in lattice constant as a result of Cd-In diffusion.

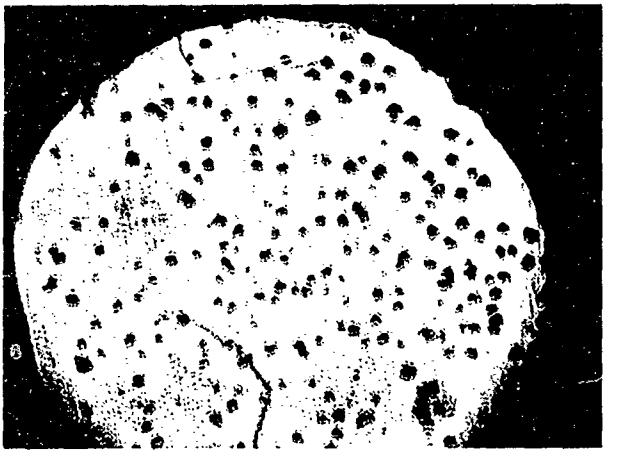

(a)

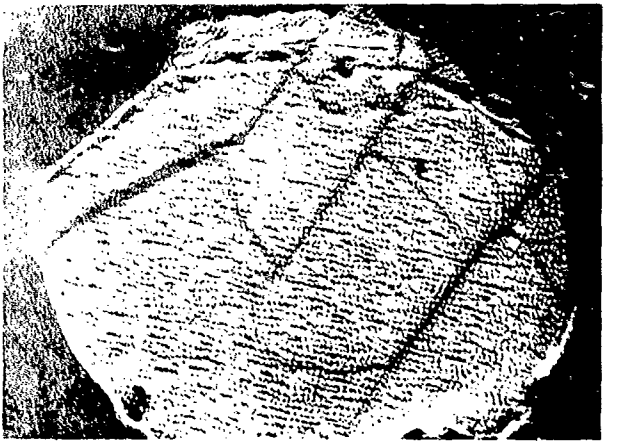

(b)

Figure 2. X-Ray topograph (X10) of a diffused (Pb,Sn)Te. (a) diffusion into (111) surface, and (b) diffusion into (100) surface. Diffusion conditions are the same as in the previous figure.

(a)

(b)

Figure 7. Electron micrograph of (a) diffused (Pb,Sn)Te and (b) typical pit. The sample was diffused with Cd-In at 750°C, and the surface was etched before pictures were taken.

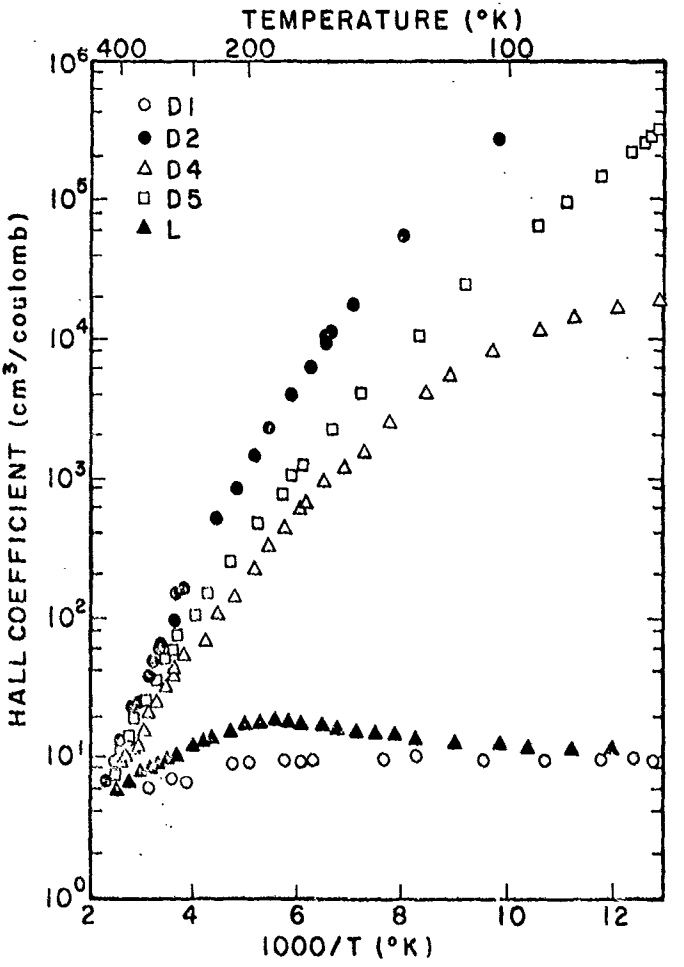

Figure 32. Hall coefficient as a function of reciprocal temperature for the samples listed in Table 3 between 85K and 400K.

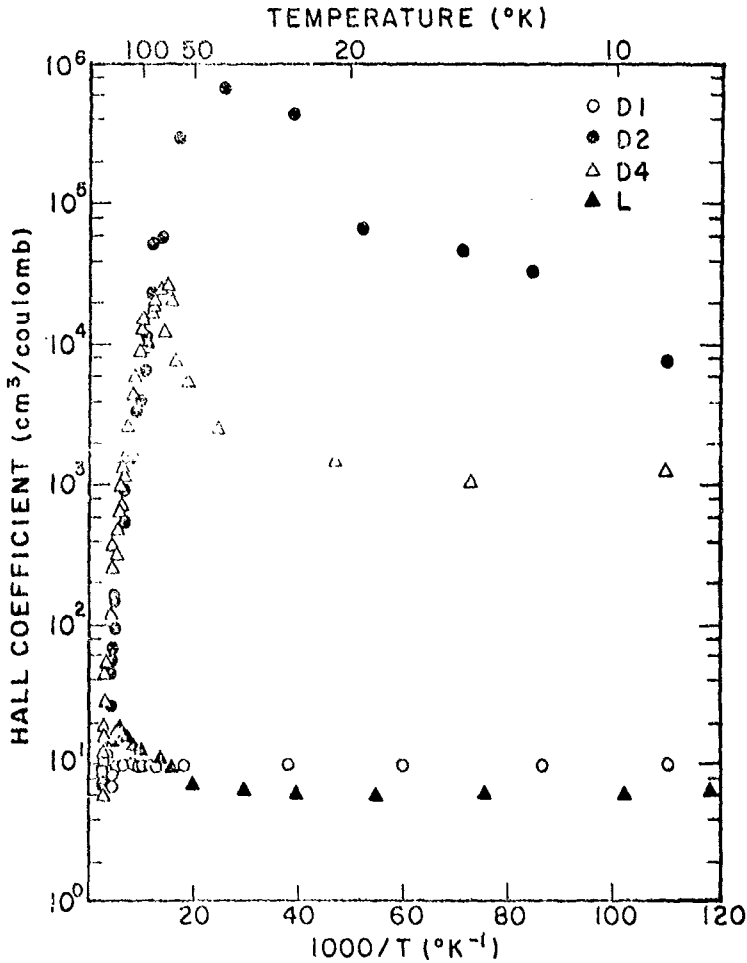

Figure 33. Hall coefficient as a function of reciprocal temperature for the samples listed in Table 3 between 8K and 120K.

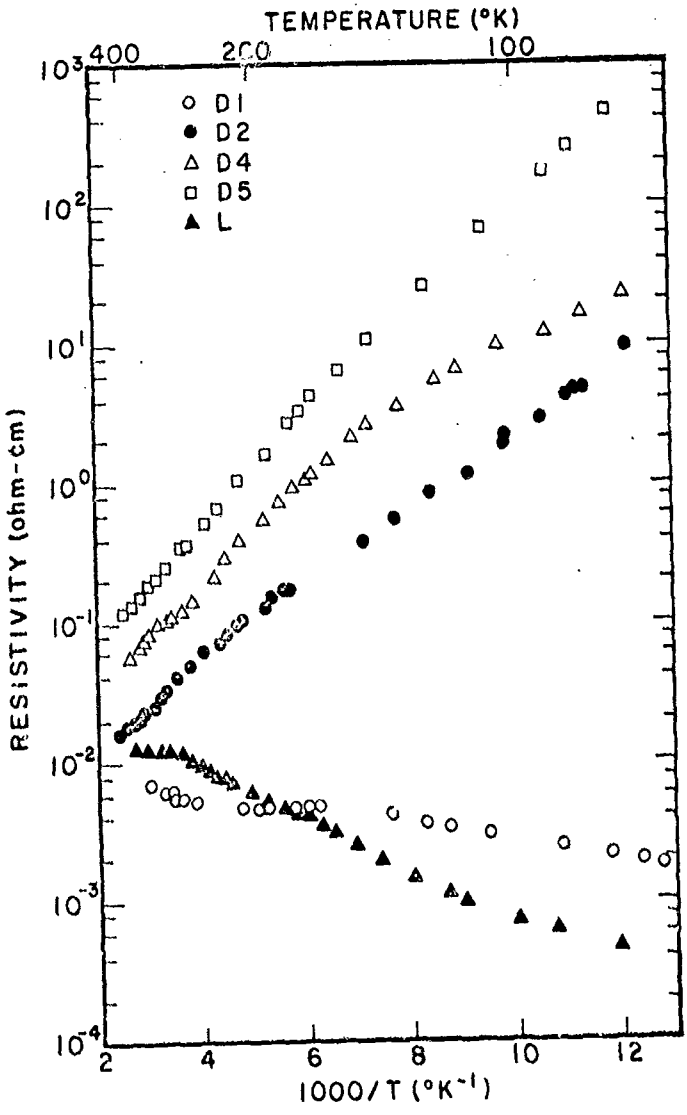

Figure 34. Resistivity as a function of reciprocal temperature for the sample listed in Table 3 between 85K and 400K.

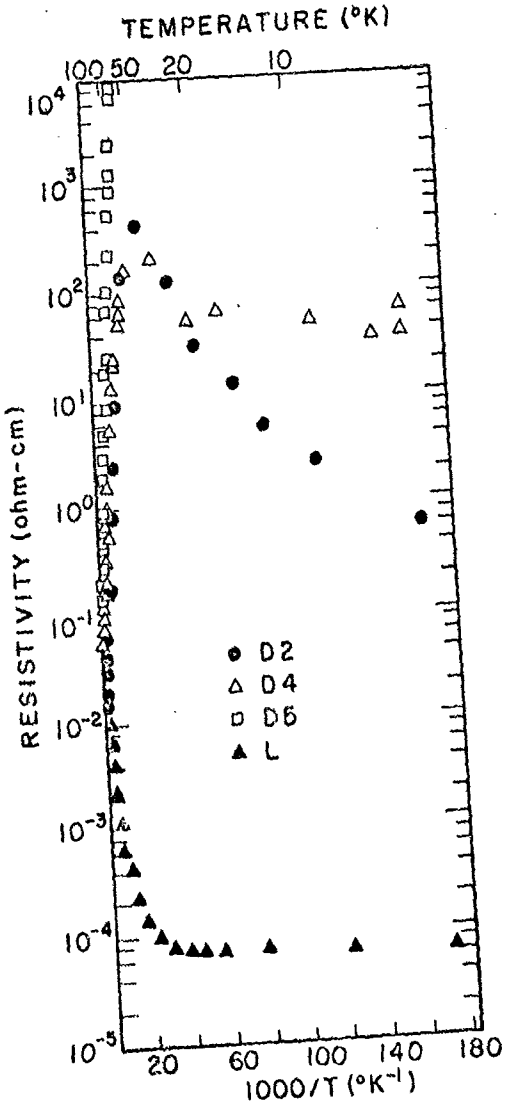

Figure 35. Resistivity as a function of reciprocal temperature for the samples listed in Table 3 between 5K and 110K.

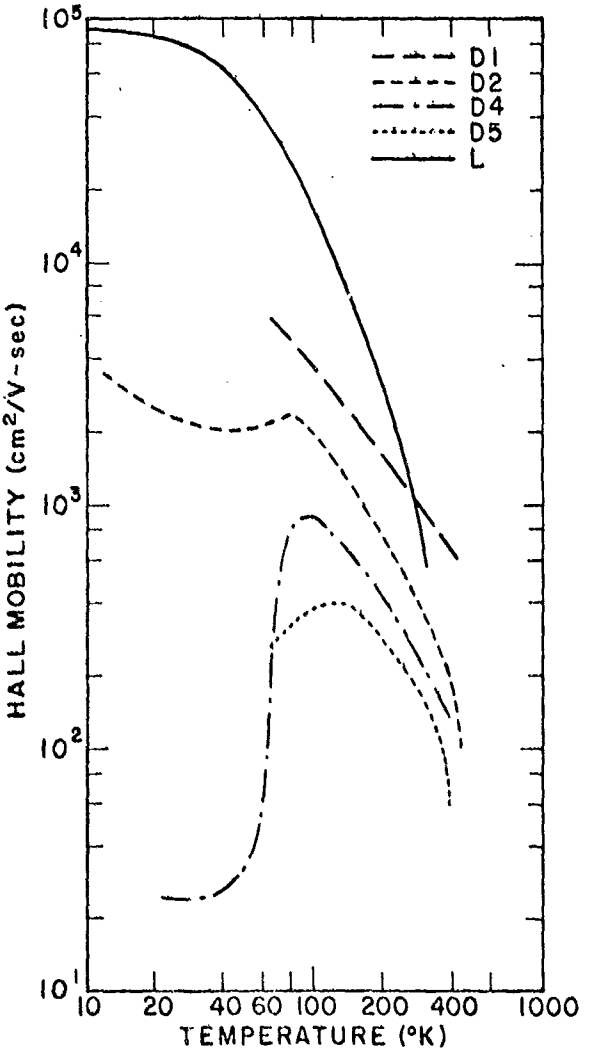

Figure 36. Hall mobility as a function of temperature for the samples listed in Table 3 between 10K and 400K.

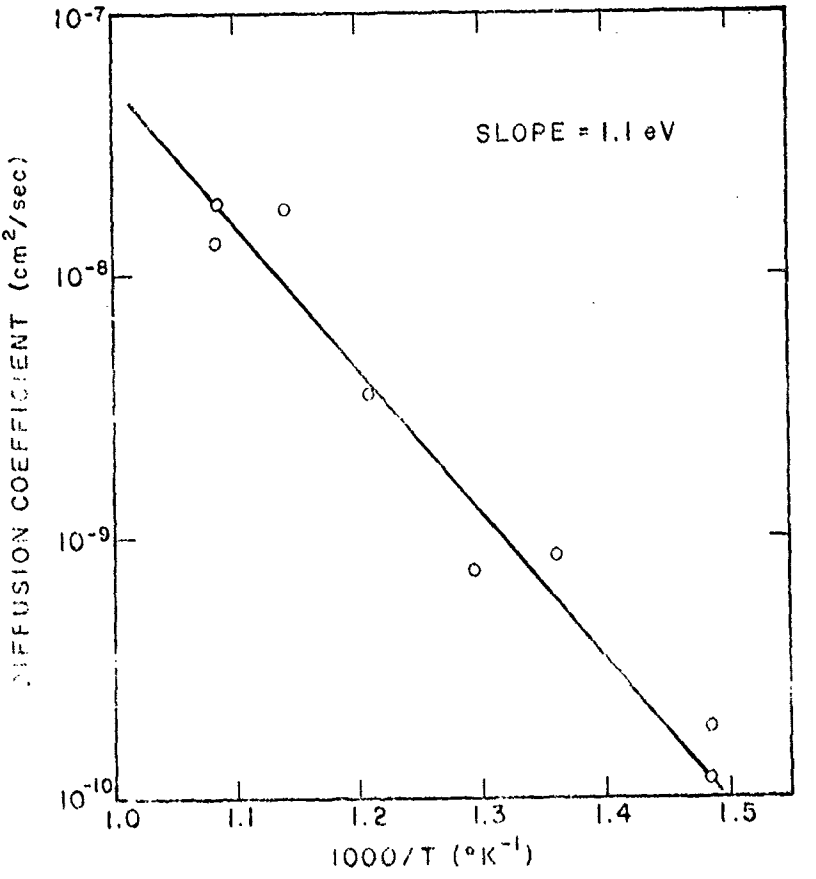

Figure 37. Diffusion coefficient as a function of reciprocal diffusion temperature for Cd diffusion in $Pb_{0.79}Sn_{0.8}Te$. The slope is the diffusion activation energy.

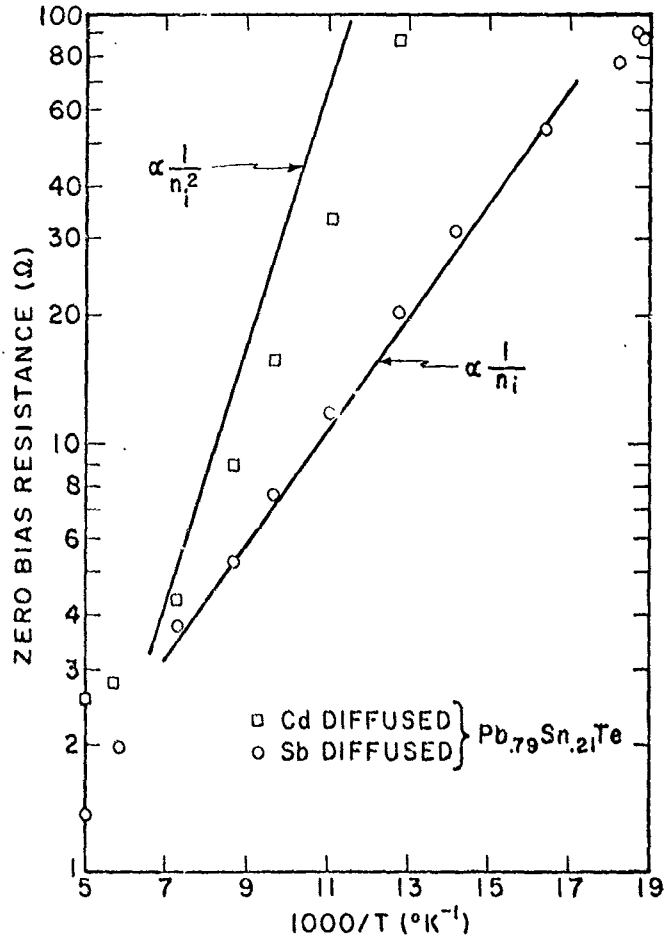

Figure 38. Zero Bias resistance of two diodes as a function of reciprocal temperature. Generation-recombination current is dominant in the Sb diffused diode while diffusion current is major in the Cd diffused diodes.

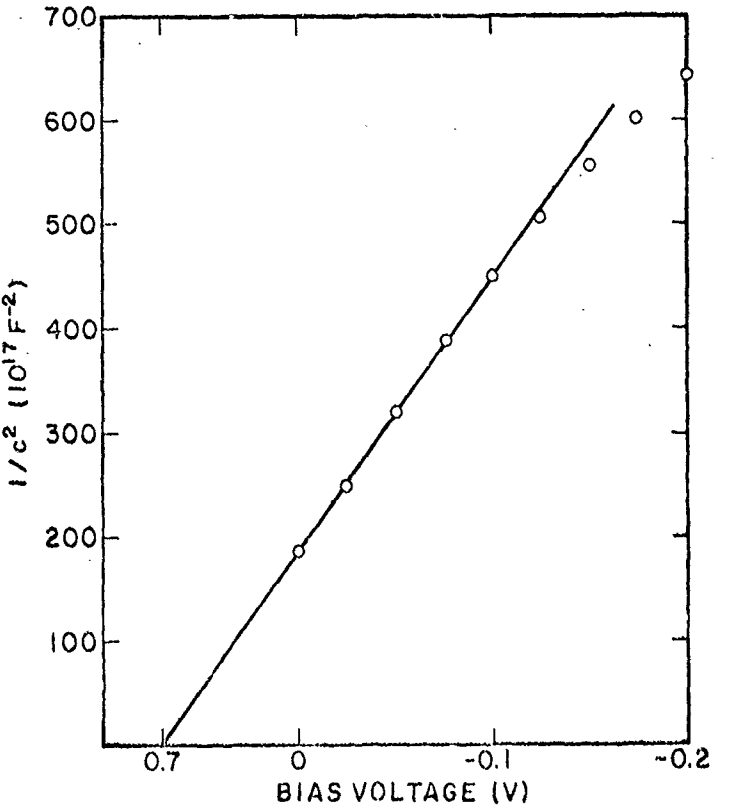

Figure 39. Measured capacitance as a function of reverse bias for Cd diffused diode at 77K. The junction obeys the one-sided abrupt model with a built-in voltage of 0.7 V.

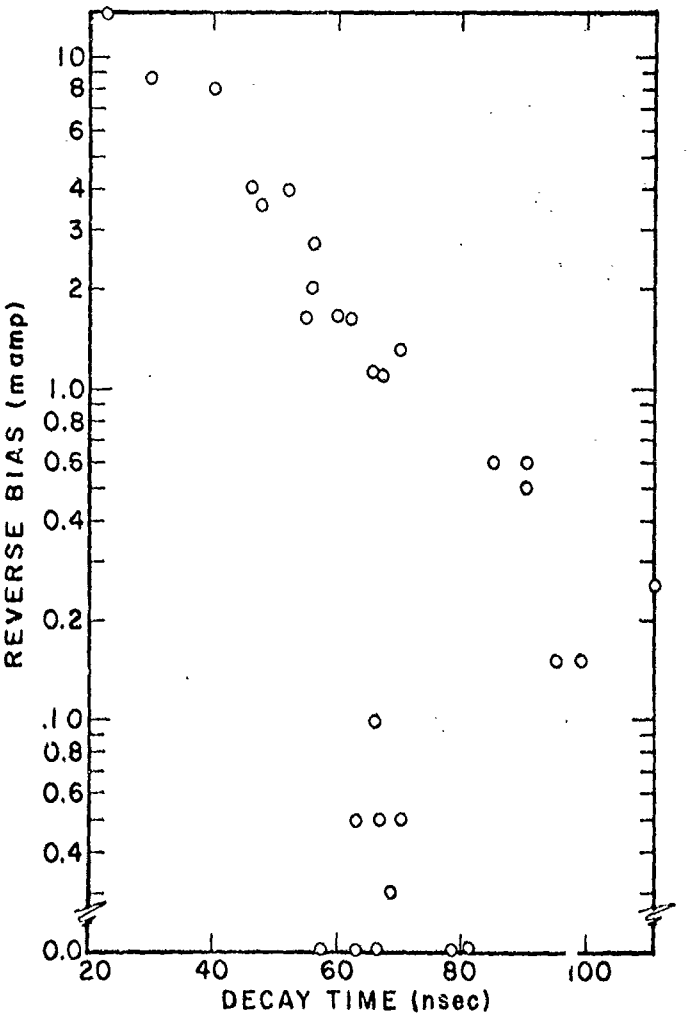

Figure 40. Decay time as a function of bias. Since the response time in RC limited, the diode capacitance could be obtained from the above results.

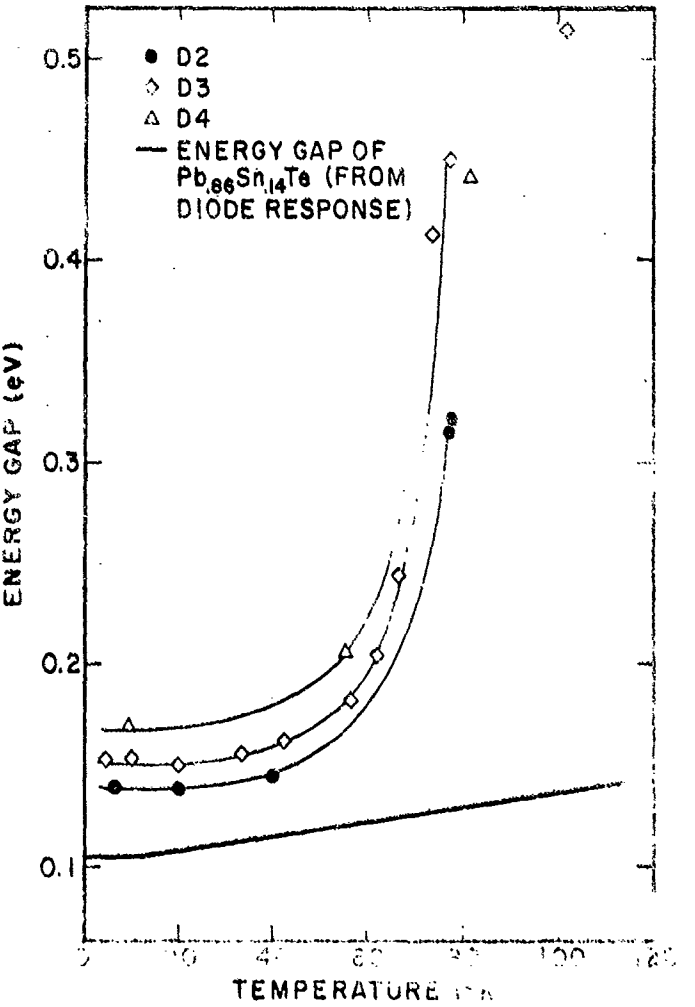

Figure 41. Optical energy gap as a function of temperature for the samples listed in Table 5.

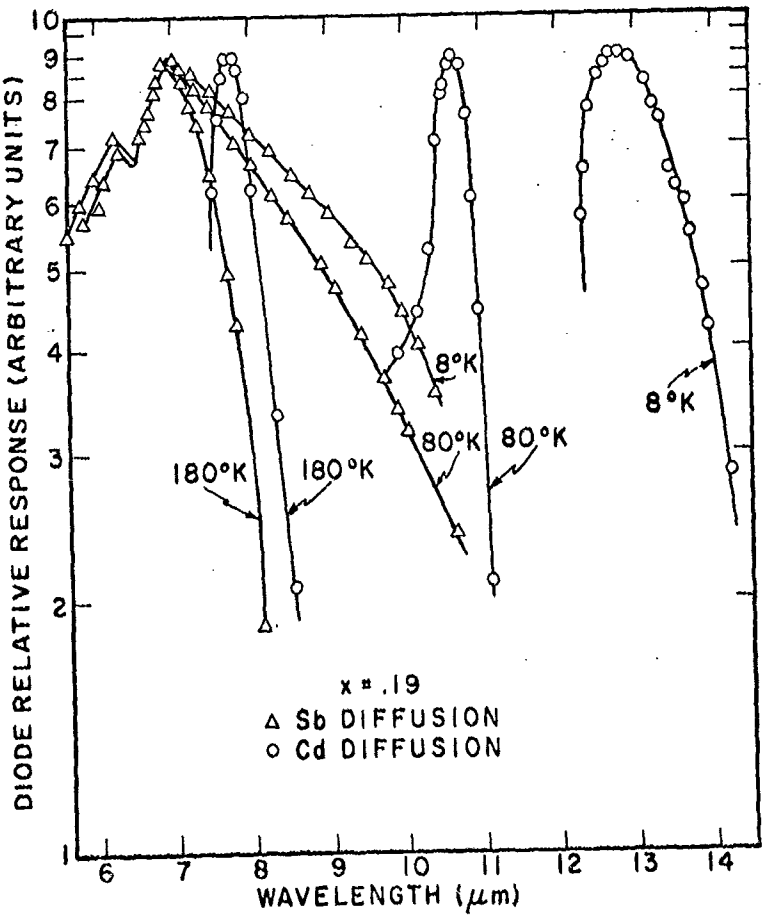

Figure 42. Relative response of Sb and Cd diffused $Pb_{0.81}Sn_{0.19}Te$ photodiodes at three selected temperatures. The curves were normalized to have the same peak hight.

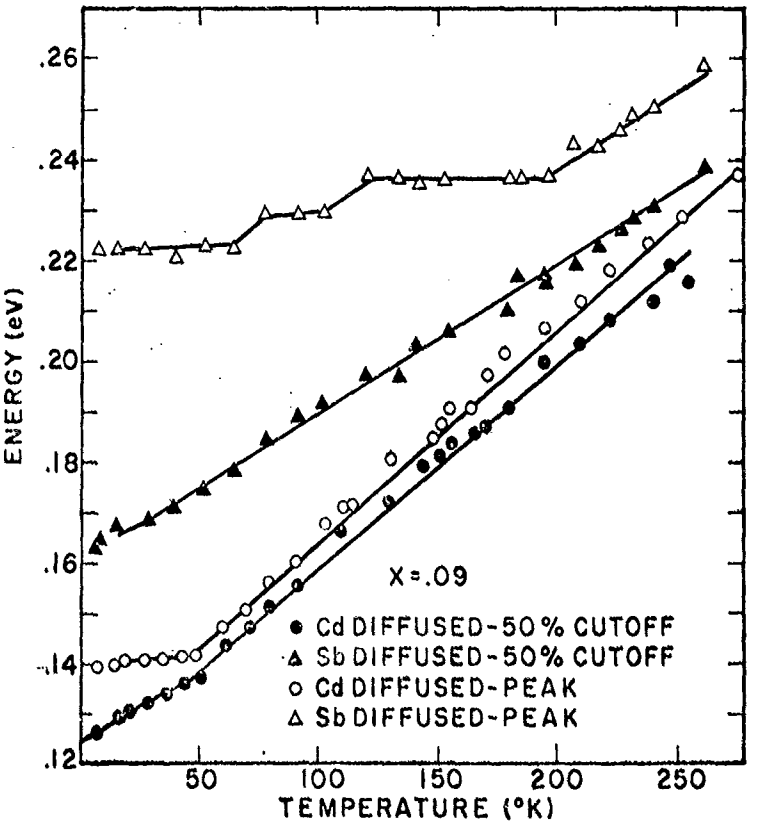

Figure 43. Cutoff and peak of response energy as a function of temperature for Cd and Sb diffused $Pb_{0.91}Sn_{0.09}Te$ photodiodes.

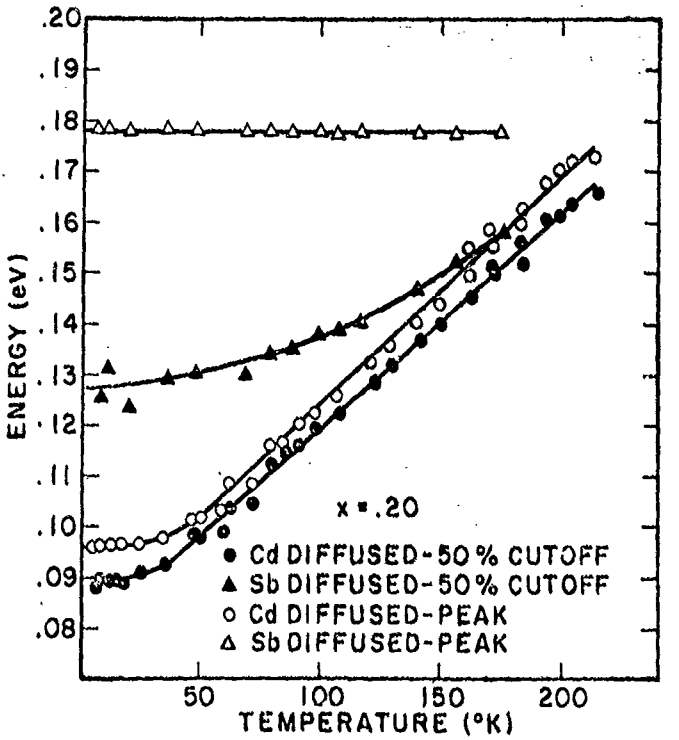

Figure 44. Cutoff and response peak energy as a function of temperature for Cd and Sb diffused $Pb_{0.80}Sn_{0.20}Te$ photodiodes.

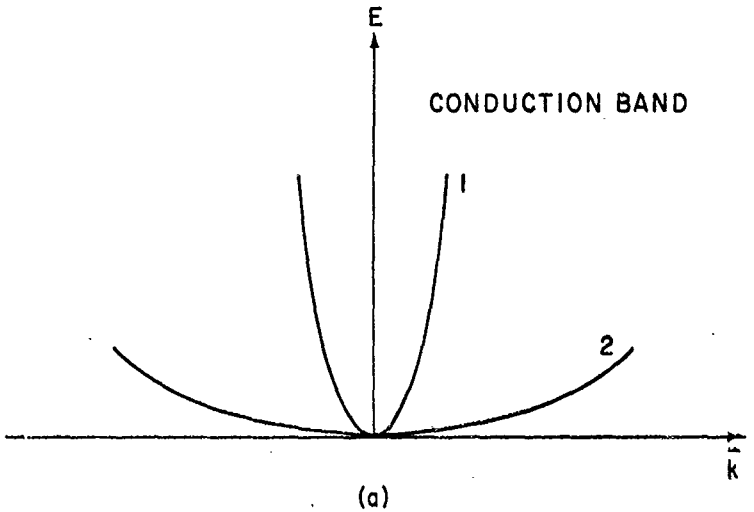

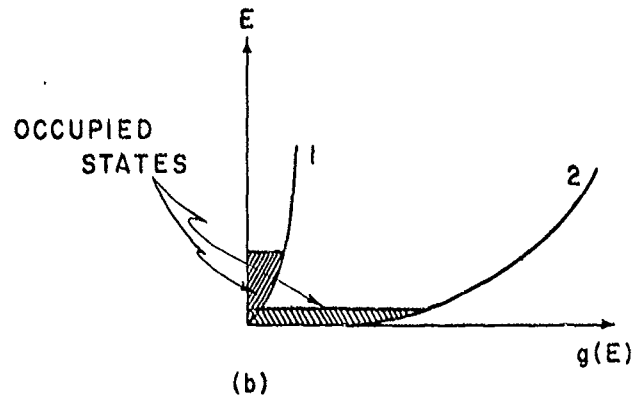

Figure 45. Schematic diagram of (a) E-$\vec{k}$ dispersion relations and (b) the corresponding density of states functions at 0 K. Curve 1 represents smaller effective mass than curve 2.

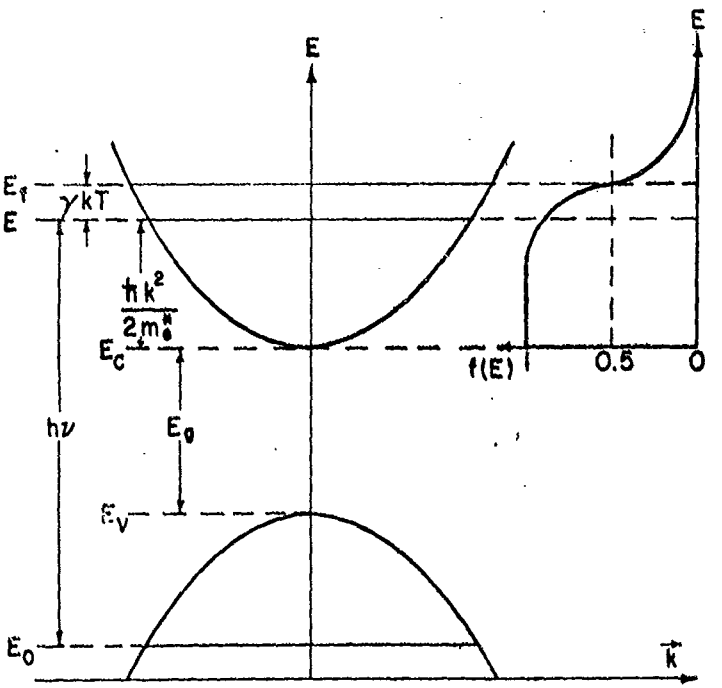

Figure 46. Energy-wave vector diagram for degenerate n-type (Pb,Sn)Te. The Fermi level, E_f, is in the conduction band, E_g is the energy gap and hν is in the minimum photon energy required for direct transition.

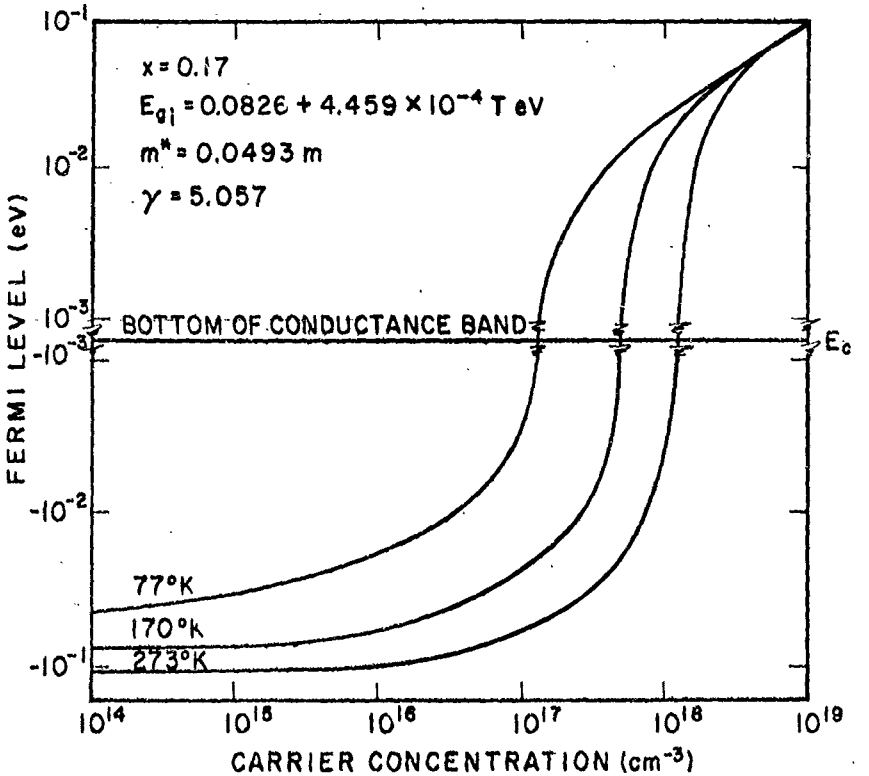

Figure 47. Calculated Fermi energy as a function of carrier concentration for $Pb_{0.83}Sn_{0.17}Te$.

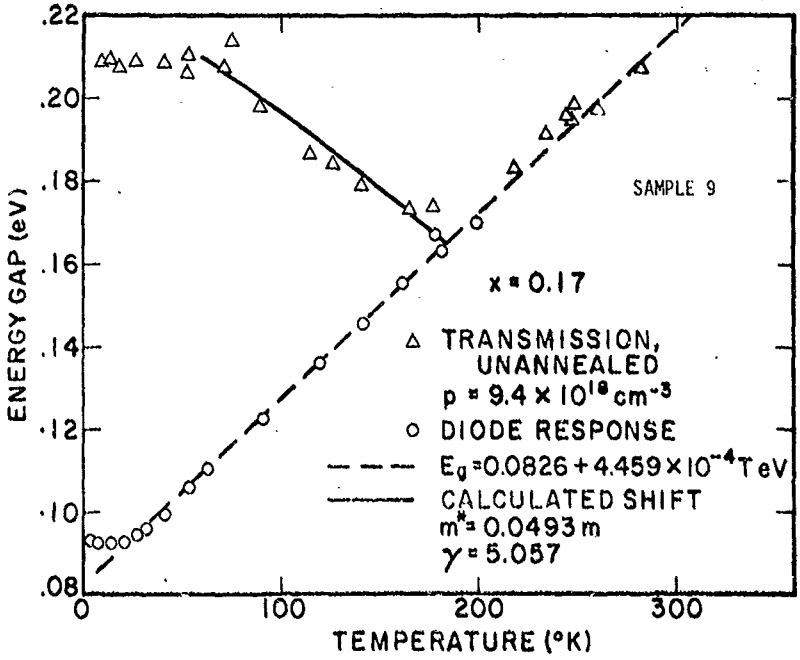

Figure 48. Experimental and calculated absorption edge shift as a function of temperature for degenerate $Pb_{0.83}Sn_{0.17}Te$. The nondegenerate optical gap is shown for comparison.

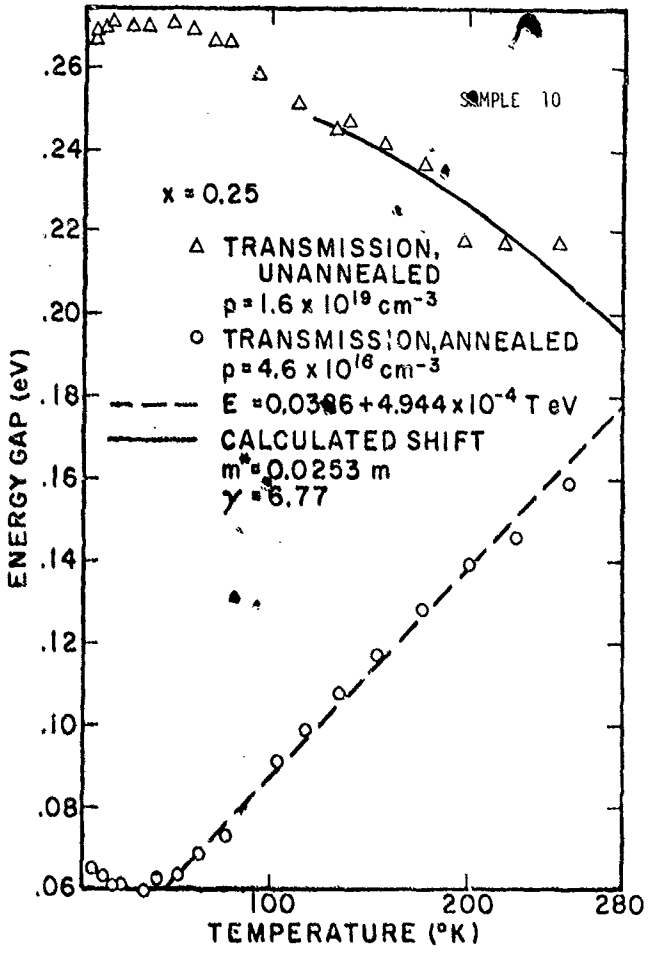

Figure 49. Experimental and calculated absorption edge shift as a function of temperature for degenerate $Pb_{0.75}Sn_{0.25}Te$. The nondegenerate optical gap is shown for comparison.

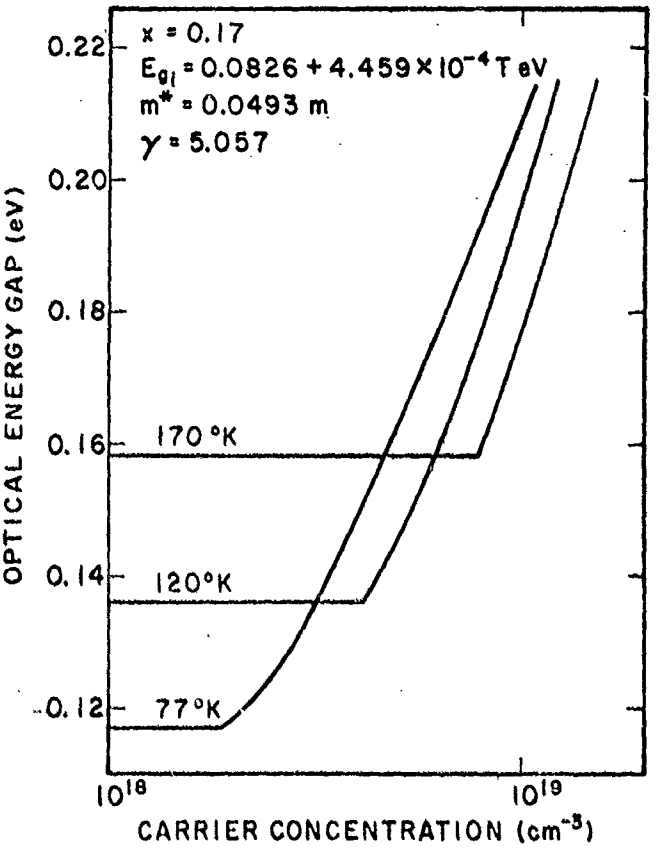

Figure 50. Calculated absorption edge shift as a function of carrier concentration for degenerate $Pb_{0.83}Sn_{0.17}Te$ at three selected temperatures.

REFERENCES

1. I. Melngailis and T. C. Harman, in Semiconductors and Semimetals, Vol. 5, edited by R. K. Willardson and A. C. Beer (Academic Press, New York, 1970).

2. T. C. Harman and I. Melngailis, in Applied Solid State Science, Vol. 4, edited by (Academic Press, New York, 1974).

3. A. Lockwood, Ph.D. Thesis, (Syracuse University, Syracuse, New York, 1972).

4. E. Burstein, Phys. Rev. 93, 632 (1954).

5. E. O. Kane, J. Phys. Chem. Solids, 1, 249 (1957).

6. J. A. Kafalas, R. F. Brebrick, and A. J. Strauss, Appl. Phys. Lett. 4, 93 (1964).

7. M. Balkanski, J. of Luminescence 7, 451 (1973).

8. N. R. Short, Brit. J. Appl. Phys., Series II, 1, 129 (1968).

9. R. F. Bias and J. R. Dixon, J. Appl. Phys., 40, 1918 (1969).

10. A. R. Calawa, T. C. Harman, M Finn, and P. Youtz, Trans. Met. Soc. AIME 242, 374 (1968).

11. J. W. Waynes and R. K. Willardson, ibid., p. 366.

12. J. O. Dimmock, I. Melngailis, and A. J. Straus, Phys. Rev. Lett. 16, 1163 (1966).

13. L. Esaki, Proc. Int. Conf. Phys. of Semiconductors, Kyoto, J. Phys. Soc. Jap. 21 Suppl., 589 (1966).

14. A. F. Gibson, Proc. Phys. Soc., London, B 65, 378 (1952).

15. D. G. Avery, Proc. Phys. Soc., London, B 67, 2 (1954).

16. P. M. Nikolic, Brit. J. Appl. Phys. 18, 897 (1967).

17. R. N. Tauber, A. A. Machonis, and I. B. Cadoff, J. Appl. Phys. 37, 4855 (1966).

18. R. M. Tauber and I. B. Cadoff, J. Appl. Phys., 38, 3714 (1967).

19. I. Melngailis and T. C. Harman, Appl. Phys. Lett., 13, 180 (1968).

20. I. Melngailis and A. R. Calawa, Appl. Phys. Lett., 9, 304 (1966).

21. J. F. Butler, A. R. Calawa, and T. C. Harman, Appl. Phys. Lett. 9, 427 (1966).

22. J.F. Butler, T. C. Harman, Appl. Phys. Lett. 12, 942 (1968).

23. J. R. Dixon and R. F. Bis, Phys. Rev. 176, 942 (1968).

24. Y. W. Tung and M. L. Cohen, Phys. Rev. 180, 823 (1969).

25. S. H. Wemple, Phys. Lett. 45A, 401 (1973).

26. Y. W. Tsang and M. L. Cohen, Phys. Rev. B3, 1254 (1971).

27. T. C. Harman, J. Nonmetals 1, 183 (1973).

28. A. J. Strauss and R. F. Brebrick, Journal De Physique C4, 21 (1968).

29. R. F. Brebrick and R. S. Olgaier, J. Chem. Phys. 32, 1826 (1960).

30. J. S. Blakemore, Semiconductor Statistics, (Pergamon Press, Oxford, 1962).

31. T. C. Harman, J. M. Honig, and B. M. Tarmy, J. Phys. Chem. Solids 24, 835 (1963).

32. T. C. Harman, A. R. Calawa, I. Melngailis, and J. O. Dimmock, Appl. Phys. Lett. 14, 333 (1969).

33. See, for example, B. I. Boltaks, Diffusion in Semiconductors, (Academic Press, New York, 1963).

34. See, for example, S. M. Sze, Physics of Semiconductor Devices, (John Wiley and Sons, New York, 1969).

35. J. O. Dimmock, in Semimetals and Narrow Gap Semiconductors, edited by D. L. Carter and R. J. Bate (Pergamon Press, Oxford, 1971).

36. T. S. Moss, Photoconductivity in the Elements, (Butterworths Scientific Publications, London, 1952).

37. H. Kimura, J. Electron. Mater. 1, 166 (1972).

38. S. G. Parker, J. E. Pinnell, and R. E. Johnson, J. Electron. Mater. 3, 731 (1974).

39. T. C. Harman and J. P. McVitte, J. Electron. Mater. 3, 843 (1974).

40. P. Winchell, Energy Conversion 8, 81 (1968).

41. H. E. Bates and M. Weinstein, Advan. Energy Conv. 6, 177 (1966).

42. V. V. Sokolov, V. I. Belovsov, V. B. Sholts, and L. N. Sidorov, Russ. J. Phys. Chem. 40, 885 (1966).

43. D. A. Northrop, J. Phys. Chem. 75, 118 (1971).

44. D. A. Northrop, J. Electrochem. Soc. 118, 1365 (1971).

45. Klug and Alexander, X-Ray Diffraction Procedures, (John Wiley and Sons, New York, 1954).

46. B. D. Cuttity, Elements of X-Ray Diffraction, (Addison Wesley, Mass., 1960).

47. R. E. Johnson and S. G. Parker, Final Technical Report, Texas Instruments, Contract No. DAAK02-72-C-0389.

48. C. S. Barrett, Trans. AIME 161, 15 (1945).

49. J. B. Newkirk, Trans. AIME 215, 483 (1959).

50. T. S. Moss, Optical Properties of Semi-Conductors, (Butterworths Scientific Publications, London, 1959).

51. P. Norton, Ph.D. Thesis, (Syracuse University, Syracuse, New York, 1970).

52. E. H. Putley, The Hall Effect and Semiconductors Physics, (Dover Publications, New York, 1968) p. 46.

53. C. T. Sah, R. N. Noyce, and W. Shockley, Proc. IRE 45, 1228 (1957).

54. We thank Mr. W. E. Leyshon of the Advanced REliability Studies Electronics Laboratory, General Electric Co., Syracuse, New York, for performing this investigation.

55. M. R. Johnson, Final Technical Report, Texas Instrument Contract No. DAAK 02-72-0330.

56. P. Norton and P. Chia, (unpublished).

57. M. Tanenbaum and H. B. Briggs, Phys. Rev. 91, 1561 (1953).

58. T. S. Moss, Proc. Phys. Soc., B67, 775 (1954).

59. E. J. Johnson, in Semiconductors and Semimetals, vol. 3, edited by R. K. Willardson and A. C. Beer (Academic Press, N.Y. 1967).

60. H. Y. Fan, Rept. Prog. Phys., 19, 107 (1956).

61. H. B. Bebb and C. R. Ratliff, J. Appl. Phys., 42, 3189 (1971).

PART III

PREPARATION AND ANALYSIS OF HgCdTe

CHAPTER I

INTRODUCTION

HgCdTe is a semiconducting pseudobinary alloy system which has been the subject of many investigations since 1960. Whether for device applications or for more fundamental studies of physical processes, all investigations begin with the requirement of high purity single crystals. Various crystal growth techniques have evolved for this system including modified Bridgman methods[1,2], vertical zone melting[3,4], solid state recrystallization[5], slush recrystallization[6], and a number of epitaxial techniques[7,8]. The goal of this study has been to understand the physical parameters which affect crystal growth in solid state and slush recrystallization.

Both solid state and slush recrystallization provide high quality single crystals but each method has its own advantages. Solid state recrystallization has the capability of providing a high yield of extremely homogeneous material whereas slush recrystallization has a lower yield but more versatility in providing a wider range of compositions. In Section II the mechanisms for crystal growth of the two methods are discussed. Material perparation, including zone purification of the elements, is described in Section III. Experimental details for both methods of crystal growth are discussed in Section IV. In Section V the quality of single crystals grown by the two techniques is examined by means of X-ray topography.

CHAPTER II

THEORY OF CRYSTAL GROWTH

A. Solid State Recrystalization

Crystal growth of HgCdTe alloys by means of solid state recrystallization (SSR) consists of the rapid quenching of molten alloys followed by a

high temperature anneal to permit grain growth[9]. A rapid quench is necessary to lock in the overall compositional uniformity of the crystal. Figure 1 gives the T-x projection of the HgCdTe pseudobinary phase diagram. In normal cooling processes the liquid to solid transformation takes place too rapidly for equilibrium conditions to be met (solid state diffusion is too slow). Compositional gradients are set up in the liquid and solid due to rejection of HgTe from the solid-liquid interface during solidification. These gradients can be extensive due to the wide separation between the liquidus and solidus lines, and make growth of homogeneous alloys difficult.

Consider a molten alloy with a composition of x = b which has been heated to a point above the liquidus line as shown in Figure 1. As the alloy is cooled the temperature drops until the liquidus line is met. At T_A solidification begins with the freezing out of alloy with a composition of x = a, and the liquid at the solid-liquid interface becomes enriched with HgTe. Since there is no time for homogenization the next solid to freeze at a slightly lower temperature is richer in HgTe than the first because the liquid from which it freezes is richer in HgTe. The average composition of solidified alloy now lies between the initial solid composition and that just deposited. This process continues with the solidification of alloys richer and richer in HgTe until the average composition of the solidified alloy becomes b, the same as the initial composition of the molten alloy. The solidification proceeds to a temperature below T_B as shown in Figure 1 where a non-equilibrium solidus line has been schematically drawn to represent this freezing process. This result is

known as coring[10] (or microsegragation) since the center of the solidified grains consists of high melting alloys surrounded by a low melting, last to solidify shell. The extent of compositional variation between the center of the grain and its boundaries depends upon the rate of freezing and the separation between the solidus and liquidus lines. The more rapidly the alloy is cooled the larger the compositional variation within the solidified grain. The lattice constants for HgTe and CdTe are nearly the same allowing for large compositional variations to be accommodated within a grain. At first this seems contradictory to the statement that a fast quench locks in the compositional uniformity of the crystal, but the answer is that with a rapid quench the grain size is limited. Thus a rapid quench limits the spatial compositional variation and enables solid state diffusion to equilibrate the system during the high temperature anneal.

A rapid quench is also necessary to provide a fine grained matrix suitable for the recrystallization process. Recrystallization and grain growth processes have been studied in metals for many years[12,13], but only recently have they been applied to semiconducting alloys[5]. Grain growth occurs at temperatures greater than half of the absolute melting point where atomic mobility is sufficient to allow some grains to grow at the expense of others. The driving force for grain growth is the decrease in free energy associated with the total decrease in grain boundary area. Recrystallization is the nucleation of new equiaxed grains within a deformed matrix. Recrystallization in metals takes place at relatively low temperatures, usually below half

of the absolute melting point. The driving force for recrystallization is the lowering of the internal free energy stored in the lattice during some prior deformation of the lattice. There are a number of experimental laws governing recrystallization and these are given in Table VI.

Recrystallization can be used to obtain large single crystals of an alloy. Referring to Table VI we note that there is a certain critical deformation necessary for the onset of recrystallization. At this critical strain only a few new grains are formed, and if the ingot is then heated slowly or passed through a steep temperature gradient one of these new grains will consume the other before they grow to any extent. This method is known as the strain-anneal method. Large single crystals may also be formed by a process known as secondary recrystallization or exaggerated grain growth. After primary recrystallization has been completed grain growth occurs to minimize the grain boundary energy associated with a polycrystalline matrix. When some factor inhibits normal grain growth so that a few grains grow very large at the expense of others, exaggerated grain growth is said to occur. The inhibition of normal grain growth by the presence of a dispersed second phase material has been attributed to single crystal growth of HgCdTe by means of solid state recrystallization[9]. Thus single crystal growth by means of solid state recrystallization encompasses three distinct processes: grain growth, strain-anneal, and exaggerated grain growth.

B Liquid Mass Transport or Slush Recrystallization.

Crystal growth by means of liquid mass transport (LMT)[6] involves the quenching of a molten HgCdTe alloy to a position within a temperature gradient such that the bottom portion of the alloy is frozen but the top part remains molten. The ampoule is then left in this position and after a period of time a high quality single crystal is found to form in the slush region. In order to determine the mechanism for crystal growth we need to examine the schematic T-x phase diagram for the HgCdTe system as shown in Figure 1. Consider a HgCdTe alloy with a composition x = b which has been heated to a point above the liquidus line. When the ingot is quenched into its crystal growing position the top portion of the ingot with $T>T_A$ will contain molten alloy with a composition x = b. In the bottom part of the ampoule where $T<T_B$ the alloy will freeze with an average composition x = b. In the slush region where the temperature varies from the solidus (T_B) to the liquidus (T_A) there is a two phase mixture with an average composition of x = b. In order to determine the actual composition of the phases in equilibrium at any temperature within the slush region a tie line (a line drawn parallel to the composition axis) is drawn to the boundaries of the two phase region and the compositions at the points of intersection are read. The relative amounts of each phase at a given temperature is determined by the lever rule[10].

At the solid-slush interface ($T = T_B$) the slush is a mixture of solid phase with x = b and liquid phase with x = b as shown by the tie line labeled mn in Figure 1. According to the lever rule the slush at T_B consists almost

entirely of the solid phase. At the slush-liquid interface ($T = T_A$) the slush is a mixture of liquid phase with x = b and solid phase with x = a as shown by tie line op, and by the lever rule the slush consists almost entirely of the liquid phase. Hence as the temperature varies from T_B to T_A the composition of the liquid phase varies from c to b whereas the composition of the solid phase varies from b to a. Equilibrium exists when a system shows no propensity for change. Temperature and pressure must be constant and the composition must be uniform within each of the phases present. Introducing the chemical potential which is related to the effective concentration of a component (HgTe or CdTe) in a given phase, equilibrium is established when the chemical potentials of each component are equal in all phases. Since the temperature gradient forces the composition of the phases to vary throughout the slush region there will be chemical potential gradients established. These chemical potential gradients are the driving force for slush recrystallization. Each component, HgTe and CdTe, interdiffuse through the slush region to establish equilibrium. The CdTe component diffuses from the slush-liquid interface to the solid-slush interface whereas the HgTe component goes in the opposite direction. As the CdTe content of the slush at the solid-slush interface increases $Hg_{1-x}Cd_xTe$ alloy with x>b freezes out of the slush. In this way crystal growth occurs and the growing interface moves up through the slush region until a composition of x=a is reached.

CHAPTER III

MATERIAL PREPARATION

Preparation of high quality single crystal HdCdTe is directly related to the initial purity of the starting material. The material currently being used in this study has been purchased from Cominco[14]. The tellurium and cadmium is designated 69 grade-double zone refined and the mercury is their standard 69 grade material. Typical impurity analysis as supplied by Cominco is given in Table I. The mercury is used in the as-received state but the tellurium and cadmium are further purified by means of zone refining.

The zone purification of tellurium has been described by many researchers[15,16]. The effective distribution coefficients for impurities in tellurium vary depending on the experimental arrangement, but in general seem to be such as to make zone refining an efficient means of purification. Movlanov[17,18] has found the distribution coefficients for Se and Hg impurities to be 0.56 and 0.11 respectively. Krapukhin [19] found that Cv and Ag have values of 0.0095 and 0.022 respectively. Krapukhin [19,20] also observed an increase in the effectiveness for zone refining the following impurities: Cv, Ag, Pd, Mn, Si, Fe and Bi when an electric field in the direction of growth was applied. Kujawa[21] has found that if many impurities were present the one with the greatest concentration influences the segragation of the other impurities due to the formation of multicomponent systems. An analysis of the cadmium-impurity phase diagrams indicates that most impurities present will be effectively zone refined, only those elements which are close neighbors to cadmium in the periodic table cause trouble[22]. A partial listing of distribution coefficients in tellurium and cadmium is reproduced in Table II[23]. As can be seen there is some disagreement with the values for some impurities as given above.

The experimental apparatus for the zone refining of tellurium and cadmium is shown schematically in Figure 2. The basic features are: (a) hydrogen purification system, (b) multiple resistance zone heaters, (c) a mechanical drive which produces motion of the zone heater assembly by means of a lead screw, and (d) a completely enclosed system, permitting operation at a slight over-pressure?

The hydrogen purifier[24] provides a source of dry, ultra-pure hydrogen by selective diffusion through a palladium-silver alloy membrane. There are a number of reasons for choosing hydrogen over some inert gas. The flow of hydrogen over the tellurium or cadmium provides a reducing atmosphere which helps remove any oxide films present. The removal of selenium impurities from tellurium ingots has been enhanced in a hydrogen atmosphere perhaps due to the formation of hydrogen selenide[25]. The flow of hydrogen down the guide tube also tends to prevent volatile impurities from depositing back on the purifier ingot. The hydrogen purifier is capable of providing a flow of 150 ml/min., however the apparatus is typically operated at an over-pressure of 1.1 to 1.2 atmospheres to prevent any seepage of air into the system. The ultrapure hydrogen flows from the purifier into the quartz guide tube and then exits into a series of filters packed with glass wool. The filters enable any tellurium or cadmium vapor to cool and condense. The hydrogen is ignited and burned off at the outlet side of the system.

The heater assembly consists of coils of Kanthal resistance wire and can maintain molten zones with widths of one centimeter. The assembly is

mounted on a screw drive permitting travel rates varying from 0.5 cm/hr to 10 cm/hr. The element to be purified is loaded into quartz boats which have a diameter of 22 mm. Typical ingot lengths are 30 cm giving a value of 30 for the ratio of ingot length to molten zone width. The solid-liquid interface is nearly perpendicular to the direction of travel for a two centimeter wide molten zone but as the zone is made smaller more curvature in the interface is introduced. It was extremely difficult to maintain stable zone lengths when cadmium was zone refined due to its higher thermal conductivity. When zone refining tellurium three passes would be done at the rate of 3 cm/hr followed by a slow pass at 1 cm/hr. This cycle was repeated until 40 to 60 passes had been performed.

Whereas the zone refining of tellurium was relatively easy, cadmium presented two problems: its high affinity for oxygen and its good thermal conductivity. The problem with the thermal conductivity has already been mentioned and presents a practical problem of programming the amount of power delivered to the molten zones. The first problem was much more difficult since we want to remove any oxide films before further processing. With tellurium any oxide film on the surface of the ingot would be removed to the butt end of the ingot by the zone refining process within a few passes. With cadmium the oxide layer was thicker and much more difficult to remove. The CdO layer, unlike TeO_2, would not be zone refined to the butt end of the ingot.

Recently a scale for the oxygen affinity of metals has been proposed based on the negative logarithm of the oxygen pressure in equilibrium with the metal and its oxide at 1000°K[26]. This scale is reproduced in Table III.

According to this scale of the three constituents of HgCdTe alloys, cadmium has the greatest affinity for oxygen. The oxide layer causes two problems, first CdO wets quartz surfaces and consequently as the cadmium ingot cools the quartz boats crack due to the different contractions. Secondly the CdO layer may bind up impurities thereby posing as a source of contamination for the purified ingot.

Two methods have been devised for the removal of a CdO layer. The first technique is similar to decanting in that it makes use of the different densities between cadmium and CdO. The cadmium ingot is lightly etched in a solution of 20% HNO_3 and 80% methanol followed by a rinse with methanol. Care must be taken in etching the cadmium so as not to further oxidize the surface.

The ingot is then placed in a narrow quartz tube, evacuated, and then sealed off. The ampoule is heated allowing the cadmium to melt and the CdO being lighter than the cadmium floats to the top of the ampoule. The ingot is cooled and the top portion containing the CdO is removed with a carborundum saw. This process may be repeated to remove most of the dissolved CdO.

The second technique for removal of a CdO layer was to reduce the CdO in a reducing atmosphere. The cadmium was prepared for zone refining but prior to beginning the entire ingot was melted and allowed to sit in the hydrogen atmosphere. In Figure [illegible] the rate of reduction of CdO by H_2 is shown as a function of time and temperature. As the temperature is increased the rate of reduction also increases but since cadmium is rather volatile [illegible] amounts of cadmium is lost from the melt. Note also in Table III that H_2O and CdO lie fairly close to one another on the oxygen scale which indicates that hydrogen is not the most efficient reducing agent of CdO. Boric oxide (B_2O_3) may provide a more efficient means of dissolving the CdO layer although this has not been tried in the present study.

CHAPTER IV

GROWTH OF SINGLE CRYSTAL HgCdTe

A. Solid State Recrystallization.

Solid state recrystallization is a two step process consisting of a compounding-quench step and a high temperature anneal. To prepare for the first step the purified elements are weighed to the nearest 0.1 mg. in the proper proportions using a Mettler microbalance. The cadmium is cut with a carborundum saw, removing all the old surfaces, so that there is no oxide on any surface. Prior to weighing the cadmium is lightly etched in a 20% HNO_3 and 80% methanol solution[23] and is rinsed in methanol. The tellurium pieces are cleaved from the zone refined bar and are used without any chemical etching of the surfaces. The mercury is used in the as-received state. The ultrapure elements are handled with pre-cleaned teflon tweezers and beakers and care is taken to avoid any contamination from the environment.

The weighed-out elements are placed in pre-cleaned and dried quantz ampoules. The ampoules are cleaned by a rinse with a solvent followed by washing with a detergent solution. The ampoules are thoroughly rinsed and then etched with white etch, a mixture of HNO_3 and HF in the proportion of 3:1. A final rinse with deionized-distilled water completes the quartz preparation. The quartz used has been purchased from Amersil Quartz, Inc. For fabrication of reaction ampoules the quartz tubing has an inner diameter of 8 mm and a wall thickness of 3mm. Small diameters and thick walls are

required to contain the high mercury vapor pressure encountered at the compounding temperature. The P-T phase diagram of Fighre 4 shows that for HgCdTe alloys with x = 0.20 pressures in the range of 15-30 atmospheres may be encountered. The high vapor pressure of mercury also causes mercury to be lost from the melt as the ampoule is heated. In order to support the vapor pressure of mercury and maintain a stoichiometric melt a little excess mercury is added to the ampoule prior to sealing-off. The amount of excess mercury to be added is calculated assuming the ideal gas law to be valid. The volume used in the calculation is the void volume in the sealed-off ampoule. Typically, 150 mg of mercury is added to maintain a pressure of 20 atmospheres over the melt.

Once loaded the ampoules are evacuated using an oil diffusion pump with a liquid nitrogen cold-trap and sealed-off with hydrogen-oxygen torch. Typical reaction ingots weigh 20 gm and are no longer than 6 cm. Ampoule lengths are 10-12 cms and hence have a void length of about 5 cm.

The temperature profile for the reaction oven is given in Figure 5 and is basically isothermal. A cross-section of the oven showing the position of the reaction ampoule is shown in Figure 6. At one end of the oven there is a 1/4 inch diameter quartz tube which allows a stream of nitrogen gas to enter the oven and rapidly cool the ampoule [9]. The ampoule is centered in the oven and positioned about 1-2 cm from this tube. The top half of the ampoule (the void space) is wrapped with two layers of 1/16 inch asbestos tape in order to insulate it from the gas quench. This is done to prevent the top

half of the ampoule from cooling more rapidly than the melt during the quench. The asbestos prevents the sudden drop in pressure over the melt which would occur if the mercury vapor was able to condense on the ampoule walls. The ampoule is centered in the oven by means of three pieces of thermocouple tubing placed concentrically about the top half of the ampoule as shown in Figure 6. This permits the free flow of nitrogen through the oven during the quench.

Once placed in their proper positions within the reaction furnace, the ampoules are heated at a rate of 20-50° C/hr to a temperature above the liquidus. For compositions in 20% range this temperature has been 830° C. The exact kinetics of the reaction forming the solid solution is not known, but it seems that it proceeds in two distinct steps. A heating curve for a number of HgCdTe reactions has been obtained by a thermocouple in close contact with the quartz ampoule. As the ampoules are heated the temperatures are recorded. Figure 7 shows one portion of the heating curve obtained for a HgCdTe reaction as well as a HgZnTe reaction. At a temperature of 410° C there is a sharp endothermic peak followed immediately at 414°C by a sharp exothermic peak. The endothermic peak is related to the formation of the Te-HgTe eutectic which has an eutectic temperature of 409 ± 2° C and forms at a composition of 88% atomic percent of tellurium[27]. The Hg-Te phase diagram showing the eutectic point is given in Figure 8. The exothermic peak represents the reaction forming the HgCdTe alloy. The ingot is then heated to 800°C in 50°C/hr steps to insure that there are no liquid pockets within the solid and for homogenization. The ampoule is rocked through an angle of -5° to 45° with the horizontal for a period of five hours before quenching to room temperature.

Perhaps the most critical step in the whole sequence is the quench. A rapid quench is needed to lock in macroscopic compositional homogeneity and provide a suitable matrix for recrystallization, however if the quench is too fast there is extensive damage to the crystalline structure. The damage is caused by the columnar grain structure which forms during solidification. As the alloy cools grains nucleate on the ampoule walls and then grow radially inward. The resulting contraction of material away from the center causes the damage and in the extreme case (water quench) the damage is so extensive that a large hole forms along the axis of the crystal ("piping"). Any extensive damage acts like a barrier and prevents grain growth. Hence the need for a rapid quench must be balanced against the damage it does.

The nitrogen gas quench developed at Texas Instruments[9] provides a quench slow enough so as not to damage the crystal structure but fast enough to insure homogeneity. The cooling curves shown in Figure 9 were measured by placing a thermocouple in the center of a stainless steel plug (1.2 cm diameter, 7.0 cm in length) which is placed in the same position as the ampoule. The cooling rates given for the flow rates of 5, 15, 30, 45 and 80 liters/min are for comparitive purposes and do not necessarily represent the cooling rates of the HgCdTe alloys. During the quench the mechanism of heat removal is by conduction and radiation in the gaseous flow. This type of quench is relatively slow when compared to a water quench where vaporization of the water removes heat quite rapidly. The cooling rates for the gas quenched varied linearly from 1° C/s to 8° C/s

as the flow was increased from 5 ℓ/min to 80 ℓ/min. whereas with a water quench a cooling rate of 70° C/s was measured.

A columnar grain structure was found in the ingots quenched with higher flow rates. This type of structure forms because grains which nucleate near the ampoule walls within a certain chill layer begin to grow inwards due to heat conduction through the ampoule walls. Any new grains formed in the liquid are consumed by the advancing interface. In Figure 10 a schematic drawing of a columnar ingot is presented. The average grain size depends on the quench rate as shown by the series of $Hg_{.8}Cd_{.2}Te$ ingots in Figure 11. These ingots were quenched at rates of 4, 5, 20 and 50 ℓ/min. The ingot quenched at 50 ℓ/min has a columnar grain structure and the grains are typically a few mm on a side. The ingot quenched at 4 ℓ/min does not have a definite columnar structure and the few grains present are fairly large. Ingots quenched at higher flow rates have smaller grain diameters but piping damage begins to occur. The optimal quench ranged from 40 ℓ/min to 50 ℓ/min ingot size and furnace arrangement used in this study.

Once properly quenched ingots have been obtained the second stage of recrystallization consisting of the grain-growth anneal is carried out. The quenched ingots which should be completely free in the reaction ampoules (no oxide adhering to walls) are removed in a clean room environment and reloaded in larger diameter quartz ampoules (10mm diameter, 3 mm wall thickness). Again a small amount of excess mercury is placed in the ampoule to support the partial pressure of mercury which is in equilibrium with the CdTe alloy.

The amount of excess mercury added is again determined by assuming that the mercury vapor acts like an ideal gas at pressures below the saturation value. The amount of mercury added is a critical parameter since the solidus line depends upon the partial pressure of mercury as shown in Figure 4. From this phase diagram it can be seen that the solidus has considerable curvature at partial pressures greater than 20 atm. and less than 1.0 atm. Note also that there is a region at high partial pressures where the HgCdTe ingots have a high solubility in the vapor phase. This dissolution line should be avoided during the processing of the ingots. Typical partial pressures used in the recrystallization anneal have been in the range of 20 to 25 atms.

After transferring the quenched ingots to larger ampoules and adding excess Hg the ingots are ready for recrystallization. For this anneal the ampoules are placed in a vertical furnace which has been pre-heated to the anneal temperature. A copper pipe is placed within the furnace to insure an isothermal profile. A vertical furnace facilitates the separation (a quartz spacer is used) of the ingot and the liquid mercury thereby preventing alloying during the initial heating of the ingot. For ingots with compositions of 21 percent the optimal anneal temperature is 690°C ± 3°C with partial pressures in the 20 atm. range. At this temperature and pressure sufficient grain growth takes place in two weeks. Figure 13 and Table IV represents a summary of most of the crystals grown by this method in this study. Each point in Figure 12 represents an ingot quenched at a given rate (see Table IV for the quench rate) and then recrystallized for two weeks or more at the temperature and pressure shown. Circled data points are

those crystals with fewer than four grains after the anneal, the other points may have undergone some recrystallization but in general were polycrystalline. From Figure[12] it is clear that optimum conditions occurred in a narrow band of temperatures and pressures. Temperatures fluctuated somewhat during the anneal due to a lack of precise temperature control (± 3°C) and pressure values may be off due to inaccuracies in determining the void volume.

After the grain growth period the crystals are removed from the furnace and allowed to cool to room temperature. In Figures 13, 14 and 15 different recrystallized ingots with quality ranging from good to poor are shown. The quench and recrystallization parameters for these crystals have been taken from Table IV and are summarized in Table V. In Figure 13 two ingots, SSR30 and SSR51, exhibiting good single crystal quality are shown. The ingots have been cut down the center with a string saw (some saw marks are visible in some of the pictures) to reveal only large angle grain boundaries. Both crystals in Figure 13 are almost entirely single with only small regions of different orientation. In Figure 14 the two ingots presented, SSR33 and SSR34, again show good single regions but there now is a lacy network of holes starting at the top of the ingot and running down the center of the ingot. This damage will later be shown to extend into the regions which appear good in the photograph and is caused by "piping". Comparing the ingots in Figure 13 with those in Figure 14 we see that the recrystallization parameters are nearly the same, all four ingots were annealed at the temperature of 690°C with a partial pressure of mercury of 20 atms. The difference between them is in the quench rate where the first set of ingots was quenched

at a rate of 40-50 ℓ/min whereas the second set was quenched at a rate of 70-75 ℓ/min. It was found that a quench of 50 ℓ/min was as rapid a quench as possible without incurring some damage along the center line. This damage does not impede the recrystallization of the rest of the ingot although it will be shown in the topograph section that damage runs the length of the ingot.

Whereas the type of damage seen in Figure 14 is due to improper quenching that seen in Figure 15 is due to improper recrystallization. The ingots shown in Figure 15, SSR43 and SSR44, exhibit little or no grain growth and the damage lies along the grain boundaries. From Table V it is evident that the damage is not due to the quench since these ingots had the slowest quench of all the ingots. The recrystallization temperatures are no higher than the previous ingots but the mercury over-pressures are much higher. The damage is caused by the high pressure in combination with the anneal temperature. As seen in Figure 4 there is considerable curvature of the solidus line towards lower temperatures as the pressure is increased. Since recrystallization depends upon anneals at temperatures very close to the solidus, this lowering of the solidus at high mercury pressure is enough to produce localized melting of the ingot along the grain boundaries. The localized melting would take place at the grain boundaries because this is where the lowest melting alloy solidifies during the freezing process (micro-segregation or coring). Thus for SSR43 and SSR44 with over-pressures of 30 atm. and 40 atm. the anneal temperatures of 685°C and 670°C were too high and melting occurred at the grain boundaries.

This damage occurs before any grain growth takes place isolating the grain and preventing any further recrystallization. Best results for recrystallization were obtained when the solidus was approached but not exceeded. For 20 percent alloys anneal temperatures of 690°C and over-pressures of 20 atm. have worked well.

B Slush Recrystallization

Slush recrystallization proceeds in three steps: reaction of the elements to form a HgCdTe alloy, a quench from the liquid phase to a point where the solid and liquid phases are present simultaneously, and finally an anneal period to allow crystal growth to take place. Unlike solid state recrystallization all three steps take place within the same ampoule. As discussed in the theory section the initial composition of the charge is smaller by a factor of about three from the final composition. Figure 16 shows the relationship between the nominal initial liquid composition and the peak composition in the recrystallized slush region.

Preparation for slush recrystallization proceeds similarly to that of solid state recrystallization except for the difference in initial compositions for the same final composition. Since a longitudinal compositional gradient is inherent in this method of crystal growth, quartz tubing with as large a diameter as possible is used (12 mm X 10 mm). Also since an important consideration in slush recrystallization is that the volumes of the liquid portion be much larger than that of the slush portion, the typical charge is quite large, about 100 g. Once loaded the ampoule is evacuated, sealed-off and placed in a vertical oven where it is slowly heated

to a point above the liquidus. After homogenization for 4-5 hours the ampoule is lowered quickly through a temperature gradient of 10°C/cm, see Figure 17, to a position where the bottom inch of the ingot will solidify. The temperature of this point as recorded by a thermocouple attached to the outside of the ampoule is 650°C for a melt composition of 6-8 percent. Once quenched into position the ampoule anneals in the temperature gradient for a period of 30 to 45 days to allow for compositional diffusion and the resulting crystal growth. Since the layers which freeze out of the slush are at the solidus temperature, subsequent recrystallization occurs.

After the anneal period the furnace is shut off and the ampoule is allowed to cool slowly. The crystal is then cut into slices, the slush region being entirely single crystal. After the peak composition slice is reached a pinkish core region begins to develop in the center of the slice. Its origin is not known although it may be CdTe rich material. Figure 18 shows the compositional profile along an ingot and Figure 19 shows the composition, as determined by density measurements, of succeeding slices within the slush region. The profile of IMT 10 with an extended range of useable material was achieved by lowering the ampoule an additional 0.5 cm every week throughout the anneal period.

Of the two methods of crystal growth slush recrystallization was the easier to use. In slush recrystallization there seems to be no critical parameters, everything works as it should. Once a temperature gradient across a slush region has been established crystal growth occurs readily. The ease in growing single crystal HgCdTe and its ability to produce alloys

in the range of 40-50 percent CdTe are the chief advantages of slush recrystallization. However this method has a drawback in that only about 20% of the ingot is useable and only a few slices at any specific composition. Solid state recrystallization has many critical parameters but once mastered produces large quantities of homogeneous single crystals.

CHAPTER V

TOPOGRAPHICAL ANALYSIS

X-ray diffraction topography is an extremely powerful tool for investigating lattice defects and crystalline quality in semiconducting crystals[28, 29, 30]. Of the many different methods the Berg-Barret technique (B-B) has been chosen for the practical advantage of its simplicity[31]. B-B camera designs[32, 33] and experimental techniques[34,35] have been described previously but the methods employed here will be described below.

The technique consists of mounting the crystal within a roughly collimated X-ray beam at the proper Bragg angle so that a given set of planes will diffract the characteristic radiation of the source onto a photographic emulsion, Figure 20. For the present experiments a standard CA-7 diffracting tube was used with the sample placed about 25 cm from the target at a take off angle of about 7 deg. Since the area of the sample surface which will reflect a given wavelength depends directly on the projected horizontal length of the X-ray target, the front port of the diffracting tube was used giving a horizontal length of 1 cm. A Blish topograph camera[36] was purchased to provide the goniometer needed to adjust the Bragg angle, collimator slits for limiting unused portions of the X-ray beam, and a film cassette to hold the photographic plate. The X-ray tube and camera are enclosed in an 1/8 in lead box topped with an equivalent thickness of leaded glass for operator safety. Adjustments are made through slits in the lead box. A fluorescent screen is used in place of the film to initially adjust the Bragg angle so that

the Kα radiation is diffracted from a set of planes. Once a suitable spot is chosen the fluorescant screen is replaced with the photographic emulsion. The film used in this study has been Kodak Industrex[37] (single coated) which is an ultra fine grain X-ray film. This film is about 50 times faster than high resolution places and can provide maximum enlargements of about 35 diameters, furthermore the processing is simple and quick. With this film exposure times of 10 min. are typical. Since the topograph is a point-to-point mapping of the reflectivity of the surface onto the X-ray film the resolution depends chiefly on the sample to film distance and should be minimized. Image contrast is determined mainly by misorientation of low angle subgrains within the crystal and inhomogeneous lattice strain resulting in a reduction of primary X-ray extinction.

Crystals produced by both techniques have been examined by means of topography. Figures 21 and 22 are topographs taken of two different crystals grown by means of slush recrystallization. Both topographs show a radial pattern of low angle grain boundaries. The difference in orientation between adjacent grains is extremely small otherwise the Bragg condition would not be satisfied. The radial distribution may be due to the fact that in slush recrystallization the crystal fills the ampoule. As the ampoule cools strain may be introduced into the crystals, the radial pattern of grain boundaries then would be generated to relieve the strain. A second possibility has to do with the isotherms running through the ingot. Constant temperature is not maintained across the ingot, if only due to heat conduction from the liquid

alloy resting above the slush region. In this way if a cut was made through the ingot at the interface of crystal growth, instead of a uniform layer of a given composition freezing out there would be a ring of single crystal but the core would be slightly hotter and remain as slush. In this way a clear radial pattern of low angle grain boundaries would develop. If this is true the composition should vary from the outside edge radially inwards. However a composition profile of a slice taken by examining the variation in absorption edge across the slice shows no radial pattern, Figure 23.

Solid state recrystallization ingots have been cut longitudinally and topographs taken of different sections. Figure 24 has a topograph of a slice of SSR-34 cut from the middle, well below the visible damage seen in Figure 1 . The topograph shows good crystalline perfection, but the damage due to high quench rates which was thought to be localized to the top centimeter of the ingot extends all the way down the crystal. Since this slice is from the middle of the crystal this damage would tend to disappear as succeeding slices are cut. The bands of light and dark may be strain introduced in mounting the slice. Figures 25 and 26 are topographs of SSR5i (see Figure 14). From the topographs it is clear that there is little damage from the quench and only the section containing the large-angle circular grain has any damage. The origin of this damage is not known and may either be due to processing of the slice or to the crystal growth itself. All the other sections represent nearly perfect slices of HdCdTe.

Table I

Impurity Analysis of Cominco Material

Impurity*	Al	Ag	Bi	Ca	Co	Fe	Pb	Mg	O	S	Se	Si
Te	.1	<.1	.1	.1	.1	.1	<.1	<.1	<4.0	.3	<1.0	.2
Hg	<.001	<.001		<.001	<.001	<.001	<.001	.002				.003
Cu		<.1	.1	.1	<.1	.1	.1	<.1				.1

*all in ppm

Table II

Distribution Coefficients of Impurities in Te and Cd[23]

(a) Tellurium

k	
10^{-5}	: Cu, Ag, Au
10^{-4}	: Fe, Sn, Mg, As
10^{-3}	: Bi, Ge, Ca, Tl, Ni
10^{-2}	: Sb, In, Pb, I
10^{-1}	: Hg, Se, Cr, Mn
2	: Cd

(b) Cadmium

10^{-2}	: Pb, Sn
10^{-1}	: Ga, In, Se, Tl, Sb, Na, Cu, Co, Pt
0.4	: Au
0.5	: Zn, Hg
1.5	: Li
3.0	: Ag

Table III

Oxygen Affinity of Metals[26]

Oxide	pO*	Oxide	pO	Oxide	pO
Hg_2O	-6.5	NiO	16.2	VO	34.5
Au_2O_3	-5.5	CdO	16.6	B_2O_3	35.4
Ag_2O_3	-3.3	GeO_2	18.4	SiO_2	36.3
PtO	-1.3	Rb_2O	19.0	TiO	44.2
PdO	-1.1	SnO_2	19.7	ReO	46.3
IrO_2	0.9	H_2O	20.1	Al_2O_3	47.2
RuO_2	2.8	MoO_2	20.1	ZrO_2	47.2
Rh_2O	4.2	FeO	20.6	HfO_2	48.1
O_8O_4	5.0	CO	21.3	Li_2O	48.5
TeO_2	7.2	WO_2	21.2	MnO	48.6
Tl_2O	8.1	K_2O	23.3	Sc_2O_3	50.3
Cu_2O	9.6	In_2O_3	24.1	CrO	51.2
BiO	11.4	ZnO	25.8	BeO	52.0
PbO	12.7	Ga_2O_3	26.2	MgO	52.7
TeO_2	13.6	Na_2O	26.9	Y_2O_3	52.9
ReO_2	13.6	P_2O_3	29.7	$(RE)_2O_3$	53.3
Au_2O_3	14.9	Cr_2O_3	30.1	ThO	55.5
Sb_2O_3	15.3	MnO	32.6	CaO	55.5
Cs_2O	15.3	Ta_2O_5	33.2	Ac_2O_3	56.4
CoO	16.2	NbO	33.7		

*pO= -log p_{O_2} for oxygen in equilibrium

Table IV

Summary of Crystals Grown by Solid State Recrystallization

Crystal		T(°C)	1000/T	P(atm.)	Q(l/min)	Holes	Single
SSR 19	x=.20	667	1.069	34	55	N	---
SSR 20	x=.21	665	1.066	30	50	G.B.	---
SSR 21	"	665	1.066	30	60	G.B.+C.L.	---
SSR 22	"	672	1.058	28	60	G.B.	---
SSR 23	"	665	1.066	27	60	C.L.	~80%
SSR 24	"	673	1.057	16	65	N	---
SSR 25	"	660	1.072	20	75	N	---
SSR 26	"	680	1.049	19	65	N	---
SSR 27	"	695	1.033	22	60	C.L.	~100%
SSR 28	"	683	1.046	22	60	N	---
SSR 29	"	685	1.044	--	60	C.L.	---
SSR 30	"	690	1.038	26	50	N	~90%
SSR 31	"	692	1.036	30	75	G.B.	~100%
SSR 32	"	672	1.058	25	75	N	---
SSR 33	"	694	1.034	21	75	N	~100%
SSR 34	"	695	1.033	23	75	N	~100%
SSR 35	(T1)	---	-----	--	--	N	---
SSR 36	x=.21	699	1.030	24	60	N	~100%
SSR 37	"	694	1.034	24	60	Few C.L.	~90%
SSR 38	} H$_2$/ZnTe						
SSR 39							
SSR 40							
SSR 41	x=.21	680	1.047	31	50	C.L.	~100%
SSR 42	"	670	1.060	32	40	---	---
SSR 42-2	"	680	-----	35	--	G.B.	---
SSR 43		685	-----	31	30	G.B.	---
SSR 44		670	1.060	40	50	G.B.	---
SSR 45		698	1.030	27	10	G.B.	---
SSR 46		695	1.033	19	15	N	---
SSR 47		690	1.029	12	20	C.L.	~80%
SSR 48		---	-----	--	--	---	---
SSR 49	"	690±5	1.038	14	30	N	~50%
SSR 50	"	695±5	1.033	18	40	C.L.	---
SSR 51		688	1.041	14	40	N	~90%
SSR 52		698	1.041	~12	50	N	---

Table VI

Laws of Primary Recrystallization [13]

1) A minimum deformation is necessary to initiate recrystallization.

2) The smallerthe degree of deformation, the higher is the temperature required to initiate recrystallization.

3) Increasing the annealing time decreases the temperature required for recrystallization.

4) The final grain size depends chiefly on the degree of deformation and to a lesser degree upon the annealing temperature,normally being smaller the greater the degree of deformation and the lower the annealing temperature.

5) The larger the original grain size, the greater the amount of deformation required to give equivalent recrystallization temperature and time.

6) New grains do not grow into deformed grains of identical or slightly deviating orientation.

7) The amount of deformation required to give equivalent deformational hardening increases with increasing temperature of working.

Table V

Growth Parameters for Crystals Appearing in Figures 13, 14, and 15

Fig.	Crystal	Quench(l/min)	Anneal Temp.(°C)	Pressure(atm.)
13	SSR 30	50	690	20
	SSR 51	40	688	19
14	SSR 33	75	694	21
	SSR 34	70	695	23
15	SSR 43	30	685	31
	SSR 44	30	670	40(saturated)

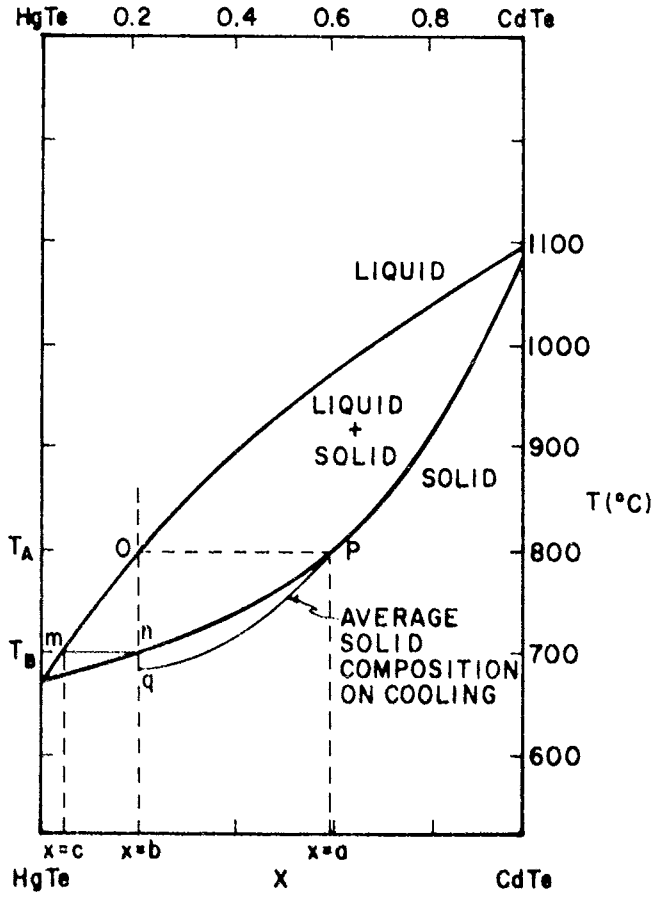

Figure 1. Solidus and liquidus temperatures for the $Hg_{1-x}Cd_xTe$ alloy system as a function of composition.

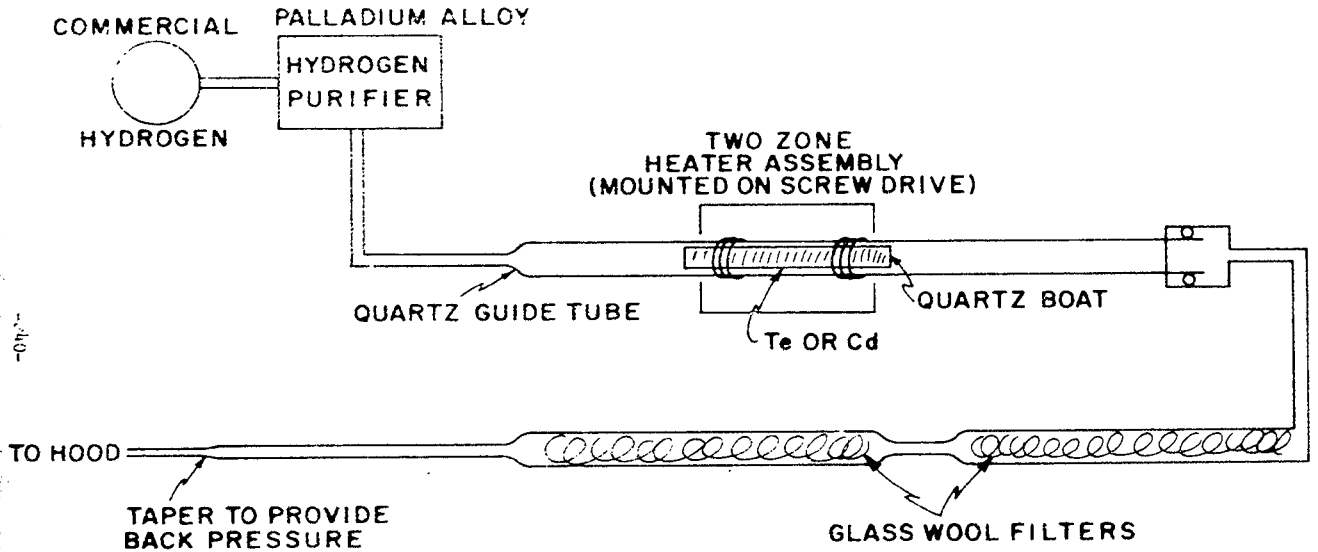

-40-

...ation apparatus.

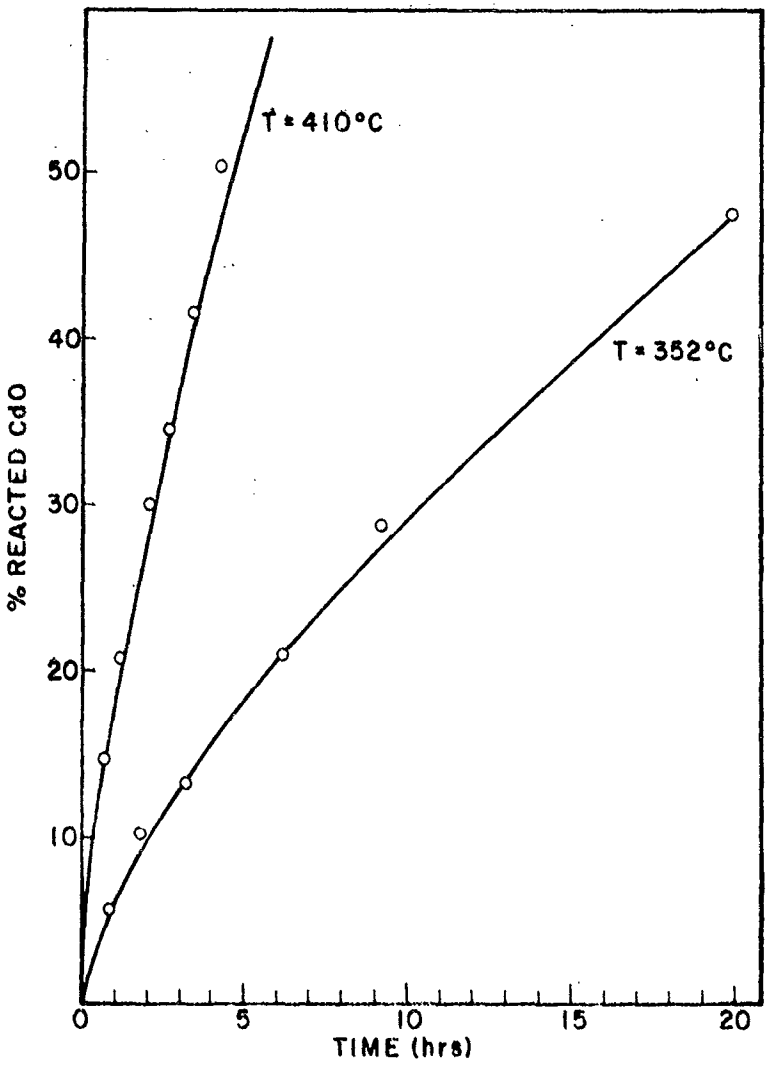

Figure 3. Rate of reduction of cadmium oxide in a hydrogen atmosphere as a function of time and temperature.

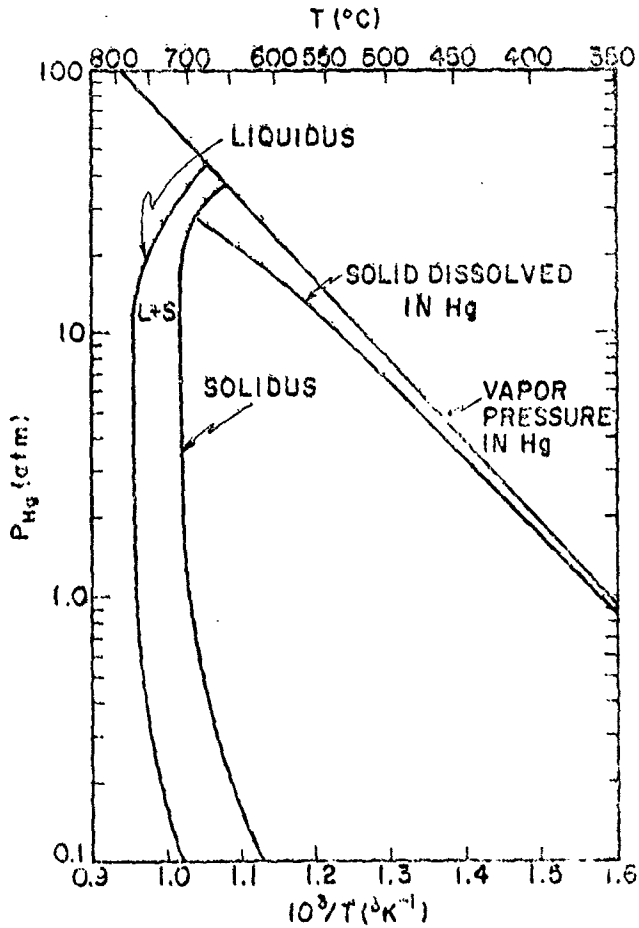

Figure 4. Partial pressure of mercury in equilibrium with $Hg_{.8}Cd_{.2}Te$ as a function of inverse temperature.[59]

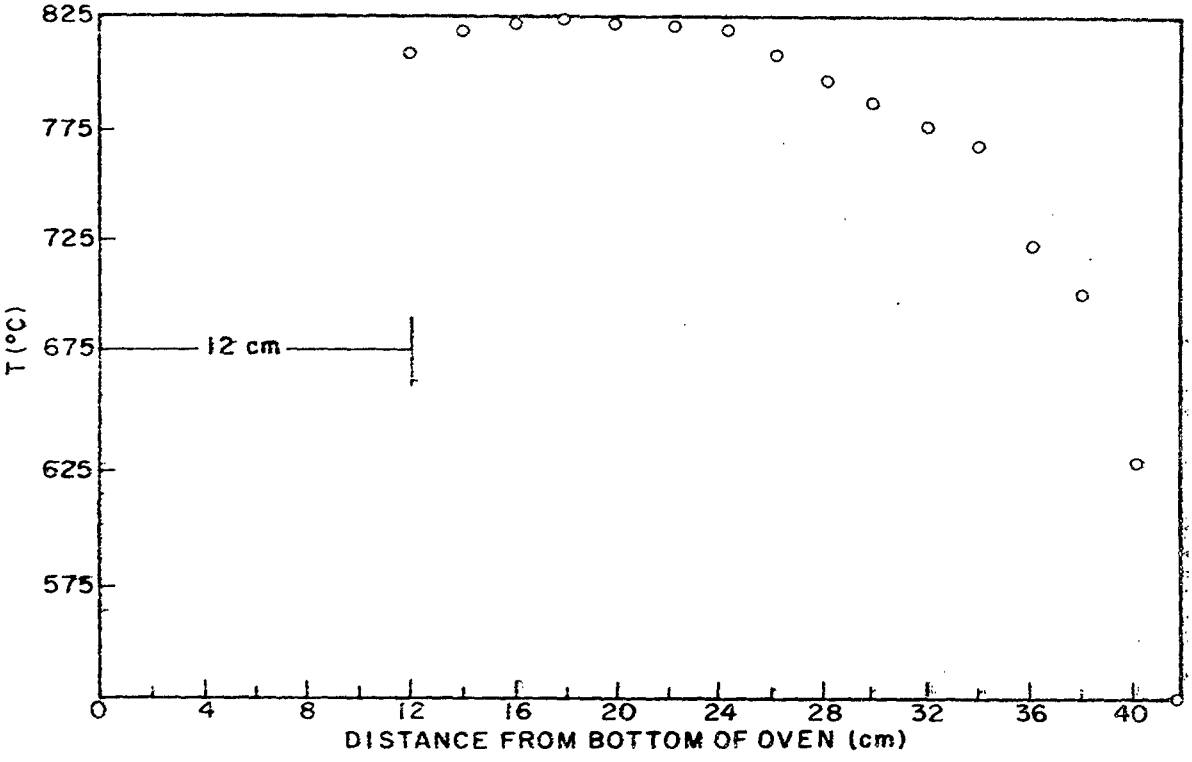

Figure 5. Temperature profile of reaction oven.

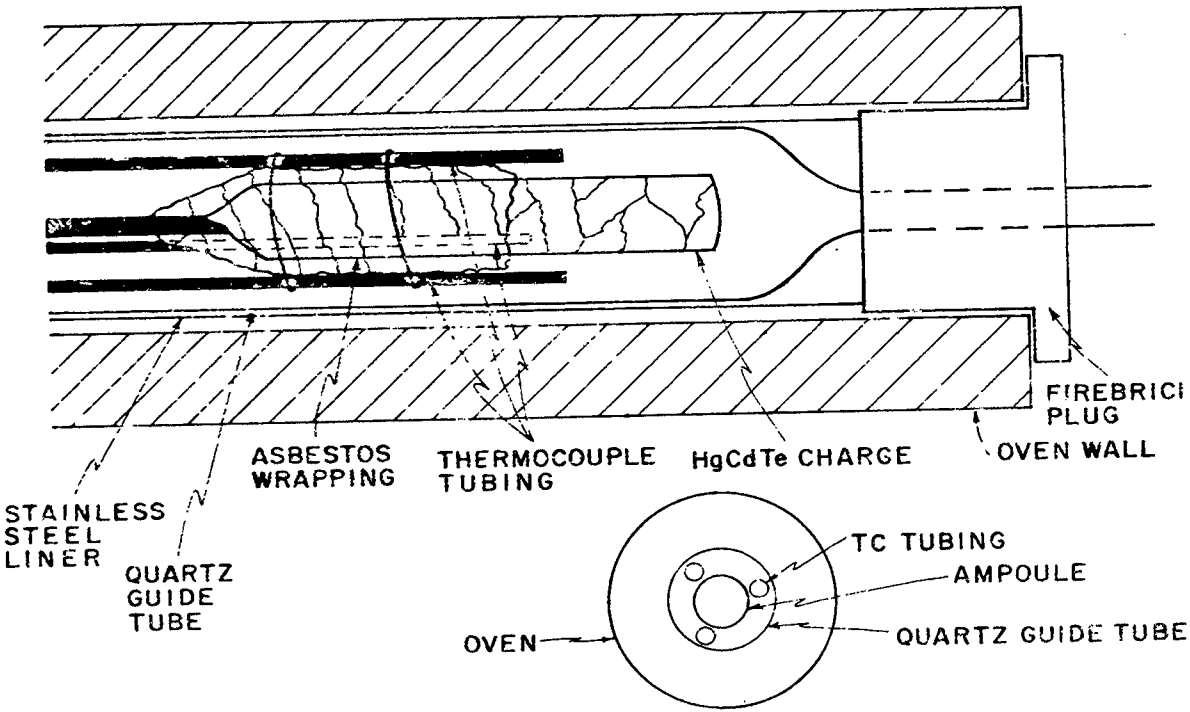
STAINLESS STEEL LINER
QUARTZ GUIDE TUBE
ASBESTOS WRAPPING
THERMOCOUPLE TUBING
HgCdTe CHARGE
OVEN WALL
FIREBRICK PLUG
TC TUBING
AMPOULE
QUARTZ GUIDE TUBE
OVEN

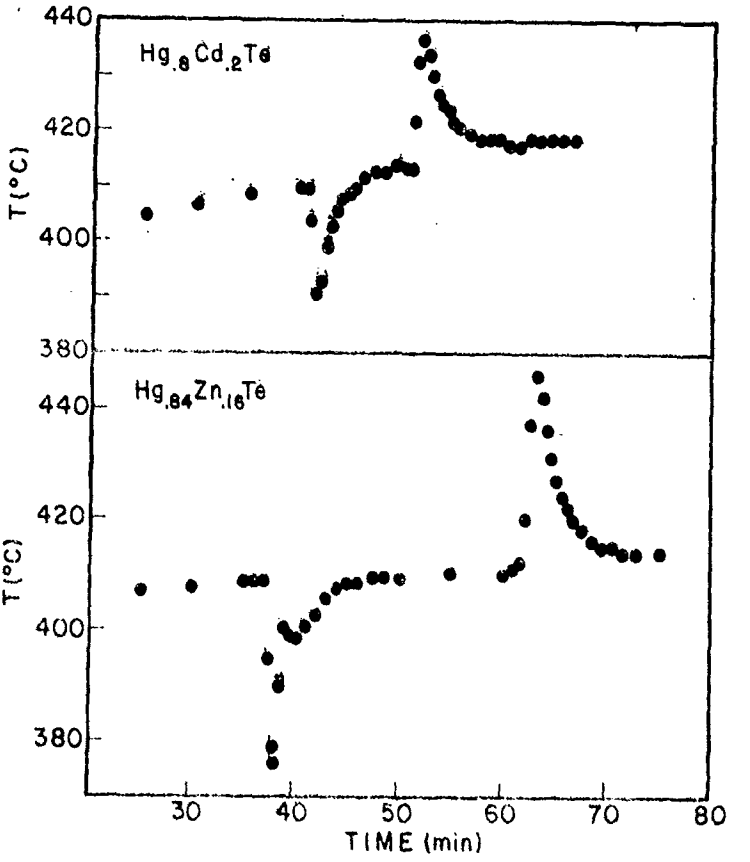

Figure 7. Heating curves for a $Hg_{.8}Cd_{.2}Te$ and a $Hg_{.84}Zn_{.16}Te$ reaction showing sharp endothermic peaks followed by exothermic peaks at the same temperature.

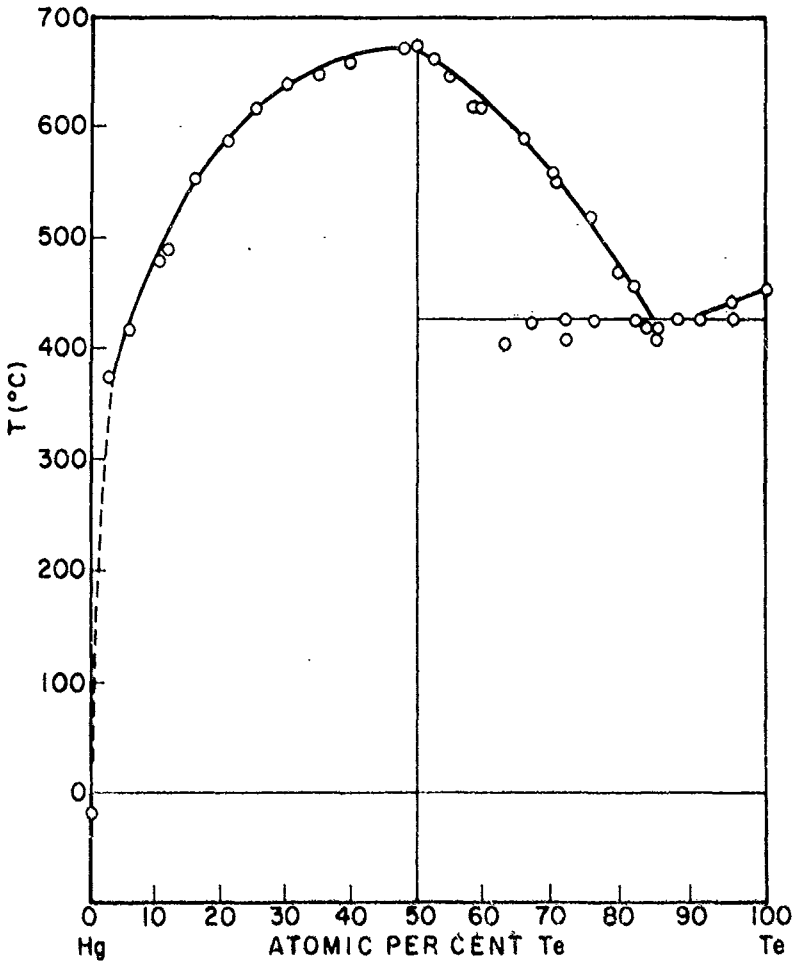

Figure 9. Phase diagram of HgTe showing the Te-HgTe eutectic at 410°C.[1]

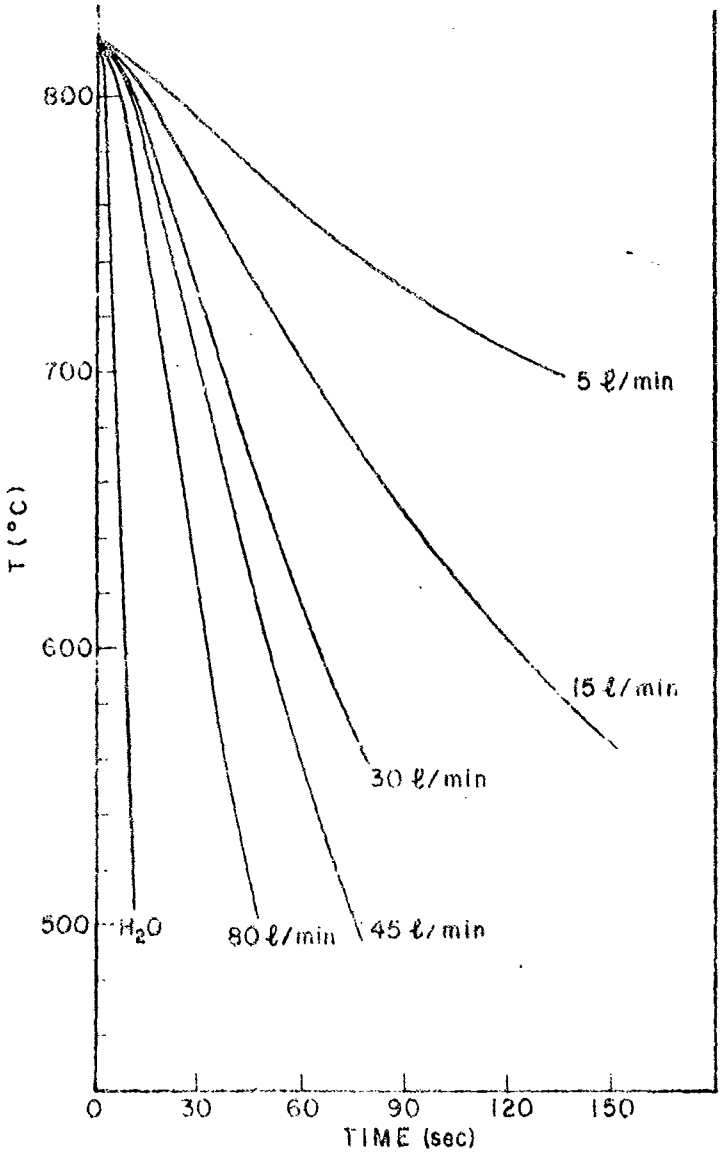
800
700
600
500
T (°C)
5 ℓ/min
15 ℓ/min
30 ℓ/min
45 ℓ/min
80 ℓ/min
H_2O
0
30
60
90
120
150
TIME (sec)

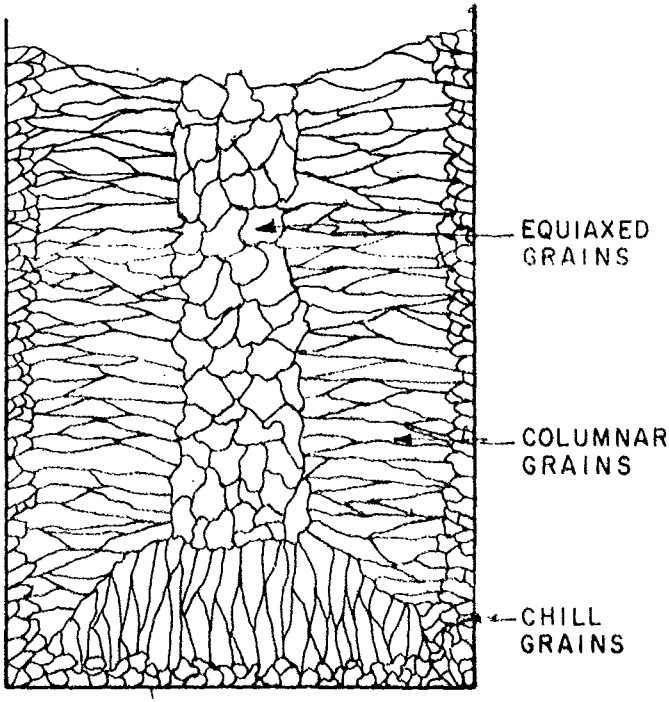

Figure 10. Schematic representation of the grain structure resulting when an ingot is cooled by heat conduction through the ampoule walls. In quenched Hg$_{0.8}$Cd$_{0.2}$Te ingots only the columnar grains are apparent.

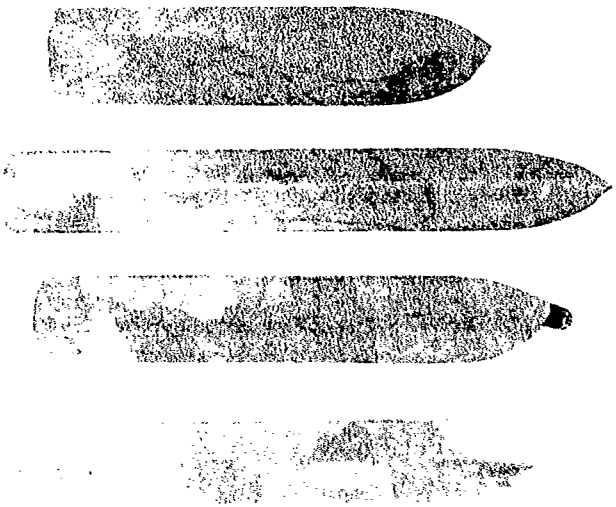

Figure 6. Quenched ignots of $Pr_{0.8}Nd_{0.2}Fe$ for quench rates of 4, 5, 20, and 50 liters/minute.

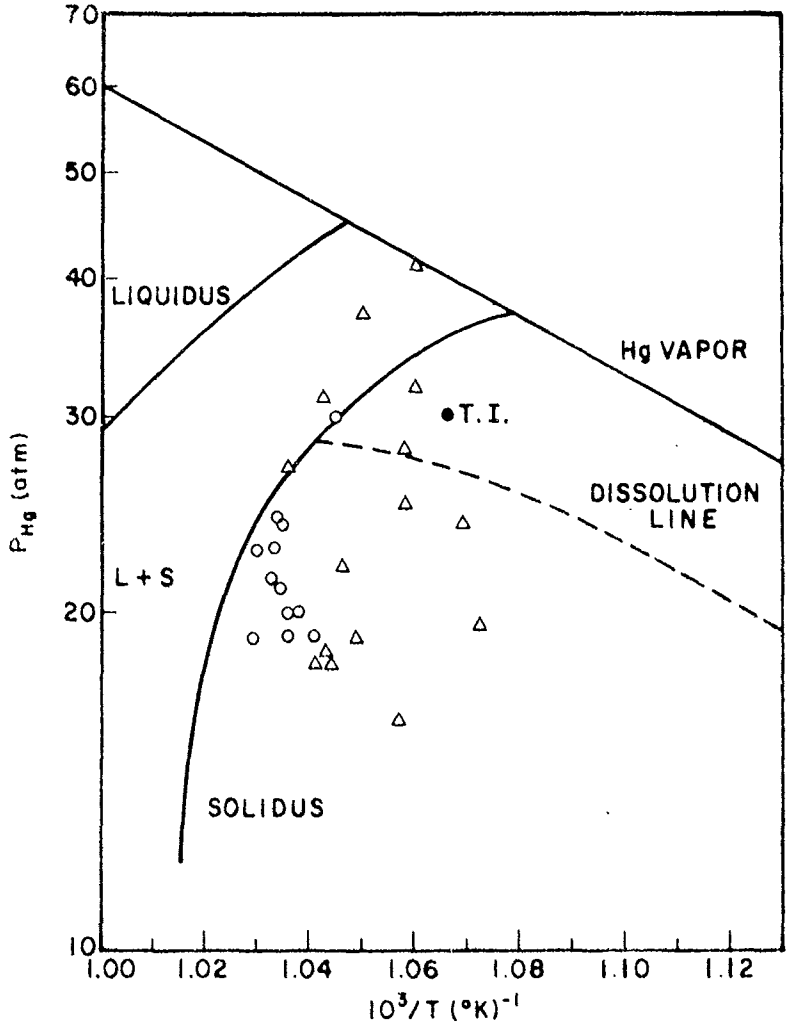

. . . . . mercury crystals grown by the solid state recrystallization method superimposed onto a portion of the P-T phase diagram. Each point represents a crystal recrystallized at the temperature and pressure as a zero.

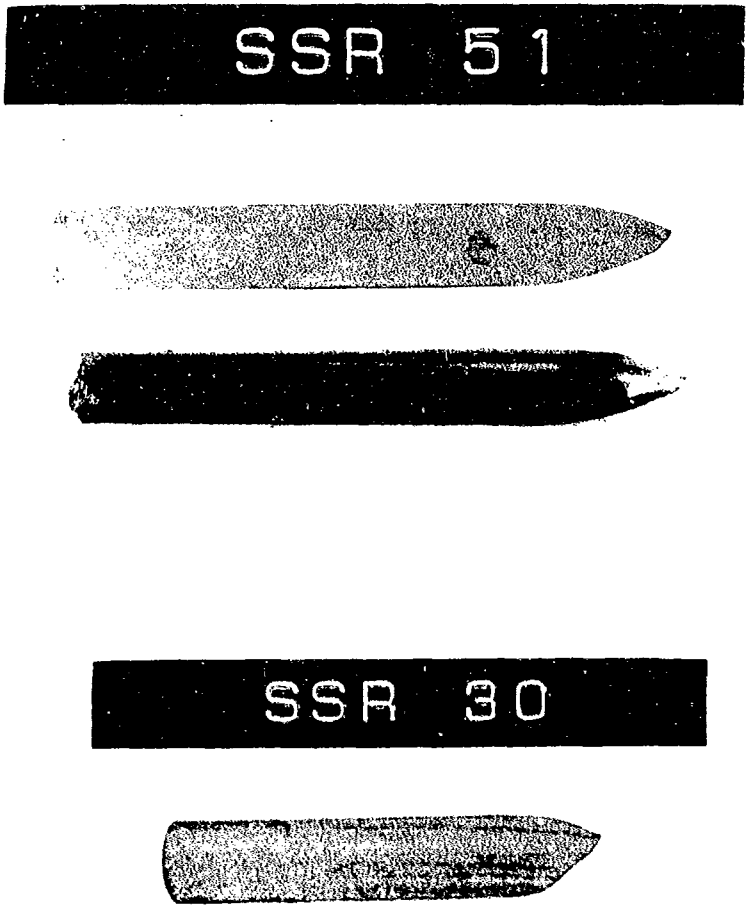

Figure 7: Recrystallized ingots of $Hg_{.8}Cd_{.2}Te$ showing large single crystal regions.

Figure 4 Recrystallized ingots of $Hg_{.8}Cd_{.2}Te$ showing large single crystal regions and damage down center line due to high quench rates.

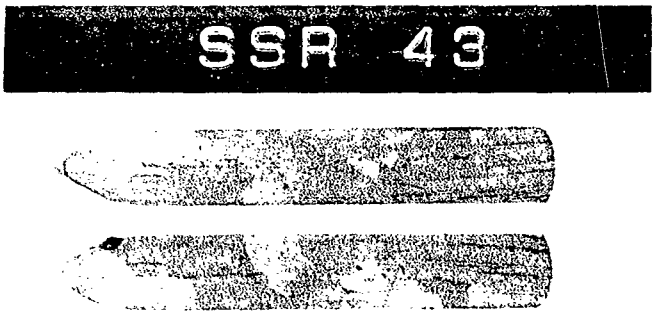

Fig. 5. Recrystallized ingots of $Hg_{.8}Cd_{.2}Te$ showing poor grain growth and damage along grain boundaries due to high mercury over-pressure.

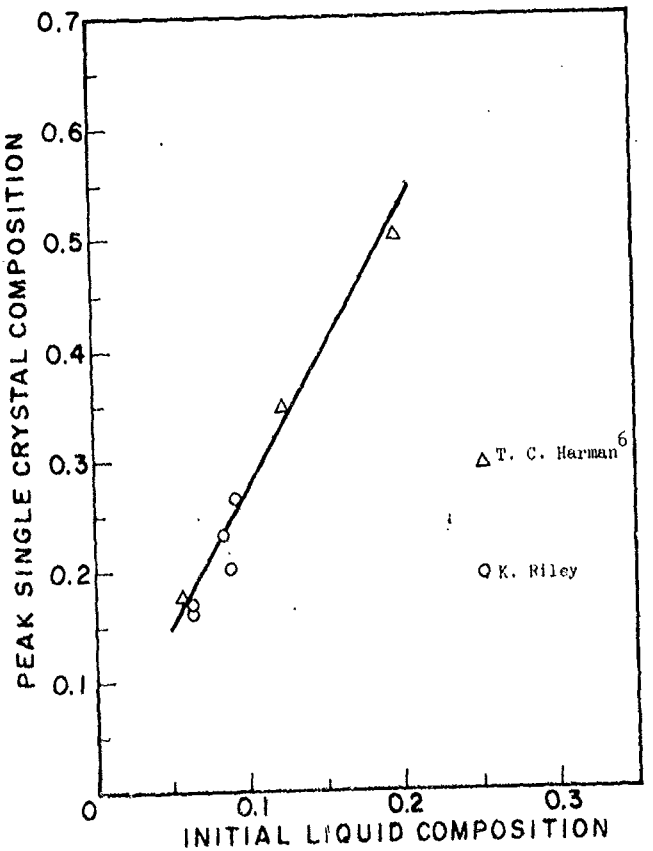

Figure 10. Relationship between the initial composition of the alloy and the peak composition in the single crystal region for crystals grown by the slush recrystallization method.

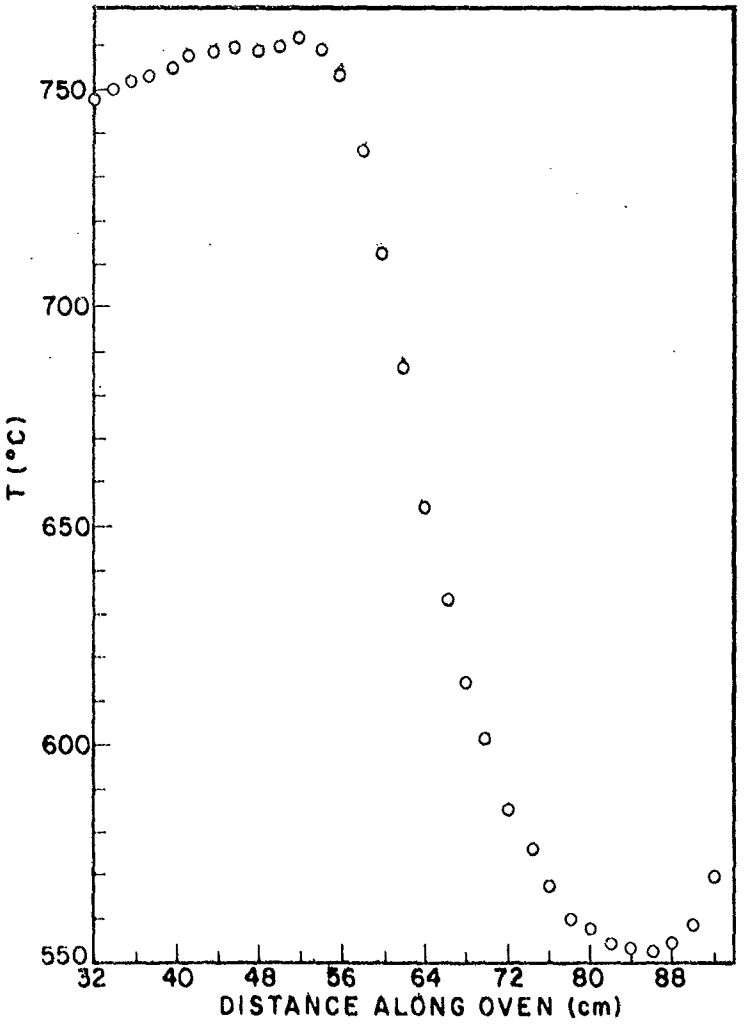

Figure 17. Temperature profile of the slush recrystallization oven

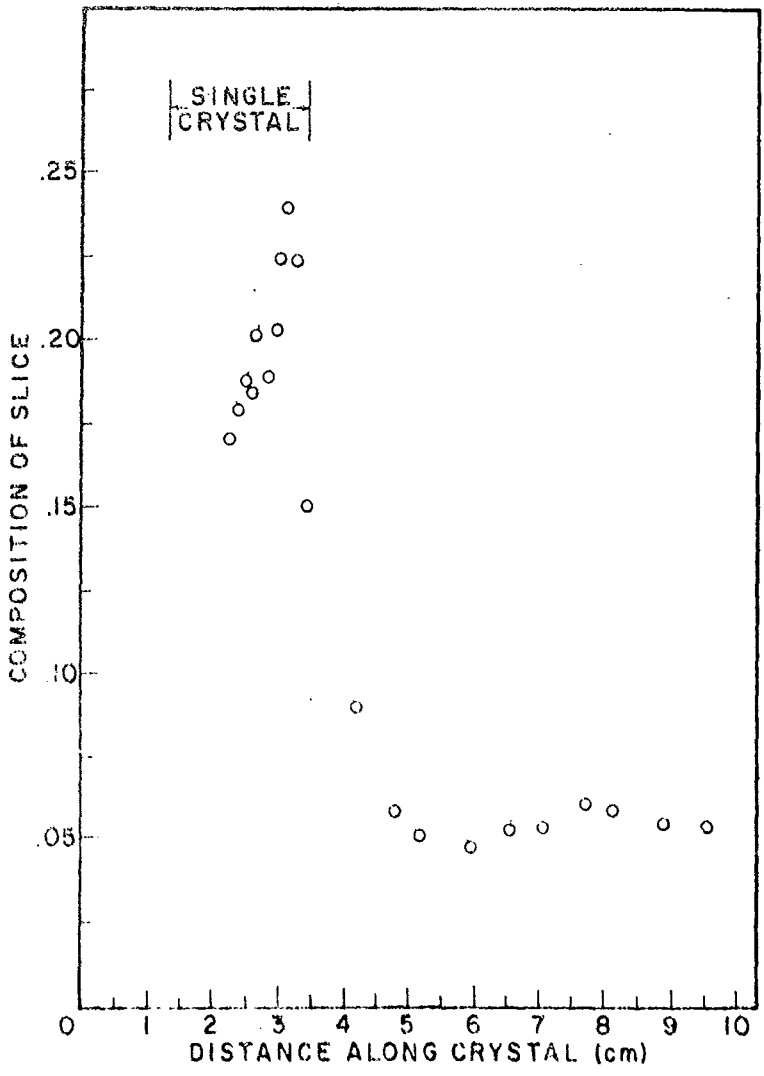

Figure 19. Composition profile of a crystal grown by the
[illegible] technique mark 4.

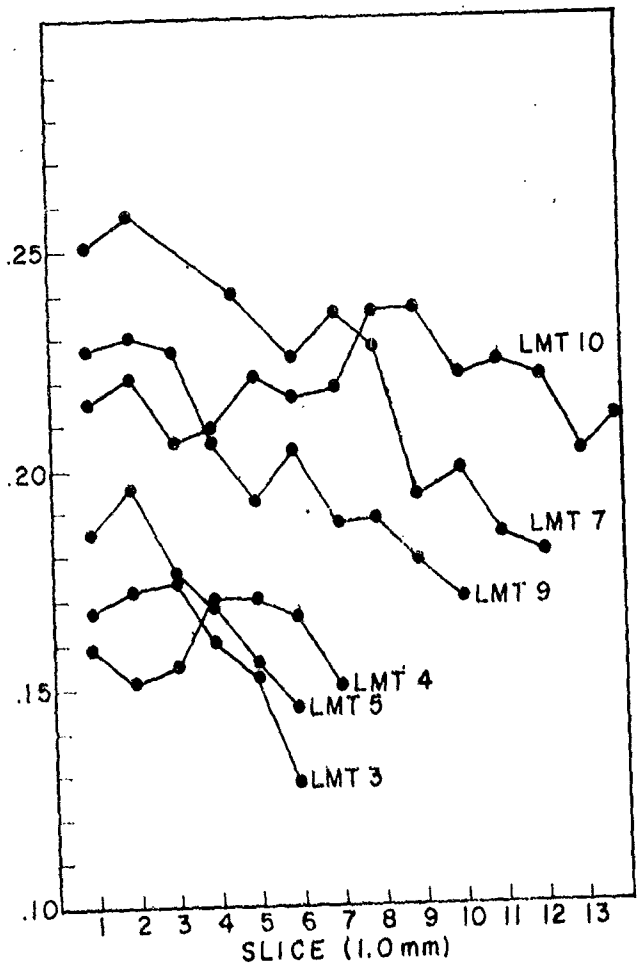

Figure 19. Resistivity profiles of the crystals grown by strain recrystallization. All slices are cut from the single crystal region.

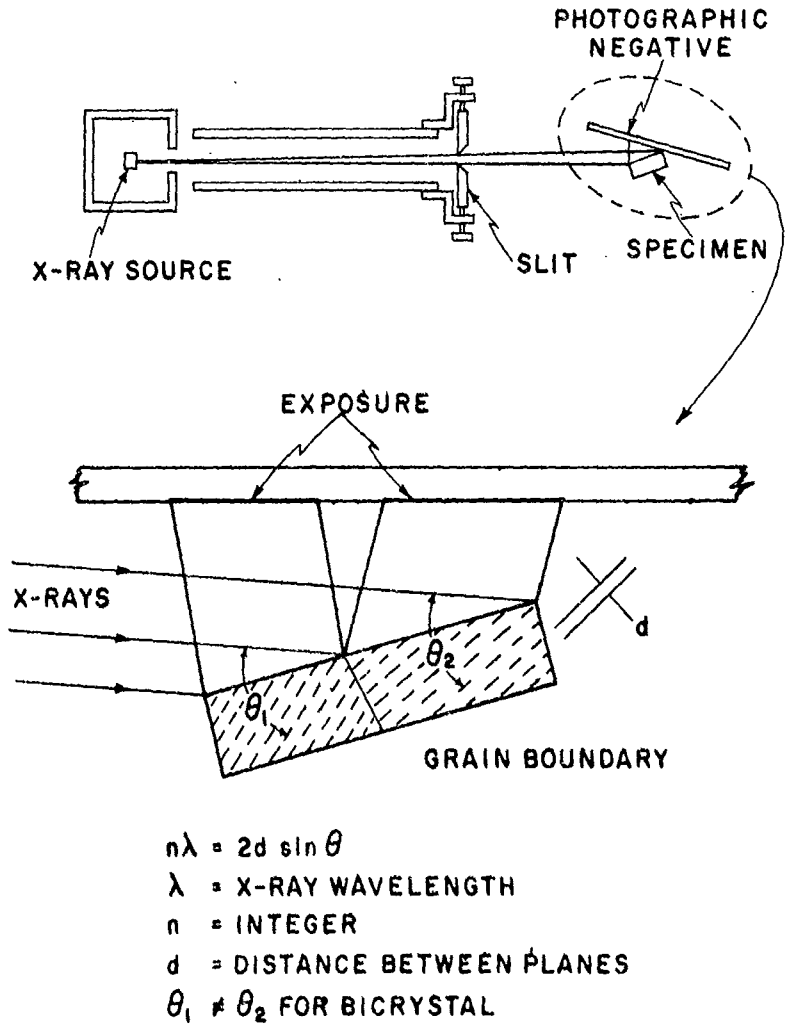

Figure 20. Berg-Barrett X-ray camera geometry.

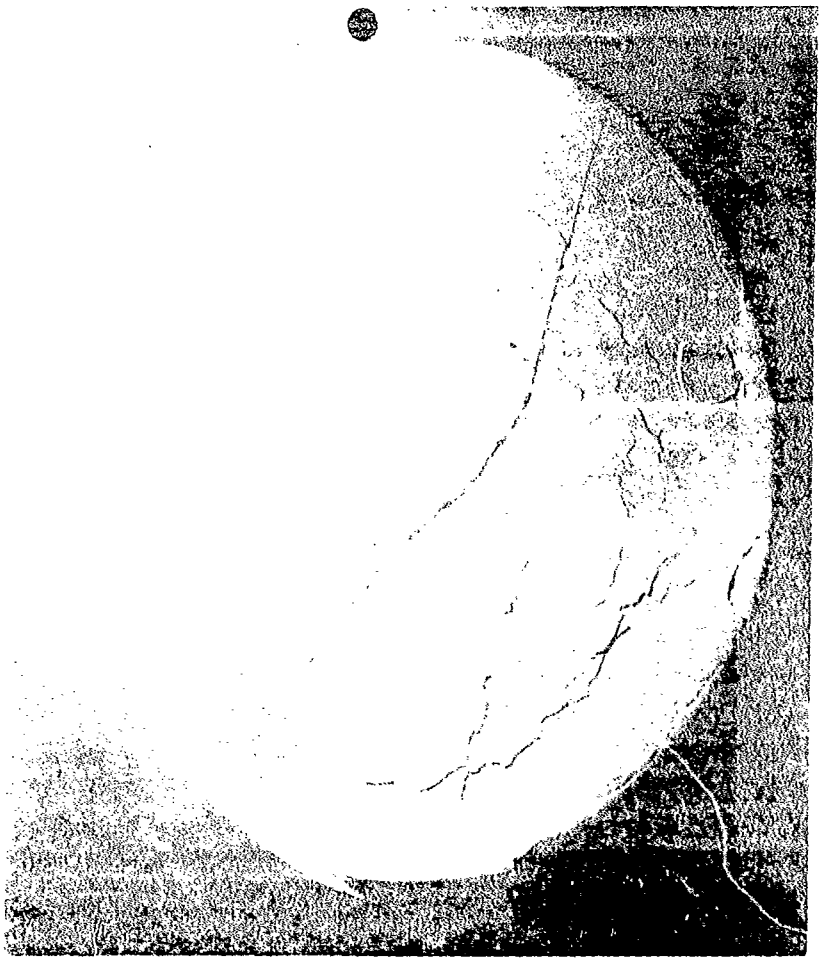

Figure XV Berg-Barrett topograph of IMT-3. Note the radial pattern of low angle grain boundaries.

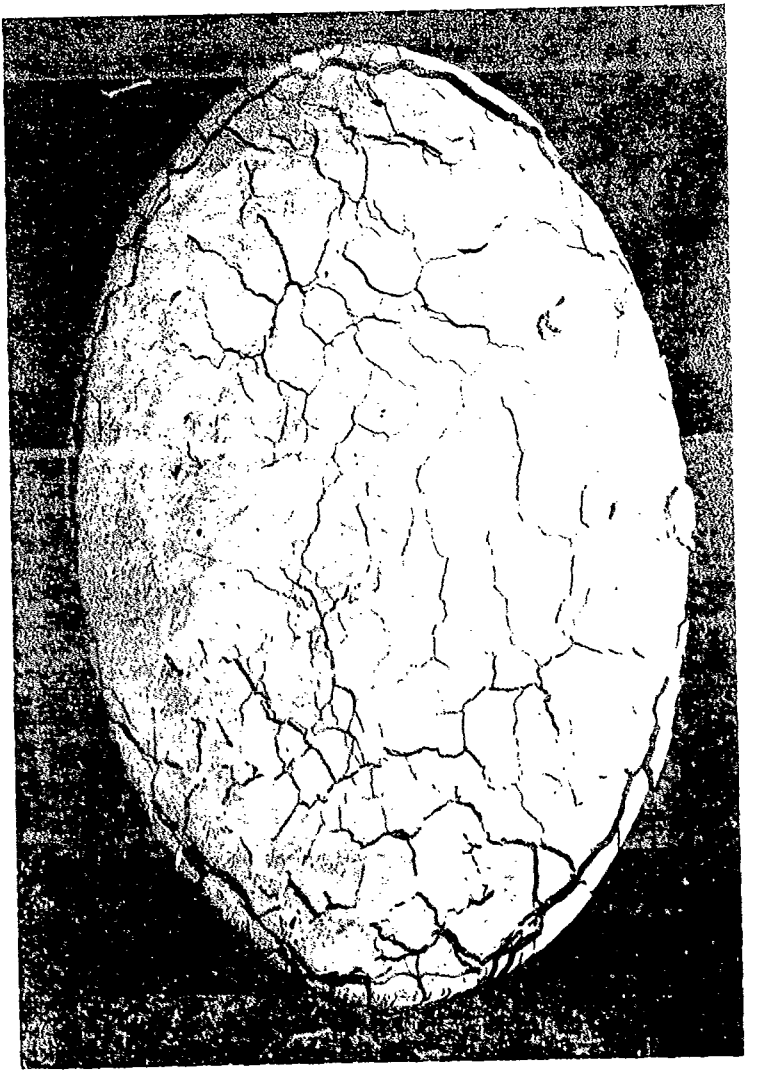

Figure 20. Bare-Barrett topograph of LMT-7.

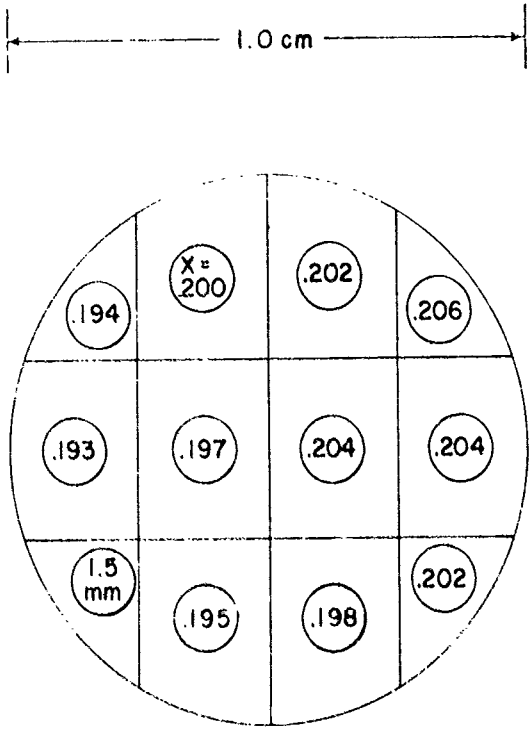

Figure [illegible] Matrix [illegible] for [illegible] surface area by [illegible] proportional area method. Composition was [illegible] by [illegible] measurements.

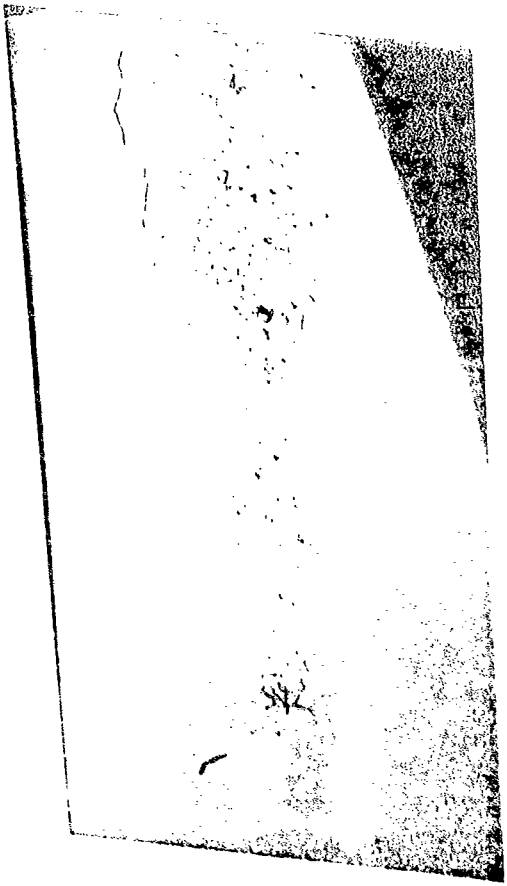

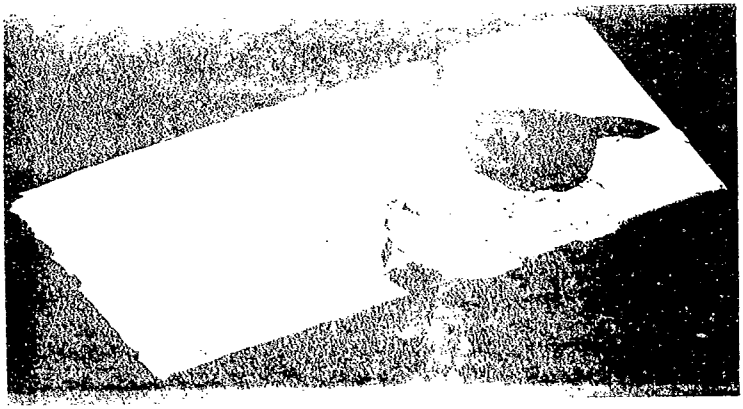

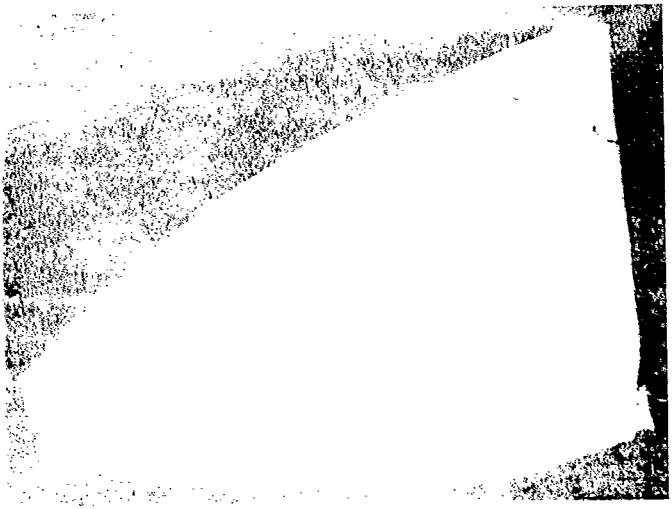

Figure [illegible] of [illegible] in the

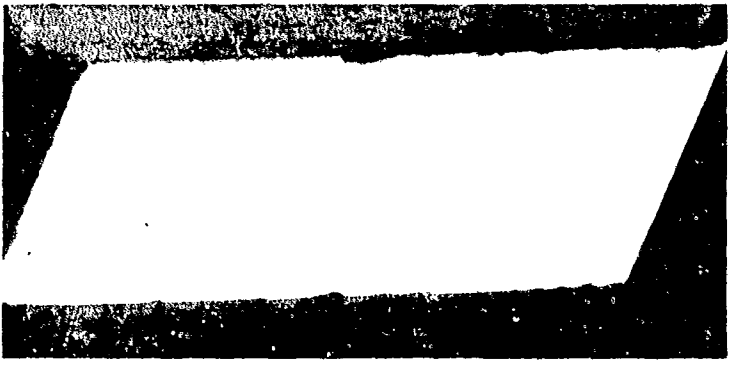

Figure 5. Cross-Everett topograph of the top half of SSR-51.

References

1. T. C. Harman, Physics and Chemistry of II-VI Compounds, M. Aven and J. S. Prener, editors (North Holland Publishing Co.; Amsterday, 1967).
2. B. E. Bartlett, J. Deans, and P. C. Ellen; J. Mater. Sci. 4, 266 (1969).
3. E. Z. Dziaba, J. Electro. Chem. Soc; 116, 104 (1960).
4. R. Ueda, O. Ohtsuki, K. Shinohara, and Y. Ueda, J. Cryst. Growth 13/14, 668 (1972).
5. L. N. Swink and M. J. Braw, Met. Trans. 1, 629 (1970).
6. T. C. Harman, J. Electron. Mater. 1, 230 (1972).
7. G. Cohen-Solal, Y. Margaing, F. Bailey, and M. Rodot, Compt. Rend. 261, 31 (1965).
8. O. N. Tufte and E. L. Stelzer, J. Appl. Phy. 40, 4559 (1969).
9. M. J. Brau, M. J. Williams, and J. P. Smith, Technical Report AFML-TR-73-88 (1973).
10. G. A. Chadwick, Metallography of Phase Transformations, (Crane, Russak and Co., Inc., New York 1972).
11. J. C. Woolley and B. Ray, J. Phys. Chem. Solids 13, 151 (1960).
12. K. T. Aust, The Art and Science of Growing Cyrstals, J. J. Gilman, editor (John Wiley and Sons, New York, 1963).
13. R. W. Cahn, Physical Metallurgy, R. W. Cahn, editor (John Wiley and Sons, Inc. New York 1965).
14. Cominco American, Spokane, Washington.
15. W. G. Pfann, Zone Melting, 2nd ed., (Wiley, New York, 1966).
16. M. Zeif and W. R. Wilcox, Fractional Solidification v.1, (Dekker, New York, 1967).

17. Sh. Movlanov and A. A. Kuliev Izv. Akad, Nauk Azerb. SSR, Ser. Fiz.-Mat. i Tekhn, Nauk 1, No. 3, 55 (1961).

18. Sh. Movlanov and A. A. Kuliev, Tr. Inst. Fiz., Akad, Naul Azerb. SSR 11, 35 (1963).

19. V. V. Krapukhin, I. S. Tsokov, and Yu. O. Mamaev. Izv. Akad. Nauk SSR, Neorgan. Materialy 2(7), 1180 (1966).

20. Krapukhin, V. V.; Mamaev, Yu.; Tsalev, D. L. Izv. Akad Nauk SSSR, Neorg. Mater., 6(8), 1401 (1970).

21. Roland V. Kujawa, Z. Physik. Chem. 232 (5-6), 425 (1966).

22. Vigdorovic, V. N.; Selin, A. A. Izv. Akad. Nauk SSSR, Metal. (2) 82 (1971).

23. B. Schaub, C. Potard, Proceedings of the International Symposium on CdTe a Material for Gamma-Ray Detectors, Strasbourg, France, 29-30 June 1971.

24. Model XH-A Serfass Hydrogen Purifier, Milton-Roy Co., St. Petersburg, Florida.

25. A. A. Kuliev and S. Movlanov, Izv Akad, Nauk SSSR, Met Toplivo, No. 1, 76 (1962).

26. T. B. Reed, Solid State Research/Lincoln Laboratory, No. 4, 17 (1968).

27. M. Hansen, Constitution of Binary Alloys, and ed., 840 (McGraw-Hill, New York, 1958).

28. V. K. Bonse, M. Hart, and J. B. Newkirk, Advan. X-Ray Anal. 10, 1 (1966).

29. W. W. Webb, Direct Observation of Imperfections in Crystals, J. B. Newkirk and J. H. Wernick, editors (Interscience, New York, 1962).

30. S. Weissmann and F. H. Kalmann, Techniques of Metals Research 2 pt 2, R. F. Bunshah ed., (Interscience, New York, 1969).

31. J. B. Newkirk, Trans. AIME 215, 483 (1959).

32. S. J. Lang and D. P. Pope, Rev. Sci. Inst. 44, 956 (1973).

33. G. M. Arnstein, M. I. Shapiro, and A. C. Raghuram, Rev. Sci. Inst. 43, 684 (1972).

34. S. B. Austerman and J. B. Newkirk, Advan. X-Ray Anal. 10, 134 (1966).

35. A. P. L. Turner, T. Vreeland, and D. P. Pope, Acta Cryst. A24, 452 (1968).

36. Blake Industries, Springfield, N. J.

37. Kodak Publication FI-3, 12/72.

38. D. M. Chizhikov, Cadmium , (Pergamon Press, N.Y., 1966).

39. J.L. Schmidt and C. J. Speerschneider, Infared Phy. 3, 247 (1963).

PART IV

APPENDIX

PHYSICAL REVIEW B VOLUME 8, NUMBER 12 15 DECEMBER 1973

Impurity and Lattice Scattering Parameters as Determined from Hall and Mobility Analysis in n-Type Silicon*

P. Norton,† T. Braggins, and H. Levinstein
Department of Physics, Syracuse University, Syracuse, New York 13210
(Received 4 June 1973)

The carrier concentration and mobility, as determined from the Hall effect, have been analyzed using a computer for a series of n-type silicon samples doped with Sb, P, and As. Mobility calculations, performed numerically, were based on the general treatment given by Herring and Vogt. Ionized-impurity scattering was calculated from two theories and compared with experiment. Lattice-scattering parameters for intervalley and accoustic modes were determined from a comparison of the results between theory and experiment, using as many as four intervalley phonons. The conclusions support the earlier work of Long, and a partial explanation of the disagreement with parameters determined from other measurements is suggested. Scattering by neutral impurities is found to be temperature dependent, unlike the theoretical model of Erginsoy.

I. INTRODUCTION

The Hall effect has been studied and analyzed in detail for a series of n-type silicon samples doped with antimony, phosphorus, and arsenic. Measurements were made on samples with doping densities ranging from 4×10^{13} to 8×10^{18} cm^{-3}, generally between 20 and 160 K, but over a wider temperature range in some cases. Almost all the data were taken in the high-magnetic-field limit so that Hall-factor corrections were not needed to determine the carrier concentration and drift mobility. We have analyzed both the carrier concentration and the mobility as a function of temperature. For the mobility analysis, the model of Herring and Vogt[1] was adopted to approximate the anisotropic nature of the conduction band. By using the results of both carrier-concentration and mobility analyses, we have been able to determine independently the density of compensating acceptors in these samples. Therefore, a quantitative comparison could be made between two models of ionized-impurity scattering, since this mechanism is coupled directly to the compensation density at low temperatures. In particular, we have compared the formulation of Brooks,[2] Herring, and Dingle[3] given for isotropic scattering, to the theory given by Samoilovich *et al.*,[4-6] calculated expressly for the case of spheriodal anisotropic bands.

Recent controversy over the intervalley lattice scattering process in silicon has been examined, and lattice scattering parameters have been fit to our data using a number of proposed models. Our two purest samples were used for this purpose. The results of this test are in good agreement with similar results of Long,[7] but do not support parameters determined from the analysis of photoconductivity and recombination-radiation experiments. In part, a reinterpretation of some optical experiments is suggested to clarify the present disagreement between optical and transport measurements.

We have found that neutral-impurity scattering is not well described by present theory. Experimental data for the mobility due to neutral-impurity scattering are shown to have a substantial temperature dependence, not accounted for by the Erginsoy[8] formulation of this problem. Part of this discrepancy is qualitatively resolved in terms of resonant scattering involving a possible bound state for the scattered electron as described by Sclar.[9] At higher temperatures, however, inelastic scattering may explain the temperature dependence. A much weaker neutral-impurity scattering interaction is apparent for arsenic-doped silicon than for antimony- or phosphorus-doped samples. No explanation could be found for this difference.

II. HALL-EFFECT MEASUREMENTS AND CARRIER-CONCENTRATION ANALYSIS

The experimental apparatus for measuring the Hall effect has been described previously.[10] In the case of silicon, bridge-type samples were contacted with welded gold wires containing 0.6-at.% Sb. Orientation of the magnetic field was in the ⟨111⟩ direction. The electric field was applied along the ⟨110⟩ or ⟨211⟩ axis.

Analysis of the Hall effect in silicon has been complicated by the Hall factor r which depends on the strength of the various scattering mechanisms, and the details of the band structure.[11] Long and Myers[12] used an iterative procedure to calculate the Hall factor in their analysis of carrier concentration and mobility as a function of temperature. In the limit of high magnetic fields, the Hall factor becomes unity and can be ignored. Since very little data have been published on the variation of the Hall coefficient with magnetic field, we ran a

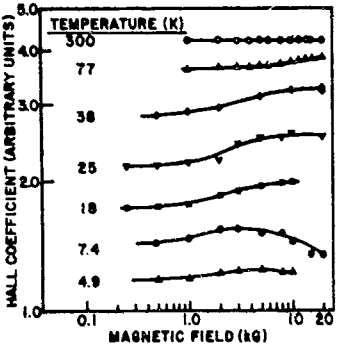

FIG. 1. Hall coefficient (arbitrary units) as a function of magnetic field, as measured for Si: As 1 (see Table I). The decrease in the Hall coefficient at high fields at the lowest temperatures is probably fictitious, due to the field dependence of the carrier lifetime.

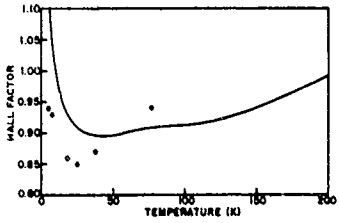

FIG. 2. Ratio of low-field to high-field Hall coefficient, as shown in Fig. 1 for Si: As 1, compared to the calculated Hall factor r. The Hall factor is calculated from Eq. (1), using the parameters determined for this sample listed in Table VI and mobility parameters for lattice scattering listed in Table IV.

series of magnetic field sweeps on an arsenic-doped lightly compensated sample. Figure 1 shows the Hall coefficient as a function of magnetic field strength for a number of temperatures in the range 5–300 K. The data below about 20 K were obtained by magnetic field sweeps of the photo-Hall coefficient. 300-K background illumination, filtered by cold InSb, restricted the radiation to $\lambda > 5$ μm. The slight decrease in the photo-Hall coefficient at the highest magnetic fields, as seen in Fig. 1, is probably due to the Hall voltage approaching the region where carrier lifetime becomes dependent on the electric field. The ratio of the low- to high-field coefficient is shown in Fig. 2 as a function of temperature. For comparison, we have calculated the Hall factor r using the expression given by Herring and Vogt,[1] and in agreement with Long[7]:

$$r = \frac{3(\langle\tau^4\rangle/m_\perp^{*2} + 2\langle\tau_\perp^2\tau_\parallel\rangle/m_\perp^{*2}m_\parallel^*)}{[2(\langle\tau_\perp\rangle/m_\perp^*) + \langle\tau_\parallel\rangle/m_\parallel^*]^2}, \qquad (1)$$

where $\perp$, $\parallel$ refer to the transverse and longitudinal directions of the ellipsoidal bands and τ and m^* are the relaxation times and masses of the electrons. These will be fully explained in Sec. III. It should be mentioned that a somewhat less exact expression was used for calculating r by Long and Myers, since isotropic scattering was assumed.[19] As can be seen, there is fair agreement between the values deduced from the field sweep data and those calculated from Eq. (1). Disagreement at the lowest temperatures may be due, in part, to a ionized-impurity scattering in this region, and also from the lack of an adequate theory to correctly describe neutral-impurity scattering which was quite strong in this sample. For our purposes, we have used data taken from the high-field limit and set the Hall factor equal to unity. This approximation is good for temperatures below about 100 K, depending on the strength of impurity scattering. We have used data up to about 160 K in some cases without correction. This should introduce very little error, even though the high-field limit cannot quite be reached at 20 000 G, the Hall factor approaches unity in this temperature region. Figures 3 and 4 show the measured mobilities for phosphorus-doped samples (except Si: P 6); and

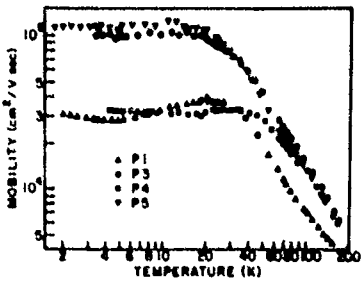

FIG. 3. Mobilities as measured for four phosphorus-doped silicon samples. Sample properties are listed in Table I. Open data points are measured with thermal carrier generation. Solid data points are taken with the sample illuminated with 300-K background radiation

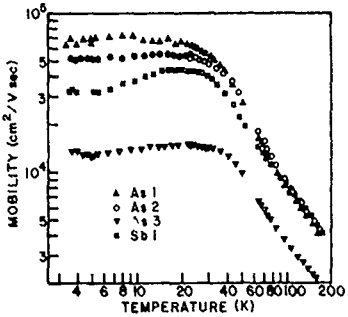

FIG. 4. Mobilities as measured for three arsenic-doped and one antimony-doped silicon samples.

for arsenic- and antimony-doped samples. A rough estimate of the high-field limit region is found from the condition on the mobility-field product $\mu E > 1\times10^{8}$ G cm^2/V sec. Section III deals directly with the mobility analysis of these samples. We now present the theory and results of the analysis of carrier concentration as a function of temperature.

The twelvefold (including spin) $1S$ state of group-V donors[14,15] in silicon is split into a twofold-degenerate ground state, $1S(A_1)$, and two groups of higher states, $1S(T_1)$ and $1S(E)$. In addition, excited states of these impurities lie closer to the band edge. Kohn[14] has calculated the excited-state energy levels and degeneracies, while the $1S$-state splittings have been measured by Aggarwal.[16]

These energy states are related to the carrier concentration n, donor and acceptor densities N_d and N_a, and the density of states in the conduction band N_c, as[17,18]

$$\frac{n(n+N_a)}{N_d-N_a-n} = \frac{N_c e^{-E_d/kT}}{2+6e^{-D/kT}+4e^{-(D+d)/kT}+e^{-E_d/kT}\sum_i g_i e^{E_i/kT}}, \tag{2}$$

where E_d is the energy of the ground state $[1S(A_1)]$, D and d are the $1S$-state splittings,[16] and E_i and g_i refer to the energy and degeneracy of the excited states. We have included three groups of excited states, near 10, 6, and 3 meV. Thus

$$\sum_i g_i e^{E_i/kT} = 24e^{-0.0120/kT}+36e^{-0.0066/kT}+24e^{-0.0036/kT}. \tag{3}$$

Equation (2) was used to determine N_d, N_a, and E_d by fitting the measured temperature dependence of the carrier concentration in a manner described elsewhere.[10] N_c was taken to be $5.29\times10^{15}T^{3/2}$ cm^{-3}, as calculated for a density-of-states effective mass of $0.32m_0$.

The results of fitting the carrier concentration as a function of temperature to Eq. (2) for the various samples are presented in Table I. With two exceptions, we have fixed the value of N_c and only varied N_d, N_a, and E_d. In the case of our two purest samples, Si : P 5 and Si : P 6, we have also fit them with N_c variable, and both results are shown in Table I. As can be seen, there is very little change in any of the parameters when N_c is permitted to vary. This was not necessarily the case in the less pure samples, for which the exhaustion region ($n \approx N_d - N_a$) was not reached be-

TABLE I. Carrier-concentration-analysis results for samples fit to Eq. (2).

Sample	N_d (cm^{-3})	N_a (cm^{-3})	E_d (meV)	$N_c/T^{3/2}$ (K$^{-3/2}$ cm^{-3}) (10^{15})	m^*/m_0	Resistivity at 300 K (Ω cm)	Stand dev. of fit (10^{-3})
Si : P 1	9.5×10^{15}	4.2×10^{15}	45.64	5.29[a]	0.3218[a]	0.66	4.17
Si : P 3	2.5×10^{14}	2.3×10^{13}	45.14	5.29[a]	0.3218[a]	17.1	0.55
Si : P 4	9.6×10^{14}	2.0×10^{14}	45.39	5.29[a]	0.3218[a]	4.76	1.02
Si : P 5	3.3×10^{14}	6.6×10^{13}	45.38	5.29[a]	0.3218[a]	13.6	0.56
	3.3×10^{14}	6.6×10^{13}	45.33	5.18	0.3175	13.6	0.57
Si : P 6	4.3×10^{13}	7.7×10^{12}	45.42	5.29[a]	0.3218[a]	123.	0.61
	4.3×10^{13}	7.1×10^{12}	45.42	4.82	0.3026	123.	0.48
Si : As 1	1.4×10^{16}	4.0×10^{15}	53.64	5.29[a]	0.3218[a]	0.43	2.75
Si : As 2	7.9×10^{15}	4.3×10^{15}	52.54	5.29[a]	0.3218[a]	0.66	1.88
Si : As 3	7.5×10^{15}	1.8×10^{15}	52.52	5.29[a]	0.3218[a]	0.13	5.36
Si : Sb 1	7.4×10^{15}	6.3×10^{14}	42.59	5.29[a]	0.3218[a]	0.68	2.53

[a]Value fixed.

low 160 K.

In several of the more impure samples having donor concentrations of about 10^{16} cm^{-3} or more, we have also tried fits with one or more data points taken at 300 K. In this case the value of n at 300 K was calculated by several methods. First, the measured resistivity was used to give a value of N_d from the graph published by Irvin.[19] Using the appropriate activation energy, we calculated n/N_d at 300 K and obtained a value of n by multiplying this ratio by N_d. The second method used the Hall coefficient measured in the low-field limit at 300 K, and corrected by the Hall factor calculated from Eq. (1), to give a value of n. The third method used the measured Hall coefficient and the Hall mobility at 300 K. Instead of calculating the Hall factor from Eq. (1), the drift mobility was calculated and the ratio of Hall to drift mobility was used as the Hall factor to correct the Hall coefficient. All three methods gave similar results, although the first and third rely on good geometry[20] for an accurate measure of the resistivity. Adding a data point at 300 K had only a slight effect on the fit, for example, Si: As 1 showed at most a 5% decrease in N_d and an 8% increase in N_a from the values obtained without a data point above 160 K. This check provides reasonable confidence in extrapolating the fitting procedure to samples for which the exhaustion region could not be measured in the high-field limit.

III. MOBILITY ANALYSIS

A. General Formulation

We have analyzed the mobility in these same samples in order to determine the density of compensating acceptors N_a and the values of various other parameters associated with the scattering mechanisms. N_a can be deduced from the strength of ionized-impurity scattering, especially at low temperatures where $n \approx N_d$ and lattice scattering is relatively weak. To do this, however, one needs to have an accurate description not only of ionized-impurity scattering in a many-valley band structure, but also lattice and neutral-impurity scattering. The anisotropy of the effective mass in silicon produces different scattering rates for the transverse and longitudinal directions in the ellipsoidal valley. Since each scattering process has a different dependence on the effective mass of the carriers, it is not possible to select an average effective mass suitable for all three types of scattering. We have separated the scattering time averages into two parts, as generally prescribed by Herring and Vogt,[1] and as done by Brooks[2] in treating lattice scattering for ellipsoidal bands. This type of treatment is valid when the scattering is either energy conserving or momentum randomizing. The mobility in this case can be written

$$\mu = \tfrac{1}{3}e\left[\langle\tau_\parallel\rangle/m_\parallel^* + 2(\langle\tau_\perp\rangle/m_\perp^*)\right], \tag{4}$$

where $\parallel$ and $\perp$ refer to the longitudinal and transverse directions, respectively. Each average of the scattering time is computed numerically by approximating

$$\langle\tau\rangle = (4/3\sqrt{\pi})\int_0^\infty e^{-x}x^{3/2}\tau(x)dx \tag{5}$$

with Simpson's rule, where $x = \epsilon/kT$. In using Simpson's rule we have taken the integral from 0 to $25kT$, and used 75 intervals; or used two regions, from 0 to $6kT$ with 24 intervals and 6 to $25kT$ with 19 intervals. The accuracy of the numerical integration using these choices was compared with taking the integral from 0 to $25kT$ in 500 intervals. Over the temperature range from 5 to 500 K, the maximum error was 1.7% (at 500 K, $N_d - 1\times10^{13}$ cm^{-3}, $N_a = 1\times10^{10}$ cm^{-3}) in the first case with one region; and 1.3% (at 300 K, $N_d = 1\times10^{11}$ cm^{-3}, $N_a = 1\times10^{10}$ cm^{-3}) in the second case with two regions. For these comparisons we used hypothetical samples with a range of donor concentrations from 10^{10} to 10^{17} cm^{-3}, having only a small amount of compensation. Since the error was almost always less with the two region integration, we used it in preference to the single region. This was also considerably faster.

The lattice scattering mechanism in n-type silicon has been the subject of much recent discussion. Electron scattering mechanisms by lattice modes are of two types: intravalley scattering by acoustic phonons, and intervalley scattering to either parallel valleys (g type) or perpendicular valleys (f type). The allowed intervalley modes have recently been agreed upon, at least theoretically, although certain experimental evidence suggesting possible scattering by forbidden intervalley modes remains to be explained. We will discuss this later Sec. IV C. In general, the transverse lattice scattering time can be written

$$\frac{1}{\tau_{L\perp}} = \frac{1}{\tau_0 T^{-3/2}\epsilon^{-1/2}}\left(1 + \sum_i \left[\alpha_i(\theta_i/T)\left[n_i(1-\theta_i/T\epsilon)^{1/2} + (n_i+1)(1-\theta_i/T\epsilon)^{1/2}\right]\right]\right), \tag{6}$$

where θ_i is the temperature of the ith intervalley phonon, $n_i = [\exp(\theta_i/T) - 1]^{-1}$, and α_i is the relative coupling strength of the electrons to the ith intervalley mode compared to the transverse acoustic mode. Long and Myers[21] determined the ratio of the acoustic mode scattering strength in the longitudinal direction to be $\frac{1}{3}$ that of the transverse direction. This has been confirmed by Neuringer and Little[22]

also using magnetoresistance measurements, and by recent experiments involving cyclotron resonance of hot electrons as measured by Kazanskii and Koshelev.[23] Intervalley scattering is assumed to be isotropic. Therefore, the scattering time in the longitudinal direction is

$$\frac{1}{\tau_{L\,0}} = \frac{1}{\tau_{L\,1}} + \frac{1}{2\tau_0 T^{-3/2} x^{-1/2}} \quad . \tag{7}$$

Neutral-impurity scattering has been calculated from Erginsoy's[8] expression derived from the study of low-energy elastic scattering of electrons from hydrogen. In the zero-order phase-shift approximation, this type of scattering is independent of carrier energy. However, it has been shown that for large concentrations of neutral impurities, coherent scattering can take place,[10,24,25] so that the scattering time may not depend directly on the inverse neutral donor concentration. Also, group-V donors in silicon are not strictly hydrogenic. Therefore, we have scaled the neutral-impurity scattering time with an adjustable constant A to be determined from the analysis of the data. With this provision, the neutral-impurity scattering time is

$$\frac{1}{\tau_N} = \left(\frac{\kappa\hbar^2}{m_t^* e^2}\right)\left(\frac{20\hbar}{m_c^*}\right)\frac{N_R}{A} = \frac{4.57\times10^{-6}}{(m_t^*/m_0)A}\,N_N \,, \tag{8}$$

where $N_N = N_A - N_D = n$ is the density of neutral donors, m_t^* is the effective mass of the conduction electron (m_l^* or m_t^*), and m_c^* is the geometric mean mass which for silicon is $0.32m_0$.

Ionized-impurity scattering has been calculated by Brooks,[1] Herring, and Dingle.[3] This formula has been quite successful in describing ionized-impurity scattering in both silicon[12] and germanium.[10] The ionized-impurity-scattering time is

$$\frac{1}{\tau_I} = \frac{N_I \pi e^4}{(kT)^{3/2}\kappa^2(2m_t^*)^{1/2}\gamma_{1,3/2}}\left[\ln(b+1) - b/(b+1)\right]$$

$$= \frac{1.68\times10^{-7}N_I}{T^{3/2}(m_t^*\,m_0)^{1/2}\gamma_{1,3/2}}\left[\ln(b+1) - b/(b+1)\right], \tag{9}$$

where

$$b = \frac{2\kappa m_t^*(kT)^2 x}{\pi\hbar^2 q^2 N'} = \frac{5.17\times10^{14}(m_t^*\,m_0)\,T^2 x}{n'} \tag{10}$$

and

$$n' = n + (n+N_A)[1-(n+N_A)/N_I] \,. \tag{11}$$

N_I is the total density of ionized impurities, namely, $2N_A + n$.

A somewhat less known treatment of ionized-impurity scattering given by Samoilovich *et al.*[26,27] has also been evaluated. The theory, similar to earlier work by Ham,[28] specifically treats anisotropic ionized-impurity scattering in a prolate spheroidal band. Neuringer and Long[27] have interpreted magnetoresistance data with respect to the relative ratio of longitudinal to transverse scattering time predicted from the theory, but we do not know of any reference dealing with the absolute magnitudes of the scattering times as predicted by Samoilovich *et al.* The expressions given here have been evaluated specifically for n-type silicon, and the reader is referred to the original papers for a complete description. With b_a evaluated as in Eq. (10), ($m_c^* = m_t^*$), we find

$$\frac{1}{\tau_{I\,1}} = \frac{4.28\times10^{-2}N_I}{(Tx)^{3/2}(1+g_1)}\left[\ln(b_a) - 2.34 + 7.88/b_a\right], \tag{12}$$

$$\frac{1}{\tau_{I\,0}} = \frac{1.18\times10^{-2}N_I}{(Tx)^{3/2}(1+g_0)}\left[\ln(b_a) - 1.75 + 4.64/b_a\right], \tag{13}$$

where g_0 and g_1 have been given graphical representation in Ref. 4. We have approximated these by the following expressions:

$$g_0 = 0.192 - 0.067\left[5/\log_{10}(b_a)\right], \tag{14}$$

$$g_1 = 0.03\left[\log_{10}(b_a) - 1\right]. \tag{15}$$

Since these functions are small corrections, we have evaluated g_0 and g_1 outside the integral, calculating b_a in this case from Eq. (10) using $x = 3$.

The total scattering time to be averaged in Eq. (5) is defined

$$\tau(x) = \left(\frac{1}{\tau_L} + \frac{1}{\tau_N} + \frac{1}{\tau_I}\right)^{-1}, \tag{16}$$

where the transverse and longitudinal averages are computed as required in Eq. (4).

Before going ahead to the results of the analysis, it is important to note that none of the several scattering mechanisms can be totally isolated in realistic material. Therefore, the results presented in Secs. III B–III D dealing with a particular scattering mechanism will have interacted with each other during the several months taken to complete this work. These interactions were always present, and although we cannot describe them totally, it is hoped that this remark will explain why minor modifications appear, for example, in the choice of A, during the development of our treatment of lattice scattering.

B. Lattice Scattering Results

Having presented the formulation of the mobility calculation, we must evaluate the lattice scattering parameters τ_0 and the n_i's given in Eqs. (6) and (7). We initially used the model proposed by Rode,[29] model 2, with only one intervalley phonon ($\theta_1 = 540$ K). Therefore, the parameters calculated by Long[4] could not be adopted, since his model assumed two intervalley phonons with temperatures 630 and 190 K. Also, the mobility due to pure lattice scattering is not clearly established in the literature. Mea-

sured mobilities range from 18 000 to 24 000 $cm^2/V sec$ at 77 K,[28] with additional uncertainties arising when the Hall factor and impurity scattering must be taken into account. We decided initially to determine τ_0 from the data taken on our two purest samples, by fitting τ_0 as a parameter using data from 20 to 77 K.[29] Both of these samples, Si: P 5 and Si: P 6, were cut with bridge shapes favorable to an accurate determination of the distance and width between resistivity arms, so that geometrical errors should be small.[30] For this fit, w_1 was fixed at 1.5 (w_{2-4} were fixed at zero) and since intervalley scattering lowers the mobility by less than 3% for this model at 77 K, this choice was unimportant. We found good agreement for both samples, using several trials with parameters N_d and A both fixed and variable. Using the temperature range from 77 K down, we found τ_0 to be 3.56×10^{-9} sec, within 1.7%. In addition, we ran a second series of fits with data from a more restricted temperature range, 20–41 K. The average values of τ_0 were 2.7% and 1.1% higher for samples Si: P 5 and Si: P 6, respectively, when only data from below 41 K was used. With τ_0 chosen to be 3.56×10^{-9} sec, we then ran a series of calculated mobilities at 300 K, varying w_1. From this series, we selected w_1 to agree with the measured drift mobility at 300 K. Drift-mobility experiments[31–34] give mobilities between 1350 and 1500 $cm^2/V sec$ at room temperature. We chose to use $w_1 = 1.45$, giving a mobility of about 1450 at 300 K, consistent with our own measurements which will be described later.

The two temperature ranges used above to determine τ_0 were chosen deliberately to see if there was a significant amount of intervalley scattering by lower temperature phonons (LA g type or TA f type) as suggested by several authors, but forbidden by the calculated selection rules. If lower temperature phonons were contributing significantly, we would expect the fitted values of τ_0 to be higher using data from the temperature range below 41 K. Also, the fit would be skewed when the temperature range up to 77 K was used, since the adjustment of τ_0 alone could not compensate for a low-temperature intervalley mode. Although there is only a slight increase in the average value of τ_0 using only data below 41 K, the fit over the 20–77-K range remained slightly skewed even when N_d and A were permitted to vary. Also, fitted values of N_d were lower when the full range of 20–77 K was used, indicating an adjustment of N_d in attempt to raise the mobility at low temperatures with respect to higher temperatures. This discrepancy, although not prominent, indicated a possible weak contribution from a low-temperature intervalley phonon.

At this point in our work it became apparent that [illegible] would be necessary to characterize the intervalley scattering process. We therefore extended the range of measurements on our purest sample, Si: P 6, to room temperature, measuring the Hall constant at both 600 and 20 000 G, along with the resistivity. Since the analysis of carrier concentration could be carried out with data taken below 100 K for this sample, the carrier concentration above 100 K could be accurately calculated from the values of N_d, N_a, and E_d as given in Table I. From this, we deduced the Hall factor and mobility up to room temperature, without relying on Eq. (1) which assumes an accurate knowledge of the scattering times. Data taken between 77 and 315 K were then compared to model I, which we will now call model I(a). Deviations between the data and model I(a) were skewed by 5 to 6%. Two modifications were then attempted on model I. First, we tried using a phonon temperature of 670 K rather than 540 K [model I(b)]. For this choice a coupling constant of 2.0 was needed to give agreement to drift mobility at 300 K. Comparison with our data above 77 K again gave deviations on the order of 6%. Next, we used a combination of both these intervalley phonons, $\theta_1 = 540$ K and $\theta_2 = 670$ K [model I(c)]. By computer adjustment of w_1 and w_2, the maximum error was reduced to about 3% over the temperature range above 77 K.

Having exhausted the possibilities of model I, we returned to the low-temperature region below 77 K to see if a low-temperature phonon would appreciably improve the fit in this region. A second model, model II, was calculated using a low-energy phonon corresponding to f-type scattering by a TA phonon, in addition to the allowed higher temperature phonons. For this series we fixed w_1 and w_2 at 0.6 and 1.2, respectively, as determined from model I(c) fit above 77 K. Using data from 20 to 77 K, and with θ_3 chosen to be 190 K,[7] we fit both τ_0 and w_3, with N_d both fixed and variable. Good agreement was again obtained between samples Si: P 5 and Si: P 6, and the results of fits below 77 K are given in Table II, together with the standard deviations. The marked improvement in the standard deviation when the forbidden intervalley phonon was included is good evidence of its importance, even though it is weakly coupled. Figures 5 and 6 illustrate the relative error between measured and calculated mobilities for these two samples, with and without the addition of a low-temperature intervalley phonon.

With the importance of a low-energy phonon established, we again went to the temperature region above 77 K and fit model II with τ_0, w_1, and w_2 variable. With this freedom, agreement was obtained to better than 2%, with the coupling constant of w_1 fitted to essentially zero ($w_1 < 0.001$), and w_2 fit to about 1.9. Since w_3 was fixed at 0.15

TABLE II. Mobility lattice parameters fit below 77 K.

Model	Sample	τ_0 (sec^{-1}) (10^{-8})	w_1[a,b]	w_2[a,b]	w_3[b]	A	N_a (cm^{-3}) (10^{12})	Stand. dev of mobility fit (10^{-2})	Temperature range (K)
I	Si:P 5	3.57	1.5	0	0[a]	5.9	9.2	5.37	20–77
I	Si:P 5	3.57	1.5	0	0[a]	5.3	8.6[c]	4.02	20–77
I	Si:P 5	3.62	1.5	0	0[a]	2.0[a]	6.0	1.04	20–77
I	Si:P 6	3.54	1.5	0	0[a]	14.2	6.2	2.35	20–77
I	Si:P 6	3.55	1.5	0	0[a]	30.5	7.7[a]	5.23	20–77
I	Si:P 6	3.53	1.5	0	0[a]	2.0[a]	5.3	1.43	20–77
I	Si:P 5	3.62	1.5	0	0[a]	4.8	8.6[a]	4.47	20–41
I	Si:P 5	3.69	1.5	0	0[a]	2.0[a]	6.5	0.32	20–41
I	Si:P 6	3.60	1.5	0	0[a]	25.5	7.7[a]	6.44	20–41
I	Si:P 6	3.60	1.5	0	0[a]	2.0[a]	5.8	0.25	20–41
II	Si:P 5	3.99	0.6	1.2	0.17	2.0[a]	8.6[a]	1.21	20–77
II	Si:P 5	3.79	0.6	1.2	0.08	2.0[a]	7.0	0.48	20–77
II	Si:P 6	3.92	0.6	1.2	0.19	2.0[a]	7.7[a]	1.33	20–77
II	Si:P 6	3.73	0.6	1.2	0.10	2.0[a]	6.3	0.73	20–77

[a]Value fixed.

[b]Coupling constants for intervalley phonons; $\theta_1 = 540$ K, $\theta_2 = 670$ K, $\theta_3 = 190$ K.

during this fit, the result is identical to that determined by Long,[7] except for a slight difference in the value of θ_3. Very little change was observed when all four variables (τ_0, w_1, w_2, and w_3) were permitted to vary, and data between 20 and 315 K was used. Results in the higher-temperature region are summarized in Table III.

At this time it had become evident not only from these samples, but also from more heavily doped ones, that ionized-impurity scattering as calculated from the expression given by Brooks, Herring, and Dingle [Eqs. (9)–(11)] was overestimating the ionized-impurity-scattering strength and that consequently whenever N_a was permitted to vary, values considerably smaller than those determined in Sec. II were obtained. Therefore, the ionized-impurity-scattering formulas given by Samoilovich *et al.* were substituted [Eqs. (12)–(15)] after it was clear that they gave a substantial improvement. We also decided to include the possibility of a fourth intervalley phonon with a characteristic temperature of 307 K, (this would be LA g-type, but not quite at 0.34X as expected) as inferred from optical measurements.[15] These changes defined what we shall call model III. With N_a, τ_0, and four w_i's variable, we fit the data on Si:P 6 between 20 and 315 K. Only w_2 and w_3 ($\theta_2 = 670$ K, $\theta_3 = 190$ K) were found to be important, but now N_a fit very close to the value determined in Sec. II. We also fit Si:P 5 between 20 and 77 K, varying N_a, τ_0, w_2, and w_3. Again, w_3 was found to be unimportant and N_a fit very close to the result for this sample found in Sec. II. Model-III results are summarized in Table IV for these two samples, and the relative errors are shown in Figs. 7 and 8.

As an additional check on our results, we calculated the Hall factor for Si:P 6 using Eq. (1) and with parameters determined from several models. These are compared to our data taken at 600 and 20 000 G between 77 and 315 K, as shown in Fig. 9. None of the models gives completely satisfactory agreement, with model III giving the best results below 100 K, and model I(a) giving the best agreement from 100 to about 250 K. It should be noted that the data taken at 20 000 G will not be

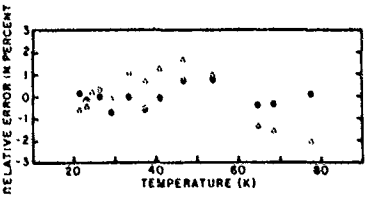

FIG. 5. Relative error in percent between calculated and measured mobility for Si:P 5 with and without the inclusion of a low-temperature intervalley phonon ($\theta_3 = 190$ K). The relative error is defined as Error $= [(\mu_m - \mu_c)/\mu_m] \times 100$, where μ_m is the measured mobility, and μ_c is the calculated mobility. The open triangles show the result without the inclusion of θ_3. The solid circles show the improved fit with θ_3 included. Values of parameters are the following: fixed, $N_a = 3.28 \times 10^{14}$, $A = 2.0$, $G = 1.0$, $w_1 = 0.6$, $w_2 = 1.2$; fit, open triangles, $N_a = 5.9 \times 10^{13}$, $\tau_0 = 3.62 \times 10^{-8}$ ($w_3 = 0.0$ fixed); fit, solid circles, $N_a = 7.0 \times 10^{13}$, $\tau_0 = 3.79 \times 10^{-8}$, $w_3 = 0.08$.

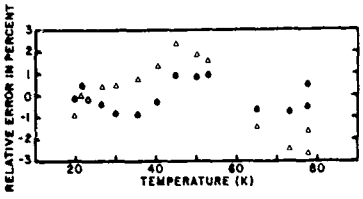

FIG. 6. Relative error as in Fig. 5, for sample Si: P 6. Values of the parameters are the following: fixed, $N_d = 4.29 \times 10^{13}$, $A = 2.0$, $G = 1.0$, $w_1 = 0.6$, $w_2 = 1.2$; fit, open triangles, $N_d = 5.3 \times 10^{12}$, $\tau_0 = 3.53 \times 10^{-9}$ ($\omega_3 = 0.0$ fixed); fit, solid circles, $N_d = 6.3 \times 10^{12}$, $\tau_0 = 3.73 \times 10^{-9}$, $w_3 = 0.10$.

in the low-field limit below 150 K.

In conclusion, we show in Fig. 10 the experimental data on Si: P 6, including photo-Hall data omitted from the fitting procedure, together with the calculated mobility curve based on model III.

C. Ionized-Impurity-Scattering Results

Ionized-impurity scattering has been treated using the expression given by Brooks, Herring, and Dingle in most of the recent experimental[15,12,36,37] and theoretical[28] work on this subject. However, as has been mentioned in Sec. III B, the agreement in fitting N_d was less than satisfactory for our purest samples Si: P 5 and Si: P 6 when the expression given by these authors was used. It was also tried on several more heavily doped samples, having stronger contributions due to ionized-impurity scattering. The values of N_d which were fit from this formula were about 30% lower in all cases than those determined from the carrier-concentration analysis given in Table I. Consequently, we also ran fits using the ionized-scattering formula given by Samoilovich *et al.*, and the results were much better. A comparison of the two results is given in Table V. The most sensitive samples for this comparison are Si: P 3 and Si: P 4, which have the largest contributions due to ionized impurities, and relatively weak contributions due to neutral scattering. Several values of the neutral scattering parameter A were tried, to verify that the fitted value of N_d did not depend upon this choice. As a counterexample, the choice of A is more important for Si: As 2, which has a fairly strong contribution due to neutral-impurity scattering. In all cases, however, the formulas given by Samoilovich *et al.* gave better agreement in determining values of compensation close to those determined from carrier-concentration analysis.

D. Neutral-Impurity-Scattering Results

Having established a reasonably good model to describe the lattice and ionized-impurity-scattering effects, we then went on to fit the remaining samples which were lightly compensated, and hence had substantial contributions due to neutral-impurity scattering. The results were disappointing. In all cases the fits between 20 and 77 K were skewed, with the calculated mobility higher at the extremes and lower than the measured mobility between about 25 and 60 K. In these samples, N_d was fixed and A and G[30] were permitted to vary. For completeness, the results of these fits are given in Table VI.

In order to understand the cause of the poor fitting, we have extracted the neutral scattering contributions from each of these samples for comparison with the Erginsoy model. To do this we calculated the mobility for each of these samples, including only the contributions due to lattice and ionized-impurity-scattering effects, with G assumed to be unity. We then estimated the neutral-scattering mobility as

$$\mu_N = (1/\mu_{\text{meas}} - 1/\mu_{\text{calc}})^{-1}. \tag{17}$$

TABLE III. Mobility lattice parameters fit above 77 K.

Model	Sample	τ_0 (sec^{-1}) (10^{-9})	w_1[a]	w_2[a]	w_3[a]	Stand. dev of mobility fit (10^{-2})	Temperature range (K)
IIa	Si: P 6	3.56[b]	1.45	0[b]	0[b]	...[c]	77–315
IIb	Si: P 6	3.56[b]	0[b]	2.00	0[b]	...[c]	77–315
IIc	Si: P 6	3.56[b]	0.58	1.19	0[b]	1.21	77–315
II	Si: P 6	3.90[b]	0.00	1.30	0.15[b]	1.02	77–315
II	Si: P 6	3.92	0.00	1.93	0.15[b]	1.02	77–315
II	Si: P 6	3.89	0.01	1.87	0.15	1.39	20–315

[a] Coupling constants for intervalley phonons, $\theta_1 = 540$ K, $\theta_2 = 670$ K, $\theta_3 = 190$ K.
[b] Value fixed.
[c] Not computer fit.

TABLE IV. Mobility lattice parameters fit with model III.

Sample	τ_0 ($\sec^{-1}$) (10^{-9})	w_1[a]	w_2[a]	w_3[a]	w_4[a]	N_d (cm^{-3}) (10^{12})	Stand. dev. of mobility fit (10^{-4})	Temperature range (K)
Si: P 6	3.63	0.0002	1.84	0.080	0.0004	7.56	0.90	20–315
Si: P 5	3.77	0.0[b]	1.83[b]	0.16	0.00007	8.40	0.47	20–77

[a]Coupling constants for intervalley phonons; $\theta_1 = 540$ K, $\theta_2 = 670$ K, $\theta_3 = 190$ K, $\theta_4 = 307$ K.
[b]Value fixed.

For comparison, the mobilities calculated in this manner were multiplied by the total concentration of neutral impurities at each temperature. In addition, we repeated the same procedure, replacing the measured mobility by the mobility calculated with the inclusion of neutral scattering from Erginsoy's formula. For this calculation a value of A was used, as indicated from our results given in Table VI, and three choices of G were assumed: 0.95, 1.0, and 1.05, corresponding to hypothetical errors in the sample geometry. Since Erginsoy predicts a temperature-independent mobility, our calculated mobility including neutral scattering was used to check if the above procedure recovered this temperature-independent behavior out of the involved averaging of scattering times. By also varying G, we could estimate the reliability of the procedure in view of probable errors in geometry, and observe the consequences of such *errors*.

We have included in this procedure both Hall and photo-Hall data, the latter being taken at temperatures between 1.5 and 20 K with 300-K background radiation. Lower temperature bounds for the validity of this data arise in two ways. First, the condition of the Born approximation used in calculating the ionized-impurity-scattering contribution means that we must have $|\vec{k}a| \gg 1$,[36] where $\vec{k}$ is the carrier wave number and a is the scattering length. For silicon, this becomes $|\vec{k}a| \gg 1.28 \times 10^3 T(m^*/m')^{1/2}$, with m' given by Eq. (11). The second requirement for these data to be valid is that the thermalization time of the photoexcited carriers must be much *shorter than the carrier lifetime*. Carrier lifetimes were determined for most of these samples from the decay of the photoresponse to a pulsed CO_2 *laser*. The *results of these measurements* have been published.[36] We can estimate the thermalization time for electrons in n-type silicon from the energy loss rate due to acoustic phonon emission.[40] In all cases, the greatest lower bound in temperature is determined by considering the problem of thermalization time in comparison to lifetime. Data were used only for temperatures above $2T'$, *where* T' *is* the temperature at which the lifetime and thermalization times are equal, as determined for each sample.

Figure 11 shows the results found for Si: P 1. As can be seen, the strength of neutral scattering decreases slightly from around 5 to 50 K, and then increases rather sharply above 50 K, causing the mobility (per scattering center) to decrease. For comparison, the calculated results found from the same procedure using the expression for neutral scattering given by Erginsoy are also shown. As expected, very little temperature dependence is evident in the calculated curves, except at the highest temperatures for those cases with hypothetical errors in sample geometry. It should be noted that in no case will a fixed geometrical error yield a temperature dependence similar to our experimental results. It is also clear why the computer fits between 20 and 77 K were high at the extremes and low between about 25 and 60 K, as we have stated.

Figures 12–16 give the same information for samples Si: P 5 (marginal amounts of neutral scattering), Si: As 1, Si: As 2, Si: As 3, and Si: Sb 1.

Two conclusions can be drawn by comparing these figures. First, a general pattern of increasing mobility up to about 50 K is seen, followed by a decrease from 50 to 100 K. Second, the average mobility for the arsenic-doped samples was substantially larger than that of either phosphorus- or antimony-doped samples. These conclusions will be discussed in Sec. IV E.

IV. COMPARISON WITH THEORY AND OTHER EXPERIMENTS

A. Carrier Concentration Analysis

The principal advantage of our work over the earlier analysis of Long and Myers[12] is that here

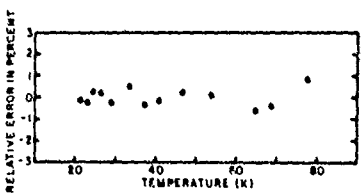

FIG. 7. Relative error for Si: P 6, with model III. Values of the parameters are listed in Table IV.

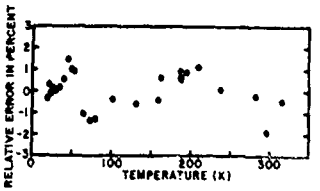

FIG. 8. Relative error for Si: P 6, with model III. Values of the parameters are listed in Table IV.

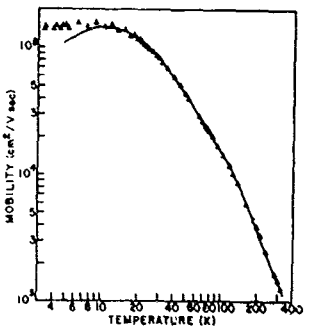

FIG. 10. Experimental data points and calculated mobility curve for Si: P 6. Experimental data include photo-Hall measurements (solid circles) below 20 K which were not included in the fitting procedures. Deviation between the data and calculation below 10 K occurs because the photoexcited carriers are no longer able to completely thermalize at the lowest temperatures. Parameters from Table III are used for the calculation. Figure 8 shows the details of the difference between calculation and data above 20 K.

no iterative procedure was necessary to determine Hall-factor corrections, since our data were taken in the high-field limit. This independence of the carrier-concentration analysis with respect to the mobility analysis has allowed the two methods to be compared, rather than seeking a self-consistent fusion of the analysis as done by Long and Myers.

All of the samples were analyzed with an activation energy which was assumed to be independent of doping concentration and temperature. This approximation is valid at low temperatures for lightly doped samples without a large number of compensating acceptors. For more heavily doped samples, approaching the exhaustion region will appreciably lower the activation energy, although it should be noted that the dependence of carrier concentration on activation energy in this region is not strong. Early measurements by Pearson and Bardeen[41] and more recently by Penin *et al.*[42] have been analyzed,

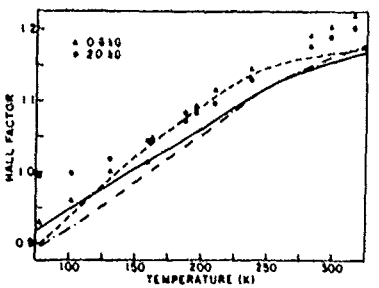

FIG. 9. Hall factor, as measured at 600 and 20 000 G; for Si: P 6. Data taken with 20 000 G were not in the low-field limit below about 150 K. Calculated curves of the Hall factor are model I(a) shown as dashed line, model I(b) shown as dash-dot line, model III shown as solid line. Parameters used for the calculation are given in Tables III and IV.

following Debye and Conwell[43] with the activation energy assumed to be related to the total ionized impurity concentration $N_I = 2N_a + n$ as

$$E_d = E_d(0) - \alpha N_I^{1/3}, \tag{18}$$

where α was determined by Penin *et al.* to be 3.6×10^{-8} eV cm, giving an activation energy of zero for phosphorus impurities at a concentration of 2×10^{18} cm^{-3}. If we use this value of α to compute the lowering of the activation energy in the freeze-out region for our purest samples, Si: P 5 and Si: P 6, with about 8×10^{12} cm^{-3} acceptors, we find a calculated shift of nearly 1 meV. If we add this to the values of E_d determined in Table I for these samples, we find $E_d(0)$ to be about 46.3 meV. Since this is larger than the optical activation energies found by Aggarwal and Ramdas[44] in accordance with the recent theory of Faulkner[45] (45.53 meV), there is some doubt as to the validity of Eq. (18) at these low concentrations. Penin *et al.* also give an expression for the variation of E_d with the principal dopant density, and this gives negligible reduction in activation energy for these lightly doped samples, since it involves a term proportional to e^{-r_d/a^*}, where r_d is the average spacing between donors, namely, $r_d = (3/4\pi N_d)^{1/3}$, and a^* is the effective Bohr radius. Another approach, taken by Neumark,[46] basically involves the effect of screening by impurities on the activation energy. This depends only on the ionized-

TABLE V. Comparison of the compensation densities fit from two different formulas for ionized-impurity scattering, as given by Brooks, Herring, and Dingle (BHD) and by Samoilovich *et al.* (SKDI).

Sample	N_d from carrier-conc. analysis (cm^{-3})	N_d from mobility analysis (cm^{-3})	Theory	A	G	Stand. dev. of fit (10^{-2})
Si: P 3	2.3×10^{13}	1.49×10^{13}	BHD	1.6[a]	1.12	1.5
		1.53×10^{13}	BHD	2.0[a]	1.12	1.5
		1.55×10^{13}	BHD	2.4[a]	1.12	1.5
		2.04×10^{13}	SKDI	1.6[a]	1.12	1.1
Si: P 4	2.0×10^{14}	1.43×10^{14}	BHD	1.6[a]	1.12	0.5
		1.46×10^{14}	BHD	2.0[a]	1.12	0.5
		1.49×10^{14}	BHD	2.4[a]	1.12	0.5
		1.93×10^{14}	SKDI	1.6[a]	1.13	0.7
Si: P 5	8.6×10^{12}	6.97×10^{12}	BHD	2.0[a]	1.00[a]	0.5
		8.40×10^{12}	SKDI	1.6[a]	1.00[a]	0.5
Si: P 6	7.7×10^{12}	6.32×10^{12}	BHD	2.0[a]	1.00[a]	0.7
		7.56×10^{12}	SKDI	1.6[a]	1.00[a]	0.9
Si: As 2	4.3×10^{13}	2.52×10^{13}	BHD	5.3[a]	1.04	1.2
		3.02×10^{13}	SKDI	5.3[a]	1.01	1.9
		5.20×10^{13}	SKDI	31	0.95	1.0

[a]Value fixed.

impurity concentrations, to first order, and gives a reduction in the activation energy of approximately 0.3 meV at 30 K for phosphorus impurities with sample concentrations representative of Si: P 5 and Si: P 6. Even this modest decrease in activation energy is sufficient to imply a value of $E_d(0)$ greater than the optical results, although the discrepancy is certainly small. In spite of the uncertain nature of these calculations, we compare in Table VII the value of $E_d(0)$ calculated from Eq. (18) and from the expression given by Neumark,[47] namely,

$$\frac{E_A}{E_d(0)} = 1.00 - 1.81a^*\left(\frac{4\pi e^2}{\kappa k}\right)^{1/2}\left[\frac{N_a}{T}\left(1-\frac{N_a}{N_d}\right)\right]^{1/2} + 0.81a^{*2}\left(\frac{4\pi e^2}{\kappa k}\right)\left[\frac{N_a}{T}\left(1-\frac{N_a}{N_d}\right)\right]. \quad (19)$$

where we have assumed that $n \ll N_a$ over the temperature range for which the computer fit of E_d is established most critically, and that the impurity ions are not mobile; i.e., $T_m \to \infty$ in Eq. (13) of Ref. 46. Equation (19) was evaluated at 30 K, a temperature characteristic of the exponential freeze-out region measured. As can be seen from the comparison of the two results, both give reasonably consistent values among the several samples of phosphorus- and arsenic-doped crystals, although the two theories disagree by about 0.5 meV. In all cases, the theory of Neumark gives results closer to the optical activation energy. We are necessarily reluctant to conclude much more than this, since a meaningful test of this problem would require more heavily doped and some heavily compensated samples, which we have not measured.

TABLE VI. Results of fitting the mobility for samples having significant amounts for neutral-impurity scattering using the Erginsoy formula [Eq. (81)].

Sample	N_a (cm^{-3})[a]	A	G	Stand. dev. of fit (10^{-2})	Compensation ratio N_a/N_d[b]
Si: P 1	4.1×10^{17}	1.6	1.00	5.1	0.00044
Si: As 1	6.0×10^{17}	5.9	1.04	3.1	0.00043
Si: As 2	4.3×10^{17}	11.7	0.96	1.1	0.0055
Si: As 3	1.8×10^{17}	6.2	0.74	2.9	0.00024
Si: Sb 1	5.3×10^{17}	1.5	1.11	5.0	0.00072

[a]Values fixed. [b]N_a and N_d from Table I.

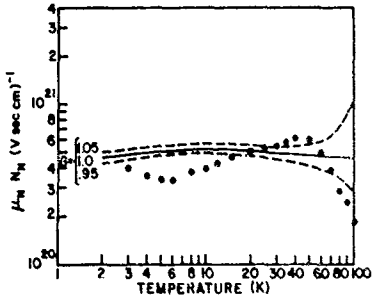

FIG. 11. Temperature dependence of the neutral-impurity scattering mobility for Si : P 1 (normalized to unit density of neutral impurities) shown as solid circles, as calculated from Eq. (17). Solid curve shown for the same procedure, but with the measured mobility replaced by the mobility calculated with Erginsoy's formula, with $A = 1.6$ and $G = 1.0$. Other values of G are also shown as dashed lines.

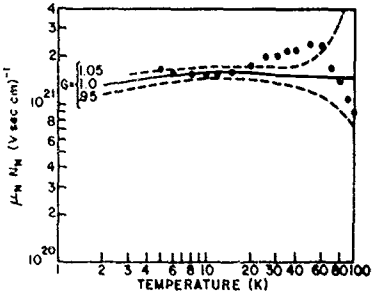

FIG. 13. Same as Fig. 11, for Si : As 1, with calculated curves for $A = 5.0$.

In the two cases in which we allowed N_c to vary in fitting Si : P 5 and Si : P 6, the results agree very well with the calculated values. This is not unexpected, but is a satisfying check on our procedure.

B Mobility Analysis: General

With the exception of neutral-impurity scattering in n-type silicon samples, we have shown that the general procedure outlined by Herring and Vogt[1] can be made to give very accurate results[16] with a more suitable expression for neutral-impurity scattering. It is expected that the mobility can be calculated to within a few percent between 20 and 300 K for doping levels less than 10^{17}–10^{18} cm^{-3}. In addition, the Hall factor can also be calculated to about this same level of accuracy. Conversely, the accuracy of the mobility formulation permits us to determine the compensation density if the strength of the ionized-impurity scattering is at least comparable to that produced by neutral impurities. This may be especially useful if uncompensated impurities of two types are present; e.g., $N_{phosphorus} - N_{arsenic} > N_a$, where the assumption of an equation of the form of Eq. (2) would give ambiguous results. The usefulness of such an alternate approach has been demonstrated by an analysis of impurities in p-type germanium.[10,16]

C Lattice Scattering

It is of interest to first review the present understanding of this subject, as regards the various

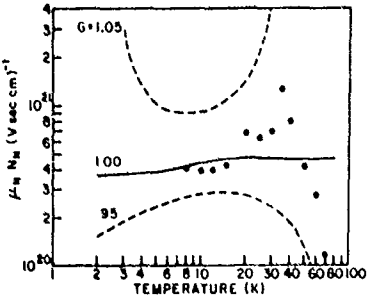

FIG. 12. Same as Fig. 11, for Si : P 5.

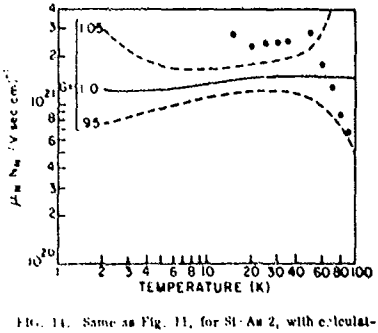

FIG. 14. Same as Fig. 11, for Si : As 2, with calculated curves for $A = 5.0$.

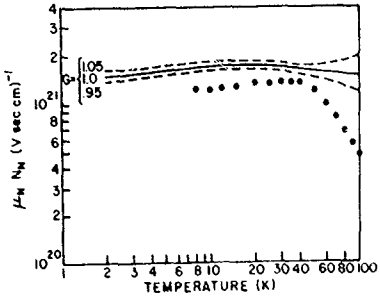

FIG. 15. Same as Fig. 11, for Si : As 3, with calculated curves for $A = 5.0$.

types of intervalley scattering, and the basis upon which several views have been adopted. Information on this subject has been sought in a number of ways; by theory, calculating the allowed intervalley transitions, and in principle, the matrix elements for these transitions; from experimental observations, including optical phenomena such as photoconductivity spectrum, hot electron effects in which intervalley transitions are important in balancing energy gained from the electric field, and, as in our present case, from Ohmic mobility or other transport phenomena.

The allowed transitions for intervalley scattering have recently been agreed upon by the principal authors who have concerned themselves with these calculations. As summarized by Streitwolf,[50] and agreed upon by Lax and Birman,[51] the allowed electron one-phonon selection rules permit LO g-type transitions (at 0.34X), and LA TO f-type transitions (at S on the phonon Brillouin zone face). The characteristic temperatures and energies of these phonons are LO (720 K, 62 meV), LA(560 K, 48 meV), and TO (680 K, 59 meV). It is to be noted that in this respect, no low-energy phonons are possible. An earlier misunderstanding concerning the selection rules had indicated that g-type LA phonons would be allowed, such phonons having energy 21 meV (240 K). Also specifically forbidden are f-type TA phonon transitions. In view of recent work in InSb[52] and Ge,[53,54] however, it is important to keep in mind that although TA f-type and LA g-type transitions are forbidden when considering a one-phonon collision, such restrictions may not apply when other processes are considered. Recent evidence of two-phonon Raman spectral lines in silicon,[55] involving TO and TA phonons, has shown that multiphonon processes are probably very important. The experimental data on Si : P 6 are presently being reanalyzed with two-phonon terms included.[56]

The experimental analysis of intervalley scattering began in 1960 and immediately established two opposing schools of thought. Dumke,[57] analyzing the radiative recombination data of Haynes *et al.*,[58] found contributions from 23-meV phonons (presumed to be g-type at 0.36X) and 46-meV phonons (f-type LA at S) which he assumed were due to intervalley scattering. Evaluating the matrix elements he found g-type scattering to dominate over f type by a factor of 2.5 to 1 at room temperature. The opposite conclusion was simultaneously reached by Long[7] from his analysis of mobility. Long found the higher-temperature phonon, in this case 54 meV (an average of TO, LO, and LA f type), to be dominant in the scattering of electrons, compared to a representative low-temperature phonon of 16 meV. In this case, with Long's coupling constants, f-type scattering (high-temperature phonons) dominates g type at room temperature by a ratio of more than 5 to 1, although the contribution due to acoustic mode intravalley scattering is assumed to be more important in Long's analysis than in Dumke's.[59] This interesting controversy was then taken up by Aubrey *et al.*[10] using piezoresistance and piezo-Hall effect data. Their work supported Long, in that the room-temperature ratio of zero to saturation resistivity could be calculated more accurately with the coupling constants determined by Long.

Asche *et al.*[60] introduced a new twist into this situation on the basis of hot electron experiments. From their data they claim to have shown that g-type scattering is dominant over f type, but assume that g-type scattering can occur with both high- and low-temperature phonons. Thus, using a high-temperature phonon of 62 meV, they fit their data

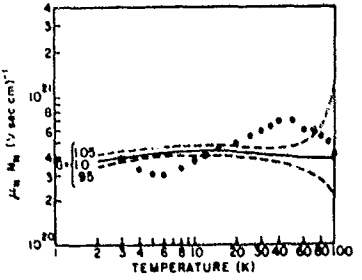

FIG. 16. Same as Fig. 11, for Si : Sb 1, with calculated curves for $A = 1.3$.

TABLE VII. Comparison of calculated activation energies, in the limit of vanishing impurity concentration, for two theories, Penin *et al.* (Ref. 42) and Neumark (Ref. 47).

Sample	E_d from expt. (meV)	Penin *et al.* $E_d(0)$ from Eq. (18) (meV)	Neumark $E_d(0)$ from Eq. (19) (meV)	Optical value of $E_d(0)$ (meV)
Si:P 1	45.64	46.37	45.90	
Si:P 3	45.14	46.43	45.72	
Si:P 4	43.39	46.04	44.95	45.53[a]
Si:P 5	45.38	46.31	45.75	
Si:P 5	45.42	46.32	45.74	
Si:As 1	53.64	54.46	54.01	
Si:As 2	52.54	54.13	53.51	53.73[a]
Si:As 3	52.52	53.71	53.14	
Si:Sb 1	42.59	43.38	42.86	42.73[a]

[a]Value taken from Aggarwal and Ramdas (Ref. 44), but with corrected value of the activation energy of the $3P_+$ state as calculated by Faulkner (Ref. 45).

with a coupling constant for this phonon of 3.0, and chose the low-temperature phonon coupling constant an order of magnitude smaller. This result is not particularly inconsistent with Long, in that mobility data cannot distinguish an f-type from a g-type process, but is contrary to Dumke, since the high-temperature phonon was found to dominate over the low-temperature one.

A reanalysis of radiative recombination data as measured by Dean *et al.*,[61] was made by Folland.[62] His initial result reported in 1968 gave further support to the contention of Long that the high-temperature intervalley phonon processes were dominant. In this case, Folland found coupling constant values for three modes; 0.44 for a 23-meV phonon, 0.06 for a 46-meV phonon, and 1.5 for a 62-meV phonon. A more refined result, given in 1970 by Folland,[63] gave slightly larger contributions of the low-temperature phonon, now estimated to be 25 meV. Use of these refined coupling constants made it possible to reproduce the mobility data to an accuracy of about 8% between 100 and 300 K. An important consideration in attempting to understand this work is that Folland used selection rules permitting g-type LA phonons (25 meV at 0.40X). This was based on the earlier results of Lax and Hopfield,[64] and shown to be incorrect by Streitwolf.[50] However, further evidence for a transition involving phonons of about this same energy was reported by Onton[35] in 1969.

The experiments of Onton were based on a prediction by Stocker[65] that intervalley scattering transitions would be evident in the spectral response of extrinsic photoconductivity. Stocker predicted dips in the photocurrent, corresponding to intervalley transitions from states high in the conduction band of one valley to the bottom of the band in another valley. Since the carrier lifetime is much shorter for carriers near the bottom of the band, such transitions should reduce the photocurrent. Onton found such dips corresponding to energy transitions of 27 and 47 meV as analyzed by Stocker's model. The magnitude of the dip was assumed to be indicative of the phonon coupling strength, and roughly equal amounts of g-type (27 meV) and f-type (47 meV) scattering were predicted from the data.

Computations of hot electron effects were made by numerous authors around this same time. In certain cases, the coupling constants of Long were adopted (Jørgensen and Meyer,[66] Kawamura,[67] Jørgensen,[68] Basu and Nag,[69] Holm-Kennedy and Champlin,[70] Glushkov and Markin[71]), while in other cases the coupling constant of Dumke and Onton were used (Costato and Scavo,[72] Costato and Reggiani,[73] Costato, Fontanesi, and Reggiani[74]). As already mentioned, the conclusions of Asche *et al.*[60] and also those of Heinrich and Kriechbaum,[75] did not particularly support either view. We are not prepared to evaluate the validity of any of these calculations, which have at times concluded that g-type scattering was dominant while other workers found f-type scattering more important. Since the experimental measurement of hot electron effects can preferentially heat or cool certain valleys by the choice of electric field orientation and therefore provide information which ought to distinguish g-type and f-type scattering modes, the disagreement in the interpretation of this data is probably due to the extremely difficult nature of the calculations, in which various approximations regarding the carrier distribution function are typically involved. This subject has been reviewed recently by Conwell.[76]

TABLE VIII. Analysis of the photoconductivity data taken by Onton (Ref. 35) based on a proposed model in which a photon of energy $h\nu$ is absorbed at an impurity site, leaving the impurity in an excited state, accompanied by the emission of an intervalley phonon of energy $\hbar\omega$. The impurity is assumed to be originally in the $1S(A_1)$ ground state.

Sample	dip A $h\nu$ (meV)	$1S(T_1)$ $\hbar\omega$ (meV)	$1S(E)$ $\hbar\omega$ (meV)	dip B $h\nu$ (meV)	$2P_0$ $\hbar\omega$ (meV)	dip C $h\nu$ (meV)	$2P_\pm$ $\hbar\omega$ (meV)
Sb	69.4	59.9	57.3	89.6	58.3	94.7	58.5
P	71.5	59.9	58.6	92.0	57.9	97.5	58.4
As	80.1	59.0	57.6	100.9	58.6	106.5	59.1

Impurity transition energies

$1S(A_1)$ to:	$1S(T_1)$	$1S(E)$	$2P_0$	$2P_\pm$
Sb	9.55[a]	12.14[a]	31.26[b]	36.20[d]
P	11.62[a]	12.95[a]	34.12[c]	39.14[c]
As	21.09[a]	22.50[a]	42.26[b]	47.36[d]

[a]Reference 44, Table IV.
[b]Reference 44, Figs. 3 and 4.
[c]Reference 83, Fig. 1.
[d]Reference 44, Tables II, III, and IV.

by the appropriate choice of excited-state transitions, all the observed dips in photoconductivity can be explained in terms of a phonon of about 58 meV. Our choice of transitions was based on the work of Dean *et al.*[41] in analyzing recombination radiation effects in which an exciton decays in the presence of an impurity, leaving the impurity in an excited state. To summarize, we propose that optical absorption can occur at an impurity site, with the emission of an optical phonon and the simultaneous excitation of the impurity to an excited state.

If the photoconductivity experiments can be reconciled in view of the above comments, a problem yet remains in the analysis of radiative recombination data made by Dumke and Folland. Their analysis has implied intervalley phonons of energy near 23 meV, in contrast to the 27-meV phonons claimed by Onton and Gutchar *et al.* If the conduction-band minimum is located at $0.83X$, then the intervalley g-type transitions will occur at $0.34X$. The LA-phonon branch at this point gives an energy of 21 meV. This is substantially less than the energies found by Onton and Gutchar *et al.*, but clearly not as far from the value of 27 meV found from the recombination radiation data. Since the LA-phonon dispersion is large in this region, it is possible that recombination radiation is taking place with an LA g-type phonon, but it is unlikely that the precision involved in both experiments can reconcile the 3–4 meV difference in the determination of this phonon energy. It is not entirely clear to us how the recombination radiation analysis should be modified. If the free-electron approximation is considered together with the selection rules, then LA g-type intervalley phonons cannot initiate the recombination process, but perhaps can terminate it without violation.

The remaining problem in all this work is the apparent presence of TA f-type scattering, as found by Long and in this investigation from mobility analysis, and considered important by Holm-Kennedy and Champlin[10] in explaining warm carrier experiments. TA f-type scattering is forbidden by the selection rules, but nevertheless seems to be present in weak amounts. Even these relatively weakly coupled modes are found important for a complete explanation of experimental data; as was shown in Sec. III B. The most amusing statement that could be made to interpret these results is that time reversal symmetry is broken in silicon, since it is this condition which forbids the TA process.[16] More reasonable approaches could be pursued along the lines of two-phonon scattering to resolve this issue. The negligible amounts of LA f-type scattering found in our work, but not expressly forbidden by the selection rules, also remains to be explained.

For comparison and reference, we list in Table IX the calculated values of lattice mobility between 10 and 500 K, using lattice parameters as analyzed from sample Si P 6 with model III as listed in Table IV. Also shown are the results of Long, as calculated from his parameters. Surprisingly, the mobility values are quite different at low temperatures (18% at 20 K). This may be due to a combination of systematic errors encountered by Long in correcting for the Hall factor, and the use of an isotropic scattering formulation of ionized-impurity scattering based on the Brooks, Herring, and Dingle equations, which overestimates the strength of this type of scattering.

TABLE IX. Calculated lattice mobility using parameters determined from Si: P 6, model III, and listed in Table IV. Also shown for comparison is the result of Long (Ref. 7).

Temperature (K)	Lattice mobility (cm^2/V sec) This result	Long's result[a]
10	5.68×10^5	6.74×10^5
20	2.01×10^5	2.38×10^5
30	1.09×10^5	1.29×10^5
40	7.01×10^4	8.23×10^4
60	3.72×10^4	4.27×10^4
77.5	2.46×10^4	2.77×10^4
100	1.59×10^4	1.75×10^4
130	9.66×10^3	1.03×10^4
160	6.19×10^3	6.46×10^3
200	3.73×10^3	3.81×10^3
250	2.18×10^3	2.26×10^3
300	1.43×10^3	1.47×10^3
350	1.01×10^3	1.06×10^3
400	7.48×10^2	7.82×10^2
500	4.79×10^2	5.07×10^2

[a]Long's results have been calculated for phonon temperatures of 630 and 190 K with coupling constants of 2.0 and 0.15, respectively. A value of $\tau_0 = 4.31\times10^{-3}$ sec was used to give Long's result at 300 K (Ref. 7).

D. Ionized-Impurity Scattering

It is difficult to compare the results of Long and Myers[12] with this present analysis, since they assumed isotropic scattering by ionized impurities, and we have not assumed this to be the case. However, we did find in comparing the theory of Brooks, Herring, and Dingle with that of Samoilovich *et al.* that the former overestimated the strength of ionized-impurity scattering when it was substituted into the prescription given by Herring and Vogt. This is why a larger value of coupling constant for low-temperature intervalley phonon scattering is obtained in model II, Table II, when N_t is fixed rather than varied. Extra intervalley scattering was preferred in this case, since the relative mobility at low temperatures was enhanced, in part compensating for the overestimate of ionized-impurity scattering. The values of u_1 found under these circumstances are nearly identical to the value determined by Long, and in this respect our conclusion that u_1 should be about half the value found by Long can be understood.

A handicap of our work is that more heavily-doped heavily-compensated samples were not measured, so that a test of ionized-impurity scattering could not be made under conditions where this type of scattering dominated the mobility. Keeping in mind the restrictions imposed by remaining in the high-magnetic-field limit, so that Hall-factor corrections are unnecessary, it should be possible to measure somewhat more heavily-doped samples in this same way.

Rode[28] has lately criticized the use of the spherical band approximation for calculating ionized-impurity scattering in germanium and silicon. We believe the failure of his calculation to describe accurately the mobility of electrons at 300 K for "free carrier concentrations" between 10^{16} and 10^{19} cm^{-3} is more complicated than a simple inadequacy of ionized-impurity scattering, whatever the formulation. Redfield and Afromowitz[24] have recently shown that the screening approximations are invalid in the temperature region and impurity concentration region calculated by Rode. More important, we feel, is the questionable association of free-carrier concentration with impurity concentration and the omission of neutral-impurity scattering. For silicon impurities, even assuming a concentration-dependent activation energy, we find that far from all the impurities are ionized at 300 K. For a value of α given by Penin *et al.* and a concentration of phosphorus impurities of 3×10^{17} cm^{-3}, we find 33% are un-ionized at 300 K. With Erginsoy's formula, and $A = 1$, we find the neutral scattering strength is nearly twice that of ionized impurities at 300 K. Extending our calculations to higher concentrations of N_d we can achieve a result exactly opposite to that of Rode, in that the mobility we calculate for zero compensation is less than indicated by experiment. From this it is clear that a very careful treatment, including the possibility of revising the screening formulas, including neutral scattering, and taking into account not only the temperature dependence of the impurity activation energy, but the eventual formation of an impurity band and the need for degenerate statistics, is required to make reliable calculations in this heavily doped region.

To emphasize the above point, we have plotted in Fig. 17 the calculated mobility between donor concentrations of 10^{13} and 10^{14} cm^{-3}, with $A = 1.0$, and the carrier concentration evaluated with an activation energy dependent upon N_t as in Eq. (18). Also shown are the partial mobilities, μ_I and μ_N for ionized and neutral scattering. As can be seen, at the highest concentration of donors, neutral rather than ionized scattering is dominant. Whether this is true in reality is not clear, since at 300 K the partial-wave theory is probably not accurate in calculating the strength of neutral scattering. Nevertheless, the mobility calculated by this assumption is in good agreement with the drift mobility as summarized by Sze and Irvin[18] near concentrations of 10^{18} cm^{-3}. To complete this comparison, we graph the calculated values of resistivity as a function of donor concentration in Fig. 18, along with the curve given by Irvin. Also shown are the values of resistivity for the samples measured in this investigation. Figure 19 shows

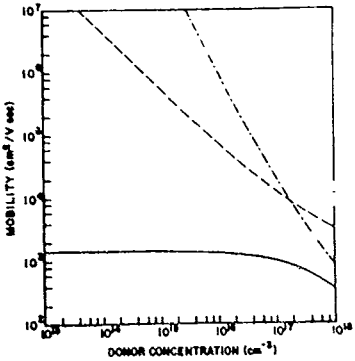

FIG. 17. Electron mobility in n-type silicon as a function of donor concentration at 300 K, as calculated from the equations presented in the text. Also shown are the partial mobilities for ionized (dashed line) and neutral (dash-dot line) impurity scattering.

the Hall factor calculated as a function of donor concentration. The values calculated for this comparison are listed in Table X.

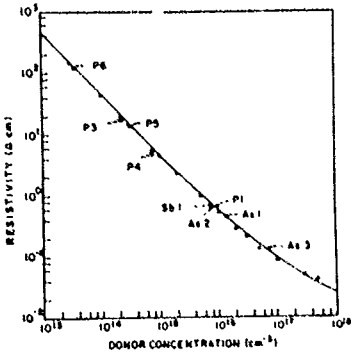

FIG. 18. Calculated resistivity values shown as triangles, compared with the curve of Irvin (Ref. 13) as a function of donor concentration at 300 K. Labeled points show the experimentally determined values from samples measured in this work, circles, while the solid and square data points for Si: P 3 and Si: P 4 give the resistivity as corrected by the factor G, given in Table X. Accurate geometry corrections could not be made for the more heavily doped samples studied, since neutral impurity scattering was important, but not well characterized by theory.

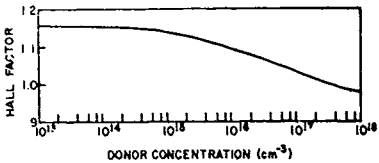

FIG. 19. The Hall factor as a function of donor concentration, as calculated at 300 K.

E. Neutral-Impurity Scattering

The most serious discrepancy between experiment and present theory is evident in the measurements of neutral-impurity scattering. A part of this problem can be resolved in the theory given by Sclar,[9] which included the possibility of bound states in the electron-hydrogenic impurity scattering problem. This was originally suggested by Ansel'm,[65] by noting that hydrogen can have a bound state for two electrons.[66] Sclar's calculation of this effect gives a mobility which varies as $T^{1/2}$ for kT above the binding energy of this two-electron bound state. The data presented in Figs. 11–16 show such a dependence up to 50 K. If values appropriate for silicon are substituted into the expression given by Sclar, the result is not in very good agreement with the data, although the qualitative features are observed. A comparison of Erginsoy's expression and that given by Sclar is shown in Fig. 20. Data from Si: Sb 1 have been included for reference. Examination of the formula given by Sclar shows that more quantitative agreement would be found for a weaker binding energy of the second electron at the impurity center. This conclusion is in conflict with the determination of the binding energy of such centers, as measured by Dean *et al.*[61] and by Gershenzon *et al.*,[67] but in agreement with recent work by Thornton and Honig.[68] We have also plotted the curve for a choice of $\frac{1}{4}E_i'$, where E_i' is the binding energy of the second electron at the impurity center, as predicted by the hydrogenic scaling model. Whether fitting the value of E_i' to the measured mobility data to determine this quantity, as suggested by Sclar, gives a reasonable estimate is open to question, considering the difference in this binding energy determined by other methods. It is also possible that a careful reexamination of the model will give better results, but the conclusion of this must await such calculations. It is encouraging to see that the general increase in neutral mobility up to 50 K can be accounted for by such a model. Much more recent calculations of neutral impurity scattering at low tem-

TABLE X. Calculated carrier concentration and transport properties as a function of donor density at 300 K.

Donor density (cm^{-3})	Carrier[a] conc. (cm^{-3})	Mobility (cm^2/V sec)	Resistivity (Ω cm)	Hall factor	Partial mobilities (cm^2/V sec) μ_I[b]	μ_N[c]
1×10^{13}	9.99×10^{12}	1.43×10^{3}	4.38×10^{2}	1.15	3.69×10^{7}	4.79×10^{11}
3×10^{13}	2.99×10^{13}	1.43×10^{3}	1.46×10^{2}	1.15	1.37×10^{7}	6.64×10^{10}
1×10^{14}	9.99×10^{13}	1.43×10^{3}	4.39×10^{1}	1.15	4.49×10^{6}	6.53×10^{9}
3×10^{14}	2.99×10^{14}	1.42×10^{3}	1.47×10^{1}	1.15	1.64×10^{6}	7.45×10^{8}
1×10^{15}	9.94×10^{14}	1.40×10^{3}	4.49×10^{0}	1.14	5.48×10^{5}	7.83×10^{7}
2×10^{15}	1.98×10^{15}	1.38×10^{3}	2.28×10^{0}	1.13	2.95×10^{5}	2.05×10^{7}
5×10^{15}	4.89×10^{15}	1.34×10^{3}	9.54×10^{-1}	1.11	1.32×10^{5}	3.58×10^{6}
1×10^{16}	9.61×10^{15}	1.29×10^{3}	5.05×10^{-1}	1.09	7.29×10^{4}	9.85×10^{5}
2×10^{16}	1.86×10^{16}	1.22×10^{3}	2.75×10^{-1}	1.08	4.12×10^{4}	2.82×10^{5}
3×10^{16}	2.72×10^{16}	1.17×10^{3}	1.97×10^{-1}	1.07	2.90×10^{4}	1.39×10^{5}
5×10^{16}	4.35×10^{16}	1.09×10^{3}	1.32×10^{-1}	1.05	2.03×10^{4}	5.85×10^{4}
1×10^{17}	8.01×10^{16}	9.51×10^{2}	8.21×10^{-2}	1.03	1.24×10^{4}	1.92×10^{4}
3×10^{17}	2.00×10^{17}	6.67×10^{2}	4.69×10^{-2}	1.00	6.14×10^{3}	3.82×10^{3}
5×10^{17}	3.00×10^{17}	5.21×10^{2}	4.00×10^{-2}	0.98	4.59×10^{3}	1.91×10^{3}
1×10^{18}	5.12×10^{17}	3.41×10^{2}	3.58×10^{-2}	0.98	3.18×10^{3}	7.86×10^{2}

[a] Carrier concentration is calculated with a ground-state activation energy according to Eq. (18), with $\alpha = 3.6\times10^{-8}$ eV cm. The structures of 1S (T_2) and 1S (E) states, and the excited states given in Eqs. (2) and (3), are assumed to move towards or even into the conduction band, keeping the same spacing relative to the 1S (A_1) ground state. An iterative procedure is used, with E_d chosen initially as 45.4 meV. The value of n determined from this assumption is substituted into Eq. (18) to give a new value of E_d, and the procedure is repeated until n changes by less than one part in 10^5.

[b] These values of μ_I are determined from the relaxation times given by Samoilovich *et al.* (Refs. 4–6) given in Eqs. (12)–(15), and are used to calculate the mobility analytically in this case with the usual approximation that the logarithmic term and the terms g_3 and g_4 are taken outside the integral and evaluated at $x = 3$.

[c] The neutral-impurity mobility values are calculated from Erginsoy (Ref. 8) with $A = 1$. Thus, $\mu_N = 3.8\times10^{20}/N_N$ cm^2/V sec. We chose a value of unity for A so that the data would coincide exactly with the Erginsoy equation, although at 300 K the approximation used by Erginsoy is no longer valid. An alternate expression, given by Sclar (Ref. 9) using the Born approximation, gives $\mu_N = 1.5\times10^{20}/N_N$ cm^2/V sec at 300 K. Neither approximation is valid, however, since $ka_0 \approx 1$ for silicon at 300 K. The Born approximation, and our experimental data near 100 K, indicate that perhaps even larger neutral-impurity scattering contributions may occur than are indicated above.

peratures have been announced by Blagoskloskaya *et al.*[10] They find a decrease in the mobility at low temperatures, but a temperature-independent mobility at higher temperatures. Such a dependence is not supported by our data. Since both the calculations of Sclar and Blagoskloskaya *et al.* take resonant scattering into account, it is not apparent why different dependencies of temperature exist in their results.

In all samples we have seen a noticeable decrease in the neutral [illegible]ity mobility for temperatures above 50 K, [illegible] in Figs. 11–16. A natural explanation [illegible] can be found if one considers inelastic co[illegible] between electrons and neutral donors. Such collisions can result in energy transfer to the donor impurity, leaving it in an excited state or even ionized. The minimum carrier energy for which this can occur is given by the splitting of the 1S states. Thus, for antimony and phosphorus, about 12 meV is required, while about 21 meV is needed for this transition in arsenic-doped samples. Since the decrease observed begins at about 50 K, for phosphorus and antimony impurities the effect is accounted for with carriers at about $3kT$ or more. For arsenic impurities, the carriers would need to be $\geq 6kT$. Since, however, the mobility is larger in arsenic-doped samples at 50 K, it could be argued that for this impurity a smaller effect will be more noticeable than in the phosphorus- and antimony-doped samples which have lower mobilities at the same temperature. Another way in which the mobility can be lowered at high temperatures is seen by also considering the relative populations of neutral donors in the 1S (A_1) state compared to higher-energy 1S states (T_2 and E). Since the population of these higher states will be significant above 50 K, it is expected that this will also lower the mo-

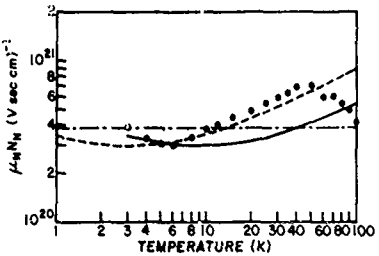

FIG. 20. Comparison of neutral-impurity mobility (for unit density) between Si:Sb 1 (Fig. 16) and the theory of Sclar (Ref. 9), calculated for two choices of the binding energy of the second electron at a donor impurity. The solid line shows Sclar's theory with the binding energy of the second electron scaled from the hydrogen-minus ion according to the effective-mass approximation. The dashed line is calculated for a binding energy of $\frac{1}{3}$ the value calculated from the effective-mass formula. The temperature-independent theory of Erginsoy (Ref. 8) is also shown for comparison as a dash-dot line, with A equal to unity.

bility since the spatial size of the wave function of such states will be larger than for the ground state, and the expected scattering length will be correspondingly greater.

The larger mobility values found for neutral scattering by arsenic impurities in comparison to antimony and phosphorus are not understood. Considering the approximation involved in treating neutral-impurity scattering by the zero-order partial-wave method, one expects the scattering cross section to vary with the square of the scattering length,[10] taken to be the effective-mass Bohr radius in the theory of Erginsoy. Correcting the Bohr radius by the quantum-defect method, one expects the cross section to decrease as the ratio of the effective-mass binding energy to the observed impurity binding energy. This indicates that Erginsoy's result should be multiplied by 1.4, 1.5, and 1.8 to calculate the mobility for antimony, phosphorus, and arsenic, respectively. This is in fair agreement with the averaged computer-fitted values found for A in Table VI, in the case of antimony and phosphorus, but not in good agreement for arsenic-doped samples. We cannot explain this result.

V. SUMMARY AND CONCLUSIONS

Carrier-concentration analysis and mobility analysis have been shown to give excellent agreement in determining the density of compensating acceptor impurities in n-type silicon, when the strength of neutral-impurity scattering was weak to moderate by comparison. In contrast, neutral-impurity scattering has been shown to be poorly described by the present theory, except for the general order-of-magnitude strength in the case of neutral antimony and phosphorus impurities. The density-of-states effective mass, when fit as a parameter in the carrier-concentration analysis of relatively pure samples, has been found to agree well with the values calculated from the established band structure.

A quantitative comparison of several lattice scattering models, currently proposed in the literature, has been made. In particular, we have found that the intervalley scattering contributions can be fitted to a model almost identical to that proposed by Long. This required the inclusion of weakly coupled modes which are forbidden by the selection rules. Other models, based chiefly on data from photoconductivity and radiative recombination data have been examined. Alternative interpretations suggested for some of these data may lead towards a greater concensus on the question of intervalley scattering transitions.

ACKNOWLEDGMENTS

We would like to thank Allen Miller for helpful clarification of the location of the f-type and g-type intervalley phonons. Donald Long kindly supplied us with detailed graphs of his data. We have shared several useful discussions on the selection rules and their implications with Dan Rode, Kai Ling Ngai, and N. O. Folland. The technical assistance of Susan Norton in part of this work is gratefully acknowledged.

*Work supported in part by the Air Force Avionics Laboratory.
†Present address: Bell Telephone Laboratories, Allentown, Pa. 18103.
[1]C. Herring and E. Vogt, Phys. Rev. 101, 944 (1956).
[2]H. Brooks, Phys. Rev. 83, 879 (1951); in *Advances in Electronics and Electron Physics*, edited by L. Marton (Academic, New York, 1955), Vol. 7, p. 85.
[3]R. B. Dingle, Philos. Mag. 46, 831 (1955).
[4]A. G. Samoilovich, I. Ya. Korenblit, and I. V. Dakhovskii, Dokl. Akad. Nauk SSSR 139, 355 (1961) [Sov. Phys.-Dokl. 6, 606 (1962)].
[5]A. G. Samoilovich, I. Ya. Korenblit, and I. V. Dakhovskii, Fiz. Tverd. Tela 3, 2939 (1961) [Sov. Phys.-Solid State 3, 2148 (1962)].
[6]A. G. Samoilovich, I. Ya. Korenblit, and V. D. Iskra, Fiz. Tverd. Tela 3, 3285 (1961) [Sov. Phys.-Solid State 3, 2385 (1962)].
[7]D. Long, Phys. Rev. 120, 2024 (1960).
[8]C. Erginsoy, Phys. Rev. 79, 1013 (1950).
[9]N. Sclar, Phys. Rev. 104, 1559 (1956).

[10]P. Norton and H. Levinstein, Phys. Rev. B 6, 470 (1972). The only change in the experimental apparatus was the installation of a new platinum resistance thermometer, a Model 118LX manufactured by Rosemount Engineering.
[11]For a general review of galvanometric measurements, see A. C. Beer, in *Solid State Physics*, edited by F. Seitz and D. Turnbull (Academic, New York, 1963), Suppl. 4.
[12]D. Long and J. Myers, Phys. Rev. 115, 1107 (1959).
[13]Reference 11, p. 215.
[14]W. Kohn, in Ref. 11, Vol. 5, p. 257.
[15]R. A. Faulkner, Phys. Rev. 184, 713 (1969).
[16]R. L. Aggarwal, Solid State Commun. 2, 163 (1964).
[17]J. S. Blakemore, *Semiconductor Statistics* (Pergamon, New York, 1962).
[18]D. Long and J. Myers, Phys. Rev. 115, 1119 (1959).
[19]J. C. Irvin, Bell Syst. Tech. J. 41, 387 (1962); S. M. Sze and J. C. Irvin, Solid-State Electron. 11, 599 (1968).
[20]It is more difficult to accurately measure the length and width between resistivity probes, than to measure the sample thickness. Geometrical errors have been considered in Refs. 10 and 21.
[21]D. Long and J. Myers, Phys. Rev. 120, 39 (1960).
[22]L. J. Neuringer and W. J. Little, in *Proceedings of the International Conference on the Physics of Semiconductors, Exeter, 1962* (The Institute of Physics and the Physical Society, London, 1962), p. 614.
[23]A. G. Kazanskii and O. G. Koshelev, Fiz. Tekh. Poluprovodn. 6, 953 (1972) [Sov. Phys.-Semicond. 6, 826 (1972)].
[24]E. Otsuka, K. Murase, and K. Takesawa, in *Proceedings of the Ninth International Conference on the Physics of Semiconductors, Moscow, 1968* (Nauka, Leningrad, 1968), p. 292.
[25]A. Honig and R. Maxwell, in Ref. 24, p. 1117.
[26]F. Ham, Phys. Rev. 100, 1251 (1955).
[27]L. J. Neuringer and D. Long, Phys. Rev. 135, A788 (1964).
[28]D. L. Rode, Phys. Status Solidi B 53, 245 (1972).
[29]The fitting details are given in Ref. 10. Briefly, the parameters are adjusted to minimize the sum of the squares of the difference between the logarithms of experimental and calculated values.
[30]The samples in all cases were approximately 10 mm long, 1 mm thick, and 1.5 mm wide. Three pairs of arms for attaching leads were spaced along the length. Most samples had center to center spacings of the arms of 1.4 mm, and arm widths of 0.7 mm. Sample resistivity was calculated from the voltage drop between one center arm and an adjacent arm. Samples Si:P 5 and Si:P 6 has only two pairs of arms. The two nearest the center, but slightly off set, were used to measure the Hall voltage. One of these and one of the second pair served to measure the voltage drop for computing the resistivity. The arms were spaced by 4.0 mm and were approximately 0.5-mm wide. Thus, the arm-width-to-spacing ratio is much better for these samples. For the other samples, a geometrical factor G was included in the analysis. The parameter G, discussed in Ref. 10, is a constant multiplying the calculated mobility. An adjustment of G can compensate for errors in measuring the sample geometry, as required. See also, Ref. 20.
[31]M. B. Prince, Phys. Rev. 93, 1204 (1954).
[32]G. W. Ludwig and R. L. Watters, Phys. Rev. 101, 1699 (1956).
[33]D. C. Cronemeyer, Phys. Rev. 105, 522 (1957).
[34]J. Messier and J. M. Flores, J. Phys. Chem. Solids 24, 1539 (1963).
[35]A. Onton, Phys. Rev. Lett. 23, 288 (1969).
[36]M. Cuevas, Phys. Rev. 164, 1021 (1967).
[37]D. M. Brown and R. Bray, Phys. Rev. 127, 1593 (1962).
[38]N. Sclar, Phys. Rev. 104, 1548 (1956).
[39]P. Norton, T. Braggins, and H. Levinstein, Phys. Rev. Lett. 30, 488 (1973).
[40]P. Norton and H. Levinstein, Phys. Rev. B 6, 478 (1972).
[41]G. L. Pearson and J. Bardeen, Phys. Rev. 75, 865 (1949).
[42]N. A. Penin, B. G. Zhurkin, and B. A. Volkov, Fiz. Tverd. Tela 7, 3188 (1965) [Sov. Phys.-Solid State 7, 2580 (1966)].
[43]P. P. Debye and E. M. Conwell, Phys. Rev. 93, 693 (1954).
[44]R. L. Aggarwal and A. K. Ramdas, Phys. Rev. 140, A1246 (1965).
[45]The conclusions of Ref. 44 were based on the energy level of the $3P_1$ state, as calculated by Kohn (Ref. 14), namely 2.90 meV. These have been revised according to the results of Faulkner (Ref. 15) who finds a calculated value of 3.12 meV. Hence, the results of Ref. 44 should be adjusted by 0.22 meV.
[46]G. F. Neumark, Phys. Rev. B 5, 408 (1972).
[47]These equations include a modificatin of Ref. 46 to include screening by preferential compensation, as provided by Eq. (11) of this paper. We wish to thank Dr. Neumark for sending us this revised treatment prior to publication, and for an interesting discussion of these effects.
[48]E. M. Eagles and D. M. Edwards, Phys. Rev. 138, A1706 (1965).
[49]P. Norton and H. Levinstein (unpublished data on mercury-doped germanium).
[50]H. W. Streitwolf, Phys. Status Solidi 37, K47 (1970).
[51]M. Lax and J. L. Birman, Phys. Status Solidi B 49, K153 (1972).
[52]K. L. Ngai and E. J. Johnson, Phys. Rev. Lett. 29, 1607 (1972).
[53]P. J. Lin-Chung and K. L. Ngai, Phys. Rev. Lett. 29, 1610 (1972).
[54]Yu. A. Astrov and A. A. Kastal'skii, Fiz. Tekh. Poluprovodn. 6, 1773 (1972) [Sov. Phys.-Semicond. 6, 1528 (1973)].
[55]P. A. Temple and C. E. Hathaway, Phys. Rev. B 7, 3685 (1973).
[56]The two-phonon analysis is being conducted in collaboration with Kai Lung Ngai at the Naval Research Laboratory, who suggested this process to one of us (P.N.) as a possible explanation for our experimental evidence of TA phonon scattering.
[57]W. P. Dumke, Phys. Rev. 118, 938 (1960).
[58]J. R. Haynes, M. Lax, and W. F. Flood, J. Phys. Chem. Solids 8, 392 (1959).
[59]J. E. Aubrey, W. Gubler, T. Henningsen, and S. H. Koenig, Phys. Rev. 130, 1667 (1963).
[60]M. Asche, B. I. Boichenko, W. M. Bondar, and O. G. Sarbej, in Ref. 24, p. 793.
[61]P. J. Dean, J. R. Haynes, and W. F. Flood, Phys. Rev. 161, 711 (1967).
[62]N. O. Folland, Phys. Lett. A 27, 708 (1968).
[63]N. O. Folland, Phys. Rev. B 1, 1648 (1970).
[64]M. Lax and J. J. Hopfield, Phys. Rev. 124, 115 (1961).
[65]H. J. Stocker, Solid State Commun. 6, 125 (1968).
[66]M. H. Jørgensen and N. J. Meyer, Solid State Commun. 3, 311 (1965).
[67]N. Kawamura, J. Phys. Chem. Solids 27, 919 (1966).
[68]M. H. Jørgensen, Phys. Rev. 156, 834 (1967).
[69]P. K. Basu and B. R. Nag, Phys. Rev. B 1, 627 (1970).
[70]J. W. Holm-Kennedy and K. S. Champlin, J. Appl. Phys. 43, 1878 (1972). J. Appl. Phys. 43, 1889 (1972).
[71]M. V. Glushkov and A. I. Markin, Fiz. Tverd. Tela 14, 3525 (1972) [Sov. Phys.-Solid State 14, 2967 (1973)].
[72]M. Costato and S. Scavo, Nuovo Cimento B 52, 236 (1967), Nuovo Cimento B 54, 169 (1968).
[73]M. Costato and L. Reggiani, Nuovo Cimento B 58, 489 (1968), Phys. Status Solidi 36, 665 (1970), Phys. Rev. B 3, 1501 (1971).
[74]M. Costato, S. Fontanesi, and L. Reggiani, Nuovo Cimento Lett. 1, 946 (1969), J. Phys. Chem. Solids 34, 547 (1973).

[75]H. Heinrich and M. Kriechbaum, J. Phys. Chem. Solids 31, 927 (1970).
[76]E. M. Conwell, in Ref. 11, Suppl. 9.
[77]P. K. Basu and B. R. Nag, Phys. Rev. B 5, 1633 (1972).
[78]P. K. Basu and B. R. Nag, Phys. Status Solidi B 53, K61 (1972).
[79]T. Nishino and Y. Hamakawa, Phys. Status Solidi B 50, 345 (1972).
[80]E. E. Godik and V. I. Mirgorodskii, Fiz. Tekh. Poluprovodn. 6, 826 (1972) [Sov. Phys.-Semicond. 6, 715 (1972)].
[81]J. M. Guichar, F. Proix, C. Sebenne, and M. Balkanski, Phys. Rev. B 5, 3013 (1972).
[82]M. Lax, Phys. Rev. 119, 1502 (1960).
[83]R. L. Aggarwal and A. K. Ramdas, Phys. Rev. 137, A602 (1965).
[84]D. Redfield and M. A. Afromowitz, Philos. Mag. 19, 831 (1969).
[85]A. I. Ansel'm, Zh. Eksp. Teor. Fiz. 24, 85 (1953).
[86]S. Chandrasekhar, Rev. Mod. Phys. 16, 301 (1944).
[87]E. M. Gershenzon, G. N. Gol'tsman, and A. P. Mel'nikov, Zh. Eksp. Teor. Fiz. Pis'ma Red. 14, 281 (1971) [JETP Lett. 14, 185 (1971)].
[88]D. Thornton and A. Honig (private communication).
[89]L. E. Blagosklonskaya, E. M. Gershenzon, Yu. P. Ladyzhinskii, and A. P. Popova, Fiz. Tverd. Tela 11, 2967 (1969) [Sov. Phys.-Solid State 11, 2402 (1970)].